2012

Winding Resistance and Winding Power Loss of High-Frequency Power Inductors

Rafal P. Wojda
Wright State University

WINDING RESISTANCE AND WINDING POWER LOSS OF HIGH-FREQUENCY POWER INDUCTORS

A dissertation submitted in partial fulfillment

of the requirements for the degree of

Doctor of Philosophy

By

Rafal Piotr Wojda

B. Tech., Warsaw University of Technology, Warsaw, Poland, 2007

M. S., Warsaw University of Technology, Warsaw, Poland, 2009

2012

Wright State University

WRIGHT STATE UNIVERSITY

GRADUATE SCHOOL

August 20, 2012

I HEREBY RECOMMEND THAT THE DISSERTATION PREPARED UNDER MY SUPERVISION BY **Rafal Piotr Wojda** ENTITLED **Winding Resistance and Winding Power Loss of High-Frequency Power Inductors** BE ACCEPTED IN PARTIAL FULFILLMENT OF THE REQUIREMENTS FOR THE DEGREE OF **Doctor of Philosophy**.

Marian K. Kazimierczuk, Ph.D.
Dissertation Director

Ramana V. Grandhi, Ph.D.
Director, Ph.D. in Engineering Program

Andrew Hsu, Ph.D.
Dean, Graduate School

Committee on Final Examination

Marian K. Kazimierczuk, Ph.D.

Raymond E. Siferd, Ph.D.

Sayiu Ren, Ph.D.

Ronald Riechers, Ph.D.

Ronald Coutu, Ph.D.

Abstract

Wojda, Rafal Piotr. Ph.D., Engineering Ph.D. Program, Wright State University, 2012. *Winding Resistance and Winding Power Loss of High-Frequency Power Inductors.*

The scope of this research is concentrated on analytical winding size optimization (thickness or diameter) of high-frequency power inductors wound with foil, solid-round wire, multi-strand wire, and litz-wire conductors.

The first part of this research concerns analytical optimization of the winding size (thickness or diameter) for the inductors conducting a sinusoidal current. Estimation of winding resistance in individual inductor layers made of foil, taking into account the skin and proximity effects is performed. Approximated equations for the winding power loss in each layer are given and the optimal values of foil thickness for each layer are derived.

A low- and medium-frequency approximation of Dowell's equation for the multilayer foil winding is derived and analyzed. A new closed-form equation for the optimum foil thickness at which the global minimum of the winding ac resistance occurs is derived and an equation for the foil winding hill thickness at which the local maximum of the winding ac resistance is obtained is given.

An analytical optimization of solid-round-wire windings conducting a sinusoidal current is performed. New closed-form analytical equations are derived for the normalized valley diameter, normalized hill diameter, and normalized critical diameter.

An approximate model for multi-strand wire winding, including litz-wire winding is presented. The proposed model is evaluated using Dowell's equation. The model takes into consideration the existence of proximity effect within the litz-wire bundle, i.e., between the strands as well the skin effect. New closed-form analytical equations are derived for the normalized strand diameter to achieve the local minimum of the

ac winding losses for sinusoidal current.

The second part of this research concerns analytical optimization of the winding size (thickness or diameter) for the inductors conducting harmonic currents with and without dc offset. Analytical winding power loss minimization of foil inductors conducting ac harmonic currents with and without dc offset is presented.

Equations for the optimum foil thickness of inductors operating with multi-harmonic ac currents and equation for the optimum foil thickness of inductors operating with multi-harmonic ac currents superimposed on the dc current are derived. The design procedure for the foil inductor with optimized foil thickness is presented for a pulsewidth-modulated (PWM) dc-dc boost converter operating in discontinuous conduction mode (DCM).

An analytical optimization of solid-round-wire windings conducting both the dc and ac non-sinusoidal periodic currents is performed. Closed-form analytical equations for the normalized total-power-valley diameter and the normalized total-power-critical diameter are derived for inductors conducting ac non-sinusoidal periodic currents superimposed on the dc component. A design procedure of the inductor with an optimized winding diameter operating in PWM dc-dc buck converter in DCM is also presented.

Experimental verification of an analytical equations for foil, solid-round-wire, and litz-wire windings conducting sinusoidal currents is performed. Likewise, experimental verification of an analytical equations for foil and solid-round-wire winding inductors operating in PWM dc-dc power converters conducting non-sinusoidal periodic currents is also performed.

Contents

1 Introduction **1**

1.1 Background 1

1.2 Winding Types 2

1.3 Objectives 3

2 Foil Winding Resistance and Power Loss in Individual Layers of Inductors Conducting Sinusoidal Current **7**

2.1 General Equation for Resistance of Individual Layers 8

2.2 Optimum Thickness of Individual Layers 13

2.3 Approximation of $R_{wn}/R_{w1(HF)}$ 15

2.4 Example for Optimum Winding Resistance 20

2.5 Minimum Winding Resistance for Inductors With Uniform Foil Thickness 24

2.6 Conclusion 32

3 Analytical Optimization of Foil Windings Conducting Sinusoidal Current **33**

3.1 Foil Winding Power Loss Due to Ac Sinusoidal Current 33

3.2 Dowell's Equation for Winding Resistance of Foil Inductors 34

3.3 Low- and Medium-Frequency Approximation of Dowell's Equation . . 35

3.4 Foil Inductor Model 36

3.5 Experimental Results 37

3.6 Conclusion 38

4 Analytical Optimization of Solid-Round Wire Windings Conducting Sinusoidal Current **40**

4.1 Solid-Round Wire Winding Resistance 42

4.2 Low- and Medium-Frequency Approximation of Dowell's Equation . . 47

4.3 High-Frequency Approximation of Dowell's Equation 50
4.4 Boundary Between Low and Medium Frequencies for Solid-Round Wire Windings 51
4.5 Experimental Results 52
4.6 Conclusion 58

5 Winding Resistance of Litz-Wire and Multi-Strand Wire Inductors Conducting Sinusoidal Current 63
5.1 Proposed Model of Litz-Wire and Multi-Strand Wire Windings 65
5.2 Relationships Between Litz-Wire and Solid-Round Wire Windings . . 69
5.3 Solid-Round Wire Winding Resistance 69
5.4 Modified Dowell's Equation for Litz-Wire and Multi-Strand Wire Windings 72
5.5 Optimum Strand Diameter 76
5.6 Boundary Between Low and Medium Frequencies for Litz-Wire and Multi-Strand Wire Windings 79
5.7 Comparison of Winding Ac Resistances of Litz-Wire and Solid-Round Wire 82
5.8 Relationship Between R_w, ESR, and Measured Data 82
5.9 Experimental Verification 84
5.10 Conclusion 93

6 Analytical Winding Foil Thickness Optimization of Inductors Conducting Harmonic Currents 96
6.1 Introduction 96
6.2 Dowell's Equation for Winding Resistance of Foil Inductors at n-th Harmonic 97
6.3 Ac Power Loss in Foil Inductors 99

6.4 Total Power Loss in Foil Inductors 100
6.5 Low- and Medium-Frequency Approximation of the Winding Ac Resistance For Foil Inductors 102
6.6 Optimum Foil Thickness for Inductors Conducting Ac Harmonic Currents 105
6.7 Optimum Foil Thickness for Inductors With Dc and Ac Harmonic Currents 107
6.8 Model of Foil Inductors 108
6.9 Design Example of Inductor with Optimum Foil Winding Thickness and Minimum Power Loss 109
6.10 Experimental Results 111
6.11 Conclusion 111

7 Analytical Optimization of Solid-Round-Wire Windings Conducting Dc and Ac Non-Sinusoidal Periodic Currents 115

7.1 Winding Power Loss in Solid-Round-Windings Due to Dc and Ac Harmonic Currents 118
7.2 Dowell's Equation of Solid-Round-Wire Windings For Harmonics . . . 121
7.3 Low- and Medium-Frequency Approximation of Dowell's Equation for Harmonics 125
7.4 High-Frequency Approximation of Dowell's Equation for Harmonics . 129
7.5 Inductor Design 131
7.6 Experimental Verification 137
7.7 Conclusion 140

8 Conclusions 145

8.1 Summary 145
8.2 Contributions 147

9 Appendices **150**

9.1 Approximation of Dowell's Equation using Maclaurin's Serieses 150

9.2 Derivation of Low- and Medium-Frequency Approximation of Dowell's Equation for Foil Windings at Harmonic Frequency 151

9.3 Fourier Series of The Inductor Current for the Pulsewidth-Modualted Dc-Dc Converters in DCM 152

9.4 Derivation of Low- and Medium-Frequency Approximation of Dowell's Equation for Solid-Round-Wire Windings at Harmonic Frequency . . 154

9.5 Derivation of High-Frequency Approximation of Dowell's Equation for Harmonics 155

Relevant Publications **156**

Bibliography **157**

List of Figures

2.1 3-D plot of ac-to-dc resistance ratio F_{Rn} as a function of h/δ_w and n. 9

2.2 Individual layers ac-to-dc resistance ratio F_{Rn} as a function of h/δ_w for each of the first several layers. 10

2.3 Plots of F_{Rn} and F_R as a function of h/δ_w for three layer foil winding inductor ($N_l = 3$) and for total resistance of three layers. 11

2.4 Skin effect factor F_S as a function h/δ_w for each layer. 12

2.5 Proximity effect factor F_{Pn} as a function h/δ_w for n-th layer in linear-log scale. 13

2.6 Proximity effect factor F_{Pn} as a function h/δ_w for n-th layer in log-log scale. 14

2.7 3-D plot of normalized ac resistance $R_{wn}/(\rho_w l_T/b\delta_w)$ as a function of h/δ_w and n. 15

2.8 Normalized ac resistance $R_{wn}/(\rho_w l_T/b\delta_w)$ as a function of h/δ_w for each of the first several layers. 16

2.9 Normalized ac resistance $R_{wn}/(\rho_w l_T/b\delta_w)$ as a function of h/δ_w for each of the first several layers in enlarged scale. 17

2.10 Exact and approximated plots of $R_{w1}/(\rho_w l_T/b\delta_w)$ as a function of h/δ_w for n=1. 18

2.11 Exact and approximate plots of $R_{w3}/(\rho_w l_T/b\delta_w)$ as functions of h/δ_w at $n = 3$ for low and medium thickness. 19

2.12 Exact and approximate plots of $R_{w3}/(\rho_w l_T/b\delta_w)$ as functions of h/δ_w at $n = 3$ for high thickness. 20

2.13 Plots of $R_{wn(min)}$ and R_{wmin} as a function of frequency f for the foil inductor. 22

2.14 Exact and approximate plots of $R_w/(\delta_w l_w/b\delta_w)$ as functions of h/δ_w for three-layer inductor $N_l = 3$ for low and medium uniform thickness. 26

2.15 Plots of R_{wmin} and R_w as functions of frequency f for the inductor with optimized thickness of each layer $h_{opt1} = 0.5$ mm, $h_{opt2} = 0.267$ mm, $h_{opt3} = 0.203$ mm and for the inductor with a constant layer of thickness $h = h_{opt1} = 0.5$ mm. 27

2.16 Plots of R_{wmin} and R_w as functions of frequency f for the inductor with optimized thickness of each layer $h_{opt1} = 0.5$ mm, $h_{opt2} = 0.267$ mm, $h_{opt3} = 0.203$ mm and for the inductor with a constant layer of thickness $h = h_{opt2} = 0.267$ mm. 28

2.17 Plots of R_{wmin} and R_w as functions of frequency f for the inductor with optimized thickness of each layer $h_{opt1} = 0.5$ mm, $h_{opt2} = 0.267$ mm, $h_{opt3} = 0.203$ mm and for the inductor with a constant layer of thickness $h = h_{opt3} = 0.203$ mm. 29

2.18 Plots of R_{wmin} and R_w as functions of frequency f for the inductor with optimized thickness of each layer $h_{opt1} = 0.5$ mm, $h_{opt2} = 0.267$ mm, $h_{opt3} = 0.203$ mm and for the inductor with a constant layer of thickness $h_{opt} = 0.245$ mm for three-layer inductor ($N_l = 3$). 30

2.19 Ratio of the winding resistance with uniform optimum foil thickness $h_{opt1} = 0.5$ mm, $h_{opt2} = 0.267$ mm, $h_{opt3} = 0.203$ mm to the winding resistance with optimum individual layer thicknesses $h_{opt} = 0.245$ mm for three-layer inductor ($N_l = 3$). 31

3.1 Winding ac resistances of foil inductors predicted by Dowell's equation R_w and by low- and medium-frequency approximation R_{wLMF} as functions of foil thickness h. 35

3.2 The equivalent RLC lumped-parameter model of foil winding inductors. 37

3.3 Measured and theoretical winding ac resistances predicted by Dowell's equation as functions of foil thickness h. 39

4.1 Normalized winding ac resistance F_r as a function of d for inductor with several number of layers $N_l = 1, 2, 3, 4, 7$, and 10 at constant frequency $f = 100$ kHz, and $\eta = 0.9$. 44

4.2 Plots of F_R, R_{wdc}, and R_w as functions of d for four-layer inductor ($N_l = 4$) with $l_T = 6.6$ cm, $N = 100$, frequency $f = 100$ kHz, and $\eta = 0.9$. 45

4.3 Plots of exact F_R, low and medium-frequency approximation F_{RLMF}, and high-frequency approximation F_{RHF} of ac-to-dc resistance ratio as functions of A for five-layer inductor ($N_l = 5$) and porosity factor $\eta = 0.9$. 47

4.4 Plots of exact F_r, low and medium-frequency approximation F_{rLMF}, and high-frequency approximation F_{rHF} of normalized winding ac resistance as functions of A for five-layer inductor ($N_l = 5$) and porosity factor $\eta = 0.9$. 48

4.5 Plots of exact normalized winding ac resistance F_r and measured values for inductors wound with AWG32, AWG30, AWG26, AWG24, and AWG20 solid round wire as functions of wire diameter d for two-layer inductor ($N_l = 2$) at frequency $f = 100$ kHz. 54

4.6 Plots of exact normalized winding ac resistance F_r and measured values for inductors wound with AWG32, AWG30, AWG26, AWG24, and AWG20 solid round wire as functions of wire diameter d for four-layer inductor ($N_l = 4$) at frequency $f = 100$ kHz. 55

4.7 Plots of exact normalized winding ac resistance F_r and measured values for inductors wound with AWG32, AWG30, AWG26, AWG24, and AWG20 solid round wire as functions of wire diameter d for two-layer inductor ($N_l = 2$) at frequency $f = 200$ kHz. 56
4.8 Plots of exact normalized winding ac resistance F_r and measured values for inductors wound with AWG32, AWG30, AWG26, AWG24, and AWG20 solid round wire as functions of wire diameter d for four-layer inductor ($N_l = 4$) at frequency $f = 200$ kHz. 57
4.9 Plots of exact normalized winding ac resistance F_r and measured values for inductors wound with AWG32, AWG30, AWG26, AWG24, and AWG20 solid round wire as functions of wire diameter d for two-layer inductor ($N_l = 2$) at frequency $f = 400$ kHz. 58
4.10 Plots of exact normalized winding ac resistance F_r and measured values for inductors wound with AWG32, AWG30, AWG26, AWG24, and AWG20 solid round wire as functions of wire diameter d for four-layer inductor ($N_l = 4$) at frequency $f = 400$ kHz. 59
4.11 Plots of exact normalized winding ac resistance F_r and measured values for inductors wound with AWG32, AWG30, AWG26, AWG24, and AWG20 solid round wire as functions of wire diameter d for two-layer inductor ($N_l = 2$) at frequency $f = 1$ MHz. 60
4.12 Plots of exact normalized winding ac resistance F_r and measured values for inductors wound with AWG32, AWG30, AWG26, AWG24, and AWG20 solid round wire as functions of wire diameter d for four-layer inductor ($N_l = 4$) at frequency $f = 1$ MHz. 61
5.1 Model of litz-wire and multi-strand wire windings. 66

5.2 Plots of the ac-to-dc winding resistance ratio F_R as a function of d/δ_w for solid-round wire with $\eta = 0.9$ and several numbers of layers $N_l = 1, 2, 4, 10$. 71

5.3 3-D plots of ac-to-dc winding resistance ratio F_R as a function of d/δ_w and number of layers N_l for power inductors. a) With solid-round wire winding. b) With $k = 225$ strand litz-wire winding at $\eta = 0.9$. 74

5.4 Plots of $F_{R(solid)}$ and $F_{R(litz)}$ as functions of d/δ_w and as functions of frequency f for $N_l = 4$, $d = 1.45$ mm, $k = 100$, $d_{str} = 145$ μm, $k = 2500$, $d_{str} = 29$ μm, and $\eta = 0.9$. (a) $F_{R(solid)}$ and $F_{R(litz)}$ as functions of d/δ_w. (b) $F_{R(solid)}$ and $F_{R(litz)}$ as functions of frequency f. 75

5.5 Plots of the number of strands k_{cr} as functions of normalized optimum strand diameter $d_{str(opt)}/\delta_w$ at different number of bundle layers $N_l = 2, 5, 10$ and $\eta = 0.7$. 78

5.6 Plots of the normalized strand diameter at the boundary between the low and medium frequencies $(d_{str}/\delta_w)_B$ for litz-wire winding as a function of number of layers N_l for $k = 30$ and $k = 300$ at $\eta = 0.7$. 80

5.7 Ratio of the winding ac resistance of the litz-wire $R_{w(litz)}$ to the winding ac resistance of the solid-round wire $R_{w(solid)}$ as function of d/δ_w and frequency f with the same cross-sectional conductor area at $d = 0.32$ mm, $N_l = 4$, $N = 114$, $l_T = 6$ cm, and $k = 10$, 100, 2000 strands at $\eta = 0.9$. (a) Ratio of $R_{w(litz)}$ to $R_{w(solid)}$ as functions of d/δ_w. (b) Ratio of $R_{w(litz)}$ to $R_{w(solid)}$ as functions of frequency f. 81

5.8 Equivalent circuit of inductors with negligible core losses. (a) Lumped-parameter equivalent circuit. (b) Equivalent series circuit. 83

5.9 Magnitude and phase of inductor impedance Z as functions of frequency for $N_l = 4$, $N = 114$, $k = 20$, $d_{str} = 80$ μm, $L = 168$ μH, $l_T = 6$ cm, and $f_r = 2.62$ MHz. (a) Magnitude of inductor impedance $|Z|$. (b) Phase of inductor impedance ϕ. 85

5.10 Measured (circles) and computed (continuous line) equivalent series resistance r and litz-wire winding ac resistance $R_{w(litz)}$ as functions of frequency f. (a) Equivalent series resistance r. (b) Litz-wire winding ac resistance $R_{w(litz)}$. 88

5.11 Measured (circles) and computed (continuous line) quality factor and reactance factor of litz-wire inductor as functions of frequency f neglecting core losses. (a) Quality factor $Q_{LRw} = \omega L/R_{w(litz)}$. (b) Reactance factor $q = x/r$. 90

5.12 Plots of measured (circles) and computed litz-wire winding ac resistance $R_{w(litz)}$ as functions of frequency f described by modified Dowell's equation in (5.4), approximate Dowell's equation in (5.22), and Sullivan's equation in (5.54). 91

6.1 3D plot of normalized winding ac resistance F_{rn} as a function of normalized foil thickness h/δ_w and order of harmonic n for the ten-layer foil winding inductor ($N_l = 10$) at a fixed frequency f. 99

6.2 Plots of P_{wdc}, P_{wac}, and $P_w = P_{wdc} + P_{wac}$ as functions of foil thickness h for 15-layer foil winding inductor. 102

6.3 The exact (continuous line) and approximate (dashed line) plots of normalized winding ac resistance F_{r1} and $F_{rLMF(1)}$ as a function of h/δ_w for the single-layer inductor ($N_l = 1$). 103

6.4 The exact (continuous line) and approximate (dashed line) plots of normalized winding ac resistance F_{r50} and $F_{rLMF(50)}$ as a function of h/δ_w for the single-layer inductor ($N_l = 1$). 104

6.5 The exact (continuous line) and approximate (dashed line) plots of normalized winding ac resistance F_{r1} and $F_{rLMF(1)}$ as a function of h/δ_w for the ten-layer inductor ($N_l = 10$). 105

6.6 The exact (continuous line) and approximate (dashed line) plots of normalized winding ac resistance F_{r50} and $F_{rLMF(50)}$ as a function of h/δ_w for the ten-layer inductor ($N_l = 10$). 106

6.7 Lumped-parameter equivalent circuit of the foil inductor. 108

6.8 Plots of actual (circles) and exact (solid line) total winding power losses as functions of foil thickness h. 112

7.1 Plots of P_w, P_{wac}, and P_{wdc} as functions of the solid-round wire diameter d for the eight-layer inductor ($N_l = 8$) of the PWM dc-dc buck converter in discontinuous conduction mode at switching frequency $f_s = 100$ kHz and with 100 harmonics. 120

7.2 Plots of F_{R5}, R_{w5}, and R_{wdc} of the solid-round-wire winding at 5-th harmonic frequency as functions of solid-round wire diameter d for the eight-layer inductor ($N_l = 8$), the fundamental frequency $f = 100$ kHz, the length of the round wire $l_w = 8$ m, and the porosity factor $\eta = d/p = 0.9$. 123

7.3 Normalized winding ac resistance at the n-th harmonic frequency F_{rn} of the solid-round-wire winding as a function of d for the eight-layer inductor ($N_l = 8$) at fundamental frequency $f = 100$ kHz ($n = 1$), the higher harmonic order $n = 5,\ 20,\ 50,\ 100$, and the porosity factor $\eta = d/p = 0.9$. 124

7.4 Plots of F_{R5}, F_{RLMF5}, and F_{RHF5} as functions of A for the eight-layer inductor ($N_l = 8$) and the porosity factor $\eta = d/p = 0.9$. 126

7.5 Plots of F_{r5}, F_{rLMF5}, and F_{rHF5} as functions of A for the eight-layer inductor ($N_l = 8$) and the porosity factor $\eta = d/p = 0.9$. 127

7.6 Plots total winding power losses P_w as a function of converter output power P_O of the designed inductor for the PWM dc-dc converter at three different input voltages $V_I = 353,\ 373$, and 393 V. 135
7.7 Plots total winding power lossesP_w as a function of converter input voltage V_I of the designed inductor for the PWM dc-dc converter at three different converter output powers $P_O = 25.5,\ 10$, and 5 W. . . . 136
7.8 Inductor current waveform factor k_w as a function of the output power P_O for the designed PWM dc-dc buck converter at $V_I = 373$ V. 137
7.9 Inductor current waveform factor k_w as a function of the dc input voltage V_I for the designed PWM dc-dc buck converter at $P_O = 25.5$ W.138
7.10 Plots of Dowell's winding ac resistance (solid line) and actual ac resistance (circles) as functions of frequency for the four-layer inductor ($N_l = 4$) wound with AWG26 operating in PWM dc-dc buck converter in DCM. 140
7.11 Plots of winding dc power loss P_{wdc}, winding ac power loss P_{wac} total power loss P_w, and actual total winding power loss for inductor wound with AWG26 round wire as function of diameter d for four-layer inductor ($N_l = 4$) of a winding conductor length $l_w = 4.664$ m operating in PWM dc-dc buck converter in DCM at full power. 141
7.12 Plots of winding power loss per unit length (solid line) P_{lw}, and actual winding power loss per unit length (circles) as function of diameter d for inductors wound with AWG26, AWG24, and AWG20 round wire for four-layer inductor ($N_l = 4$) operating in PWM dc-dc buck converter in DCM at full power. 142
9.1 Inductor current waveform $i_L(t)$ for the PWM dc-dc power converters operating in DCM. 153

List of Tables

2.1 Exact and aproximate optimum foil thickness for individual inductor layers. 21

2.2 Approximate optimum uniform foil thickness for multi-layer inductor. 25

4.1 Parameters of designed and measured inductors. 53

4.2 Diameter of inductor winding at $\eta = 0.7$. 54

4.3 Critical diameter of inductor winding at $\eta = 0.7$. 56

7.1 Parameters of designed and measured inductors. 138

Acknowledgements

At the beginning I would like to thank Two Very Important People Professor, Dr. Marian K. Kazimierczuk and Alicja Kazimierczuk for their friendship and for the fact that they have been my constant support through all those hard times.

My gratitude goes to the Polish-American Fulbright Commission, Barbara Maciejewska and Andrzej Dakowski, as well as the U.S. Embassy in Warsaw, the former U.S. Ambassador to Poland Victor Ashe, and U.S. Department of State for letting me pursue my Ph.D. degree in The United States of America.

I want to thank Dr. Raymond Siferd, Dr. Saiyu Ren, Dr. Ronald Coutu, and Dr. Ronald Riechers for serving as members of my Ph.D. defense committee.

I also want to thank the Ph.D. program, the Department of Electrical Engineering, and the Graduate School at Wright State University for giving me the opportunity to obtain my Ph.D. degree at Wright State University.

A special thanks goes to my mother, my father, and my brother for their love and patience in raising me.

1 Introduction

1.1 Background

Power electronics is a discipline spawned by real-life applications in industrial, commercial, residential, medical, military, and aerospace environments. Much of its development evolves around some immediate needs for solving specific power conversion problems. In the age of a constant improvement and advancement of new wide bandgap semiconductor devices such as silicon carbide (SiC) and gallium nitride (GaN), the problem of low efficiency at high frequencies of the switching-mode power converters due to the conduction and switching losses becomes less significant. This is mainly because these devices characterize with a low gate capacitance and low on-resistance, which permits much higher switching frequencies and much lower losses than those in competing silicon devices. However, improved performance of semiconductor devices eventually will not solve the problem of low efficiency in switching-mode power converters because of inevitable use of magnetic components. Accompanying losses in semiconductor devices for the switching-mode power converters are losses in magnetic devices [1]-[84].

Power inductors and transformers are common magnetic devices used in power electronic circuits and their importance in modern technology is ever increasing. They are used in many electrical engineering applications, such as power supplies, electric vehicles, aircraft, renewable energy, induction heating, battery chargers, energy scavenging, amplitude modulators for radio transmitters, energy harvesting, telecommunications, and other high-frequency circuits. Their role in these applications is to store and transfer energy through the magnetic field with the highest possible efficiency and also to provide filtering.

Increased operating frequencies and high values of both the dc and ac non-sinusoidal periodic currents flowing through the inductor or transformer windings become a sig-

nificant problem [12]-[30]. The results of these studies show that power losses in magnetic device windings may be similar or sometimes even greater, especially at high frequencies, than the losses in semiconductor devices.

The winding power losses of power inductors and power transformers operating in switching-mode power converters are composed of the dc loss and the ac loss. The winding dc power loss is caused by the flow of the dc current through the winding. The ac winding power loss is a result of the superposition of two self-induced eddy-current density distributions. The self-induced distributions of eddy-current densities are caused by two orthogonal effects: the skin effect and the proximity effect [1]-[51], [56]-[64], [65]-[71], [73]-[76], [78]-[84]. Both these effects increase with the operating frequency. The skin effect is caused in a conductor by the magnetic field induced by its own current, resulting in a higher current density closer to the surface of the conductor than that in the center of the conductor. The proximity effect is caused by magnetic fields induced by currents flowing in adjacent conductors, resulting in non-uniform current density distribution in the conductor cross section.

A reduction in the winding dc power loss can be achieved by increasing the cross-sectional area of the winding conductor. The skin effect and the proximity effect are greatly dependent on the winding conductor size (thickness or diameter). A reduction in the winding ac power loss can be achieved by optimization of winding conductor size (thickness or diameter).

1.2 Winding Types

Different kinds of winding conductors such as: foil, strip (rectangular), square-wire, solid-round wire, and litz-wire are used in high-frequency magnetic devices. Their application depends on the electrical, mechanical, and thermal requirements of a designed magnetic component.

Thermal, mechanical, and electrical properties of foil inductors are much better

than the properties of inductors made of round wires. First of all, thermal dissipation property of the inductor wound with a round wire is worse than the inductor wound with foil. For a multi-layer round wire inductor, the innermost layer is isolated from the ambient surroundings. In contrast, in foil inductors where the foil extends over the entire width of the inductor, every layer has two edges in contact with the surrounding environment, facilitating heat transfer. Second, mechanical vibrations or high current flow can cause loosening of round wire windings. Third, voltage stresses between the layers are constant in foil inductors, while in round wire inductors stresses between the two layers of the inductor depend on the number of turns in the layer. Fourth, foil inductors have approximately homogeneous tangential magnetic field, and 1-D Dowell's equation [2], which was derived under this assumption, gives quite accurate description of the winding resistance. Additionally, the core window utilization area for the foil inductors is higher than for the round wire inductors because of the unused space between wires and the insulation that is used to coat the wire. However, foil winding inductors tend to have relatively high self-capacitance and therefore a low first self-resonant frequency [14], [79], [80].

Solid-round-wire winding inductors are widely used in PWM dc-dc power converters, resonant power converters, resonant inverters, EMI filters, and magnetic sensors. The advantage of solid-round conductors is a low cost.

Parallel multi-strand wire, including the litz-wire or in German *Litzendraht* are used to reduce winding power losses of inductors and transformers. A multi-strand wire winding consists of at least two strands, and a litz-wire winding consists of many strands, up to couple of thousands of strands in a bundle [87].

1.3 Objectives

The study conducted in this research concerns windings made of foil, solid-round wire, and litz-wire including multi-strand wire. The objectives of this research are

twofold. Firstly, for the windings conducting only sinusoidal currents the objectives are:

- to derive an expression for the normalized valley thickness of the foil inductor windings, where the global minimum of the ac winding resistance occurs;
- to derive an expression for the normalized foil hill thickness at which the winding ac resistance reaches its local maximum;
- to derive an expression for the normalized valley wire diameter of solid-round wire inductor windings, where the local minimum of the wire ac winding resistance occurs;
- to derive an expression for the normalized critical wire diameter of solid-round wire inductor windings, where the ac winding resistance is equal to the winding resistance at the valley wire diameter;
- to determine the normalized hill diameter of the solid-round wire windings, where the local maximum of the wire ac winding resistance occurs;
- to determine the boundary frequency between the low-frequency and medium-frequency ranges for a solid-round wire windings.
- to introduce a model of litz-wire winding;
- to adapt Dowell's equation for the litz-wire winding model;
- to develop a relatively simple equation for the resistance of litz-wire winding;
- to determine the optimum strand diameter;
- to determine the number of strands in the litz-wire bundle at which the minimum winding ac resistance is obtained;

- to determine the boundary frequency between the low-frequency and medium-frequency ranges for a litz-wire winding and a solid-round wire winding;
- to compare the resistance of a litz-wire winding with that of a solid-round wire winding over a wide frequency range;
- to experimentally verify the analytical equations for foil, solid-round-wire, and litz-wire windings conducting sinusoidal currents.

Secondly, for the windings conducting ac non-sinusoidal periodic currents the objectives are:

- to derive an expression for the optimum foil thickness in order to achieve the minimum ac winding power loss of a foil inductor conducting ac harmonic currents;
- to show the relationship among the fundamental current, the dc current, and the number of layers for which the local minimum of the total dc and ac solid-round-wire winding losses exists;
- to derive an expression for the normalized total-power-valley wire diameter of the solid-round-wire windings, where the local minimum of the winding dc and ac power losses (valley) occurs;
- to derive an expression for the normalized total-power-critical wire diameter of the solid-round-wire windings (greater than the normalized total-power-valley wire diameter), where the winding dc and ac power losses are equal to the winding dc and ac power losses at the local minimum (valley);
- to present the design procedure of the inductor optimized for the minimum of winding dc and ac power losses for the PWM dc-dc buck converter operating

in discontinuous conduction mode (DCM) and to verify the optimization by measurements.

- to experimentally verify the analytical equations for the foil and the solid-round-wire winding inductors operating in PWM dc-dc power converters in DCM, conducting non-sinusoidal periodic currents.

Results obtained in this research are very useful for many designers since it helps to choose the optimum foil thickness or optimum solid-round wire/strand diameter based on the inductors operating frequency, the number of winding layers, and the current waveform.

2 Foil Winding Resistance and Power Loss in Individual Layers of Inductors Conducting Sinusoidal Current

This chapter presents an estimation of high-frequency winding resistance and power loss in individual inductor layers made of foil, taking into account the skin and proximity effects. Approximated equations for power loss in each layer are given and the optimal values of foil thickness for each layer are derived. It is shown that the winding resistance of individual layers significantly increases with the operating frequency and the layer number, counting from the center of an inductor. The winding resistance of each foil layer exhibits a minimum value at an optimal layer thickness. The total winding resistance increases with the total number of layers.

Generally, the power loss in the winding of an inductor at high frequencies is caused by two effects of eddy currents: skin effect and the proximity effect [1]-[51], [56]-[64], [65]-[71], [73]-[76], [78]-[84]. These effects influence the distribution of the current in the conductor, causing an increase in the winding resistance. Moreover, the winding resistance and the winding power loss increase with the operating frequency. The skin effect is caused in the conductor by the magnetic field induced by its own current. The skin effect is identical in all layers. The proximity effect is caused by the magnetic field induced by currents flowing in the adjacent conductors. The proximity effect increases rapidly when the layer number increases. Inductors made of copper foil have beneficial properties in designing power circuits. Its thermal, mechanical, and electrical properties are much better than the properties of round wire inductors. Foil winding are attractive in low profile inductors and transformers. In addition, they are commonly used in high current magnetic components.

The purpose of this chapter is to present the analysis of winding resistance of individual layers in multi-layer foil inductors with a magnetic core and compare their

properties with those of the uniform layer thickness.

2.1 General Equation for Resistance of Individual Layers

Inductors made up of straight, parallel foil conductor are considered. There is one winding turn in each layer. This model can be used for low profile flat inductors and inductors wound on round magnetic cores with low radius of curvature. The magnetic field H in this kind of inductors can be described by the second-order ordinary differential equation, called the Helmholtz equation,

$$\frac{d^2H}{dx^2} = \gamma^2 H, \tag{2.1}$$

where γ is the complex propagation constant described by

$$\gamma = \sqrt{j\omega\mu_0\sigma_w} = \sqrt{\frac{j\omega\mu_0}{\rho_w}} = \frac{\sqrt{2j}}{\rho_w} = \frac{1+j}{\rho_w}, \tag{2.2}$$

the skin depth is

$$\delta_w = \sqrt{\omega\mu_0\sigma_w} = \frac{1}{\sqrt{\pi f\mu_0\sigma_w}} = \frac{\rho_w}{\pi f\mu_0}, \tag{2.3}$$

$\rho_w = 1/\sigma_w$ is the conductor resistivity, f is the operating frequency, and μ_0 is the free space permeability. The solution of (2.1) leads to the distribution of the magnetic field intensity H and the current density J in the n-th winding layer. The complex power in the n-th layer is [14]

$$P_{wn} = \frac{\rho_w l_T I_m^2 \gamma}{2b}\left[\coth(\gamma h) + 2(n^2-n)\tan\left(\frac{\gamma h}{2}\right)\right], \tag{2.4}$$

where h is the thickness of foil, b is the breadth of the foil and l_T is the mean turn length (MTL). Assume that the current flowing through the inductor foil winding is sinusoidal

$$i_L = I_m \sin(\omega t). \tag{2.5}$$

The time-average real power loss in the n-th layer is

$$P_{wn} = R_{wn} I_{rms}^2 = [R_{skin(n)} + R_{prox(n)}] I_{rms}^2 = [R_{skin} + R_{prox(n)}] I_{rms}^2, \tag{2.6}$$

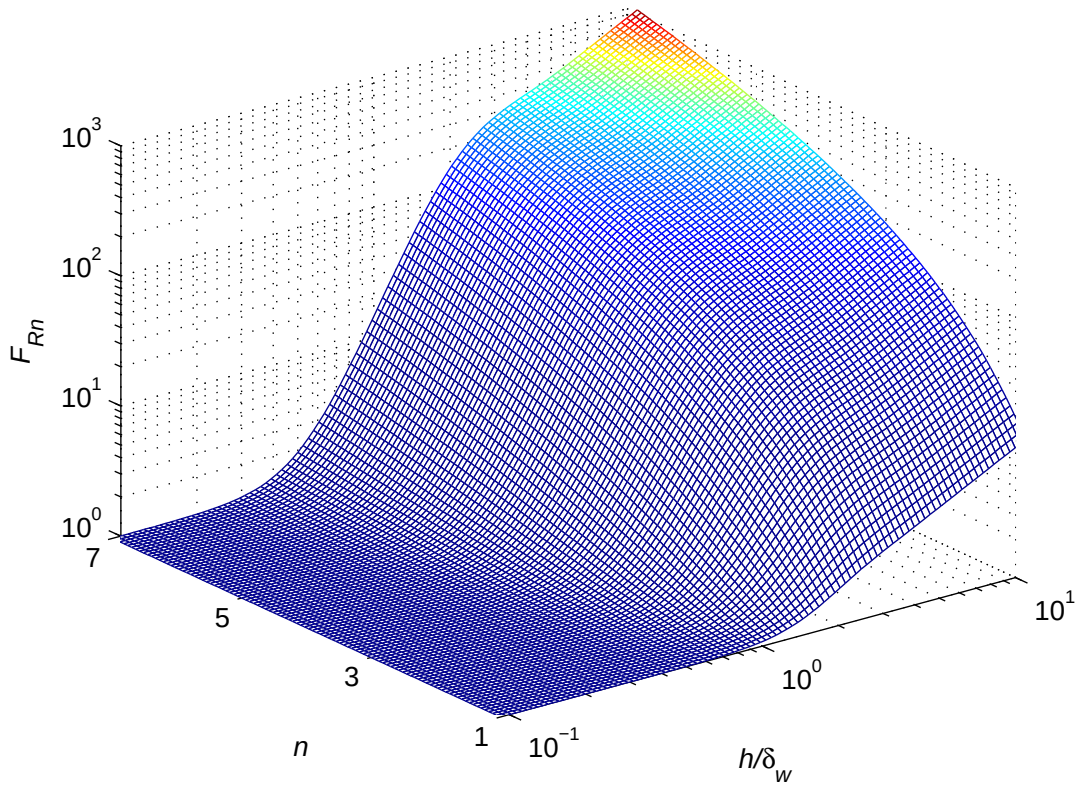

Figure 2.1: 3-D plot of ac-to-dc resistance ratio F_{Rn} as a function of h/δ_w and n.

where $R_{skin(n)} = R_{skin}$ is the resistance of each layer due to the skin effect and is the same for each layer and $R_{prox(n)}$ is the resistance of the n-th layer due to the proximity effect and appreciably increases from the innermost layer to the outermost layer. If the RMS current is equal to the dc current through the inductor, then the time-average real power loss in the n-th layer of the winding P_{wn}, normalized with respect to the dc power loss P_{wdcn}, is equal to the ac-to-dc resistance ratio of the n-th layer R_{wn}/R_{wdcn}. Hence, the ac-to-dc resistance ratio in the n-th layer is given by [2]

$$F_{Rn} = \frac{P_{wn}}{P_{wdcn}} = \frac{R_{wn}}{R_{wdcn}}$$
$$= \left(\frac{h}{\delta_w}\right)\left[(2n^2-2n+1)\frac{\sinh(\frac{2h}{\delta_w})+\sin(\frac{2h}{\delta_w})}{\cosh(\frac{2h}{\delta_w})-\cos(\frac{2h}{\delta_w})} - 4(n^2-n)\frac{\sinh(\frac{h}{\delta_w})\cos(\frac{h}{\delta_w})+\cosh(\frac{h}{\delta_w})\sin(\frac{h}{\delta_w})}{\cosh(\frac{2h}{\delta_w})-\cos(\frac{2h}{\delta_w})}\right]. \quad (2.7)$$

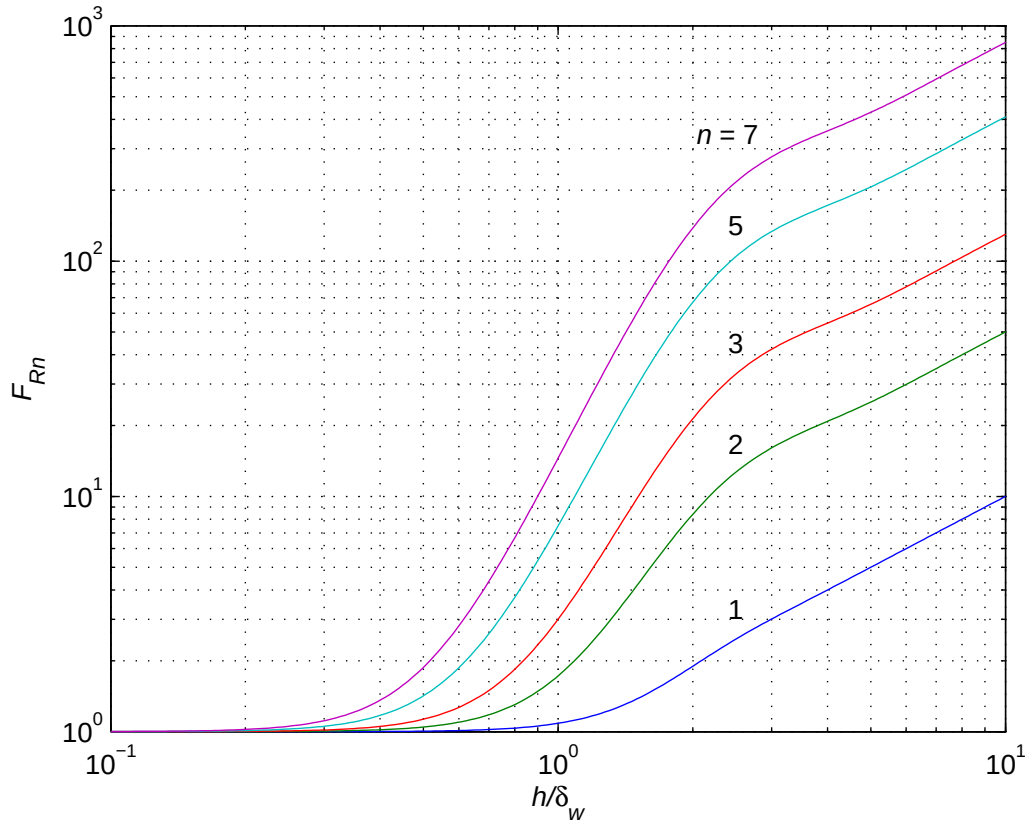

Figure 2.2: Individual layers ac-to-dc resistance ratio F_{Rn} as a function of h/δ_w for each of the first several layers.

Fig. 2.1 shows a 3-D plot of ac resistance ratio F_{Rn} as a function of h/δ_w and n. Fig. 2.2 shows plots of F_{Rn} as a function of h/δ_w for several individual layers. It can be seen that the normalized ac-to-dc resistance ratio F_{Rn} significantly increases as the ratio h/δ_w increases and as the layer number n increases, counting from the innermost layer to the outermost layer. At a fixed foil thickness h, three frequency ranges can be distinguished: low-frequency range, medium-frequency range, and high-frequency range. In the low-frequency range, $h << 2\delta_w$, the skin and the proximity effects are negligible, the current density is uniform, $R_w \approx R_{wdc}$, and therefore $F_{Rn} \approx 1$. In the medium-frequency range, the current density is no longer uniform, and thereby F_{Rn} increases with frequency. The boundary between the low and medium frequency ranges decreases as the layer number n increases. In the high-frequency range, the

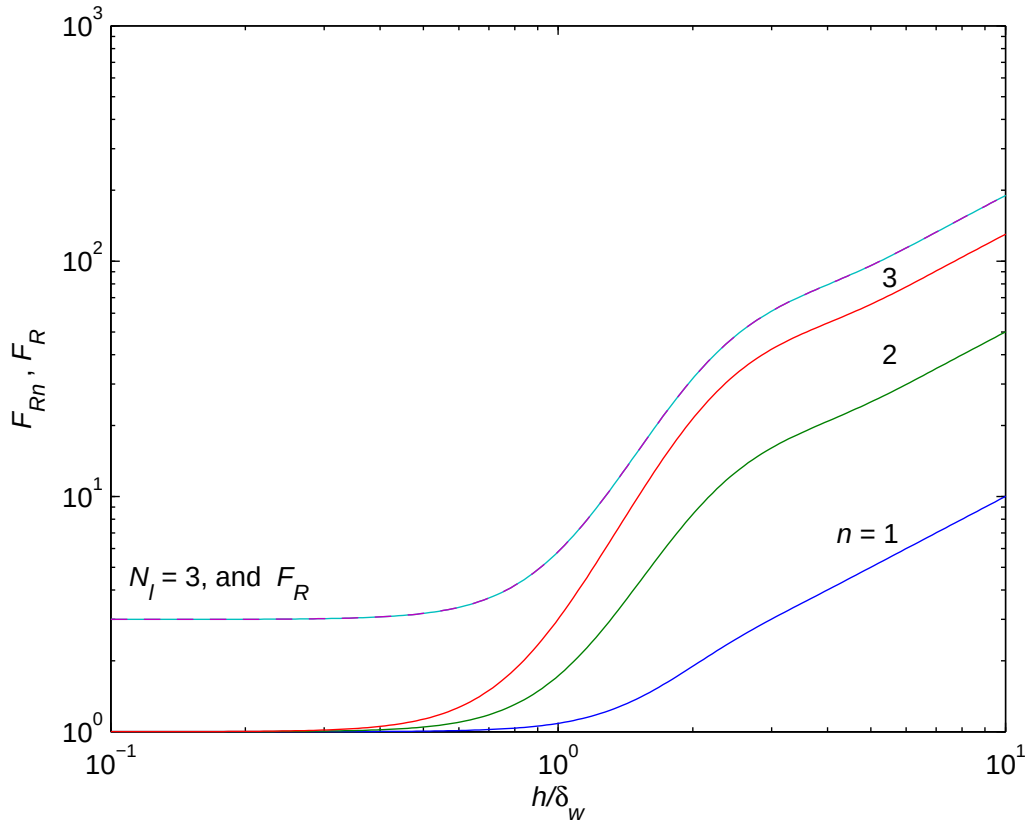

Figure 2.3: Plots of F_{Rn} and F_R as a function of h/δ_w for three layer foil winding inductor ($N_l = 3$) and for total resistance of three layers.

current flows only near both foil surfaces and F_{Rn} increases with frequency. The rate of increase of F_{Rn} in the high-frequency range is lower than that in the-medium frequency range for $n \geq 2$. The sum of the ac-to-dc resistance ratios of all layers is given by

$$F_{RNS} = \frac{R_{w1}}{R_{wdc1}} + \frac{R_{w2}}{R_{wdc2}} + \frac{R_{w3}}{R_{wdc3}} + ... + \frac{R_{wN_l}}{R_{wdcN_l}} = \sum_{n=1}^{N_l} F_{Rn}. \tag{2.8}$$

where N_l is the number of foil winding layers. Fig. 2.3 shows plots of F_{Rn} and F_{RNS} as functions of h/δ_w for three-layer foil winding inductor.

The ac-to-dc resistance ratio F_{Rn} can be expressed as

$$F_{Rn} = F_S + F_{Pn}, \tag{2.9}$$

where the skin effect ac-to-dc resistance ratio is identical for each layer and is expressed

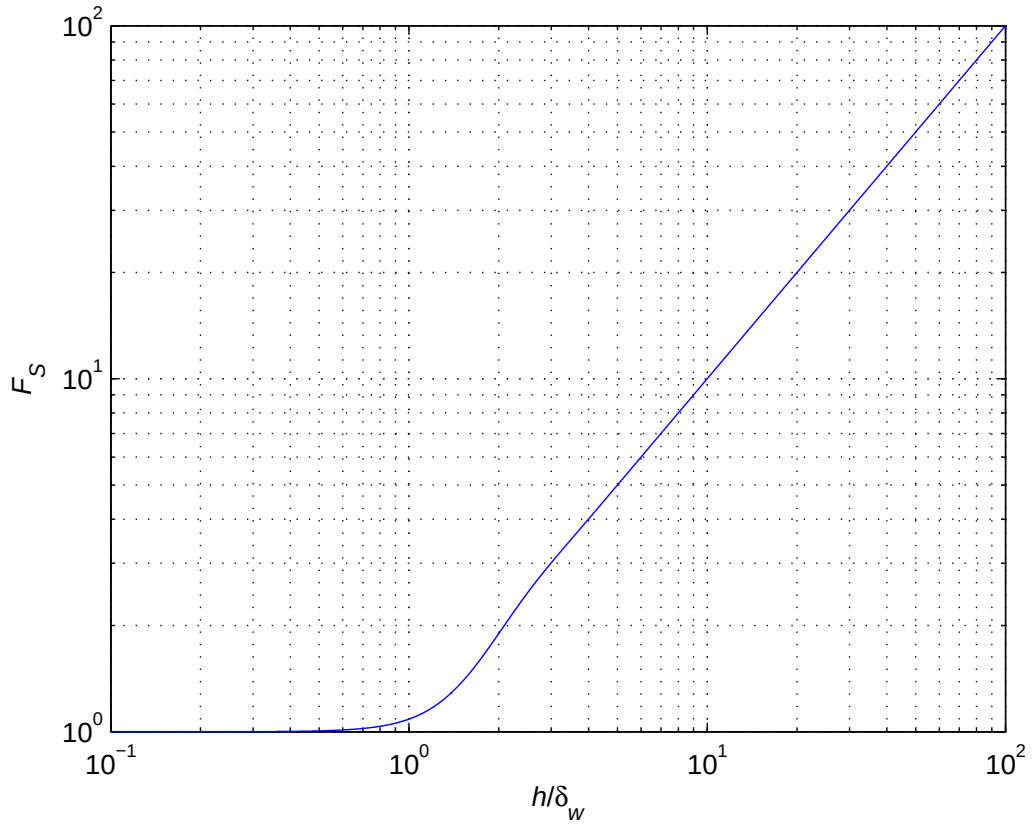

Figure 2.4: Skin effect factor F_S as a function h/δ_w for each layer.

by

$$F_S = \frac{R_{skin}}{R_{wdcn}} = \left(\frac{h}{\delta_w}\right) \frac{\sinh(\frac{2h}{\delta_w}) + \sin(\frac{2h}{\delta_w})}{\cosh(\frac{2h}{\delta_w}) - \cos(\frac{2h}{\delta_w})} \tag{2.10}$$

and the proximity effect ac-to-dc resistance ratio of the n-th layer is given by

$$F_{Pn} = \frac{R_{prox(n)}}{R_{wdcn}} = 2n(n-1)\left(\frac{h}{\delta_w}\right) \frac{\sinh(\frac{h}{\delta_w}) - \sin(\frac{h}{\delta_w})}{\cosh(\frac{h}{\delta_w}) + \cos(\frac{2h}{\delta_w})}. \tag{2.11}$$

The skin effect factor F_S is identical for all the winding layers. The proximity effect factor F_{Pn} is zero for the first layer and rapidly increases with the layer number n. For multi-layer inductors, the proximity effect becomes dominant. Fig. 2.4 shows the skin effect factor F_S as a function of h/δ_w for each layer. It can be seen that the skin effect is negligible for $h/\delta_w < 1$. For $h/\delta_w > 1$, F_S increases rapidly with h/δ_w. The proximity effect factor F_{Pn} as a function of h/δ_w is shown in Figs. 2.5 and 2.6 in linear-log and log-log scales, respectively. It can be seen from Fig. 2.5 that the

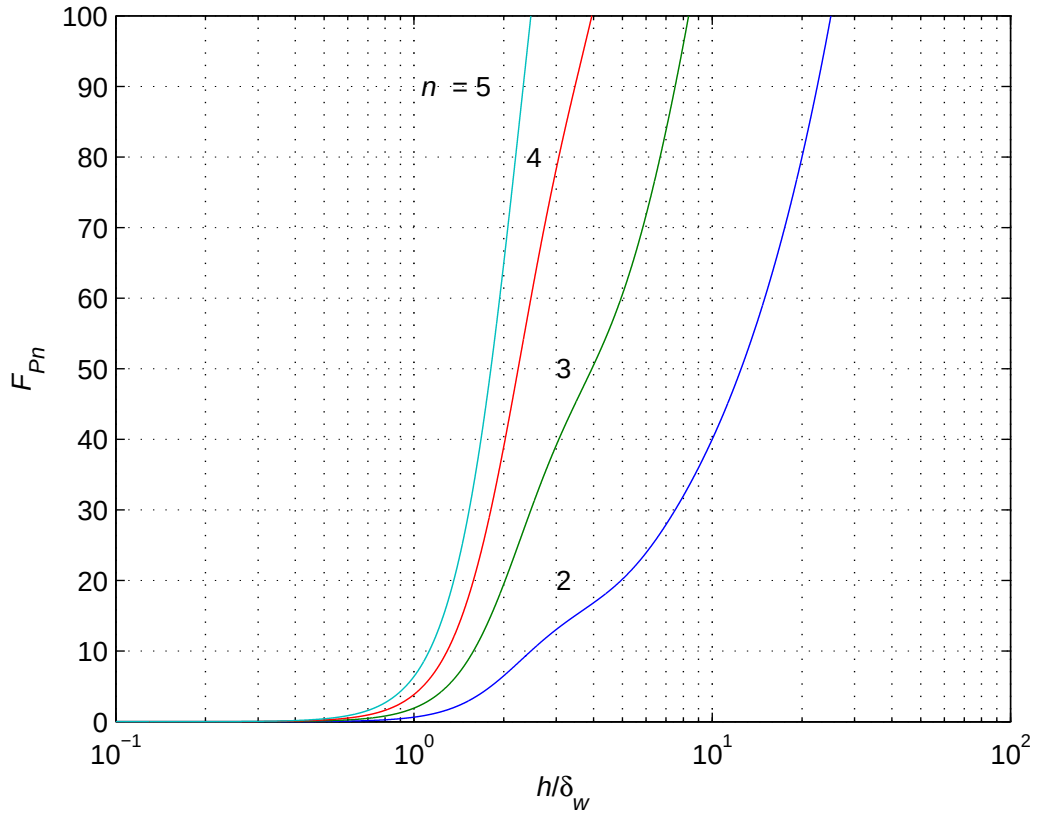

Figure 2.5: Proximity effect factor F_{Pn} as a function h/δ_w for n-th layer in linear-log scale.

proximity effect is negligible for $h/\delta_w < 1$ and does not exist for the first layer. It can be observed from Fig. 2.6 that the proximity effect factor F_{Pn} increases rapidly with h/δ_w for the range $1 < h/\delta_w < 2$ and increases with h/δ_w at a lower rate for $h/\delta_w > 2$.

2.2 Optimum Thickness of Individual Layers

The effective width of the current flow is approximately equal to the skin depth δ_w. Therefore, the winding resistance and the power loss in the innermost layer at high frequencies are, respectively,

$$R_{w1(HF)} = \frac{\rho_w l_T}{b\delta_w} \tag{2.12}$$

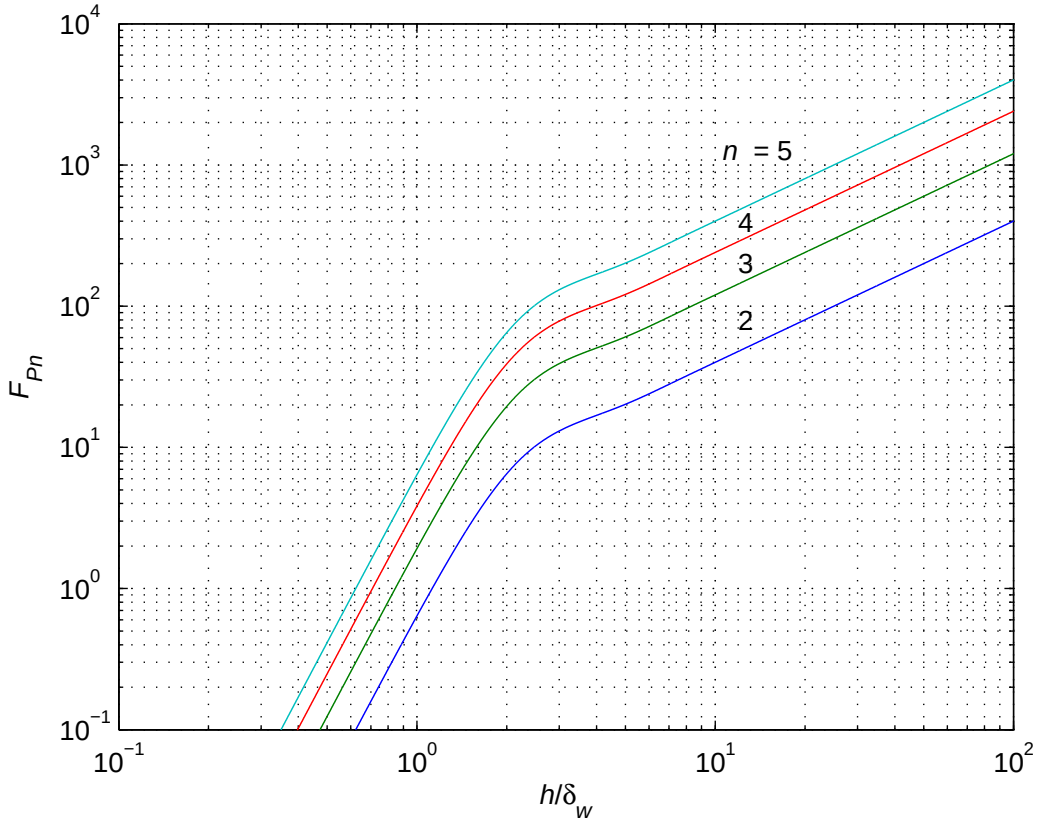

Figure 2.6: Proximity effect factor F_{Pn} as a function h/δ_w for n-th layer in log-log scale.

and

$$P_{w1(HF)} = \frac{\rho_w l_T I_{Lm}^2}{2b\delta_w}. \tag{2.13}$$

The dc resistance of a single layer is

$$R_{wdc1} = \frac{\rho_w l_T}{hb}. \tag{2.14}$$

The normalized winding resistance of the n-th layer is

$$F_{rn} = \frac{R_{wn}}{\frac{\rho_w l_T}{b\delta_w}} = \frac{R_{wn}}{R_{w1(HF)}} = \frac{F_{Rn}}{\frac{h}{\delta_w}}$$

$$= (2n^2 - 2n + 1)\frac{\sinh(\frac{2h}{\delta_w}) + \sin(\frac{2h}{\delta_w})}{\cosh(\frac{2h}{\delta_w}) - \cos(\frac{2h}{\delta_w})} - 4(n^2 - n)\frac{\sinh(\frac{h}{\delta_w})\cos(\frac{h}{\delta_w}) + \cosh(\frac{h}{\delta_w})\sin(\frac{h}{\delta_w})}{\cosh(\frac{2h}{\delta_w}) - \cos(\frac{2h}{\delta_w})}. \tag{2.15}$$

Fig. 2.7 shows a 3-D plot of normalized ac resistance $R_{wn}/(\rho_w l_T/b\delta_w)$ as a function of

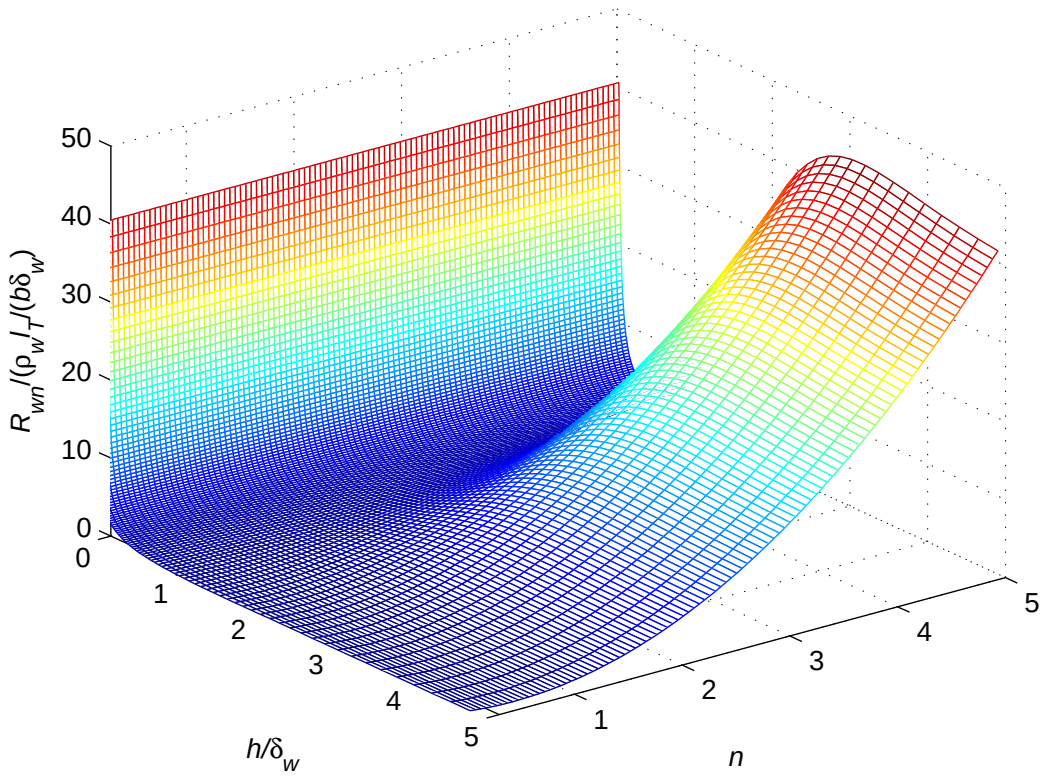

Figure 2.7: 3-D plot of normalized ac resistance $R_{wn}/(\rho_w l_T/b\delta_w)$ as a function of h/δ_w and n.

h/δ_w and n. Fig. 2.8 shows plots of $R_{wn}/(\rho_w l_T/b\delta_w)$ as a function of h/δ_w for several individual layers. It can be seen that the ac resistance reaches a fixed value at higher values of h/δ_w . It can be also seen that the plots exhibit minimum values. Fig. 2.9 shows these plots in the vicinity of the minimum values in more detail.

2.3 Approximation of $R_{wn}/R_{w1(HF)}$

An exact analytical expression for the minimum winding resistance of individual layers cannot be found from (2.15). For low and medium foil thicknesses, the winding resistance of the first layer, (2.15) can be approximated by

$$F_{rn} = \frac{R_{wn}}{\frac{\rho_w l_T}{b\delta_w}} = \frac{R_{wn}}{R_{w1(HF)}} = \frac{P_{wn}}{P_{w1(HF)}} \approx \frac{1}{\frac{h}{\delta_w}} \quad \text{for } \frac{h}{\delta_w} < 1 \text{ and } n = 1 \tag{2.16}$$

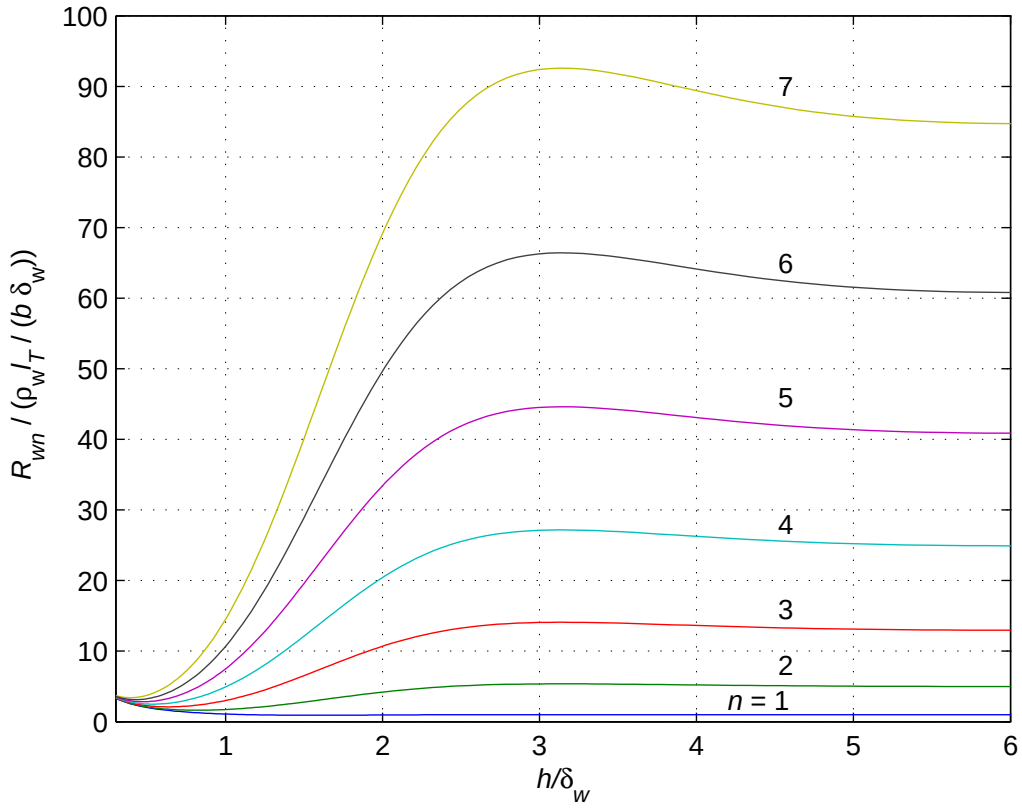

Figure 2.8: Normalized ac resistance $R_{wn}/(\rho_w l_T/b\delta_w)$ as a function of h/δ_w for each of the first several layers.

and for large foil thicknesses,

$$F_{rn} = \frac{R_{wn}}{\frac{\rho_w l_T}{b\delta_w}} = \frac{R_{wn}}{R_{w1(HF)}} = \frac{P_{wn}}{P_{w1(HF)}} \approx 1 \quad \text{for } \frac{h}{\delta_w} > 1 \text{ and } n = 1. \tag{2.17}$$

Fig. 2.10 shows the exact and approximate plots of $R_{w1}/(\rho_w l_T/b\delta_w)$ as functions of h/δ_w for the first layer. For low and medium foil thicknesses, the normalized winding resistance and normalized winding power loss in the n-th layer can be approximated by

$$F_{rn} = \frac{R_{wn}}{\frac{\rho_w l_T}{b\delta_w}} = \frac{R_{wn}}{R_{w1(HF)}} = \frac{P_{wn}}{P_{w1(HF)}} \approx \frac{1}{\frac{h}{\delta_w}} + \frac{n(n-1)}{3}\left(\frac{h}{\delta_w}\right)^3 \quad \text{for } \frac{h}{\delta_w} < 1.5 \text{ and } n \geq 2 \tag{2.18}$$

or

$$F_{Rn} = \frac{R_{wn}}{R_{wdc1}} = \frac{P_{wn}}{P_{wdc1}} \approx 1 + \frac{n(n-1)}{3}\left(\frac{h}{\delta_w}\right)^4 \quad \text{for } \frac{h}{\delta_w} < 1.5 \text{ and } n \geq 2. \tag{2.19}$$

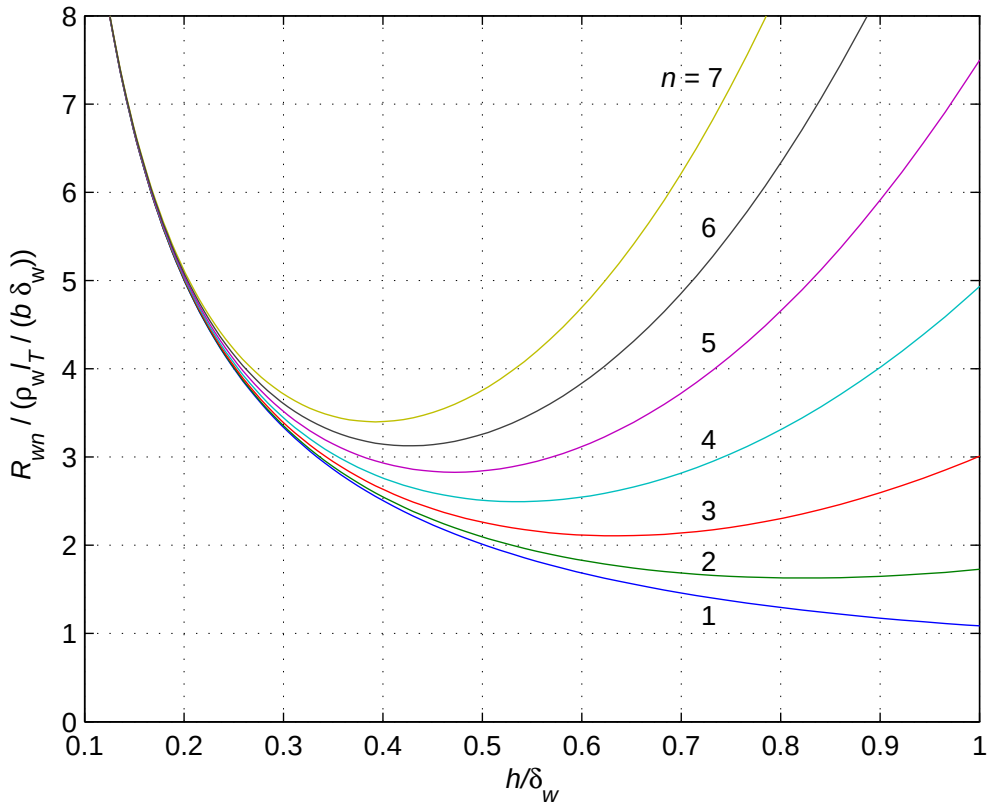

Figure 2.9: Normalized ac resistance $R_{wn}/(\rho_w l_T/b\delta_w)$ as a function of h/δ_w for each of the first several layers in enlarged scale.

Fig. 2.11 shows exact and approximate plots of $R_{w3}/(\rho_w l_T/b\delta_w)$ as functions of h/δ_w at $n = 3$ for low and medium foil thicknesses. It can be seen that the approximation is excellent in vicinity of the minimum value of the layer resistance. For high thickness of the foil, the normalized winding resistance and normalized winding power loss in the n-th layer is approximately given by

$$F_{rn} = \frac{R_{wn}}{R_{w1(HF)}} = \frac{P_{wn}}{P_{w1(HF)}} \approx n^2 + (n-1)^2 \quad \text{for } 5 \le \frac{h}{\delta_w} \le \infty \tag{2.20}$$

or

$$F_{Rn} = \frac{R_{wn}}{R_{wdc1}} = \frac{P_{wn}}{P_{wdc1}} \approx \left(\frac{h}{\delta_w}\right)\left[n^2 + (n-1)^2\right] \quad \text{for } 5 \le \frac{h}{\delta_w} \le \infty. \tag{2.21}$$

Fig. 2.12 shows exact and approximate plots of $R_{w3}/(\rho_w l_T/b\delta_w)$ as functions of h/δ_w

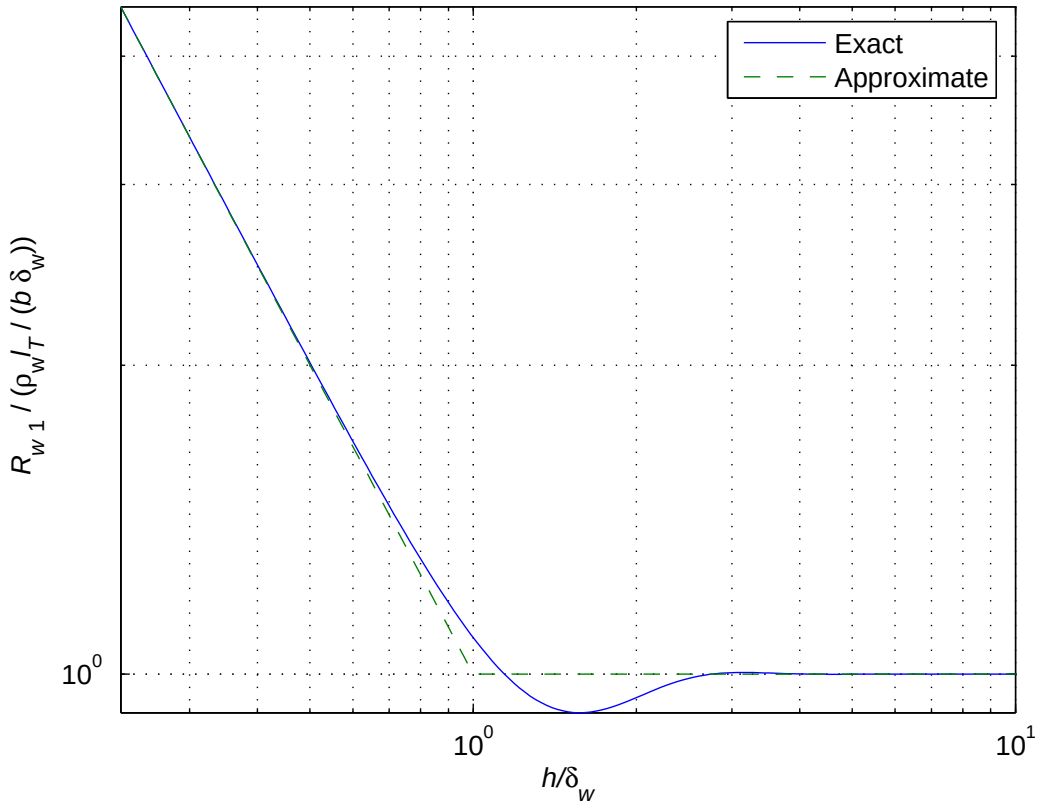

Figure 2.10: Exact and approximated plots of $R_{w1}/(\rho_w l_T/b\delta_w)$ as a function of h/δ_w for n=1.

at $n = 3$ for high foil thicknesses.

Taking the derivative of (2.7) with respect to h/δ_w, we obtain

$$\cos\left(\frac{h}{\delta_w}\right) = \frac{n-1}{n}\cosh\left(\frac{h}{\delta_w}\right). \tag{2.22}$$

For $n = 1$, (2.22) becomes

$$\cos\left(\frac{h}{\delta_w}\right) = 0, \tag{2.23}$$

which gives the optimum thickness of the first layer, subjected only to the skin effect

$$\frac{h_{opt1}}{\delta_w} = \frac{\pi}{2} \quad \text{for} \quad n = 1. \tag{2.24}$$

For $n \geq 2$, (2.22) has no closed-form solution and was solved numerically; the exact results are given in Table 2.1. In order to obtain analytical expression for h_{opt}/δ_w, we

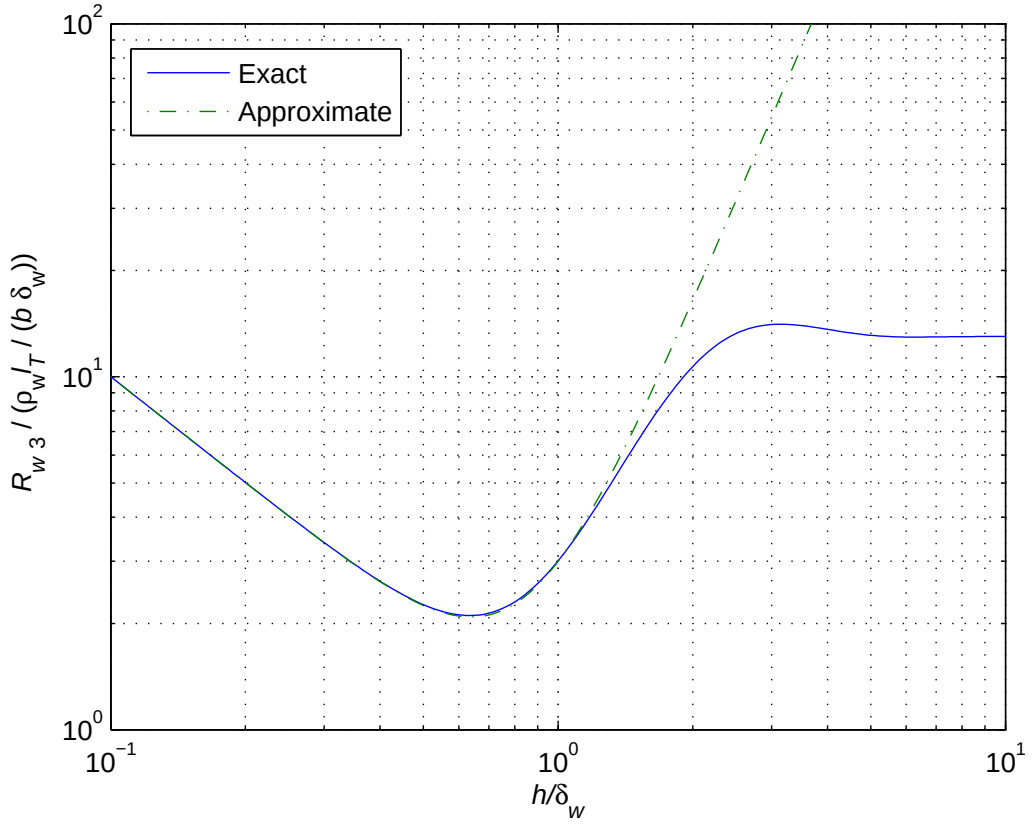

Figure 2.11: Exact and approximate plots of $R_{w3}/(\rho_w l_T/b\delta_w)$ as functions of h/δ_w at $n = 3$ for low and medium thickness.

will use (2.18). The minimum values of the ac resistance $R_{wn(min)}$ and the winding power loss $P_{wn(min)}$ in the n-th layer for $n \geq 2$ are obtained by taking the derivative of (2.18) and setting the result to zero

$$\frac{d\left(\frac{R_{wn}}{R_{w1(HF)}}\right)}{d\left(\frac{h}{\delta_w}\right)} = \frac{-1}{\left(\frac{h}{\delta_w}\right)^2} + \left(\frac{h}{\delta_w}\right)^2 n(n-1) = 0, \tag{2.25}$$

yielding the optimum thickness of the n-th layer

$$\frac{h_{optn}}{\delta_w} = \frac{1}{\sqrt[4]{n(n-1)}} \quad \text{for} \quad n \geq 2. \tag{2.26}$$

The approximated results of h_{optn}/δ_w, are listed in Table 2.1. The minimum normalized power loss in the n-th layer is

$$\frac{R_{wn(min)}}{R_{w1(HF)}} = \frac{P_{wn(min)}}{P_{w1(HF)}} = \frac{4}{3}\sqrt[4]{n(n-1)} \quad \text{for} \quad n \geq 2. \tag{2.27}$$

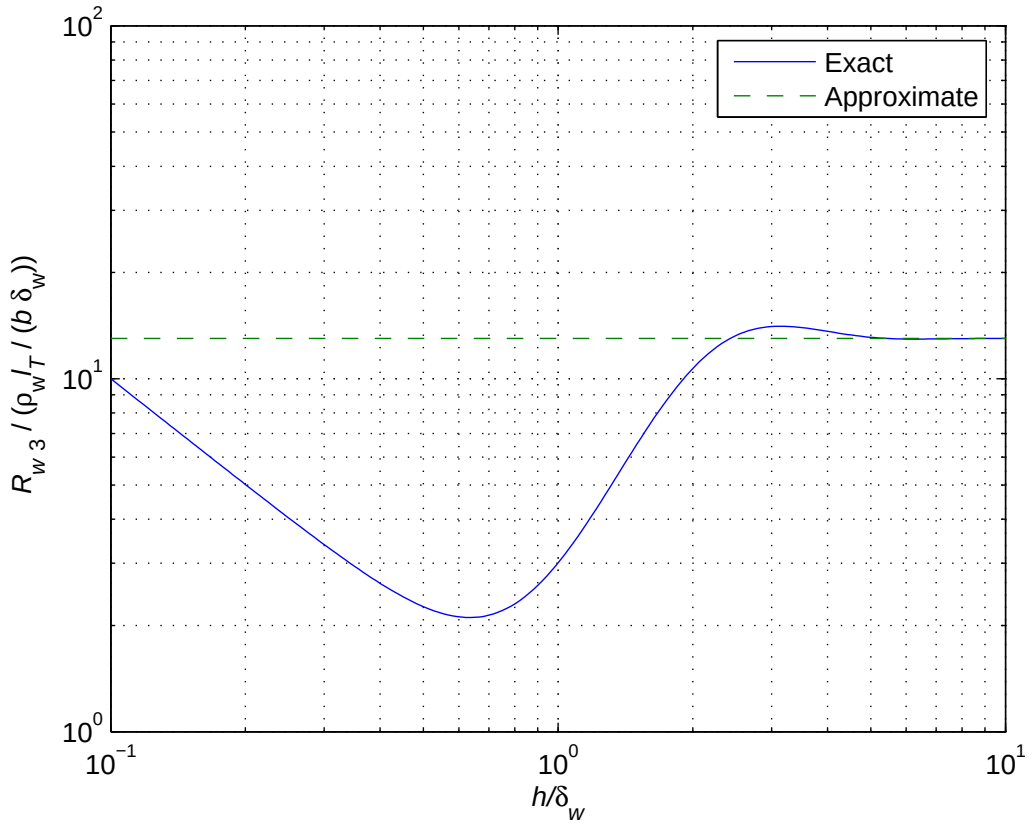

Figure 2.12: Exact and approximate plots of $R_{w3}/(\rho_w l_T/b\delta_w)$ as functions of h/δ_w at $n = 3$ for high thickness.

Dividing (2.26) by (2.24), one obtains the ratio of the optimum thickness of the n-th layer to the optimum thickness of the first layer as

$$\frac{h_{optn}}{h_{opt1}} = \frac{2}{\pi\sqrt[4]{n(n-1)}} \quad \text{for} \quad n \geq 2. \tag{2.28}$$

2.4 Example for Optimum Winding Resistance

The minimum winding resistance can be achieved when the thickness of each layer is different and equal to the optimum value given by (2.24) and (2.26). For three-layer copper inductor and conducting sinusoidal current at frequency 43 kHz, the optimum

Layer Number n	Exact h_{optn}/δ_w	Approximate h_{optn}/δ_w
1	$\pi/2$	1.5707
2	0.823767	0.8409
3	0.634444	0.6389
4	0.535375	0.5373
5	0.471858	0.4729
6	0.426676	0.4273
7	0.392413	0.3928
8	0.365274	0.3656
9	0.343089	0.3433
10	0.324512	0.3247

Table 2.1: Exact and aproximate optimum foil thickness for individual inductor layers.

thickness of the bare foil of the first layer is

$$h_{opt1} = \frac{\pi}{2}\delta_w = \frac{\pi}{2}\sqrt{\frac{\rho_w}{\pi f \mu_0}} \approx 0.5 \text{ mm}. \tag{2.29}$$

From (2.28), the optimum thickness of the bare conductor of the second layer $n = 2$ is

$$h_{opt2} = \frac{2}{\pi\sqrt[4]{2}} h_{opt1} = 0.5356 \times 0.5 = 0.267 \text{ mm}, \tag{2.30}$$

and the optimum thickness of the bare conductor of the third layer $n = 3$ is

$$h_{opt3} = \frac{2}{\pi\sqrt[4]{6}} h_{opt1} = 0.406 \times 0.5 = 0.203 \text{ mm}. \tag{2.31}$$

The ac winding resistance for n-th layer is given by

$$R_{wn} = F_{Rn} R_{wdcn}. \tag{2.32}$$

Therefore, the overall ac resistance of the foil inductor is

$$R_w = \sum_{n=1}^{N_l} F_{Rn} R_{wdcn}. \tag{2.33}$$

The breadth of the inductor, which is equal to the foil width is $b = 2$ cm. The length of each turn is $l_T = 10$ cm. The resistivity of copper at room temperature is

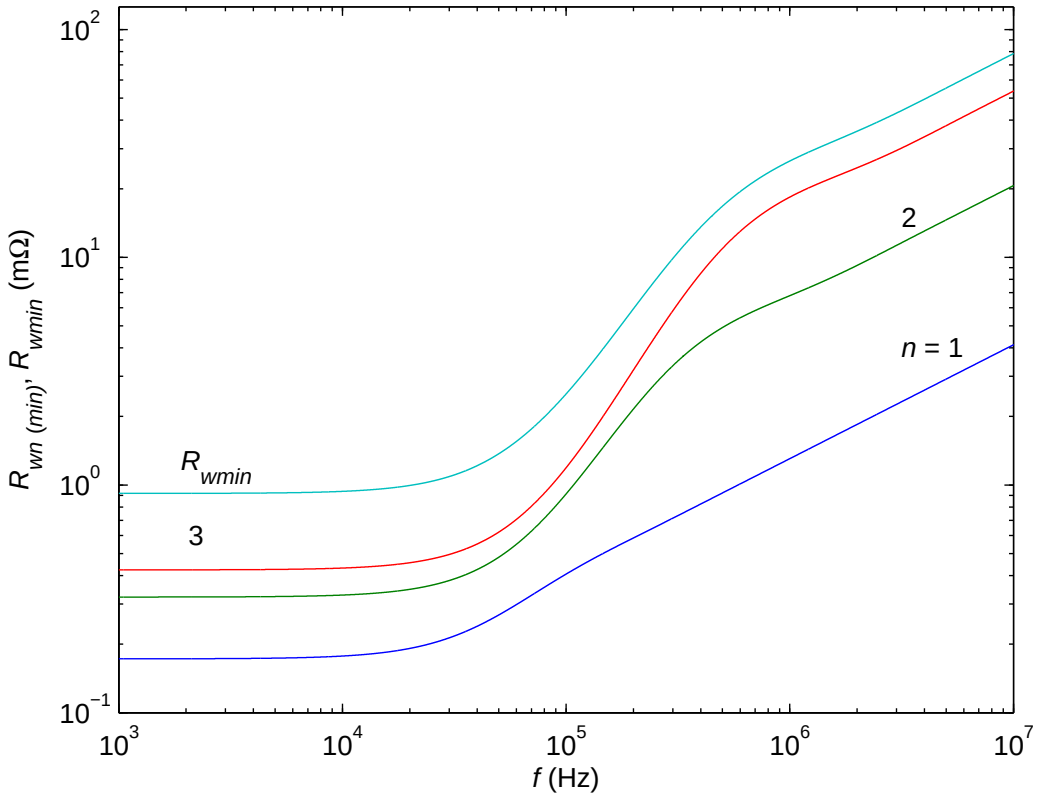

Figure 2.13: Plots of $R_{wn(min)}$ and R_{wmin} as a function of frequency f for the foil inductor.

$\rho_{Cu} = 1.72 \times 10^{-8}$ Ωm. The dc resistances of each layer is

$$R_{wdc1} = \frac{\rho_{Cu} l_T}{b h_{opt1}} = \frac{1.72 \times 10^{-8} \times 0.1}{0.5 \times 10^{-3} \times 20 \times 10^{-3}} = 0.172 \text{ mΩ}, \tag{2.34}$$

$$R_{wdc2} = \frac{\rho_{Cu} l_T}{b h_{opt2}} = \frac{1.72 \times 10^{-8} \times 0.1}{0.267 \times 10^{-3} \times 20 \times 10^{-3}} = 0.322 \text{ mΩ}, \tag{2.35}$$

$$R_{wdc3} = \frac{\rho_{Cu} l_T}{b h_{opt3}} = \frac{1.72 \times 10^{-8} \times 0.1}{0.203 \times 10^{-3} \times 20 \times 10^{-3}} = 0.423 \text{ mΩ}. \tag{2.36}$$

Since the optimum thickness h_{optn} of the subsequent layers decreases, the dc resistance of the individual layers increases with increasing layer number n.

The total dc winding resistance is a sum of dc winding resistance of each layer

$$R_{wdc} = R_{wdc1} + R_{wdc2} + R_{wdc3} = 0.917 \text{ mΩ}. \tag{2.37}$$

Assuming an RMS current of 50 A, the dc and low-frequency power loss in each layer of the inductor is

$$P_{wdc1} = R_{wdc1} I_{rms}^2 = 0.172 \times 50^2 = 0.43 \text{ W}, \tag{2.38}$$

$$P_{wdc2} = R_{wdc2} I_{rms}^2 = 0.322 \times 50^2 = 0.805 \text{ W}, \tag{2.39}$$

and

$$P_{wdc3} = R_{wdc3} I_{rms}^2 = 0.423 \times 50^2 = 1.057 \text{ W}. \tag{2.40}$$

The total dc winding power loss is a sum of dc power loss of each layer

$$P_{wdc} = P_{wdc1} + P_{wdc2} + P_{wdc3} = 0.43 + 0.805 + 1.057 = 2.292 \text{ W}. \tag{2.41}$$

It can be seen that the dc winding power loss of the subsequent layers increases with the layer number. Substituting the optimum layer thickness given by (2.24) and (2.26) into (2.7), the minimum values of the ac-to-dc resistance of n-th layer $F_{Rn(min)}$ were calculated numerically. The results are $F_{R1(min)} = 1.4407$, $F_{R2(min)} = 1.3703$, $F_{R3(min)} = 1.3458$. Hence, the ac resistances in the subsequent layers are

$$R_{w1(min)} = F_{R1(min)} R_{wdc1} = 1.4407 \times 0.172 \times 10^{-3} = 0.2478 \text{ m}\Omega, \tag{2.42}$$

$$R_{w2(min)} = F_{R2(min)} R_{wdc2} = 1.3703 \times 0.322 \times 10^{-3} = 0.4412 \text{ m}\Omega, \tag{2.43}$$

and

$$R_{w3(min)} = F_{R3(min)} R_{wdc3} = 1.3458 \times 0.423 \times 10^{-3} = 0.5692 \text{ m}\Omega. \tag{2.44}$$

The total ac winding resistance of an inductor with the optimum layer thicknesses is

$$R_{wmin} = R_{w1(min)} + R_{w2(min)} + R_{w3(min)} = 0.2478 + 0.4412 + 1.3458 = 1.2582 \text{ m}\Omega. \tag{2.45}$$

Fig. 2.13 shows the ac winding resistance $R_{wn(min)}$ of each layer and the total ac winding resistance R_{wmin} as functions of frequency f for three-layer winding ($N_l = 3$).

The ac power losses in the individual layers for a sinusoidal inductor current of RMS value $I_{rms} = 50$ A are

$$P_{w1(min)} = R_{w1(min)} I_{rms}^2 = 0.2478 \times 50^2 = 0.6195 \text{ W}, \tag{2.46}$$

$$P_{w2(min)} = R_{w2(min)} I_{rms}^2 = 0.4412 \times 50^2 = 1.103 \text{ W}, \tag{2.47}$$

and

$$P_{w3(min)} = R_{w3(min)} I_{rms}^2 = 0.5692 \times 50^2 = 1.423 \text{ W}. \tag{2.48}$$

It can be seen that the ac power loss in each layer increases with the layer number n. The total minimum ac power loss in the inductor winding is given by

$$P_{wmin} = P_{w1(min)} + P_{w2(min)} + P_{w3(min)} = 0.6195 + 1.103 + 1.423 = 3.1455 \text{ W}, \tag{2.49}$$

which gives the ratio of the ac-to-dc winding resistance and ac-to-dc winding power loss ratio

$$\frac{R_{wmin}}{R_{wdc}} = \frac{P_{wmin}}{P_{wdc}} = \frac{3.1455}{2.292} \approx 1.37. \tag{2.50}$$

2.5 Minimum Winding Resistance for Inductors With Uniform Foil Thickness

For low and medium foil thicknesses, the normalized resistance of the inductor with fixed foil thickness and any number of layers N_l can be approximated by [14]

$$\frac{R_w}{\left(\frac{\rho_w l_w}{b\delta_w}\right)} \approx \frac{1}{\frac{h}{\delta_w}} + \frac{2(N_l^2 - 1)}{17}\left(\frac{h}{\delta_w}\right)^3 \quad \text{for } \frac{h}{\delta_w} < 1.5, \tag{2.51}$$

where $l_w = N_l l_T$ is the total foil winding length. Fig. 2.15 shows exact and approximate plots of $R_w/(\delta_w l_w/b\delta_w)$ as functions of h/δ_w for three-layer inductor ($N_l = 3$) with uniform foil thickness for low and medium foil thicknesses. The minimum values of the ac winding resistance R_{wopt} and the winding power loss P_{wopt} of an inductor with uniform foil thickness are determined by taking the derivative of (2.51) and

setting the result to zero

$$\frac{d\left(\frac{R_w}{\frac{\rho_w l_w}{b\delta_w}}\right)}{d\left(\frac{h}{\delta_w}\right)} = \frac{-1}{\left(\frac{h}{\delta_w}\right)^2} + \frac{6(N_l^2-1)}{17}\left(\frac{h}{\delta_w}\right)^2 = 0, \tag{2.52}$$

yielding the optimum value of the uniform foil thickness in the inductor

$$\frac{h_{opt}}{\delta_w} = \frac{1}{\sqrt[4]{\frac{6(N_l^2-1)}{17}}} \qquad \text{for } N_l \geq 2. \tag{2.53}$$

The approximate results of h_{opt}/δ_w, are listed in Table 2.2. For $N_l = 1$, the optimum foil thickness is defined by (2.24).

In the subsequent analysis, the properties of winding with non-uniform thickness will be compared with those of the winding with uniform thickness. For a three-layer copper inductor ($N_l = 3$) with an uniform foil thickness h and conducting a sinusoidal current at frequency $f = 43$ kHz, the optimum thickness of the bare foil is

$$h_{opt} = 0.7714\delta_w = 0.7741\sqrt{\frac{\rho_w}{\pi f \mu_0}} \approx 0.245 \text{ mm}. \tag{2.54}$$

Layer Number N_l	Approximate h_{opt}/δ_w
1	1.5707
2	0.9858
3	0.7714
4	0.6593
5	0.5862
6	0.5334
7	0.4929
8	0.4605
9	0.4338
10	0.4113

Table 2.2: Approximate optimum uniform foil thickness for multi-layer inductor.

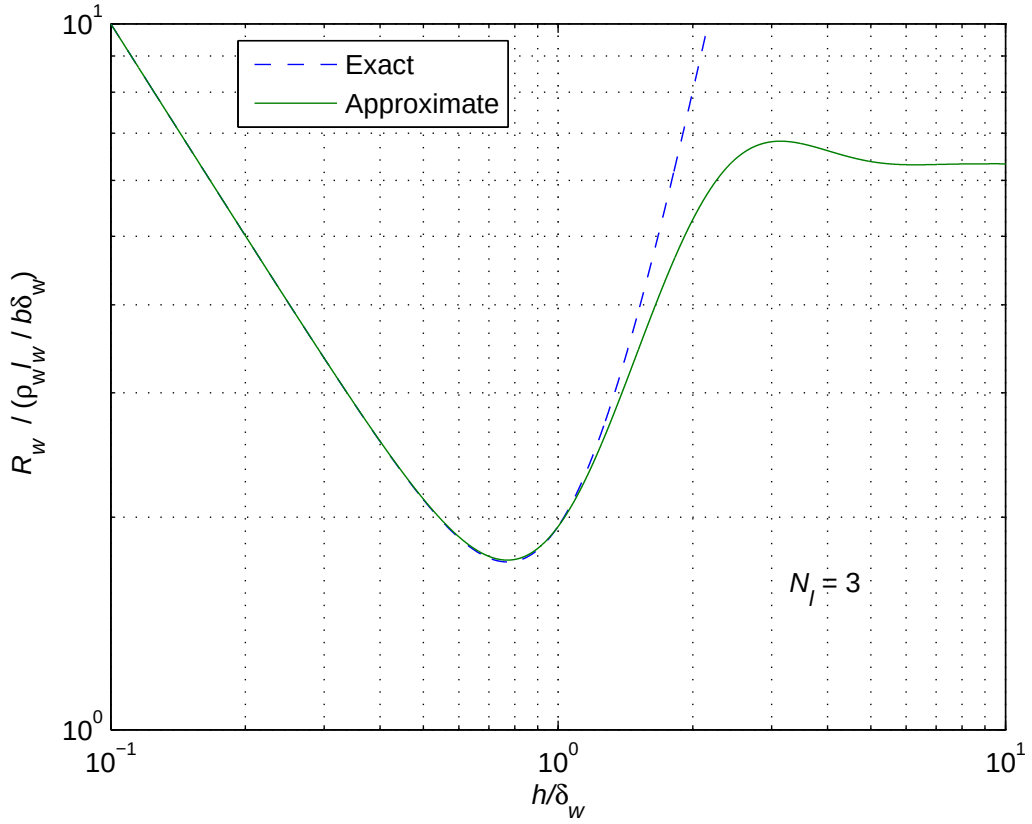

Figure 2.14: Exact and approximate plots of $R_w/(\delta_w l_w/b\delta_w)$ as functions of h/δ_w for three-layer inductor $N_l = 3$ for low and medium uniform thickness.

The dc and low frequency winding resistance is [14]

$$R_{wdc} = \frac{\rho_{Cu} l_w}{A_{wopt}} = \frac{\rho_{Cu} l_T N_l}{b h_{opt}} = 1.053 \ \ \text{m}\Omega, \tag{2.55}$$

where A_{wopt} is the cross-sectional area of the foil. Assuming an RMS current of 50 A, the dc and low-frequency power loss in all three layers ($N_l = 3$) of the inductor is given by

$$P_{dc} = R_{dc} I_{rms}^2 = 1.053 \times 10^{-3} \times 50^2 = 2.6325 \text{ W}. \tag{2.56}$$

The ac-to-dc total winding resistance ratio of three-layer inductor with an uniform optimum winding thickness [14] was calculated numerically and is given by

$$F_R = \frac{R_{wopt}}{R_{dc}} = \frac{P_{wopt}}{P_{dc}} = 1.3414. \tag{2.57}$$

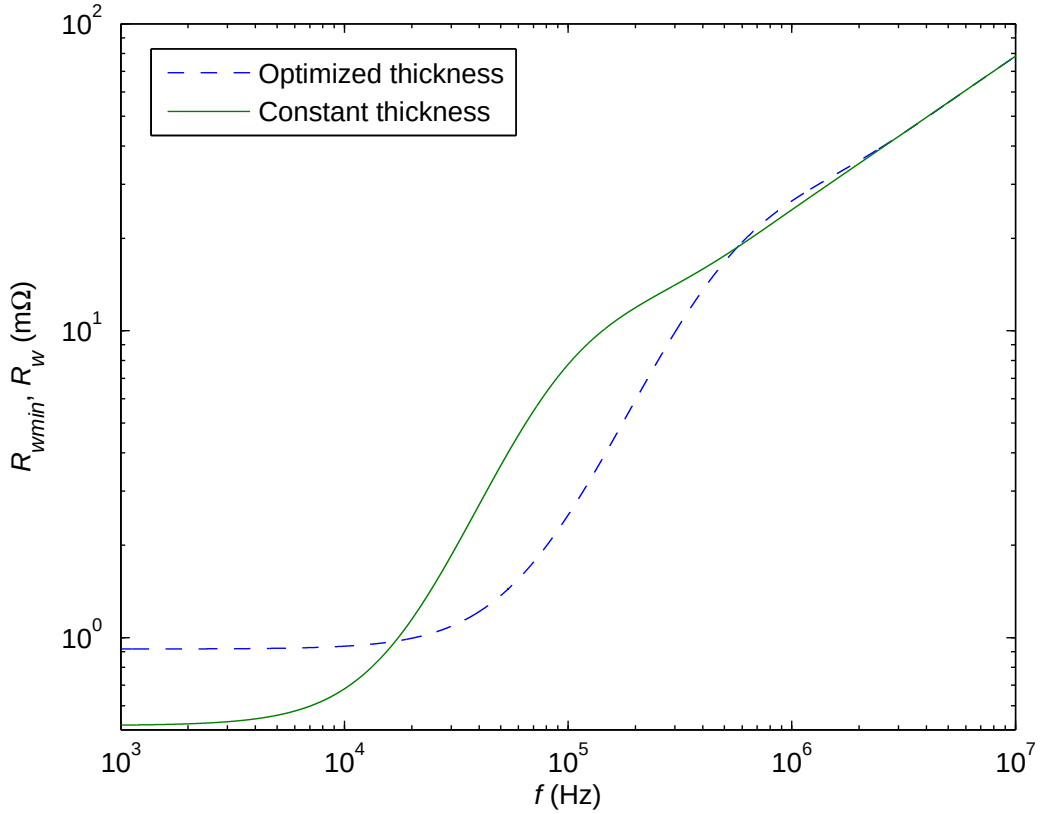

Figure 2.15: Plots of R_{wmin} and R_w as functions of frequency f for the inductor with optimized thickness of each layer $h_{opt1} = 0.5$ mm, $h_{opt2} = 0.267$ mm, $h_{opt3} = 0.203$ mm and for the inductor with a constant layer of thickness $h = h_{opt1} = 0.5$ mm.

Hence, the optimum ac winding resistance of the inductor with uniform foil thickness is

$$R_{wopt} = F_R R_{dc} = 1.3414 \times 1.053 \times 10^{-3} = 1.4125 \text{ m}\Omega. \tag{2.58}$$

The total ac winding power loss is

$$P_{wopt} = R_{wopt} I_{rms}^2 = 1.4125 \times 10^{-3} \times 50^2 = 3.5312 \text{ W}. \tag{2.59}$$

The ratio of the ac winding resistance R_{wopt} of the inductor with the optimum uniform foil thickness to the ac winding resistance R_{wmin} of the inductor with optimum foil thickness for each layer is

$$\epsilon = \frac{R_{wopt}}{R_{wmin}} = \frac{1.4125}{1.2582} = 1.1226. \tag{2.60}$$

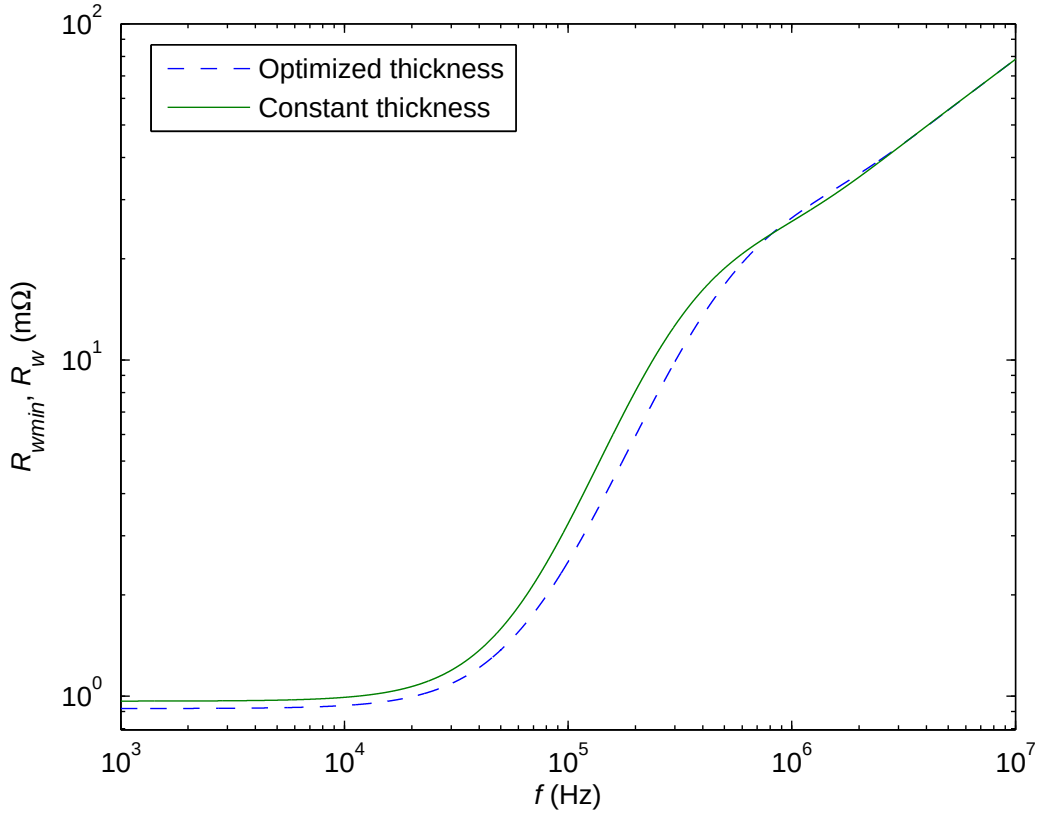

Figure 2.16: Plots of R_{wmin} and R_w as functions of frequency f for the inductor with optimized thickness of each layer $h_{opt1} = 0.5$ mm, $h_{opt2} = 0.267$ mm, $h_{opt3} = 0.203$ mm and for the inductor with a constant layer of thickness $h = h_{opt2} = 0.267$ mm.

Fig. 2.15 compares the ac winding resistance R_{wmin} of an inductor with the optimum individual layer thicknesses and the ac winding resistance R_w of an inductor with uniform foil thickness equal to the optimum thickness of the first layer $h = h_{opt1}$ for three layers. It can be seen that for the high-frequency range the ac winding resistance R_{wmin} of the inductor with the optimum individual layer thicknesses is significantly lower than the ac winding resistance R_w of the inductor with an uniform foil thickness. Fig. 2.16 compares the ac winding resistance R_{wmin} of an inductor with the optimum individual layer thicknesses and the ac winding resistance R_w of an inductor with an uniform foil thickness equal to the optimum thickness of the second layer $h = h_{opt2}$ for three layers. It can be seen that for the high-frequency range

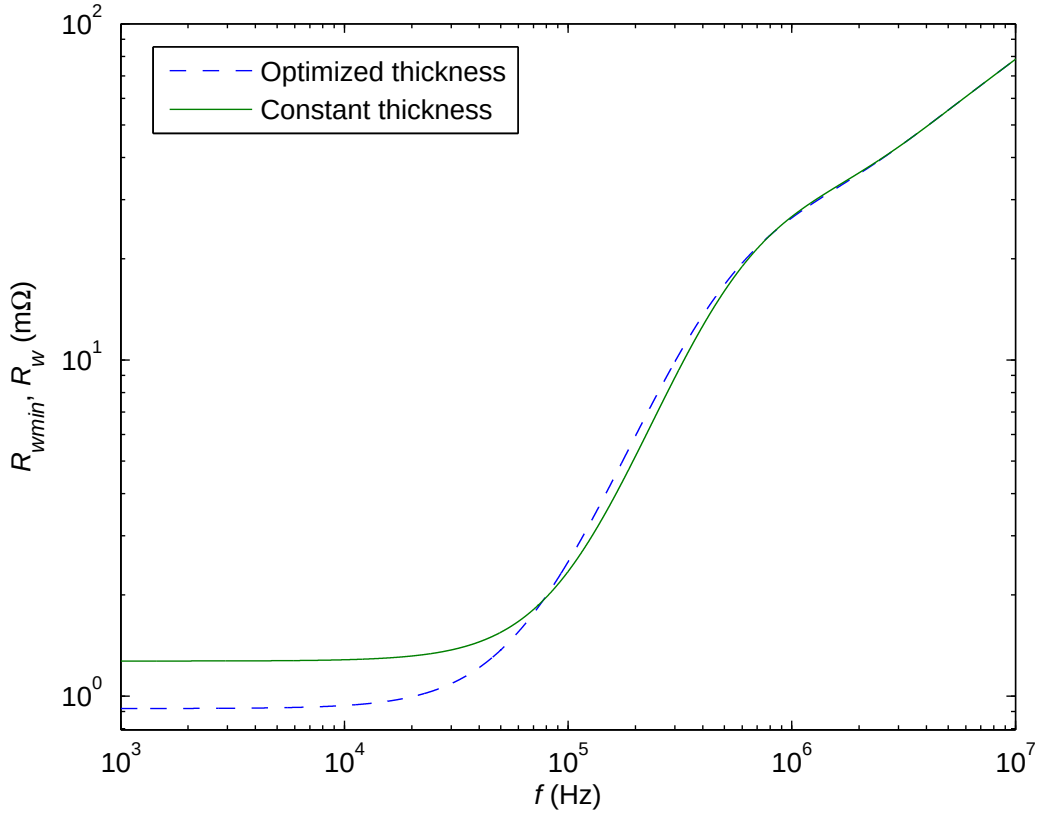

Figure 2.17: Plots of R_{wmin} and R_w as functions of frequency f for the inductor with optimized thickness of each layer $h_{opt1} = 0.5$ mm, $h_{opt2} = 0.267$ mm, $h_{opt3} = 0.203$ mm and for the inductor with a constant layer of thickness $h = h_{opt3} = 0.203$ mm.

the ac winding resistance R_{wmin} of the inductor with optimized foil thicknesses is approximately equal to the ac winding resistance R_w of the inductor with an uniform foil thickness equal to the optimum thickness of the second layer. Fig. 2.17 compares the ac winding resistance R_{wmin} of an inductor with the optimum individual layer thicknesses and the ac winding resistance R_w of an inductor with an uniform foil thickness equal to the optimum thickness of the third layer $h = h_{opt3}$ for three layers. Fig. 2.18 compares the ac winding resistance R_{wmin} of an inductor with the optimum individual layer thicknesses and the ac winding resistance R_{wopt} of an inductor with an uniform optimum foil thickness h_{opt} for three layers. It can be seen that the resistance for inductor with the optimized thickness for each layer is lower than that

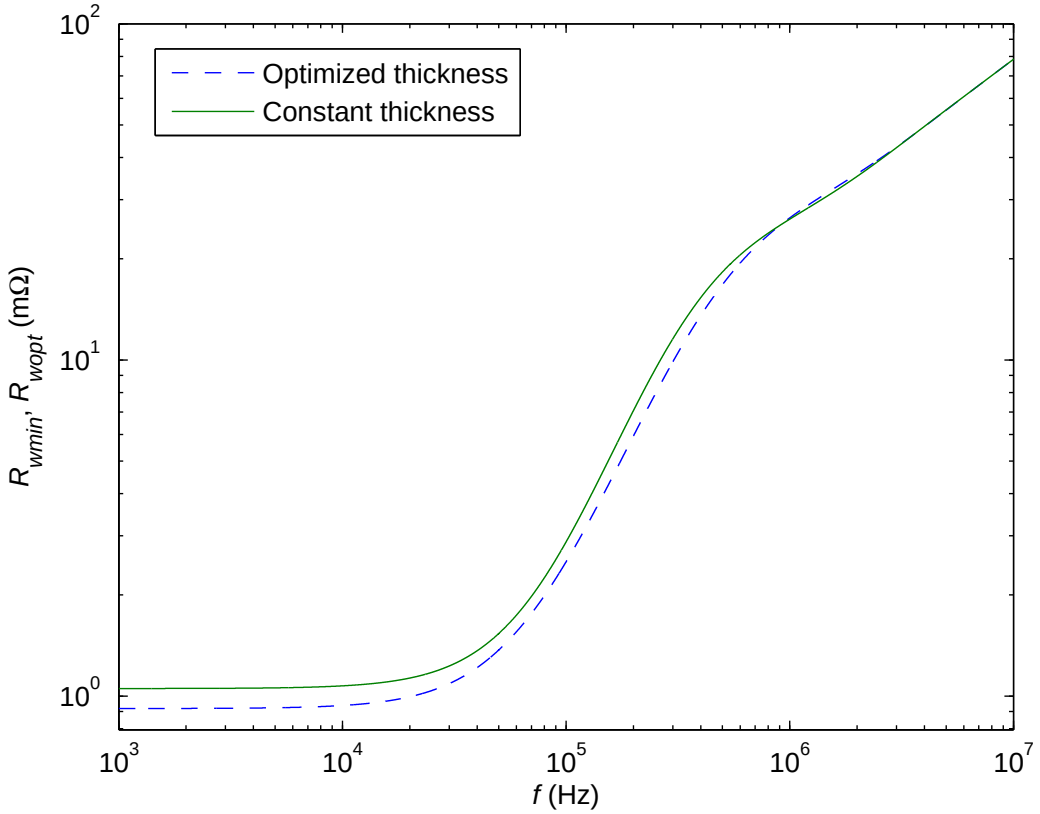

Figure 2.18: Plots of R_{wmin} and R_w as functions of frequency f for the inductor with optimized thickness of each layer $h_{opt1} = 0.5$ mm, $h_{opt2} = 0.267$ mm, $h_{opt3} = 0.203$ mm and for the inductor with a constant layer of thickness $h_{opt} = 0.245$ mm for three-layer inductor ($N_l = 3$).

of the inductor with the uniform optimum thickness. Fig. 2.19 shows the ratio of the ac winding resistance R_{wopt} with uniform optimum foil thickness to the ac winding resistance R_{wmin} with the optimum individual layer thicknesses.

It can be seen that the resistance of the inductor with the optimum uniform foil thickness for the low-frequency range is 13% higher than that of the inductor with the optimized thickness of each layer. In the medium-frequency range, the resistance of uniform inductor winding thickness increases. At a frequency of 200 kHz, the winding resistance of the inductor with the optimum uniform thickness is 21.8% greater than the winding resistance of the inductor with the optimum foil thickness

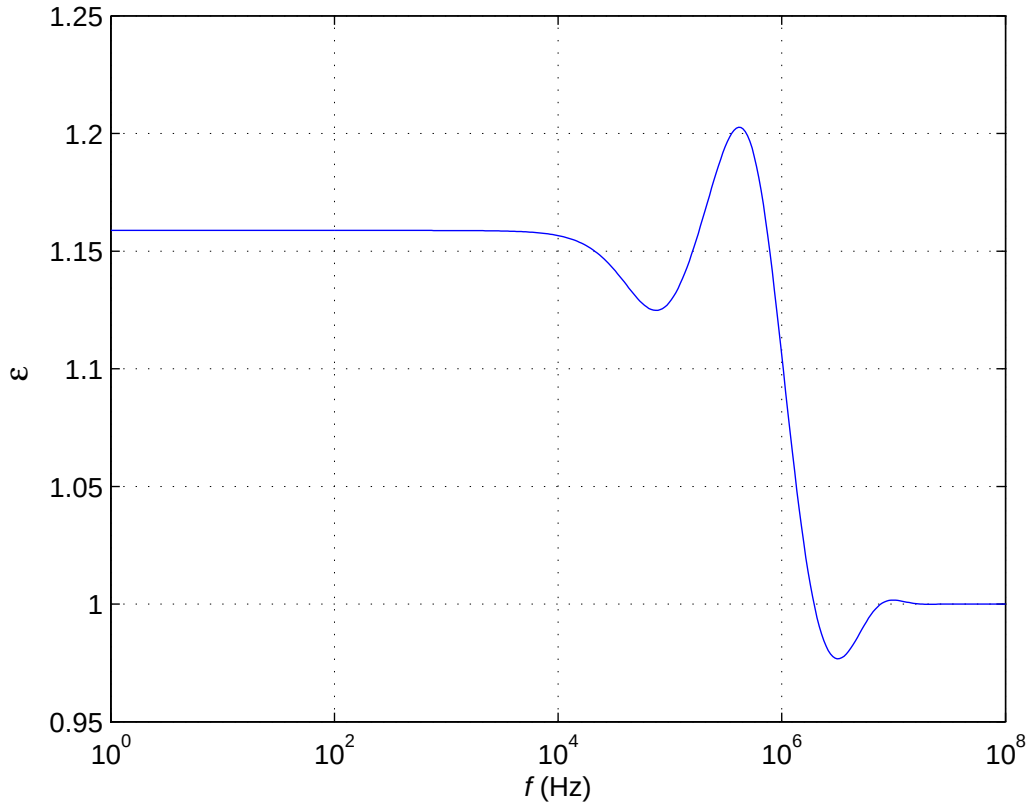

Figure 2.19: Ratio of the winding resistance with uniform optimum foil thickness $h_{opt1} = 0.5$ mm, $h_{opt2} = 0.267$ mm, $h_{opt3} = 0.203$ mm to the winding resistance with optimum individual layer thicknesses $h_{opt} = 0.245$ mm for three-layer inductor ($N_l = 3$).

of individual layers. However, in the high-frequency range, the winding resistances of both inductors are the same.

The inductance of the foil wound inductor is expressed by

$$L = \frac{\mu_{rc}\mu_0 A_c N_l^2}{b} = \frac{1800 \times 4\pi \times 10^{-7} \times 4 \times 10^{-4} \times 3^2}{2 \times 10^{-2}} \approx 407\ \mu\text{H}, \tag{2.61}$$

where $b = 2$ cm, $\mu_{rc} = 1800$ is the core permeability, $N_l = 3$ is the number of layers, and $A_c = 4$ cm^2 is the cross-sectional area of the core.

2.6 Conclusion

The equation for the winding resistance of individual layers for inductors made of foil conductor has been analysed and illustrated. This equation has been approximated to derive an expression for the optimum thickness of individual layers. The comparison of winding resistances at various values of foil thickness has been presented. It has been shown that the minimum value of the winding resistance of each individual layer at a fixed frequency occurs at different values of the normalized layer thickness h_{optn}/δ_w. The optimum normalized layer thickness h_{optn}/δ_w decreases with increasing layer number n. In addition, the resistance of each layer appreciably increases as the layer number n increases from the innermost to the outermost layer. Moreover, the approximated equation for low-frequency resistance of inductors with a uniform foil thickness has been given.

The optimum normalized value of the uniform foil thickness has been derived. It has been shown that the winding resistance of the inductor with an optimum uniform foil thickness for low-frequency range is 13% higher than that of the inductor with an optimized thickness of each layer.

In the medium-frequency range, the ratio of the winding resistance with a uniform optimum foil thickness to the winding resistance with the optimum thickness of each individual layer first increases, reaches a maximum value, and then rapidly decreases with frequency. At a frequency of 200 kHz, the winding resistance of uniform optimum foil thickness was 21.8% greater than the winding resistance of the inductor with the optimum foil thickness of each layer, in the given example. For the high-frequency range, the winding resistances of both inductors were identical. High-quality power inductors are used in high-frequency applications, such as pulse-width-modulated (PWM) dc-dc power converters [15], [16], [54], resonant dc-dc power converters [52], radio- frequency power amplifiers [12], [13], [55], and LC oscillators [53].

3 Analytical Optimization of Foil Windings Conducting Sinusoidal Current

Power inductors are important elements in resonant power amplifiers. This is because a power inductor along with a capacitor form a resonant circuit, which shapes the output voltage of the power amplifier. Moreover, inductors and capacitors serve as components of matching circuit, which match the load to the active device [52], [55].

Winding ac power losses in an inductor are caused by two eddy-current effects: the skin effect and the proximity effect [1]-[51], [56]-[64], [65]-[71], [73]-[76], [78]-[84]. Both these effects increase with the operating frequency. The skin effect is caused in a conductor by the magnetic field induced by its own current, resulting in a higher current density closer to the surface of the conductor than that in the center of the conductor.

The proximity effect is caused by magnetic fields induced by currents flowing in adjacent conductors. In this paper, inductors made up of copper foil conductor that carry sinusoidal currents are considered. The copper is used because of its low resistivity. In foil inductors, usually there is only one winding turn per layer. The skin and proximity effects in foil inductors depend on the foil thickness and are nearly independent of the foil width. Therefore, the thickness of the foil can be optimized to minimize the winding ac resistance and losses. The width of the foil can be chosen to achieve the minimum cross-sectional conductor area, constrained by the maximum amplitude of the current density [75].

3.1 Foil Winding Power Loss Due to Ac Sinusoidal Current

For the foil inductor conducting sinusoidal current $i_l(t) = I_{Lm} \sin \omega t$, the winding ac power losses are given by

$$P_w = \frac{1}{2} I_{Lm}^2 R_w = I_{Lrms}^2 R_w = I_{Lrms}^2 \frac{R_w}{R_{wdc}} R_{wdc} = I_{Lrms}^2 F_R R_{wdc} \tag{3.1}$$

where I_{Lm} is the amplitude of the sinusoidal current, $I_{Lrms} = I_{Lm}/\sqrt{2}$ is the RMS value of the sinusoidal current, $\omega = 2\pi f$ is the angular frequency, f is the frequency of the sinusoidal current, R_w is the winding ac resistance, and F_R is the ac-to-dc winding resistance ratio.

The winding dc resistance of the foil inductor is given by

$$R_{wdc} = \frac{\rho_w l_w}{A_w} = \frac{\rho_w l_w}{bh} = \frac{\rho_w l_w}{\delta_w b \left(\frac{h}{\delta_w}\right)} \tag{3.2}$$

where $\rho_w = 1/\sigma_w$ is the resistivity of the conductor, b is the foil width, h is the foil thickness, $A_w = bh$ is the cross-sectional area of the foil, $l_w = N_l l_T$ is the winding length, N_l is the number of foil layers, l_T is the foil mean turn length (MTL), and δ_w is the skin depth. The skin depth of the winding conductor at the frequency of the inductor current is given by

$$\delta_w = \sqrt{\frac{2}{\omega \mu_0 \sigma_w}} = \frac{1}{\sqrt{\pi \mu_0 \sigma_w f}} = \sqrt{\frac{\rho_w}{\pi \mu_0 f}}. \tag{3.3}$$

3.2 Dowell's Equation for Winding Resistance of Foil Inductors

Dowell's equation for the ac-to-dc winding resistance ratio F_R is expressed as [2]

$$F_R = \frac{R_w}{R_{wdc}} = A\left[\frac{\sinh(2A) + \sin(2A)}{\cosh(2A) + \cos(2A)} + \frac{2(N_l^2 - 1)}{3} \frac{\sinh(A) - \sin(A)}{\cosh(A) + \cos(A)}\right], \tag{3.4}$$

where the normalized thickness of the foil is given by

$$A = \frac{h}{\delta_w}. \tag{3.5}$$

Even though Dowell's equation describes the winding resistance in a wide frequency range taking into account both the skin and proximity effects, it is impossible to perform an analytical optimization of inductor windings. This is because Dowell's

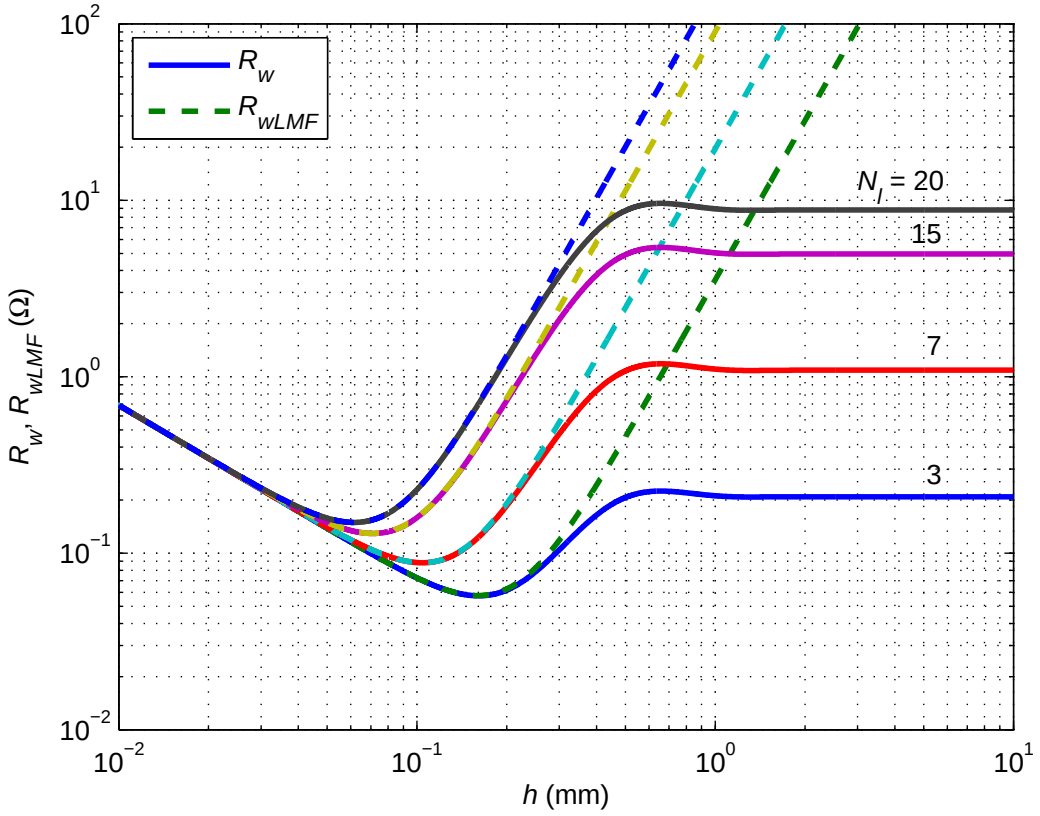

Figure 3.1: Winding ac resistances of foil inductors predicted by Dowell's equation R_w and by low- and medium-frequency approximation R_{wLMF} as functions of foil thickness h.

equation contains trigonometric and hyperbolic functions. Therefore, to perform analytical optimization, an approximation of Dowell's equation in (4.1) is used in the subsequent sections.

3.3 Low- and Medium-Frequency Approximation of Dowell's Equation

The approximate Dowell's equation for foil windings valid for low and medium frequencies derived in 9.1 is given by [45]

$$F_{RLMF} \approx 1 + \frac{5N_l^2 - 1}{45} A^4 = 1 + \frac{5N_l^2 - 1}{45} \left(\frac{h}{\delta_w} \right)^4 \quad \text{for} \quad A \leq 2. \tag{3.6}$$

The winding ac resistance of the foil inductor is

$$R_{wLMF} = F_{RLMF} R_{wdc} \approx \frac{\rho_w l_w}{\pi} \left[\frac{1}{h} + \frac{(5N_l^2 - 1)h^3}{45\delta_w^4} \right]. \tag{3.7}$$

Fig. 3.1 shows winding ac resistances of foil inductors predicted by Dowell's equation R_w and by low- and medium-frequency approximation R_{wLMF} as functions of foil thickness h. Observe that the low- and medium-frequency approximation R_{wLMF} captures the minimum of winding ac resistance R_w predicted by Dowell's equation with high accuracy.

Taking the derivative of (4.11) with respect to h and setting the result to zero, we obtain

$$\frac{d\left(R_{wLMF}\right)}{dh} \approx \frac{\rho_w l_w}{b} \left[-\frac{1}{h^2} + \frac{3\left(5N_l^2 - 1\right)h^2}{45\delta_w^4} \right] = 0. \tag{3.8}$$

Solution of this equation gives the normalized foil valley thickness at which the winding ac resistance of a foil has a minimum value

$$\frac{h_v}{\delta_w} = \sqrt[4]{\frac{15}{5N_l^2 - 1}}. \tag{3.9}$$

The ac-to-dc winding resistance ratio at the normalized foil valley thickness is

$$F_{Rv} = 1 + \frac{(5N_l^2 - 1)}{45} \times \left(\sqrt[4]{\frac{15}{5N_l^2 - 1}} \right)^4 = 1 + \frac{1}{3} = \frac{4}{3}. \tag{3.10}$$

Hence, the minimum value of the foil winding ac resistance at the valley thickness is

$$R_{wv} = F_{Rv} R_{wdc(h_v)} = \frac{4\rho_w l_w}{3bh_v} = \frac{4\rho_w l_w}{3b\delta_w \sqrt[4]{\frac{15}{5N_l^2 - 1}}}. \tag{3.11}$$

The normalized foil hill thickness at which the winding ac resistance reaches its local maximum is given by

$$\frac{h_h}{\delta_w} = \pi. \tag{3.12}$$

3.4 Foil Inductor Model

A lumped-parameter model of a foil inductor, valid for dc and ac currents, is depicted in Fig. 6.7. The model of the inductor consists of self-inductance L, winding

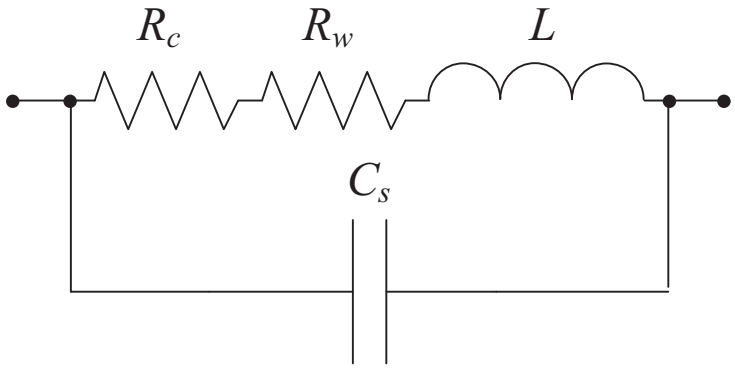

Figure 3.2: The equivalent RLC lumped-parameter model of foil winding inductors.

ac resistance R_w, series core resistance R_c, and parasitic self-capacitance or a stray capacitance C_s. In reality, L, R_w, and R_c are frequency dependent. However, in the subsequent analysis, the series core resistance is neglected ($R_c = 0$). This is because the core loss is very low at low values of magnetic flux density B, used in measurements. The impedance of the equivalent circuit depicted in Fig. 6.7, is [4],

$$Z = \frac{R_s + j\omega L\left[1 - \omega^2 LC_s - (C_s R_s^2/L)\right]}{(1 - \omega^2 LC_s)^2 + (\omega C_s R_s)^2} = r + jx \tag{3.13}$$

where $R_s = R_c + R_w$ is the total ac resistance, r is the equivalent series resistance (ESR), and x is the equivalent series reactance. Since $C_s R_s^2/L \ll 1$ [4], [14], the first parallel self-resonant frequency of the inductor model $f_r = 1/(2\pi\sqrt{LC_s})$ occurs when the imaginary part of the impedance Z in (7.43) is equal to zero. For frequencies below the first self-resonant frequency, the impedance of the inductor is inductive. For frequencies above the first self-resonant frequency, the impedance of the inductor is capacitive and the currents are shorted out. Thus, the useful frequency range of inductors is from dc to about $0.25 f_r \ll f_{max} \ll 0.45 f_r$.

3.5 Experimental Results

To verify the theory presented above, five seven-layer ($N_l = 7$) inductors for the application in a resonant power amplifier at resonant frequency $f_0 = 100$ kHz were

designed, built, and measured. The Magnetics 0R42616 ferrite pot core, made of R type material, with 00B261601 bobbin were used to build inductors. The initial permeability of the R type magnetic material is $\mu_r = 2300 \pm 25\%$. Inductors with five values of winding foil thickness $h_1 = 50$ μm, $h_2 = 100$ μm, $h_3 = 120$ μm, $h_4 = 220$ μm, and $h_5 = 500$ μm were measured. The foil width was $b = 10$ mm and MTL was $l_T = 5.3$ cm. For the seven-layer inductor ($N_l = 7$) made of copper foil and operating at frequency $f_0 = 100$ kHz, the optimum foil thickness calculated from (3.9) was $h_v = 104.06$ μm. Therefore, the foil with thickness $h_2 = 100$ μm was selected. The measured resonant frequency of the inductors was $f_r = 3.88$ MHz, the inductances of the foil inductors at $f_0 = 100$ kHz were $L = 88.6$ μH, the inductances of the foil inductors at $f_r = 3.88$ MHz were $L = L_{fr} = 530$ nH, and the measured stray-capacitances were $C_s = 3.17$ nF.

Fig. 3.3 shows measured and theoretical winding ac resistances predicted by Dowell's equation. It can be seen that Dowell's equation accurately tracks the measured winding ac resistances of the foil inductors. Observe that the inductor wound with $h_2 = 100$ μm had the lowest winding ac resistance. Therefore, the prediction of the optimum foil thickness by (3.9) ensures the lowest winding ac resistance of resonant inductors. The winding ac resistance predicted by (4.16) was $R_{wv} = 8.25$ mΩ, while the measured winding ac resistance was $R_{wvm} = 8.3$ mΩ.

3.6 Conclusion

An analytical equation for the optimum foil thickness of inductor conducting sinusoidal current has been derived. The derived equation ensures the minimum foil winding ac resistance and, hence, the minimum foil winding ac power loss. The derived equation can serve for the engineers as an easy to use tool to design the minimum winding losses inductors. Additionally, an equation for the minimum winding resistance for the foil inductors have been given. The equations for the optimum

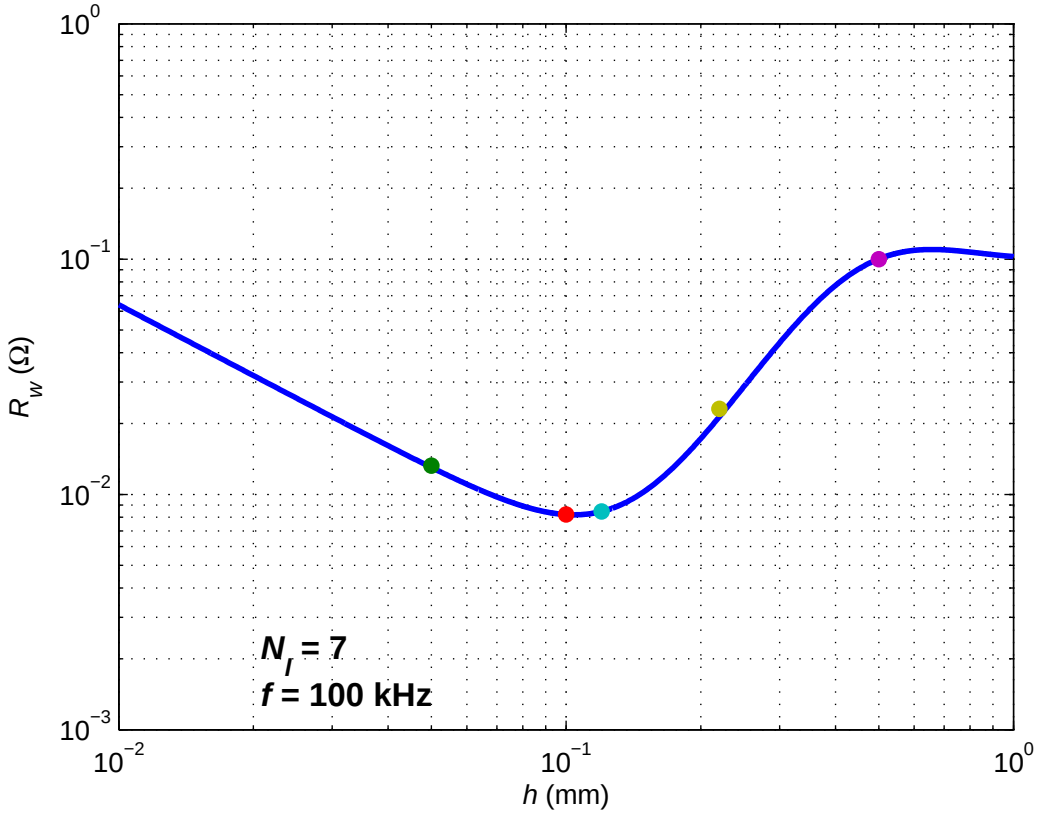

Figure 3.3: Measured and theoretical winding ac resistances predicted by Dowell's equation as functions of foil thickness h.

foil thickness and for the minimum winding ac resistance have been verified by the measurements. The measurement results justify presented theory.

4 Analytical Optimization of Solid-Round Wire Windings Conducting Sinusoidal Current

In this chapter, an analytical optimization of solid-round wire windings conducting sinusoidal current is performed. New closed-form analytical equations are derived for the normalized solid-round wire diameter to achieve minimum ac winding losses for sinusoidal current. Approximations of Dowell's equation are used to derive expressions for normalized diameter at the local minimum of winding ac resistance and normalized critical diameter. An equation for the winding ac resistance at the local minimum is derived. Additionally, equations for the normalized diameter at the local maximum of ac resistance and the normalized boundary diameter between low and medium frequency ranges are given. The formulas enable inductor and transformer designers to minimize winding loss without utilizing FEM analysis. Experimental verification of the presented theory is given.

Power inductors and transformers are common devices in power electronic circuits. Their role is to store and transfer energy through the magnetic field with the highest possible efficiency and also to provide filtering. One method of increasing the efficiency of magnetic components is to optimize the size of winding conductors. The purpose of winding optimization is to reduce the effect of eddy-current losses, and therefore to improve the overall efficiency of the power electronic system. Different kinds of windings such as foil, strip, solid-round wire, and litz-wire windings are used in high-frequency magnetic components. Their application depends on the electrical, mechanical, and thermal requirements of the designed magnetic component [14], [28], [64], [68], [73], [74]. Solid-round wire winding inductors are widely used in PWM dc-dc power converters, resonant power converters, resonant inverters, electromagnetic interference filters, and magnetic sensors [12]-[16], [28], [30], [52], [54], [70], [71], [75], [76], [77]. The main advantage of solid-round wire windings is low cost. The optimum

design of highly-efficient magnetic components using solid-round wire windings usually involves two objectives. The first objective is to minimize the influence of skin and proximity effects on the winding resistance [1]-[51], [56]-[64], [65]-[71], [73]-[76], [78]-[84]. The second objective is to maintain the amplitude of the current density in the winding below the maximum value, under specified cooling conditions [12], [14], [28], [68].

The objectives of this work are:

- to derive an expression for the normalized valley wire diameter of the solid-round wire windings, where the local minimum (valley) of the winding ac resistance occurs;
- to determine the normalized hill wire diameter of the solid-round wire windings, where the local maximum (hill) of the winding ac resistance occurs;
- to derive an expression for the normalized critical wire diameter of the solid-round wire windings (greater than the normalized valley wire diameter), where the winding ac resistance is equal to the winding ac resistance at the local minimum;
- to determine the boundary frequency between the low-frequency and medium-frequency ranges for a solid-round wire windings.

The chapter is arranged in the following order. Section 4.1 presents one-dimensional (1-D) Dowell's equation for the solid-round wire windings. The behavior of winding ac resistance in terms of wire diameter is also presented. An equation for the normalized diameter of the solid-round wire winding at which the winding ac resistance achieves its local maximum, i.e, the normalized hill diameter, is given. Section 4.2 gives the low and medium frequency approximation of Dowell's equation. This equation is used to derive expression for the normalized valley diameter and the expression

for the minimum local ac winding resistance. In Section 4.3, high frequency approximation of Dowell's equation is considered. This approximation is used to derive an expression for the normalized critical wire diameter. Section 4.4, determines the boundary between the low and medium frequency of the solid-round wire windings. The equation for the solid-round wire diameter at the boundary between the low and medium frequency ranges is derived, and an equation for the boundary frequency between low and medium frequency ranges for inductor windings is given. In Section 4.5, the experimental results are presented. The equations for the valley diameter and for the critical wire diameter of the solid-round wire windings are experimentally verified. Finally, Section 4.6 contains the conclusions.

4.1 Solid-Round Wire Winding Resistance

Dowell's equation [2] was derived from Maxwell's equations in Cartesian coordinates, using a one-dimensional (1-D) winding model. The main assumption of Dowell's derivation was that the winding consists of straight parallel foil conductors. As a result, the magnetic field is everywhere parallel to the conducting layers. The curvature, edge, and end effects are neglected. The model of the solid-round wire winding given in [7] is different than the model proposed in [2]. It is described by Bessel functions in cylindrical coordinates. This model is more complex and leads to a much more complicated equation describing the winding resistance.

For the solid-round wire inductor conducting a sinusoidal current $i_l(t) = I_{Lm} \sin \omega t$, the ac-to-dc winding resistance ratio F_R is expressed as [2], [7], [14]

$$F_R = \frac{R_w}{R_{wdc}} = A\left[\frac{\sinh(2A) + \sin(2A)}{\cosh(2A) + \cos(2A)} + \frac{2(N_l^2 - 1)}{3}\frac{\sinh(A) - \sin(A)}{\cosh(A) + \cos(A)}\right], \qquad (4.1)$$

where R_w is the winding ac resistance of a solid-round wire, I_{Lm} is the amplitude of the sinusoidal inductor current, and $\omega = 2\pi f$ is the angular frequency of the inductor

current. The dc resistance of a solid-round-wire winding is given by

$$R_{wdc} = \frac{4\rho_w l_w}{\pi d^2} = \frac{4\rho_w N l_T}{\pi d^2}, \tag{4.2}$$

where d is the diameter of a bare solid-round wire, $l_w = Nl_T$ is the total solid-round wire length, N is the number of turns, l_T is the mean turn length (MTL), $\rho_w = 1/\sigma_w$ is the conductor resistivity, and the variable A, which is the effective diameter of the solid-round wire winding, is given by [14]

$$A = \left(\frac{\pi}{4}\right)^{0.75} \frac{d}{\delta_w}\sqrt{\eta}. \tag{4.3}$$

The layer porosity factor is defined as

$$\eta = \frac{d}{p}, \tag{4.4}$$

where p is the distance between the centres of adjacent round conductors in the same winding layer. The skin depth of the wire conductor δ_w is described by

$$\delta_w = \sqrt{\frac{2}{\mu_0\sigma_w\omega}} = \frac{1}{\sqrt{\pi\mu_0\sigma_w f}} = \sqrt{\frac{\rho_w}{\pi\mu_0 f}}, \tag{4.5}$$

where μ_0 is the free space permeability.

For a round wire winding, the ac resistance may be written as

$$R_w = F_R R_{wdc} = F_R \frac{4\rho_w l_w}{\pi d^2} = F_R \frac{4\rho_w l_w}{\pi\delta_w^2\left(\frac{d}{\delta_w}\right)^2}$$

$$= \frac{\left(\frac{\pi}{4}\right)^{0.75}\sqrt{\eta}4\rho_w l_w}{\pi\delta_w^2\left(\frac{d}{\delta_w}\right)}\left[\frac{\sinh(2A)+\sin(2A)}{\cosh(2A)+\cos(2A)} + \frac{2(N_l^2-1)}{3}\frac{\sinh(A)-\sin(A)}{\cosh(A)+\cos(A)}\right], \tag{4.6}$$

which yields the normalized winding ac resistance of the solid-round wire at a fixed frequency f as

$$F_r = \frac{R_w}{\frac{4\rho_w l_w}{\pi\delta_w^2}} = \frac{F_R}{\left(\frac{d}{\delta_w}\right)^2}$$

$$= \frac{\left(\frac{\pi}{4}\right)^{0.75}\sqrt{\eta}}{\left(\frac{d}{\delta_w}\right)}\left[\frac{\sinh(2A)+\sin(2A)}{\cosh(2A)+\cos(2A)} + \frac{2(N_l^2-1)}{3}\frac{\sinh(A)-\sin(A)}{\cosh(A)+\cos(A)}\right]. \tag{4.7}$$

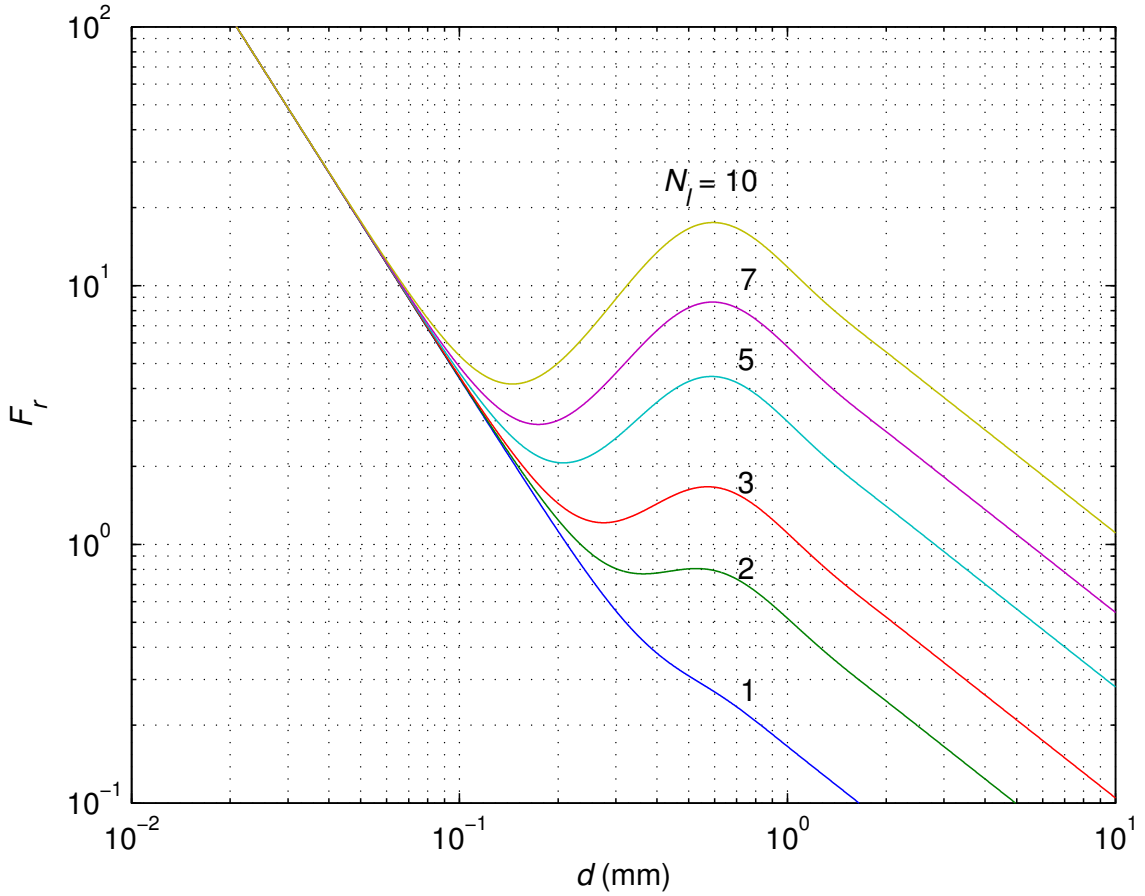

Figure 4.1: Normalized winding ac resistance F_r as a function of d for inductor with several number of layers $N_l = 1, 2, 3, 4, 7$, and 10 at constant frequency $f = 100$ kHz, and $\eta = 0.9$.

Fig. 4.1 shows the normalized winding ac resistance F_r as a function of d for the inductor with several layers $N_l = 1,\ 2,\ 3,\ 5,\ 7$, and 10 at $\eta = 0.9$ and constant frequency $f = 100$ kHz. It can be seen that the normalized winding ac resistance for a single-layer inductor ($N_l = 1$) decreases as the diameter of the wire increases. For a two-layer inductor, the normalized winding ac resistance first decreases with increasing wire diameter, then remains approximately constant, and afterwards it decreases as the wire diameter increases. As the wire diameter of the inductor with three and more layers ($N_l \geq 3$) increases, the normalized winding ac resistance first decreases, reaches a local minimum at the valley diameter d_v, then increases, reaches a local

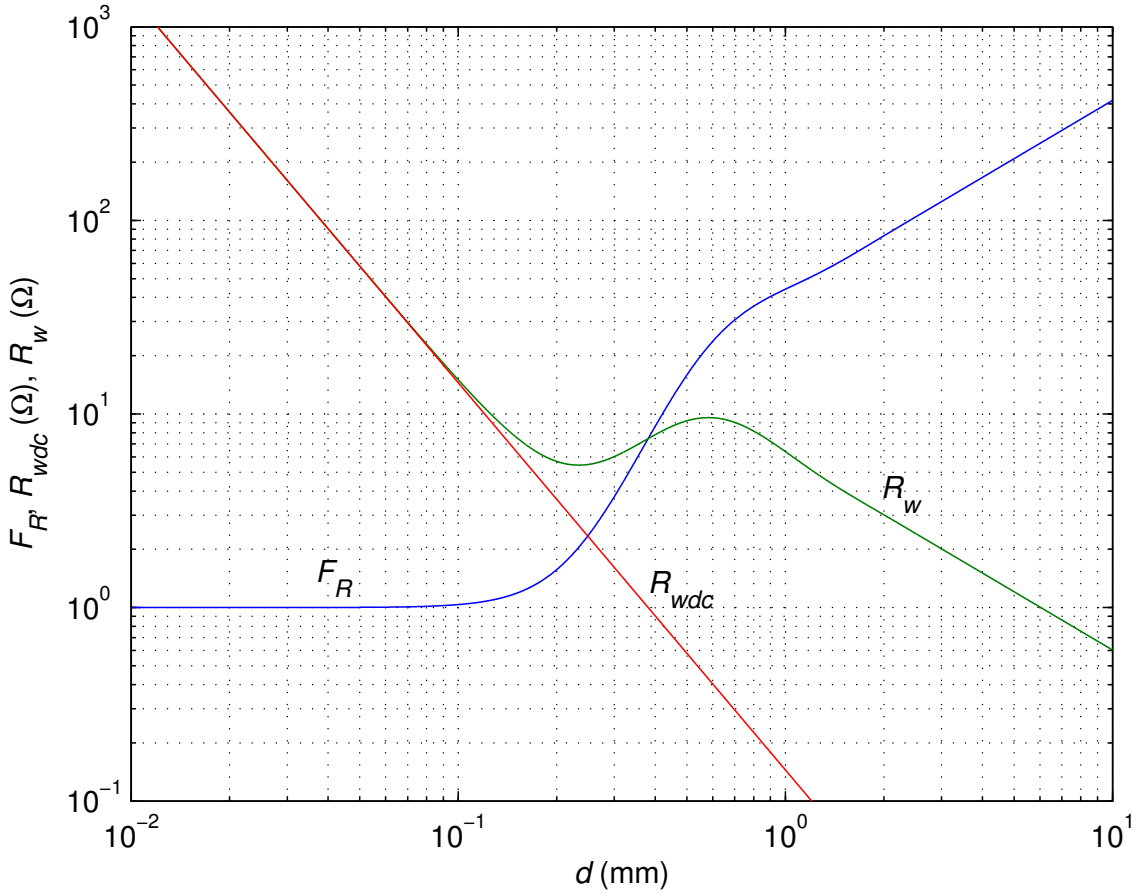

Figure 4.2: Plots of F_R, R_{wdc}, and R_w as functions of d for four-layer inductor ($N_l = 4$) with $l_T = 6.6$ cm, $N = 100$, frequency $f = 100$ kHz, and $\eta = 0.9$.

maximum at the hill diameter d_h, and finally decreases. It can be seen that the wire diameter at which the normalized winding ac resistance achieves the local maximum, i.e., the hill diameter, should be avoided in efficient inductor and transformer designs. At a certain value of the diameter $d_v \ll d$ and $d_h < d$, called the critical diameter d_{cr}, the winding resistance is the same as that at the valley diameter.

The normalized hill diameter of the bare solid-round wire at which the local maximum value of the winding ac resistance occurs is expressed as

$$\frac{d_h}{\delta_w} = \frac{2.274 - \frac{0.2576}{N_l}}{\left(\frac{\pi}{4}\right)^{0.75}\sqrt{\eta}}. \tag{4.8}$$

Fig. 4.2 shows plots of F_R, R_{wdc}, and R_w as functions of d for the four-layer

inductor ($N_l = 4$) with $l_T = 6.6$ cm, $N = 100$, frequency $f = 100$ kHz, and $\eta = 0.9$. It can be seen that the winding dc resistance R_{wdc} rapidly decreases with increasing bare wire diameter d. According to (7.2), the winding dc resistance R_{wdc} is inversely proportional to d^2. The ac-to-dc winding resistance ratio F_R is equal to one for low values of d, then rapidly increases, and finally increases proportionally to d. Consequently, the winding ac resistance $R_w = F_R R_{wdc}$ is equal to the winding dc resistance R_{wdc} at low values of d, reaches a local minimum, then increases, reaches a local maximum, and finally decreases where it is inversely proportional to d. Note that the ac-to-dc winding resistance ratio F_R at the local minimum of the winding ac resistance is equal to two ($F_R = F_{Rv} = 2$).

The characteristic property of the round wire winding is that the winding ac resistance R_w continuously decreases for $d > d_h$. This is because the winding dc resistance R_{wdc} is inversely proportional to d^2 and F_R is proportional to d for $d > d_h$. Therefore, the effect of the dc resistance is dominant. The square winding exhibits similar behavior [14]. Conversely, the winding ac resistance of foil and strip windings exhibits only a global minimum because the conductor thickness and width are independent [14].

Even though Dowell's equation describes the winding resistance in a wide frequency range taking into account skin and proximity effects, it is impossible to perform its analytical optimization. This is because Dowell's equation contains trigonometric and hyperbolic functions. Therefore, to perform analytical optimization, an approximation of Dowell's equation in (4.1) is used in the subsequent sections.

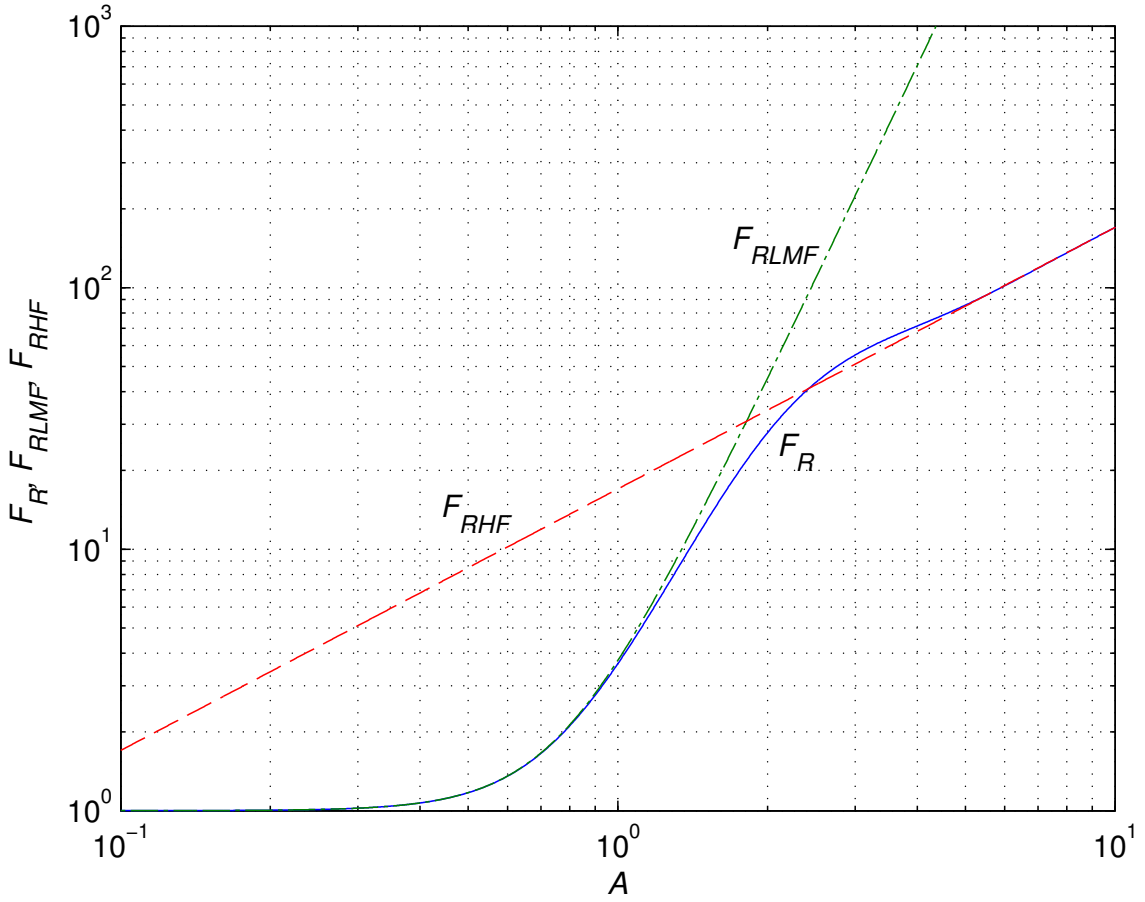

Figure 4.3: Plots of exact F_R, low and medium-frequency approximation F_{RLMF}, and high-frequency approximation F_{RHF} of ac-to-dc resistance ratio as functions of A for five-layer inductor ($N_l = 5$) and porosity factor $\eta = 0.9$.

4.2 Low- and Medium-Frequency Approximation of Dowell's Equation

The approximate Dowell's equation for solid-round wire windings valid for low and medium frequencies is [45]

$$F_{RLMF} = \frac{R_w}{R_{wdc}} \approx 1 + \frac{(5N_l^2 - 1)}{45} A^4 = 1 + \frac{\eta^2 (5N_l^2 - 1)}{45} \left(\frac{\pi}{4}\right)^3 \left(\frac{d}{\delta_w}\right)^4 \quad \text{for} \quad A \leq 2. \tag{4.9}$$

Fig. 4.3 shows plots of exact ac-to-dc resistance ratio F_R and low and medium-frequency approximation F_{RLMF} for the five-layer inductor ($N_l = 5$) at porosity factor $\eta = 0.9$. It can be seen that the low and medium-frequency approximation of the

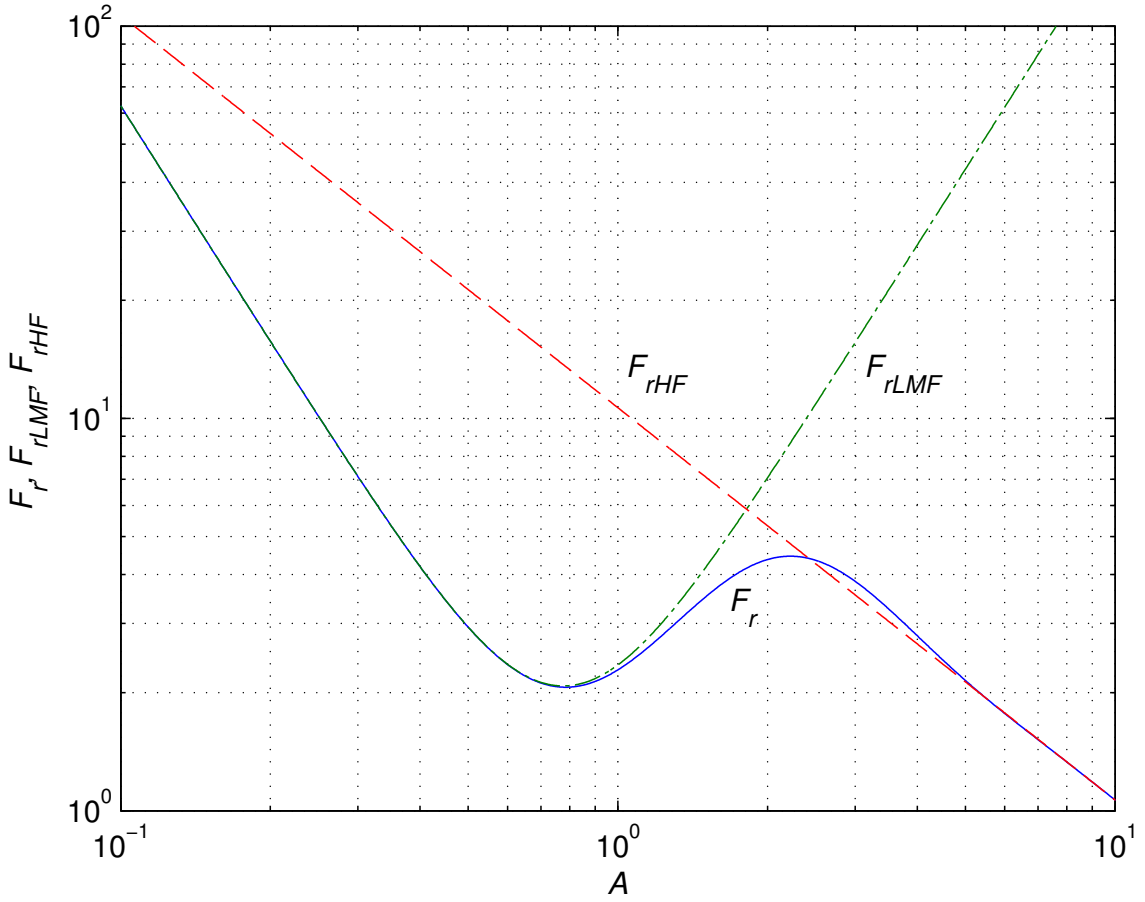

Figure 4.4: Plots of exact F_r, low and medium-frequency approximation F_{rLMF}, and high-frequency approximation F_{rHF} of normalized winding ac resistance as functions of A for five-layer inductor ($N_l = 5$) and porosity factor $\eta = 0.9$.

ac-to-dc resistance ratio for the five-layer inductor ($N_l = 5$) is valid for $A \leq 1.5$. This approximation is sufficiently accurate in the region of d at which the local minimum of R_w occurs. Therefore, the low and medium frequency approximation in (9.28) is used to derive an analytical expression for the valley diameter of the solid-round wire windings d_v.

The approximate normalized winding ac resistance of the solid-round wire windings at a fixed frequency f is

$$F_{rLMF} = \frac{F_{RLMF}}{\left(\frac{d}{\delta_w}\right)^2} \approx \frac{1}{\left(\frac{d}{\delta_w}\right)^2} + \frac{\left(\frac{\pi}{4}\right)^3 \eta^2 (5N_l^2 - 1) d^2}{45\delta_w^2}. \tag{4.10}$$

Fig. 4.4 shows plots of exact normalized winding ac resistance F_r in (4.7) and low and medium-frequency approximation F_{rLMF} in (4.10) as functions of A for a five-layer inductor ($N_l = 5$) at porosity factor $\eta = 0.9$. Assuming a constant skin depth δ_w, i.e., constant frequency, the solid-round wire winding ac resistance decreases with increasing wire diameter, reaches a local minimum value, then increases, reaches local maximum value, and finally decreases below the local minimum. From (7.2) and (9.28), the approximate winding ac resistance of the solid-round wire winding is

$$R_w \approx \frac{4\rho_w l_w}{\pi}\left[\frac{1}{d^2} + \frac{\left(\frac{\pi}{4}\right)^3 \eta^2(5N_l^2-1)d^2}{45\delta_w^4}\right]. \tag{4.11}$$

Taking the derivative of (4.11) with respect to d at a fixed δ_w and setting the result to zero, we obtain

$$\frac{dR_w}{dd} \approx \frac{4\rho_w l_w}{\pi}\left[-\frac{1}{d^3} + \frac{\left(\frac{\pi}{4}\right)^3 \eta^2(5N_l^2-1)d}{45\delta_w^4}\right] = 0. \tag{4.12}$$

Solution of this equation gives the normalized solid-round wire valley diameter at which the solid-round wire winding resistance has a local minimum value

$$\frac{d_v}{\delta_w} = \sqrt[4]{\frac{45}{\left(\frac{\pi}{4}\right)^3 \eta^2(5N_l^2-1)}}. \tag{4.13}$$

Therefore, the frequency at local minimum for the given diameter d of solid-round wire winding is expressed as

$$f_v = \frac{\rho_w}{\pi\mu_0 d^2}\sqrt{\frac{45}{\left(\frac{\pi}{4}\right)^3 \eta^2(5N_l^2-1)}}. \tag{4.14}$$

Substituting (4.13) into (9.28), we obtain the ac-to-dc winding resistance ratio at the normalized solid-round wire valley diameter d_v/δ_w

$$\begin{aligned} F_{Rv} &= 1 + \frac{\eta^2(5N_l^2-1)}{45} \times \left[\sqrt[4]{\frac{45}{\left(\frac{\pi}{4}\right)^3 \eta^2(5N_l^2-1)}}\right]^4 \\ &= 1 + 1 = 2. \end{aligned} \tag{4.15}$$

Hence, the solid-round wire winding ac resistance at the local minimum is

$$R_{wv} = F_{Rv} R_{wdc(d_v)} = \frac{8\rho_w l_w}{\pi d_v^2} = \frac{8\rho_w l_w}{\pi \delta_w^2 \sqrt{\frac{45}{\left(\frac{\pi}{4}\right)^3 \eta^2 (5N_l^2 - 1)}}}. \tag{4.16}$$

The diameter of the wire must be large enough to carry the maximum permissible amplitude of the current density J_m to avoid overheating. Typical amplitudes of current density range from 2 to 5 A/mm^2. The required conductor cross-sectional area is given by

$$A_w = \frac{I_{Lm}}{J_m}. \tag{4.17}$$

4.3 High-Frequency Approximation of Dowell's Equation

It is impossible to use Dowell's equation to find an analytical expression for the critical diameter of solid-round wire winding d_{cr} at which the winding ac resistance equals the winding ac resistance at local minimum R_{wv}. Therefore, the high-frequency approximation of (4.1) is used to derive an analytical expression for critical diameter d_{cr} of the solid-round wire winding. The approximate Dowell's equation for solid-round wire windings valid at high frequencies is [4], [14]

$$F_{RHF} = \frac{R_w}{R_{wdc}} \approx \frac{A(2N_l^2 + 1)}{3} = \left(\frac{\pi}{4}\right)^{0.75} \frac{\sqrt{\eta}(2N_l^2 + 1)d}{3\delta_w} \quad \text{for} \quad A \geq 3. \tag{4.18}$$

Fig. 4.3 shows plots of exact ac-to-dc resistance ratio F_R and high-frequency approximation of F_{RHF} as functions of A for the five-layer inductor ($N_l = 5$) at porosity factor $\eta = 0.9$. It can be seen that the high-frequency approximation of the ac-to-dc resistance ratio is valid for $A \geq 3$.

The approximate normalized winding ac resistance of the solid-round wire at a fixed frequency f is given by

$$F_{rHF} = \frac{F_{RHF}}{\left(\frac{d}{\delta_w}\right)^2} \approx \left(\frac{\pi}{4}\right)^{0.75} \frac{\sqrt{\eta}(2N_l^2 + 1)\delta_w}{3d}. \tag{4.19}$$

Fig. 4.4 shows plots of exact normalized winding ac resistance F_r in (4.7) and high-frequency approximation F_{rHF} in (4.19) as functions of A for a five-layer inductor

($N_l = 5$) at porosity factor $\eta = 0.9$. It can be seen that this approximation is sufficiently accurate in the region of $d >> d_v$ at which the solid-round wire winding ac resistance R_w is equal to winding ac resistance at the local minimum R_{wv}, i.e., at $d = d_{cr}$. Therefore, the high-frequency approximation in (9.31) is used to derive an analytical expression for the critical diameter of solid-round wire. The approximate winding ac resistance at high frequencies is given by

$$R_{wHF} \approx \frac{4\rho_w l_w}{\pi d^2}\frac{A(2N_l^2+1)}{3} = \left(\frac{\pi}{4}\right)^{0.75}\frac{4\rho_w l_w\sqrt{\eta}(2N_l^2+1)}{3\pi\delta_w d} \quad \text{for} \quad A \geq 3. \tag{4.20}$$

Equating (4.16) with (4.20), one obtains the normalized critical diameter of the solid-round wire winding

$$\frac{d_{cr}}{\delta_w} = \frac{2N_l^2+1}{6\left(\frac{\pi}{4}\right)^{0.75}}\sqrt{\frac{45}{\eta(5N_l^2-1)}}. \tag{4.21}$$

The importance of the critical diameter in the inductor and transformer design is significant because increasing the wire diameter above the critical diameter causes the decrease of winding ac resistance. Moreover, it can be inferred that increasing the diameter of the wire above the critical diameter d_{cr}:

- decreases the winding ac resistance;
- reduces current density amplitude J_m;
- increases the size of the inductor or the transformer.

4.4 Boundary Between Low and Medium Frequencies for Solid-Round Wire Windings

The boundary between the low and medium values of d/δ_w for a solid-round wire winding is defined here as the value of $(d/\delta_w)_B$ at which $F_R = 1.05$. This value is chosen because the skin and proximity effects are negligible and the winding ac resistance of a solid-round wire R_w is approximately equal to the winding dc resistance

of a solid-round wire R_{wdc}. Using (9.28), the ac-to-dc winding resistance ratio of the solid-round wire at the boundary between low and medium frequencies is

$$F_R = 1 + \frac{\eta^2(5N_l^2 - 1)}{45}\left(\frac{\pi}{4}\right)^3\left(\frac{d}{\delta_w}\right)^4_B = 1.05. \tag{4.22}$$

Solution of this equation yields the normalized solid-round wire diameter at the boundary between the low and medium frequencies

$$\left(\frac{d}{\delta_w}\right)_B = \sqrt[4]{\frac{9}{4\left(\frac{\pi}{4}\right)^3\eta^2(5N_l^2 - 1)}}. \tag{4.23}$$

Hence, the boundary frequency for the solid-round wire winding is

$$f_B = \frac{\rho_w}{\pi\mu_0 d^2}\sqrt{\frac{9}{4\left(\frac{\pi}{4}\right)^3\eta^2(5N_l^2 - 1)}}. \tag{4.24}$$

Observe that $d_v/\delta_w > (d/\delta_w)_B$ and $f_v > f_B$.

4.5 Experimental Results

The experimental verification of the equations for the solid-round wire valley diameter d_v, the critical solid-round wire diameter d_{cr}, and the normalized winding ac resistance of the solid-round wire F_r is performed in this section. For this purpose, ten inductors commonly used in resonant power converters have been wound with an AWG32, AWG30, AWG26, AWG24, and AWG20 magnet wire and measured [52].

Table 4.1 gives parameters of measured inductors, where L_{LF} is the low-frequency inductance, f_r is the self-resonant frequency, and C is the self-capacitance. All inductors were wound on the Magnetics 0R42616 ferrite air gapped pot core with the gap length $l_g = 100$ μm and with the 00B261601 bobbin. The initial permeability of the core material was $\mu_r = 2300 \pm 25\%$ and the mean turn length (MTL) $l_T = 5.3$ cm. The inductors equivalent series resistance r [14], [22] was measured using HP 4275A multi-frequency LCR meter with 16047A test fixture. The inductors were measured at frequencies $f = 10,\ 20,\ 40,\ 100,\ 200,\ 400$, and 1000 kHz. To transform

Inductor Number #	American Wire Gauge	Number of Layers N_l	Number of Turns N	Inductance L_{LF} (mH)	Capacitance C (pF)	Res. Freq. f_r (kHz)
1	32	2	88	5.01	26.95	433.53
2	30	2	70	3.47	16.8	546.25
3	26	2	40	1.27	16.8	1115.0
4	24	2	34	0.788	23	1467
5	20	2	18	0.249	111.7	2600
6	32	4	176	20.82	20	245.27
7	30	4	140	13.22	13.5	333.75
8	26	4	80	4.47	10.98	627.5
9	24	4	68	3.12	11.5	722.53
10	20	4	36	0.955	18.85	1293.7

Table 4.1: Parameters of designed and measured inductors.

the measured equivalent series resistance into the winding ac, resistance the following expression is used [4], [25], [72]

$$R_w = \frac{1 - \sqrt{1 - 4\omega^2 r^2 C^2 (1 - \omega^2 LC)^2}}{2r\omega^2 C^2}, \tag{4.25}$$

where L is the inductance at the operating frequency and C is the parasitic self-capacitance of the inductor. The resonant frequency of the inductors f_r was measured using HP 4194A impedance/gain-phase analyzer with 16047D test fixture. The first self-resonant frequency of the inductor is

$$f_r = \frac{\omega_r}{2\pi} = \frac{1}{2\pi\sqrt{LC}}. \tag{4.26}$$

Table 4.2 gives the valley diameter of the solid-round wire winding for two and four-layer inductors at different frequencies. The measurements of the inductors will be presented in the form of the normalized winding ac resistance, for ease of comparison. Figs. 4.5-4.12 show the measured and computed normalized winding resistance as a function of the wire diameter for the two-layer inductors ($N_l = 2$) and for the four-layer inductors ($N_l = 4$) at frequencies $f = 100,\ 200,\ 400$, and 1000 kHz. It

Frequency (kHz) f	Inductor Number #	Number of Layers N_l	Valley Diameter (μm) d_v	American Wire Gauge
10	10	4	822	20
20	5	2	830	20
40	8	4	411	26/25
100	3	2	371	27/26
100	7	4	260	30/29
200	2	2	263	30/29
200	6	4	184	33/32
400	1	2	186	33/32

Table 4.2: Diameter of inductor winding at $\eta = 0.7$.

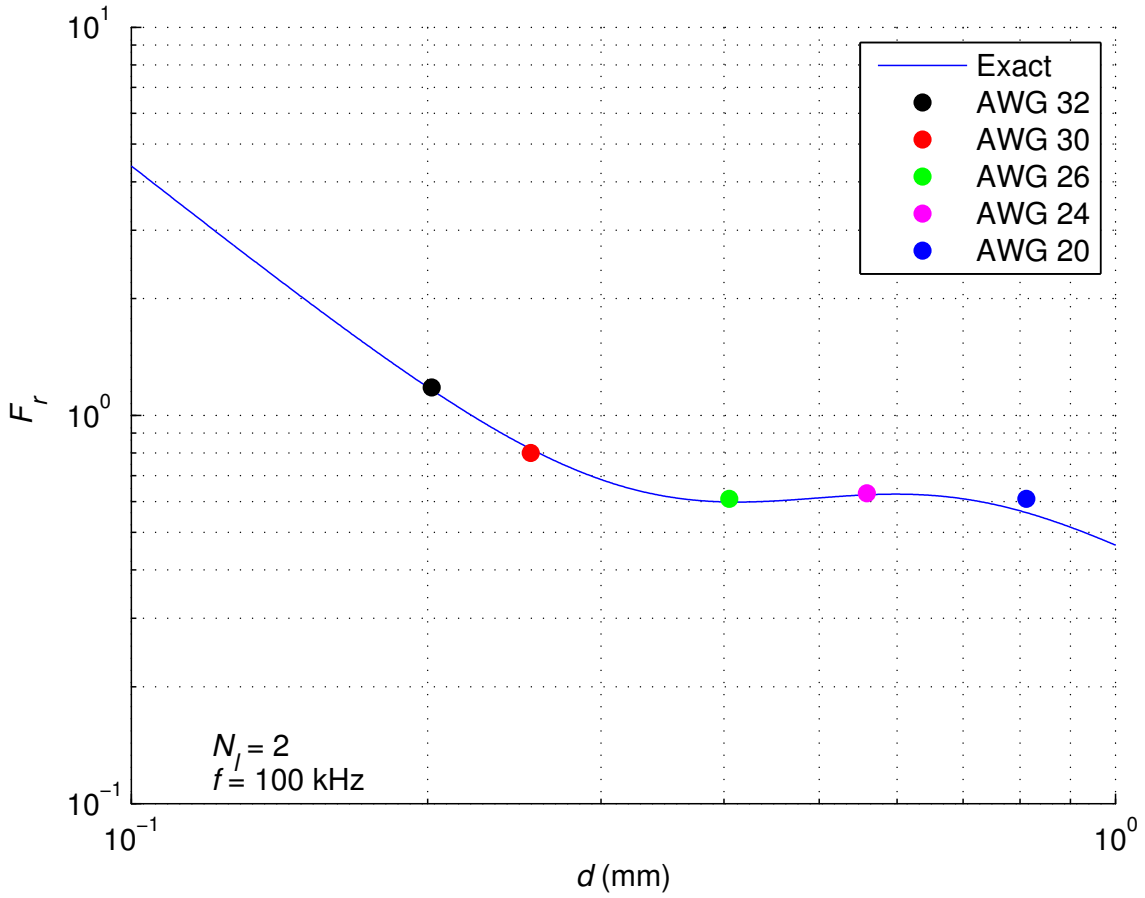

Figure 4.5: Plots of exact normalized winding ac resistance F_r and measured values for inductors wound with AWG32, AWG30, AWG26, AWG24, and AWG20 solid round wire as functions of wire diameter d for two-layer inductor ($N_l = 2$) at frequency $f = 100$ kHz.

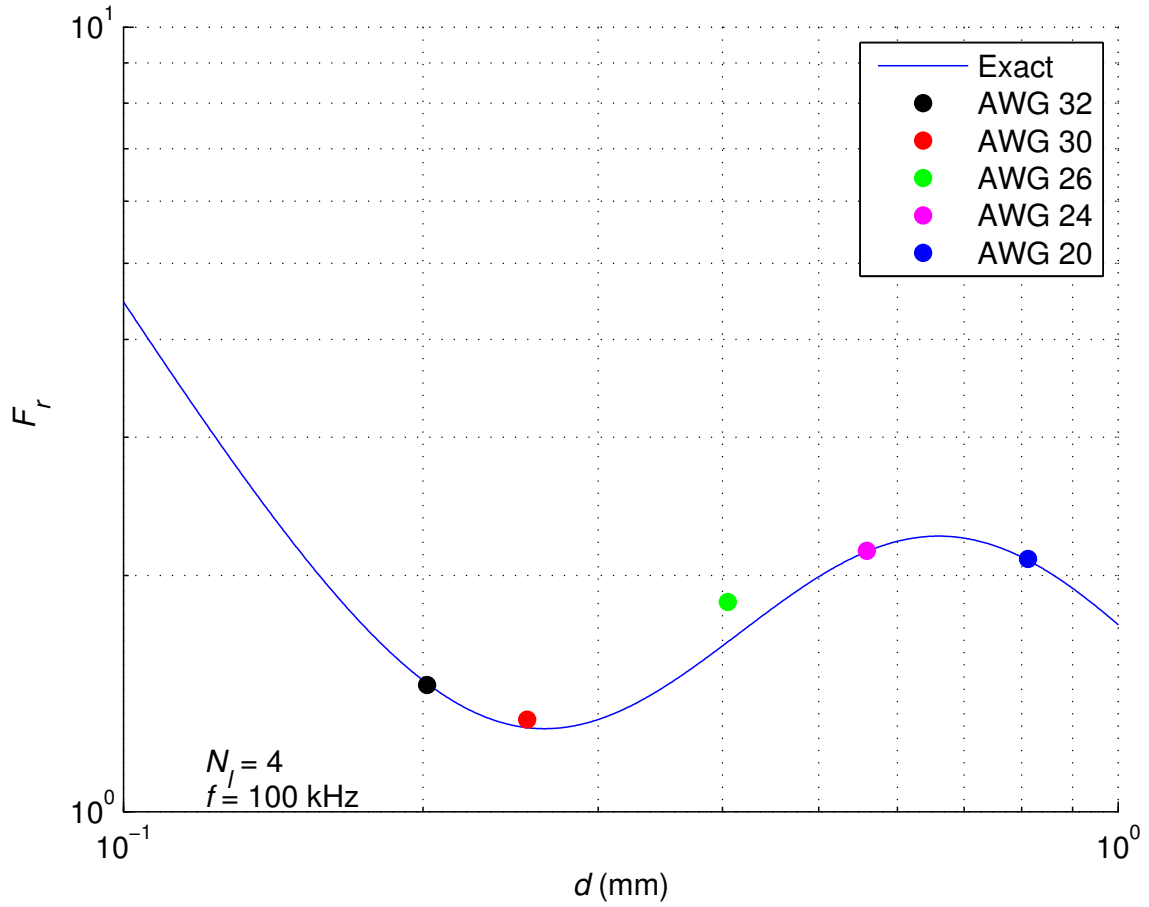

Figure 4.6: Plots of exact normalized winding ac resistance F_r and measured values for inductors wound with AWG32, AWG30, AWG26, AWG24, and AWG20 solid round wire as functions of wire diameter d for four-layer inductor ($N_l = 4$) at frequency $f = 100$ kHz.

can be seen that the predicted normalized winding ac resistance computed from (4.7) tracks the measured normalized winding ac resistance with high accuracy.

Figs. 4.5, 4.7, and 4.9 show the measured and computed normalized winding ac resistance as a function of the wire diameter for the two-layer inductor ($N_l = 2$). It can be seen from these plots that the computed valley wire diameter agreed with the measured valley diameter of inductors #1, #2, and #3, respectively, and that the resistance of these inductors at the measured frequency was minimal. Figs. 4.6 and 4.8 show the measured and computed normalized winding ac resistance as a function of the wire diameter for the four-layer inductor ($N_l = 4$). As can be seen, for the four-

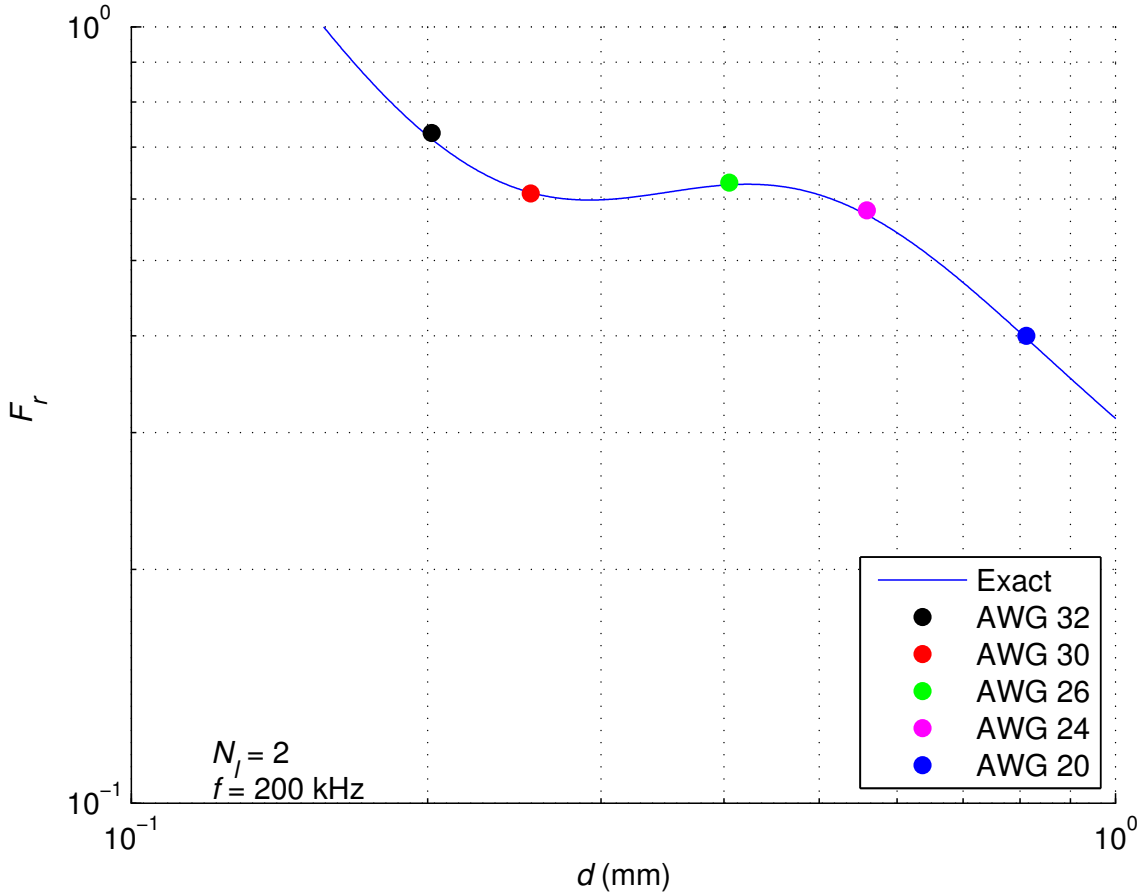

Figure 4.7: Plots of exact normalized winding ac resistance F_r and measured values for inductors wound with AWG32, AWG30, AWG26, AWG24, and AWG20 solid round wire as functions of wire diameter d for two-layer inductor ($N_l = 2$) at frequency $f = 200$ kHz.

Frequency (kHz) f	Inductor Number #	Number of Layers N_l	Critical Diameter (μm) d_{cr}	American Wire Gauge
200	4	2	489	25/24
200	10	4	879	20/19
1000	8	4	393	27/26

Table 4.3: Critical diameter of inductor winding at $\eta = 0.7$.

layer inductors, the computed valley wire diameter agreed with the measured valley diameter of inductors #7 and #6, respectively, and the resistance of each inductor at the measured frequency was minimal.

Table 4.3 gives critical diameter of the inductor winding at $\eta = 0.7$. It can be seen

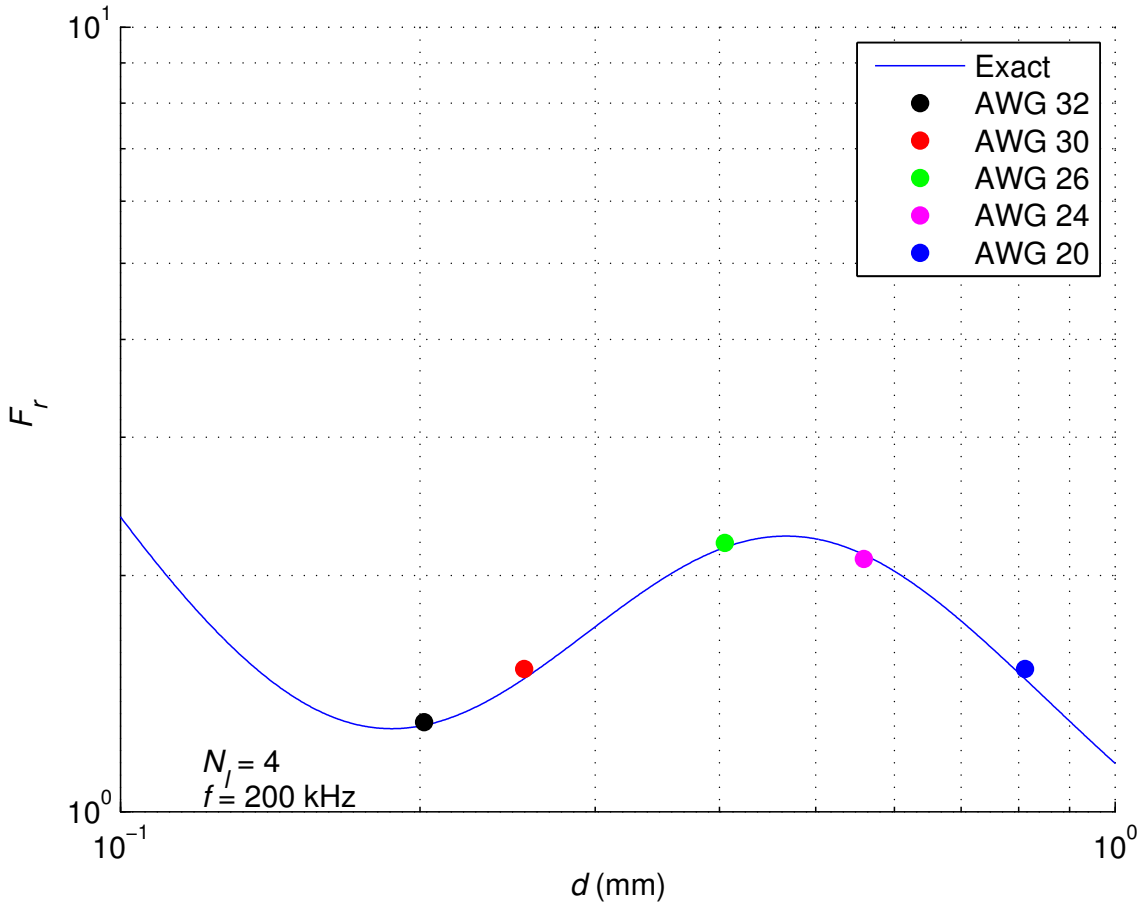

Figure 4.8: Plots of exact normalized winding ac resistance F_r and measured values for inductors wound with AWG32, AWG30, AWG26, AWG24, and AWG20 solid round wire as functions of wire diameter d for four-layer inductor ($N_l = 4$) at frequency $f = 200$ kHz.

that as the number of layers in the inductor increases, the critical wire diameter also increases. Figs. 4.7, 4.9-4.12 show that above the critical wire diameter, the measured winding ac resistance was lower than that at the local minimum. Moreover, by using the round-wire windings with a diameter equal or greater than the critical diameter, it is possible to decrease the amplitude of the current density in the wire and hence to minimize the probability of the conductor destruction by heat.

The measurements showed that at frequency $f = 1$ MHz, AWG32 is the hill diameter for the two and four-layer inductors (Figs. 4.11 and 4.12). Using (4.8), the computed hill diameter was $d_h = 203$ μm for the two-layer inductor (#1) and

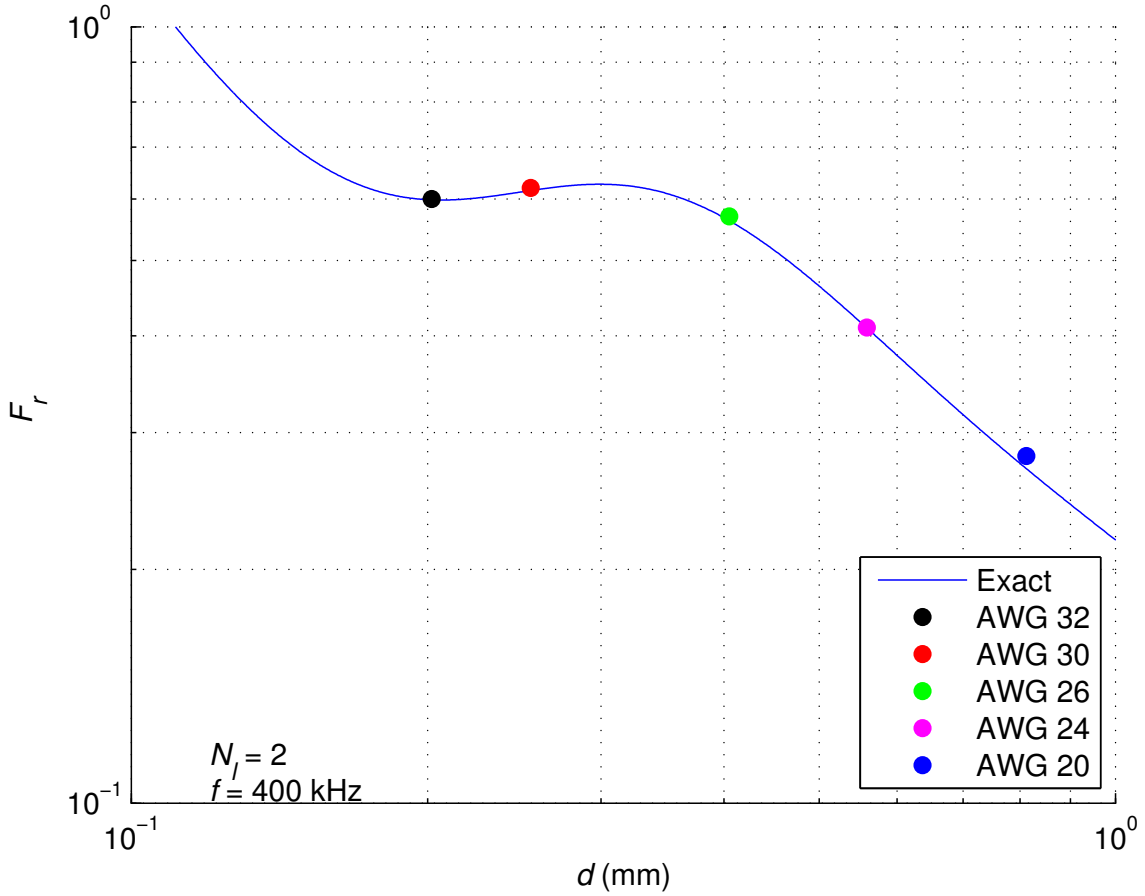

Figure 4.9: Plots of exact normalized winding ac resistance F_r and measured values for inductors wound with AWG32, AWG30, AWG26, AWG24, and AWG20 solid round wire as functions of wire diameter d for two-layer inductor ($N_l = 2$) at frequency $f = 400$ kHz.

$d_h = 209$ μm for the four-layer inductor (#6). Therefore, as the number of layers increases, the hill diameter increases.

4.6 Conclusion

In this chapter, analytical optimization of solid-round wire inductor windings has been presented. The normalized valley diameter of solid-round wire winding, at which local minimum of winding ac resistance is achieved, has been derived using low and medium frequency approximation. Equations for ac resistance at the valley diameter and for the normalized hill diameter at which local maximum of winding ac resistance

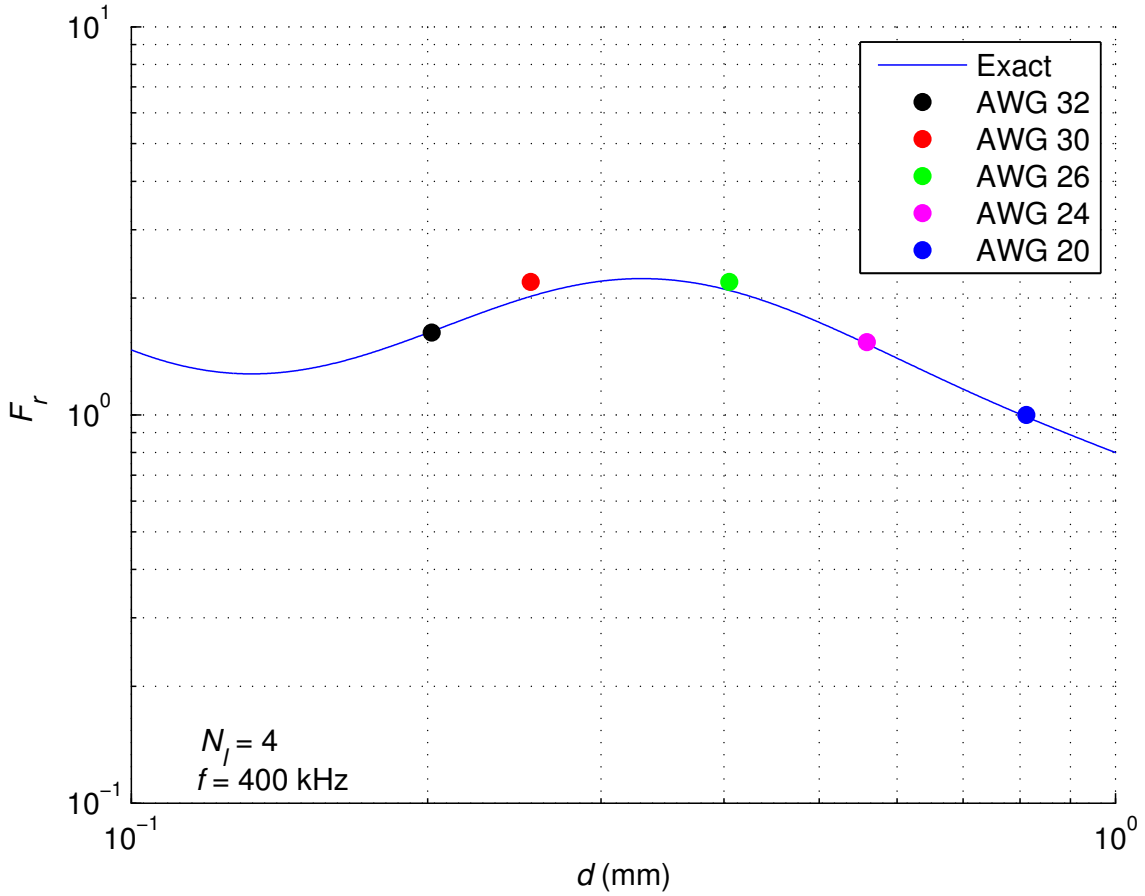

Figure 4.10: Plots of exact normalized winding ac resistance F_r and measured values for inductors wound with AWG32, AWG30, AWG26, AWG24, and AWG20 solid round wire as functions of wire diameter d for four-layer inductor ($N_l = 4$) at frequency $f = 400$ kHz.

is achieved, have been given. It has been shown that the valley diameter of the solid-round wire depends on the frequency f of the conducting current and the number of winding layers N_l in the inductor. As both the current frequency and number of layers increases, the valley diameter of the solid-round wire winding decreases. This results in a lower cross-sectional conductor area and higher amplitude of the current density in the conductor, and may result in destruction of the winding by overheating. Dowell's equation and the measurements have shown that the valley diameter assures only a local minimum of winding ac resistance. For the wire diameters much greater than the valley diameter, the winding ac resistance is the same or even lower than

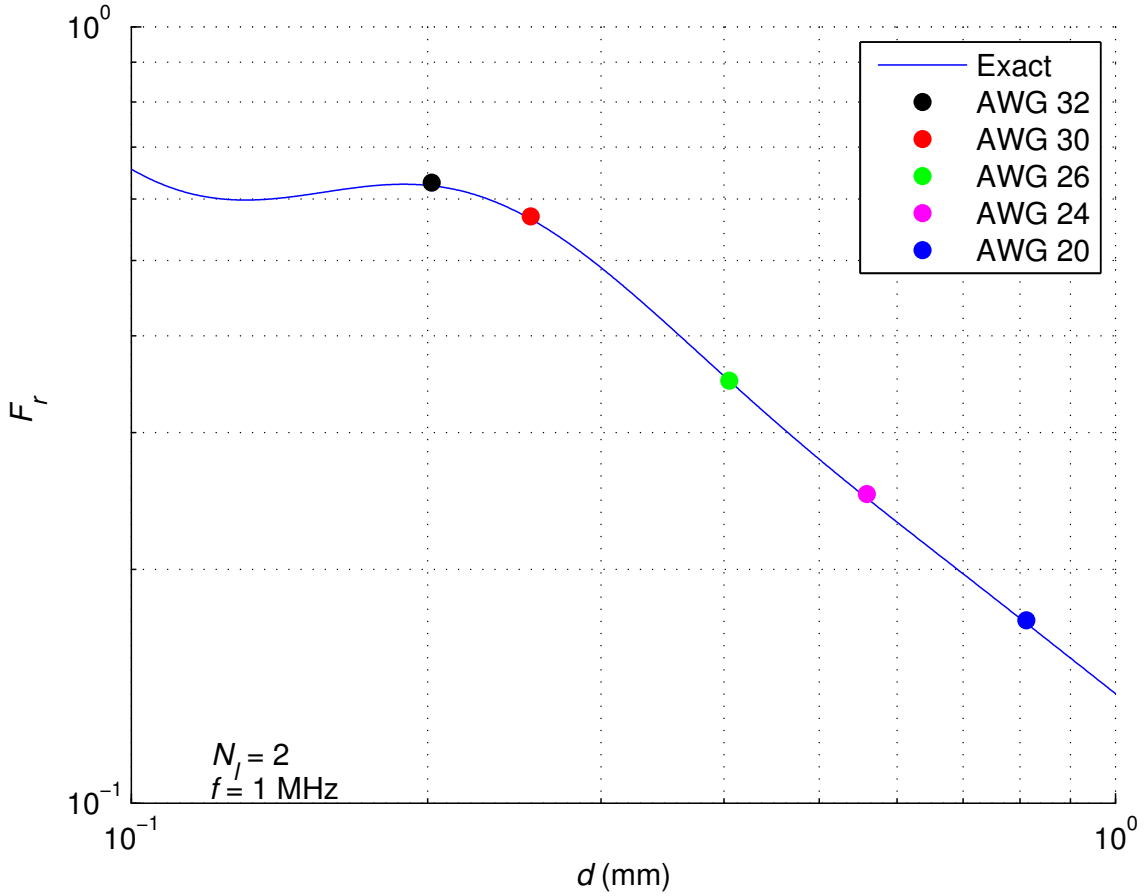

Figure 4.11: Plots of exact normalized winding ac resistance F_r and measured values for inductors wound with AWG32, AWG30, AWG26, AWG24, and AWG20 solid round wire as functions of wire diameter d for two-layer inductor ($N_l = 2$) at frequency $f = 1$ MHz.

that of the valley wire diameter. This is because the winding dc resistance is strongly dependent on the wire diameter. The diameter of the wire at which the winding ac resistance is same as the ac resistance for valley wire diameter is called the critical diameter d_{cr}. In this paper, the critical wire diameter has been derived using an approximate equation for the winding ac resistance of solid-round wire windings, valid at high-frequencies. The accuracy of equations for the normalized ac resistance, valley wire diameter, and critical wire diameter has been experimentally verified. The predicted results were in good agreement with the measured results.

The main conclusions drawn from the analysis of this chapter are as follows:

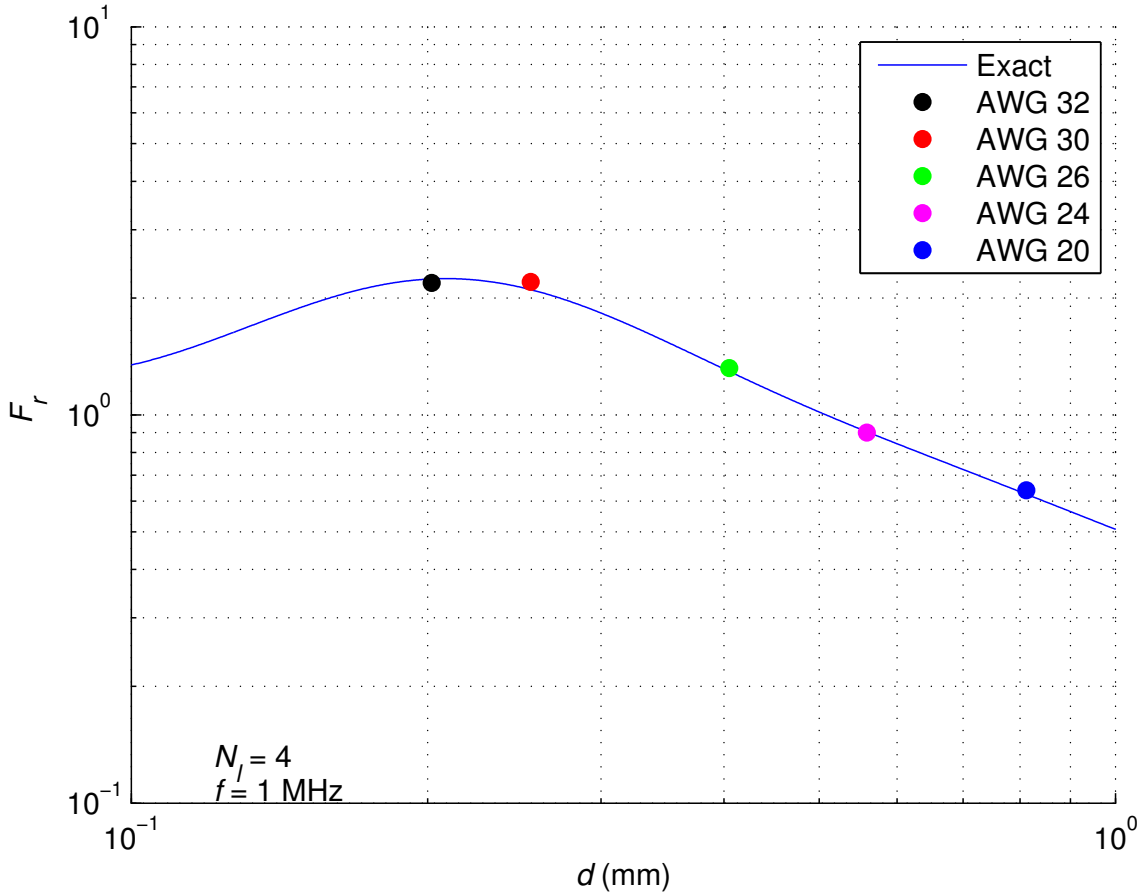

Figure 4.12: Plots of exact normalized winding ac resistance F_r and measured values for inductors wound with AWG32, AWG30, AWG26, AWG24, and AWG20 solid round wire as functions of wire diameter d for four-layer inductor ($N_l = 4$) at frequency $f = 1$ MHz.

- There is a solid-round wire diameter, called the valley diameter, at which the winding ac resistance achieves a local minimum. This diameter should be used for low-loss inductors.

- There is a solid-round wire diameter, called the hill diameter, at which the winding ac resistance reaches a local maximum. This diameter should be avoided in efficient inductor and transformer designs.

- There is a solid-round wire diameter, called the critical diameter, at which the winding ac resistance is equal to the resistance at the local minimum. An

increase in the diameter above the critical diameter, causes a decrease of the winding ac resistance. Inductors conducting large currents should use windings with a diameter equal or greater than the critical diameter.

- As the frequency of the sinusoidal current through inductor winding increases, the valley diameter, the hill diameter, and the critical diameter all decrease.
- As the number of layers in the inductor increases, the valley diameter decreases.
- As the number of layers in the inductor increases, both the hill diameter and the critical diameter increase.
- For the valley diameter of the solid-round wire winding, the ac-to-dc resistance ratio of the solid-round wire winding is equal to two ($F_R = F_{Rv} = 2$).
- For a sinusoidal current at a fixed frequency, the winding resistance of the solid-round wire winding decreases as the diameter of the wire d increases beyond the critical diameter d_{cr}.

5 Winding Resistance of Litz-Wire and Multi-Strand Wire Inductors Conducting Sinusoidal Current

This chapter presents an approximate model for litz-wire winding, including multi-strand wire winding. The proposed model is evaluated using Dowell's equation. The model takes into account the existence of proximity effect within the litz-wire bundle between the strands and between the bundles, as well the skin effect. The expressions for optimum strand diameter and number of strands at which minimum winding ac resistance is obtained for the litz-wire windings are derived. The boundary frequency between the low-frequency and the medium-frequency ranges are given for both litz-wire and solid-round wire inductors. Hence, the low-frequency range of both wire windings are determined. It is shown that litz-wire is better than the solid wire only in specific frequency range. An example of a design procedure of litz-wire winding inductor is presented. The model has been verified by the measurements, and the theoretical results were in good agreement with those experimentally measured. The chapter compares the theoretical predictions of the proposed approximate litz-wire model with models proposed by other authors and with experimental results.

Litz wire is used to reduce winding power losses of inductors and transformers. Power inductor and power transformer losses consist of winding dc loss, winding ac loss, and core losses. The dc losses are due to a high dc resistance of a winding conductor and they can be simply reduced by increasing a cross-sectional area of the conductor. The winding ac power loss at high frequencies in an inductor is caused by eddy currents. There are two effects of eddy currents: the skin effect and the proximity effect [1]-[51], [56]-[64], [65]-[71], [73]-[76], [78]-[84]. Both effects are frequency dependent and alter the current density distribution in the conductor through which the current flows. For the low-frequency operation, the conductor winding resistance is approximately equal to the dc resistance. However with increasing the operating

frequency, the winding resistance rapidly increases. In order to maintain the low winding ac resistance at higher frequencies, it is desirable to use a parallel multi-strand wire, including the litz-wire or in German *Litzendraht*. A multi-strand wire winding consists of at least two strands, and a litz-wire winding consists of many strands, up to couple of thousands of strands in a bundle [87]. Various approaches to the analysis of multi-strand and litz-wire windings have been presented [25], [31], [32], [34], [38]-[45], [47]-[51], [56].

The objectives of this chapter are to:

- Introduce a model of litz-wire winding.
- Adapt Dowell's equation for the litz-wire winding model.
- Develop a relatively simple equation for the resistance of litz-wire winding.
- Determine the optimum strand diameter.
- Determine the number of strands in the litz-wire bundle at which the minimum winding ac resistance is obtained.
- Determine the boundary frequency between the low-frequency and medium-frequency ranges for a litz-wire winding and a solid-round wire winding.
- Compare the resistance of a litz-wire winding with that of a solid-round wire winding over a wide frequency range.

Section 5.1 introduces an approximate model of litz-wire winding, including multi-strand wire winding and presents assumptions for validity of this model. Relationships between litz-wire and solid-round wire windings are given in Section 5.2. Section 5.3 includes derivation of a general expression for the boundary frequency between low and medium-frequency ranges for solid-round wire windings as a function of the

number of layers N_l. Section 5.4 adopts Dowell's expression for litz-wire windings, including multi-strand wire windings. A low and medium frequency approximation of the modified Dowell's equation for litz-wire windings is given and expressions for optimum strand diameter and required number of strands in the litz-wire bundle at which minimum winding resistance is obtained are derived. The general expression for the boundary frequency between low and medium-frequency ranges for litz-wire windings as a function of the number of layers is given. Moreover, the relation between the boundary frequency of the litz-wire windings and the boundary frequency of the solid-round wire windings is presented. The relation between normalized optimum strand diameter and normalized strand diameter at the boundary between low and medium frequencies is also given. In Section 5.7 comparison of winding ac resistance of litz-wire and winding ac resistance of solid-round wire is given. This section shows the frequency range, where the litz-wire windings exhibit lower winding losses than the solid-round wire windings. Section 5.8 describes relationship between the inductor winding ac resistance and equivalent series resistance (ESR) with negligible core losses. Additionally, the model of the measured inductor with negligible core losses as well as the equations for equivalent series resistance and equivalent series reactance are presented. Section 5.9 presents experimental verification and compares several methods to predict the ac resistance of the litz-wire windings. Finally, conclusions and discussions are conducted in Section 5.10.

5.1 Proposed Model of Litz-Wire and Multi-Strand Wire Windings

Figure 5.1 shows a proposed approximate model of litz-wire and multi-strand wire windings. The winding consists of N_l bundle layers. Each bundle contains k strands. There are different shapes of litz-wire bundles, such as round, square, rectangular, and hexagonal [87]. It is assumed that the net currents in all strands are equal (i/k),

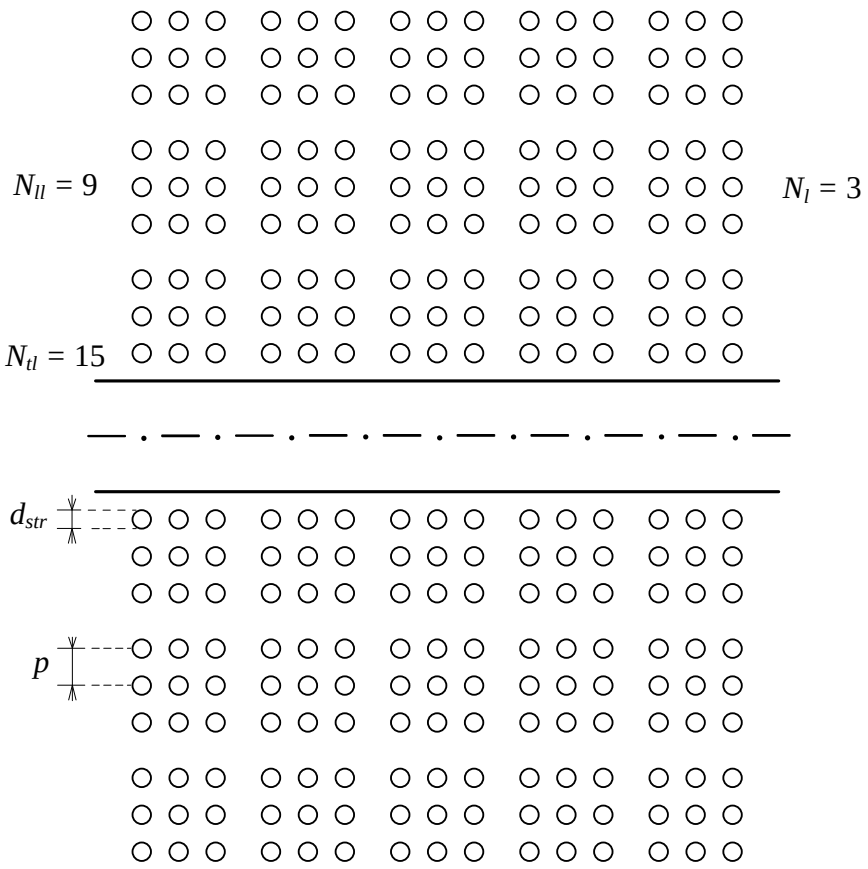

Figure 5.1: Model of litz-wire and multi-strand wire windings.

where i is the net current flowing through the litz-wire bundle. The number of layers in each bundle is $\sqrt{k}$ and the number of strand turns per inductor strand layer is N_{tl} . It is also assumed that the individual strands are parallel to the axis of the bundle, all strands within the bundle and between the bundles are uniformly spaced, and each effective bundle in the model has a square shape. Therefore, the effective number of layers of a litz-wire and multi-strand wire inductor is given by

$$N_{ll} = N_l\sqrt{k}. \tag{5.1}$$

This model will be used in the subsequent analysis.

The model of the litz-wire winding given in [25] is different than the model proposed in this chapter. It is described by Bessel functions in cylindrical coordinates. This model is more complex and leads to a much more complicated equation describ-

ing the winding resistance.

A challenging problem is to determine the winding resistance of the proposed model. In 1966, Dowell derived an analytical rigorous physics-based equation for foil winding resistance from Maxwell's equations in Cartesian coordinates, using a one-dimensional (1-D) winding model. The main assumption in his derivation is that the winding consists of straight parallel foil conductors. As a result, the magnetic field is everywhere parallel to the conducting layers. The curvature, edge, and end effects are neglected. This equation takes into account both the skin and proximity effects. Dowell's equation was adapted to other shapes of winding conductors, such as rectangular, square, and round conductors. In reality, the magnetic field exhibits also perpendicular or circumferential component in addition to the parallel component, whose distribution requires a 2-D analysis. The magnitude of the perpendicular component depends on many factors such as the distance between the turns, the actual geometry of the winding, the distance between the layers, and the number of the layers and turns. The distance between the turns is described by the porosity factor $\eta = p/d$, where d is the diameter of the bare winding conductor and p is the distance between the centres of the conductors in a layer. It has been shown in [19] that the error between 2-D and 1-D analyses "is minimal in the range $40\% \leq \eta \leq 70\%$." The porosity factor η falls into this range for litz-wire windings. The error increases for the porosity factor η close to 1 (the conductors nearly touch each other) and for small values of η (the distance between the conductors is large). Moreover, publication [19] has shown that the round wire conductor winding resistance computed from 2-D model is greater than the winding resistance predicted by 1-D Dowell's equation. A 2-D finite element analysis (FEA) in [35] has shown that 1-D Dowell's equation also underestimates winding losses in round conductor windings.

Some publications [56], [57], [46], [15], [16], [63], [65], [71], and [30] have shown that 1-D model used for round conductor windings predicts accurately the winding

resistance. In these publications, the results were verified with the experimental data. In [46], it has been shown that "the losses at the fundamental frequency are always accurate for round wire", when calculated using Dowell's equation. In [63], it has been shown that "theoretical predictions are in good agreement with the measurement data", when a 1-D field analysis is used for solid-round conductors winding. In [65], it has been shown that the 1-D model results compared with real measurements "can be appreciated the high precision of the model."

In contrast, publications [40], [47], and [48] have shown that 1-D Dowell's equation overestimates the winding resistance. In particular, the analysis in [40] showed that Dowell's equation introduces a 5% error at high values of porosity factor and a large number of layers for round winding conductors. In addition, Dowell's equation seriously underestimates the winding resistance at low values of the porosity factor and a low number of layers.

It is difficult to use a finite element analysis for simulation of litz-wire windings. This is because litz-wire bundles consist of hundreds or thousands of strands. Therefore, simulation of litz-wire windings with a sufficiently small mesh to achieve accurate eddy-currents density distribution requires long computation time [51], which is quite often a critical factor for daily industry designs. Moreover, FEA simulations give information on specific cases only, and adaptation of the solutions to other cases is a difficult task. In the subsequent analysis, the analytical Dowell's expression is transformed to describe the winding resistance of litz-wire and multi-strand wire inductors. This equation gives a lot of insight into various dependencies of winding resistances and can be easily used in industrial environment. Several methods of computing litz-wire winding resistance will be compared with each other and with experimental results in Section 5.9.

5.2 Relationships Between Litz-Wire and Solid-Round Wire Windings

The dc resistance of a litz-wire winding is

$$R_{wdc(litz)} = \frac{4\rho_w l_w}{k\pi d_{str}^2} = \frac{4\rho_w N l_T}{k\pi d_{str}^2}, \tag{5.2}$$

where $\rho_w = 1/\sigma_w$ is the winding conductor resistivity, d_{str} is the diameter of the single bare strand, $l_w = Nl_T$ is the total strand length, N is the total number of turns in the inductor, and l_T is the mean turn length (MTL).

The dc resistance of a solid-round wire winding is given by

$$R_{wdc(solid)} = \frac{4\rho_w l_w}{\pi d^2} = \frac{4\rho_w N l_T}{\pi d^2}, \tag{5.3}$$

where d is the diameter of a bare solid-round wire, $l_w = Nl_T$ is the total solid-round wire length. Equating the dc resistance of the litz-wire winding in (5.2) to the dc resistance of the solid-round wire winding in (5.3), one obtains the relationship between the diameter of a bare solid-round wire and the diameter of a litz-wire bare strand in order to ensure the same dc resistance of both windings

$$d_{str} = \frac{d}{\sqrt{k}}. \tag{5.4}$$

5.3 Solid-Round Wire Winding Resistance

For the solid-round wire inductor conducting sinusoidal current, the ac-to-dc winding resistance ratio F_R is expressed as [14]

$$F_{R(solid)} = \frac{R_{w(solid)}}{R_{wdc(solid)}} = A\left[\frac{\sinh(2A)+\sin(2A)}{\cosh(2A)-\cos(2A)} + \frac{2(N_l^2-1)}{3}\frac{\sinh(A)-\sin(A)}{\cosh(A)+\cos(A)}\right], \tag{5.5}$$

where $R_{w(solid)}$ is the ac resistance of a solid-round wire winding

$$R_{w(solid)} = F_{R(solid)} R_{wdc(solid)}$$

$$= R_{wdc(solid)} A \left[\frac{\sinh(2A) + \sin(2A)}{\cosh(2A) - \cos(2A)} + \frac{2(N_l^2 - 1)}{3} \frac{\sinh(A) - \sin(A)}{\cosh(A) + \cos(A)} \right] \tag{5.6}$$

and $R_{w(solid)}$ with compensation for 5% error [40]

$$R_{w(solid)} = F_{R(solid)} R_{wdc(solid)}$$

$$= R_{wdc(solid)} A \left[\frac{\sinh(2A) + \sin(2A)}{\cosh(2A) - \cos(2A)} + \frac{1.9(N_l^2 - 1)}{3} \frac{\sinh(A) - \sin(A)}{\cosh(A) + \cos(A)} \right]. \tag{5.7}$$

The variable A for a solid-round wire winding is given by

$$A = \left(\frac{\pi}{4} \right)^{0.75} \frac{d}{\delta_w} \sqrt{\eta}. \tag{5.8}$$

The constant η is the porosity factor defined as

$$\eta = \frac{d}{p}. \tag{5.9}$$

The skin depth of the conducting wire δ_w is described by

$$\delta_w = \sqrt{\frac{2}{\mu_0 \sigma_w \omega}} = \frac{1}{\sqrt{\pi \mu_0 \sigma_w f}} = \sqrt{\frac{\rho_w}{\pi \mu_0 f}}, \tag{5.10}$$

where μ_0 is the free space permeability. Figure 5.2 shows a plot of the ac-to-dc winding resistance ratio F_R as a function of d/δ_w for a solid-round wire winding with $\eta = 0.9$ and several numbers of layers $N_l = 1, 2, 4, 10$.

The approximate Dowell's equation for solid-round wire windings valid for low and medium frequencies is [45]

$$F_{R(solid)} \approx 1 + \frac{(5N_l^2 - 1)}{45} A^4 = 1 + \frac{\eta^2 (5N_l^2 - 1)}{45} \left(\frac{\pi}{4} \right)^3 \left(\frac{d}{\delta_w} \right)^4 \quad \text{for} \quad A \leq 2. \tag{5.11}$$

The normalized diameter of the solid-round wire at a given $F_{R(solid)}$ in the low and medium frequency range is

$$\frac{d}{\delta_w} = \sqrt[4]{\frac{45(F_{R(solid)} - 1)}{\left(\frac{\pi}{4}\right)^3 \eta^2 (5N_l^2 - 1)}}. \tag{5.12}$$

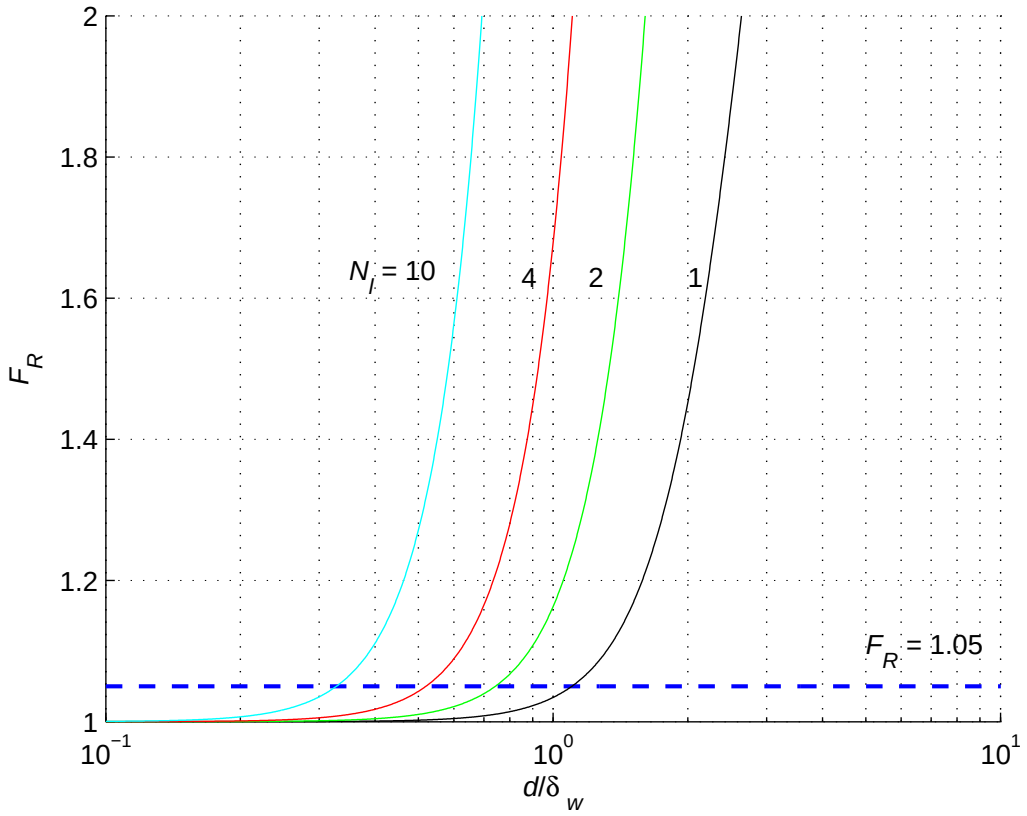

Figure 5.2: Plots of the ac-to-dc winding resistance ratio F_R as a function of d/δ_w for solid-round wire with $\eta = 0.9$ and several numbers of layers $N_l = 1, 2, 4, 10$.

The boundary between the low and medium values of d/δ_w for a solid-round wire winding is defined here as the value of $(d/\delta_w)_B$ at which $F_{R(solid)} = 1.05$ as illustrated in Fig. 5.2. This value is chosen because the skin and proximity effects are negligible and the winding ac resistance of a solid-round wire $R_{w(solid)}$ is approximately equal to the winding dc resistance of a solid-round wire $R_{wdc(solid)}$. Using (5.11), the ac-to-dc solid-round wire winding resistance ratio at the boundary between low and medium frequencies is

$$F_{R(solid)} \approx 1 + \frac{\eta^2(5N_l^2 - 1)}{45}\left(\frac{\pi}{4}\right)^3\left(\frac{d}{\delta_w}\right)_B^4 = 1.05. \tag{5.13}$$

Solution of this equation yields the normalized solid-round wire diameter at the

boundary between the low and medium frequencies

$$\left(\frac{d}{\delta_w}\right)_B = \sqrt[4]{\frac{9}{4\left(\frac{\pi}{4}\right)^3 \eta^2(5N_l^2-1)}}. \tag{5.14}$$

Hence, the boundary frequency is

$$f_{B(solid)} = \frac{\rho_w}{\pi\mu_0 d^2}\sqrt{\frac{9}{4\left(\frac{\pi}{4}\right)^3 \eta^2(5N_l^2-1)}}. \tag{5.15}$$

5.4 Modified Dowell's Equation for Litz-Wire and Multi-Strand Wire Windings

To adapt Dowell's equation to describe the ac-to-dc winding resistance ratio of the litz-wire and multi-strand wire windings $F_{R(litz)}$, the effective number of layers N_{ll} for a litz-wire and multi-strand wire windings should be taken into account. Substitution of the effective number of layers N_{ll} in (5.1) into Dowell's equation for the ac-to-dc winding resistance ratio $F_{R(solid)}$ in (5.5) yields modified Dowell's equation for litz-wire and multi-strand wire windings

$$F_{R(litz)} = \frac{R_{w(litz)}}{R_{wdc(litz)}} = A_{str}\left[\frac{\sinh(2A_{str})+\sin(2A_{str})}{\cosh(2A_{str})-\cos(2A_{str})} + \frac{2(N_{ll}^2-1)}{3}\frac{\sinh(A_{str})-\sin(A_{str})}{\cosh(A_{str})+\cos(A_{str})}\right], \tag{5.16}$$

where $R_{w(litz)}$ is the ac resistance of the litz-wire and multi-strand wire windings is

$$\begin{aligned} R_{w(litz)} &= F_{R(litz)}R_{wdc(litz)} \\ &= R_{wdc(litz)}A_{str}\left[\frac{\sinh(2A_{str})+\sin(2A_{str})}{\cosh(2A_{str})-\cos(2A_{str})} + \frac{2(N_{ll}^2-1)}{3}\frac{\sinh(A_{str})-\sin(A_{str})}{\cosh(A_{str})+\cos(A_{str})}\right] \end{aligned} \tag{5.17}$$

and $R_{w(litz)}$ with compensation for 5% error [40]

$$\begin{aligned} R_{w(litz)} &= F_{R(litz)}R_{wdc(litz)} \\ &= R_{wdc(litz)}A_{str}\left[\frac{\sinh(2A_{str})+\sin(2A_{str})}{\cosh(2A_{str})-\cos(2A_{str})} + \frac{1.9(N_{ll}^2-1)}{3}\frac{\sinh(A_{str})-\sin(A_{str})}{\cosh(A_{str})+\cos(A_{str})}\right]. \end{aligned} \tag{5.18}$$

The variable A_{str} for a round strands is

$$A_{str} = \left(\frac{\pi}{4}\right)^{0.75} \frac{d}{\delta_w}\sqrt{\frac{\eta}{k}} = \left(\frac{\pi}{4}\right)^{0.75} \frac{d_{str}}{\delta_w}\sqrt{\eta}. \tag{5.19}$$

Referring to Fig. 5.1, the equivalent porosity factor defined for the model of litz-wire and multi-strand wire windings is given by

$$\eta = \frac{d_{str}}{p}. \tag{5.20}$$

The modified Dowell's equation in (5.16) is approximated by substituting the number of layers N_l by the effective number of layers $N_{ll} = N_l\sqrt{k}$ and A by A_{str} in (5.11)

$$\begin{aligned} F_{R(litz)} &\approx 1 + \frac{(5N_{ll}^2 - 1)}{45} A_{str}^4 = 1 + \frac{\eta^2(5N_{ll}^2 - 1)}{45}\left(\frac{\pi}{4}\right)^3 \left(\frac{d_{str}}{\delta_w}\right)^4 \\ &= 1 + \frac{\eta^2(5N_l^2 k - 1)}{45}\left(\frac{\pi}{4}\right)^3 \left(\frac{d_{str}}{\delta_w}\right)^4 \quad \text{for} \quad A_{str} \leq 2 \end{aligned} \tag{5.21}$$

Figure 5.3 shows 3-D plots of ac-to-dc winding resistance ratio $F_{R(solid)}$ and $F_{R(litz)}$ as functions of d/δ_w and the number of layers N_l for inductors wound with a solid-round wire and a 225 strand litz-wire at $\eta = 0.9$. It can be seen that the skin and proximity effects for the litz-wire winding starts to increase the winding resistance at higher values of d/δ_w than those of the solid-round wire winding. Moreover, the ac-to-dc winding resistance ratio for litz-wire winding $F_{R(litz)}$ at high values of d/δ_w is much greater than that of the solid-round wire winding $F_{R(solid)}$.

Figure 5.4(a) shows plots of $F_{R(solid)}$ and $F_{R(litz)}$ as functions of d/δ_w for a solid-round wire winding and two kinds of litz-wire winding with $k = 100$ and $k = 2500$ at $\eta = 0.9$. Figure 5.4(b) shows plots of $F_{R(solid)}$ and $F_{R(litz)}$ as functions of frequency f for a solid-round wire winding and two kinds of litz-wire winding with $k = 100$ and $k = 2500$ at $\eta = 0.9$. The solid-round wire winding was made up of a round wire of the bare wire diameter $d = 1.45$ mm, four bundle layers ($N_l = 4$), and $\eta = 0.9$. The

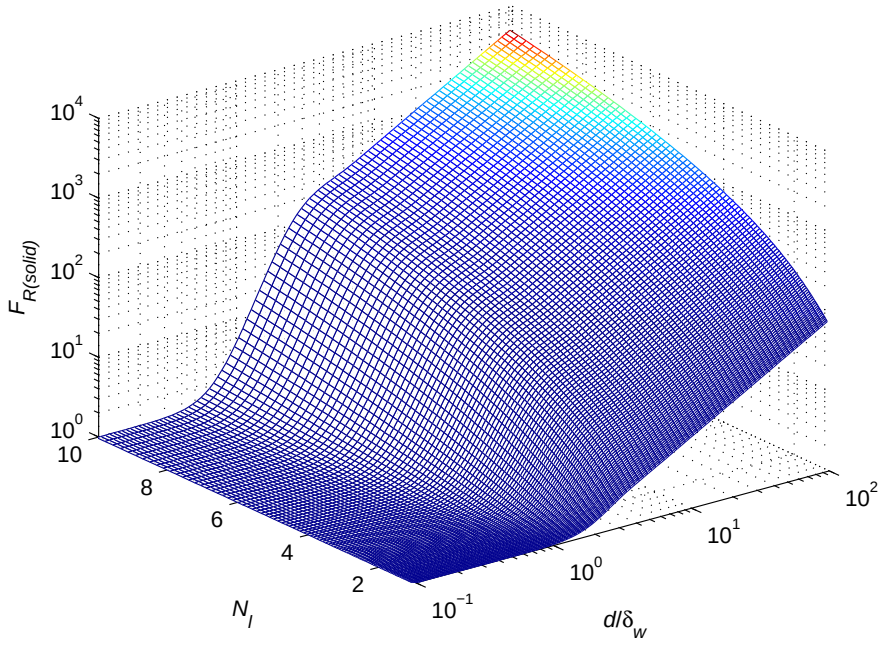

(a)

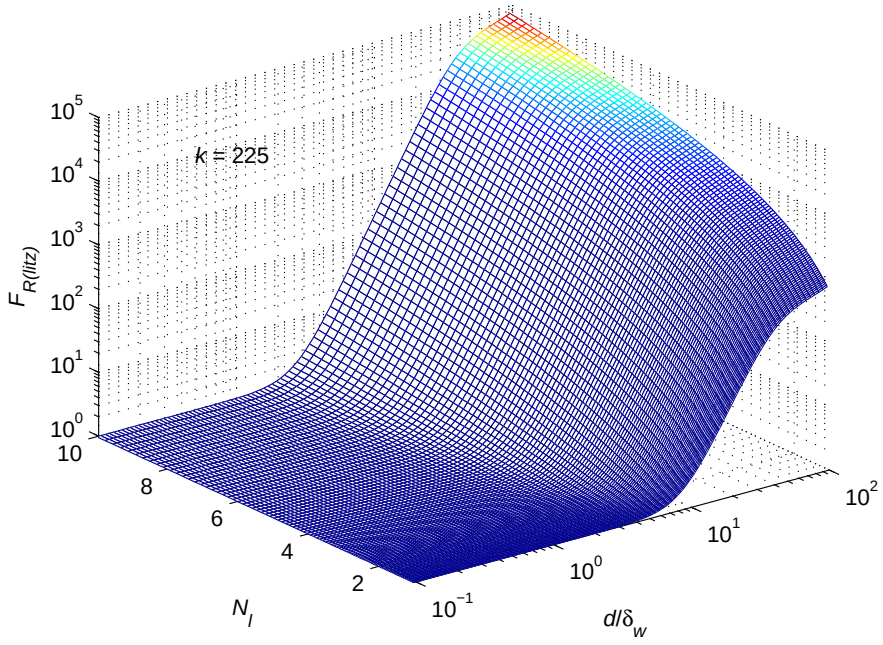

(b)

Figure 5.3: 3-D plots of ac-to-dc winding resistance ratio F_R as a function of d/δ_w and number of layers N_l for power inductors. a) With solid-round wire winding. b) With $k = 225$ strand litz-wire winding at $\eta = 0.9$.

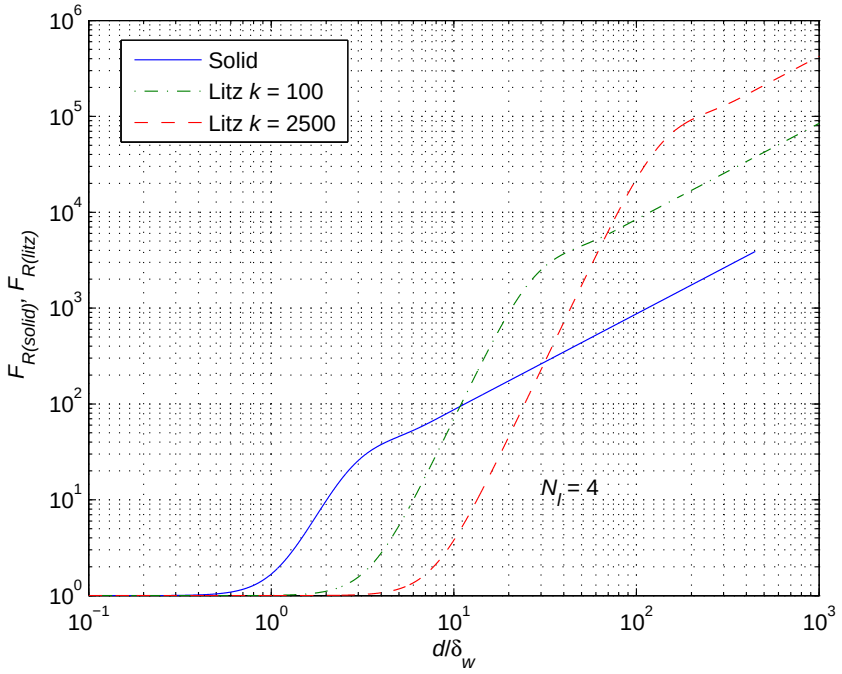

(a)

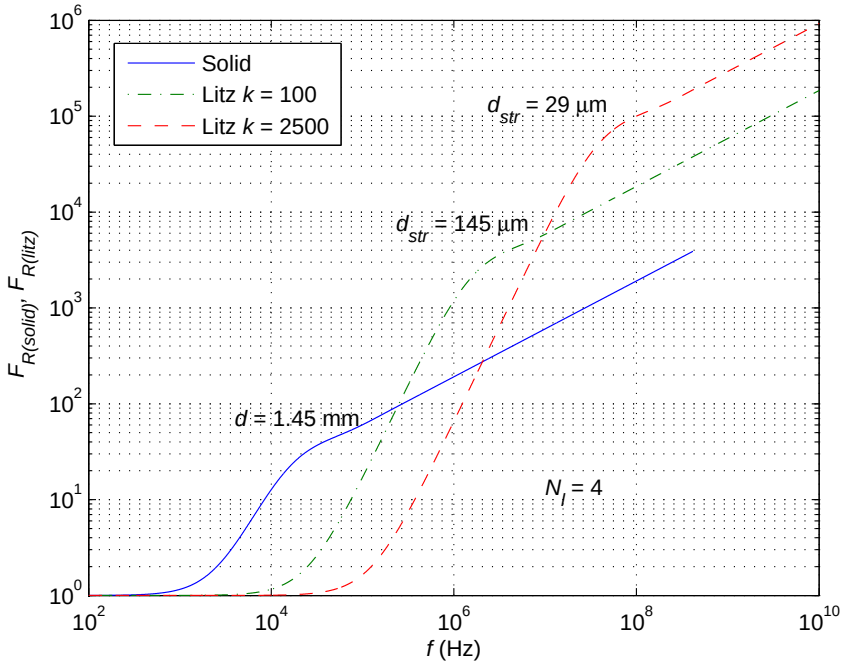

(b)

Figure 5.4: Plots of $F_{R(solid)}$ and $F_{R(litz)}$ as functions of d/δ_w and as functions of frequency f for $N_l = 4$, $d = 1.45$ mm, $k = 100$, $d_{str} = 145$ μm, $k = 2500$, $d_{str} = 29$ μm, and $\eta = 0.9$. (a) $F_{R(solid)}$ and $F_{R(litz)}$ as functions of d/δ_w. (b) $F_{R(solid)}$ and $F_{R(litz)}$ as functions of frequency f.

first litz-wire winding consisted of $k = 100$ strands, bare strand diameter $d_{str} = 145$ μm, four bundle layers ($N_l = 4$), and $\eta = 0.9$. The second litz-wire winding consisted of $k = 2500$ strands, bare strand diameter $d_{str} = 29$ μm, four bundle layers ($N_l = 4$), and $\eta = 0.9$. It can be seen from the plot that the low-frequency range of the litz-wire winding is wider than that of the solid-round wire winding. This is because the diameter of the strand in the litz-wire winding is $\sqrt{k}$ times lower than that of the solid-round wire winding, i.e, $d_{str} = d/\sqrt{k} << 2\delta_w$. Therefore, the skin and proximity effects are negligible resulting in the uniform current density in each strand. Thus, $R_{w(litz)} \approx R_{wdc(litz)}$, and therefore $F_{R(litz)} \approx 1$. At medium frequencies of the litz-wire winding, the ac-to-dc resistance ratio of the litz-wire winding is much lower than that of the solid-round wire winding with the same cross-sectional conductor area. At high frequencies of the litz-wire winding, the ac-to-dc resistance ratio of the litz-wire winding is much greater than the ac-to-dc resistance ratio of the solid-round wire winding with the same cross-sectional conductor area. This physical behavior of litz-wire windings is due to the large number of effective layers and it was also observed in other publications [19], [25], [41], [49], [50].

5.5 Optimum Strand Diameter

While designing the litz-wire winding inductor, usually the problem is how to chose the strand diameter and the number of strands in the bundle. The optimum strand diameter is derived under the following assumptions:

- The number of bundle layers is constant ($N_l = \text{const}$).
- The number of strands is constant ($k = \text{const}$).
- The number of effective layers is constant ($N_{ll} = N_l\sqrt{k} = \text{const}$).

From (5.21), the approximated equation for the ac resistance of the litz-wire winding is

$$R_{w(litz)} = F_{R(litz)} R_{wdc(litz)} \approx \frac{4\rho_w l_w}{k\pi d_{str}^2}\left[1 + \frac{(5N_{ll}^2 - 1)}{45} A_{str}^4\right]$$

$$= \frac{4\rho_w l_w}{k\pi d_{str}^2}\left[1 + \frac{\left(\frac{\pi}{4}\right)^3 \eta^2 (5N_{ll}^2 - 1)}{45}\left(\frac{d_{str}}{\delta_w}\right)^4\right]$$

$$= \frac{4\rho_w l_w}{k\pi}\left[\frac{1}{d_{str}^2} + \frac{\left(\frac{\pi}{4}\right)^3 \eta^2 (5N_{ll}^2 - 1) d_{str}^2}{45\delta_w^4}\right] \quad \text{for} \quad A_{str} \le 2. \tag{5.22}$$

Taking the derivative of (5.22) with respect to d_{str} and setting the result to zero, we obtain

$$\frac{dR_{w(litz)}}{dd_{str}} = \frac{4\rho_w l_w}{k\pi}\left[\frac{-2}{d_{str}^3} + \frac{\left(\frac{\pi}{4}\right)^3 2\eta^2 (5N_{ll}^2 - 1) d_{str}}{45\delta_w^4}\right] = 0. \tag{5.23}$$

Solution of this equation gives the normalized optimum strand diameter at which the litz-wire winding resistance has a local minimum value for specified values of $N_l, k,$ and η

$$\frac{d_{str(opt)}}{\delta_w} = \sqrt[4]{\frac{45}{\left(\frac{\pi}{4}\right)^3 \eta^2 (5N_{ll}^2 - 1)}} = \sqrt[4]{\frac{45}{\left(\frac{\pi}{4}\right)^3 \eta^2 (5N_l^2 k - 1)}}. \tag{5.24}$$

Hence, the number of strands in the litz-wire bundle at which the minimum winding ac resistance occurs is given by

$$k_{cr} = \frac{9}{\left(\frac{\pi}{4}\right)^3 \eta^2 N_l^2 \left(\frac{d_{str(opt)}}{\delta_w}\right)^4} + \frac{1}{5N_l^2}. \tag{5.25}$$

Substitution of (5.24) into (5.21) produces the ac-to-dc resistance ratio at the optimum value of $d_{str(opt)}/\delta_w$

$$F_{Rcr} = 1 + \frac{\eta^2 (5N_{ll}^2 - 1)}{45}\left(\frac{\pi}{4}\right)^3 \left[\sqrt[4]{\frac{45}{\left(\frac{\pi}{4}\right)^3 \eta^2 (5N_{ll}^2 - 1)}}\right]^4 = 1 + 1 = 2. \tag{5.26}$$

Equation (5.25) can also be obtained from (5.21) and from substituting $F_{R(litz)} = F_{Rcr} = 2$. Figure 5.5 shows plots of the number of strands k_{cr} computed from (5.25)

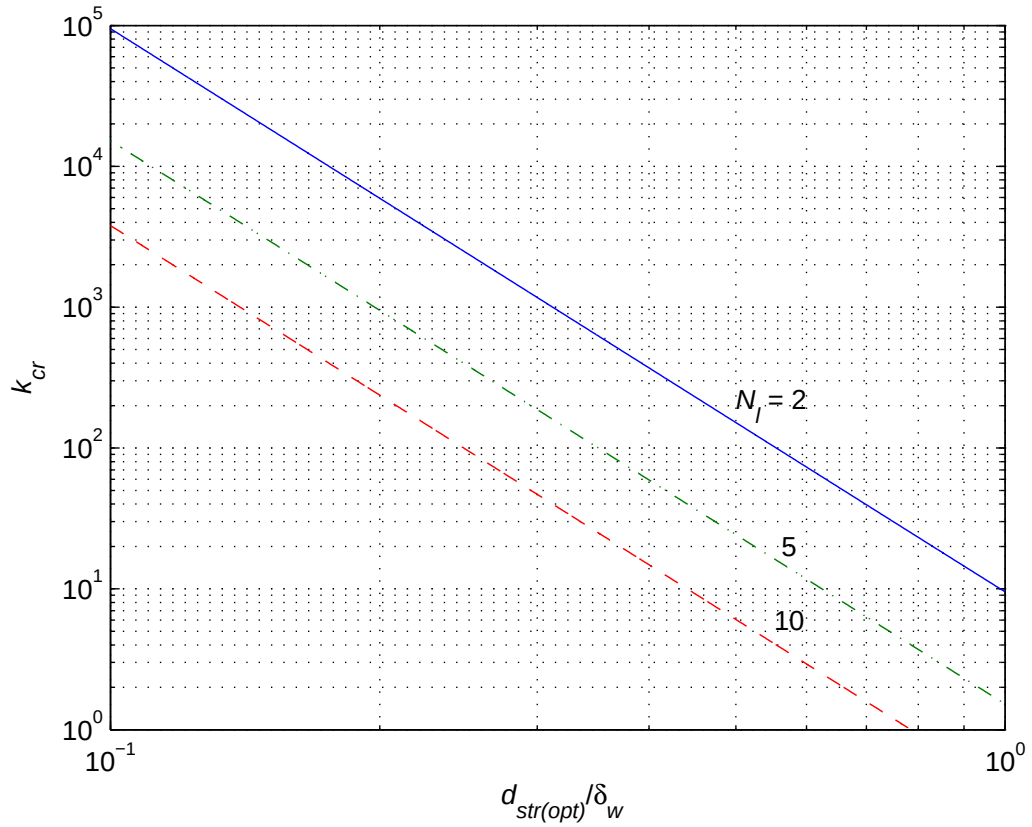

Figure 5.5: Plots of the number of strands k_{cr} as functions of normalized optimum strand diameter $d_{str(opt)}/\delta_w$ at different number of bundle layers $N_l = 2, 5, 10$ and $\eta = 0.7$.

as functions of the normalized optimum strand diameter for an inductor with different numbers of bundle layers $N_l = 2, 5, 10$ at $\eta = 0.7$. It can be seen that as the optimum strand diameter $d_{str(opt)}$ increases, the number of strands k_{cr} to achieve minimum winding ac resistance decreases.

As the strand diameter d_{str} increases beyond $d_{str(opt)}$, the litz-wire winding ac resistance first increases, reaches a maximum value, and than decreases as for solid-round wire winding [14]. At a certain value of the strand diameter $d_{str} > d_{str(opt)}$, the litz-wire winding ac resistance decreases below the local minimum value [14].

Substituting $d_{str} = d/\sqrt{k}$ into (5.21) and setting $F_{R(litz)} = F_{Rcr} = 2$, we obtain the number of strands in the litz-wire bundle at which the minimum winding resistance

occurs

$$k_{cr} = \frac{5N_l^2 + \sqrt{(5N_l^2)^2 - \frac{180}{\eta^2\left(\frac{\pi}{4}\right)^3}\left(\frac{\delta_w}{d}\right)^4}}{\frac{90}{\eta^2\left(\frac{\pi}{4}\right)^3}\left(\frac{\delta_w}{d}\right)^4}, \tag{5.27}$$

where d is the equivalent bundle bare conductor diameter determined by the current density J_m, A_w is the conductor cross-sectional area in the bundle

$$A_w = \frac{\pi d^2}{4} = \frac{I_m}{J_m}, \tag{5.28}$$

and I_m is the amplitude of the inductor sinusoidal current.

5.6 Boundary Between Low and Medium Frequencies for Litz-Wire and Multi-Strand Wire Windings

Using (5.21), one can express the ac-to-dc litz-wire and multi-strand wire winding resistances ratio at the boundary between low and medium frequencies as

$$F_{R(litz)} \approx 1 + \frac{\eta^2(5N_{ll}^2 - 1)}{45}\left(\frac{\pi}{4}\right)^3\left(\frac{d_{str}}{\delta_w}\right)^4 = 1.05. \tag{5.29}$$

Solution of this equation yields the normalized strand diameter at the boundary between the low and medium frequencies

$$\left(\frac{d_{str}}{\delta_w}\right)_B = \sqrt[4]{\frac{9}{4\left(\frac{\pi}{4}\right)^3\eta^2(5N_{ll}^2 - 1)}} = \sqrt[4]{\frac{9}{4\left(\frac{\pi}{4}\right)^3\eta^2(5N_l^2k - 1)}}. \tag{5.30}$$

Figure 5.6 shows the normalized strand diameter at the boundary between the low and medium frequencies as a function of number of layers N_l for $k = 30$ and $k = 300$ at $\eta = 0.7$. The boundary frequency for the litz-wire winding is given by

$$f_{B(litz)} = \frac{\rho_w}{\pi\mu_0 d_{str}^2}\sqrt{\frac{9}{4\left(\frac{\pi}{4}\right)^3\eta^2(5N_{ll}^2 - 1)}} = \frac{\rho_w}{\pi\mu_0 d_{str}^2}\sqrt{\frac{9}{4\left(\frac{\pi}{4}\right)^3\eta^2(5N_l^2k - 1)}}. \tag{5.31}$$

The ratio of boundary frequency of litz-wire winding to the boundary frequency of the solid-round wire winding is

$$\frac{f_{B(litz)}}{f_{B(solid)}} = \left(\frac{d}{d_{str}}\right)^2\sqrt{\frac{5N_l^2 - 1}{5N_l^2k - 1}} = k\sqrt{\frac{5N_l^2 - 1}{5N_l^2k - 1}}. \tag{5.32}$$

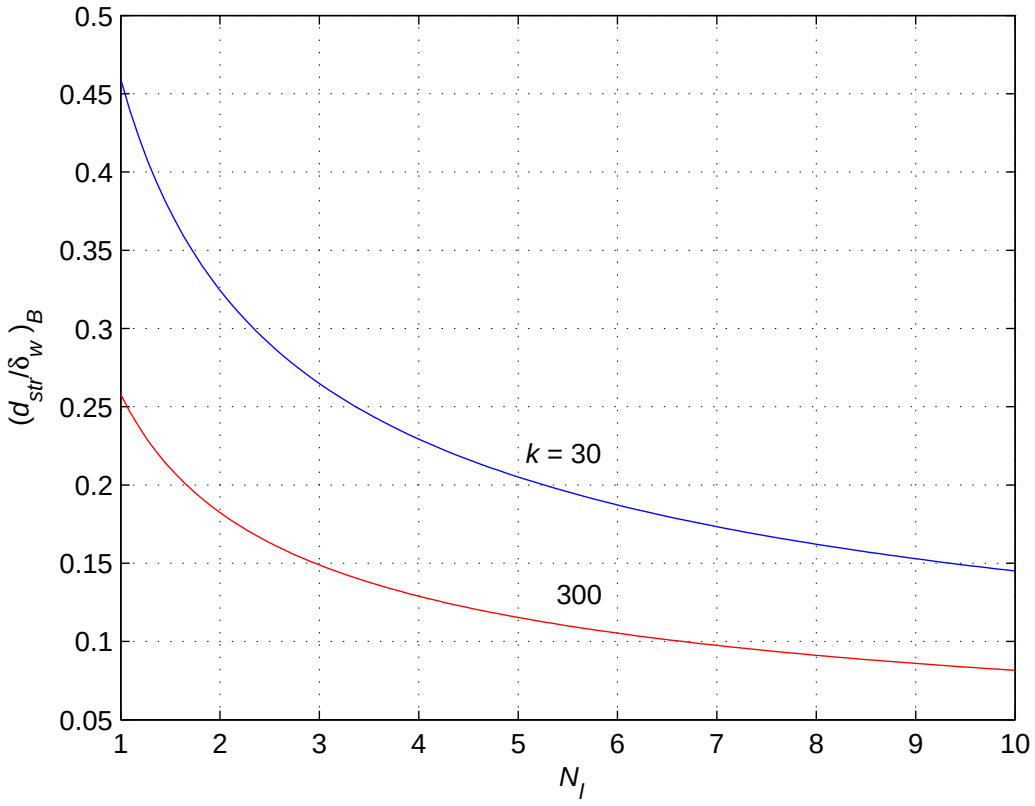

Figure 5.6: Plots of the normalized strand diameter at the boundary between the low and medium frequencies $(d_{str}/\delta_w)_B$ for litz-wire winding as a function of number of layers N_l for $k = 30$ and $k = 300$ at $\eta = 0.7$.

where $(d/d_{str})^2 = k$ for the same conductor cross-sectional area. Since $N_l^2 >> 1/5$, the ratio of the boundary frequency of the litz-wire winding to the boundary frequency of the solid-round wire winding can be approximated by

$$\frac{f_{B(litz)}}{f_{B(solid)}} \approx \sqrt{k}. \tag{5.33}$$

From (5.24) and (5.30), one obtains

$$\frac{\frac{d_{str(opt)}}{\delta_w}}{\left(\frac{d_{str}}{\delta_w}\right)_B} = \frac{\sqrt[4]{\frac{45}{\left(\frac{\pi}{4}\right)^3 \eta^2 (5N_{ll}^2 - 1)}}}{\sqrt[4]{\frac{9}{4\left(\frac{\pi}{4}\right)^3 \eta^2 (5N_{ll}^2 - 1)}}} = \sqrt[4]{20} \approx 2.1147. \tag{5.34}$$

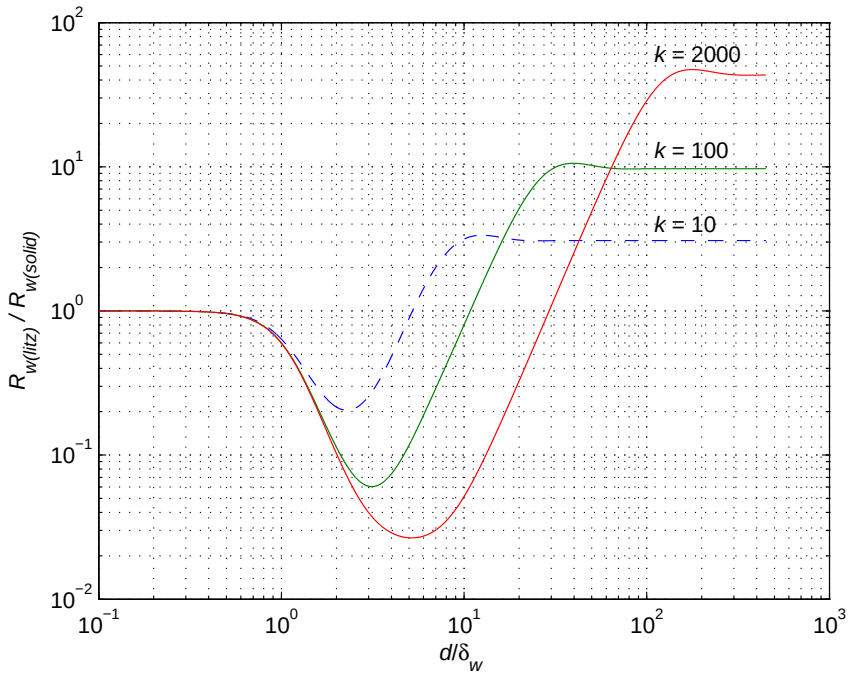

(a)

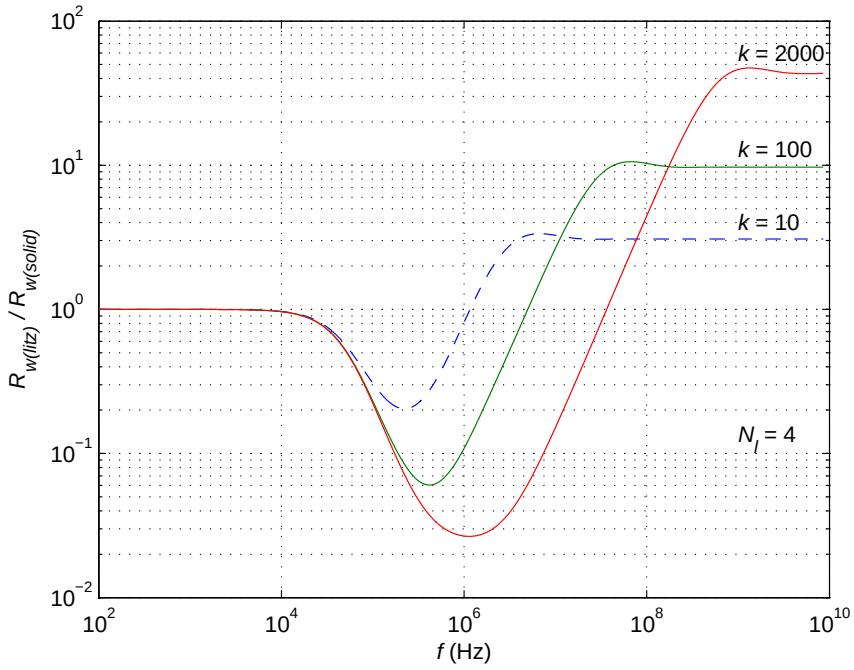

(b)

Figure 5.7: Ratio of the winding ac resistance of the litz-wire $R_{w(litz)}$ to the winding ac resistance of the solid-round wire $R_{w(solid)}$ as function of d/δ_w and frequency f with the same cross-sectional conductor area at $d = 0.32$ mm, $N_l = 4$, $N = 114$, $l_T = 6$ cm, and $k = 10$, 100, 2000 strands at $\eta = 0.9$. (a) Ratio of $R_{w(litz)}$ to $R_{w(solid)}$ as functions of d/δ_w. (b) Ratio of $R_{w(litz)}$ to $R_{w(solid)}$ as functions of frequency f.

5.7 Comparison of Winding Ac Resistances of Litz-Wire and Solid-Round Wire

The ratio of the winding ac resistance of the litz-wire $R_{w(litz)}$ to the winding ac resistance of the solid-round wire $R_{w(solid)}$ is defined as

$$\zeta = \frac{R_{w(litz)}}{R_{w(solid)}}. \tag{5.35}$$

Figure 5.7(a) shows the ratio of winding ac resistance of the litz-wire winding to the winding ac resistance of the solid-round wire winding with the same cross-sectional conductor area as functions of d/δ_w for litz-wire winding with $k = 10$, 100, 2000 strands, $N_l = 4$, $N = 114$, and $l_T = 6$ cm at $\eta = 0.9$. It can be seen that as d/δ_w is increased, the ratio ζ is first constant, then decreases, reaches a minimum value, next increases, and finally remains constant at $\zeta > 1$. When $\zeta < 1$, the litz-wire winding resistance is lower than that of the solid-round wire winding. When $\zeta > 1$, the litz-wire winding resistance is several times higher than that of the solid-round wire winding. The value of d/δ_w at which ζ has the minimum value is the optimum value $(d/\delta_w)_{opt}$ of the litz-wire winding. This value corresponds to the optimum frequency f_{opt} at a fixed value of d. In addition, the minimum value of ζ decreases as the number of strands k increases. Figure 5.7(b) shows ratio of winding ac resistance of the litz-wire winding to the winding ac resistance of the solid-round wire winding with the same cross-sectional conductor area as functions of frequency for litz-wire winding with $k = 10$, 100, 2000 strands, $N_l = 4$, $N = 114$, $l_T = 6$ cm, and $d = 0.32$ mm at $\eta = 0.9$.

5.8 Relationship Between R_w, ESR, and Measured Data

It is impossible to measure directly the winding resistance R_w at frequencies close to the self-resonant frequency because of the inductor self-capacitance. A lumped-parameter model of the inductor neglecting the core losses is depicted in Fig. 6.7(a).

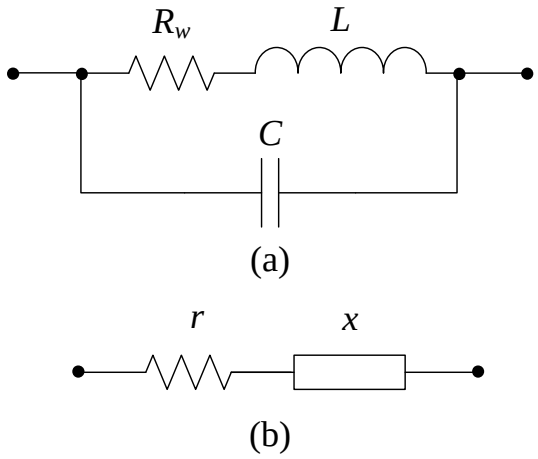

Figure 5.8: Equivalent circuit of inductors with negligible core losses. (a) Lumped-parameter equivalent circuit. (b) Equivalent series circuit.

The model of the inductor consists of self-inductance L, winding ac resistance R_w, and parasitic self-capacitance C [62], [66]. Additionally, the model may contain core resistance R_c in series with winding ac resistance R_w. However, in the subsequent analysis, the core resistance is neglected. This is because the core loss is very low at low values of the magnetic flux density B. Neglecting the core resistance, the impedance of the equivalent circuit depicted in Fig. 6.7(a) is [25], [14]

$$Z = \frac{R_w}{(1-\omega^2 LC)^2 + (\omega C R_w)^2} + j\omega L \frac{1 - \omega^2 LC - \frac{CR_w^2}{L}}{(1-\omega^2 LC)^2 + (\omega C R_w)^2} = r + jx = |Z| e^{j\phi}, \tag{5.36}$$

where r is the equivalent series resistance (ESR), x is the equivalent series reactance, $|Z|$ is the magnitude of impedance, and ϕ is the phase of impedance.

The equivalent series circuit of the inductor is shown in Fig. 6.7(b). The components r and x of the equivalent series circuit can be measured by an impedance meter. The inductor winding ac resistance is given by

$$R_w = \frac{1 - \sqrt{1 - 4\omega^2 r^2 C^2 (1-\omega^2 LC)^2}}{2r\omega^2 C^2}. \tag{5.37}$$

The first self-resonant frequency of the inductor is

$$f_r = \frac{\omega_r}{2\pi} = \frac{1}{2\pi\sqrt{LC}}. \tag{5.38}$$

Figure 5.9 shows plots of the magnitude and the phase of inductor impedance at $N_l = 4$, $N = 114$, $k = 20$, $d_{str} = 80$ μm, $L = 168$ μH, $l_T = 6$ cm, and $f_r = 2.62$ MHz. For very low-frequencies, the inductor impedance is resistive. At higher frequencies, below the resonant frequency, the inductor impedance is inductive. Above the resonant frequency, the inductor impedance is capacitive.

The inductor quality factor due to the winding ac resistance at $R_c = 0$ is defined as

$$Q_{LRw} = \frac{\omega L}{R_w}. \tag{5.39}$$

and the quality factor of an inductor due to the core series resistance $R_w = 0$ is

$$Q_{LRc} = \frac{\omega L}{R_c}. \tag{5.40}$$

The quality factor of an inductor with a magnetic core at a given frequency f due to the both Q_{LRw} and Q_{LRc} is defined as

$$Q_{Lo} = \frac{\omega L}{R_w + R_c} = \frac{1}{\frac{R_w}{\omega L} + \frac{R_c}{\omega L}} = \frac{1}{\frac{1}{\omega L/R_w} + \frac{1}{\omega L/R_c}} = \frac{1}{\frac{1}{Q_{LRw}} + \frac{1}{Q_{LRc}}} = \frac{Q_{LRw}Q_{LRc}}{Q_{LRw} + Q_{LRc}}. \tag{5.41}$$

Neglecting the core resistance, the inductor reactance factor is expressed as

$$q = \frac{x}{r} = \frac{\omega L\left(1 - \omega^2 LC - \frac{CR_w^2}{L}\right)}{R_w}. \tag{5.42}$$

5.9 Experimental Verification

In this section, the experimental verification of the proposed model and the analytical expression (5.4) for the litz-wire winding ac resistance $R_{w(litz)}$ was performed. An inductor was designed, built, and tested. This inductor was used in the class D resonant inverter with series resonant circuit [52]. The class D inverter had the following specifications: $V_I = 140$ V, $P_O = 38$ W, $f = 73$ kHz, $Q_L = 7$, and $\eta_I = 93\%$.

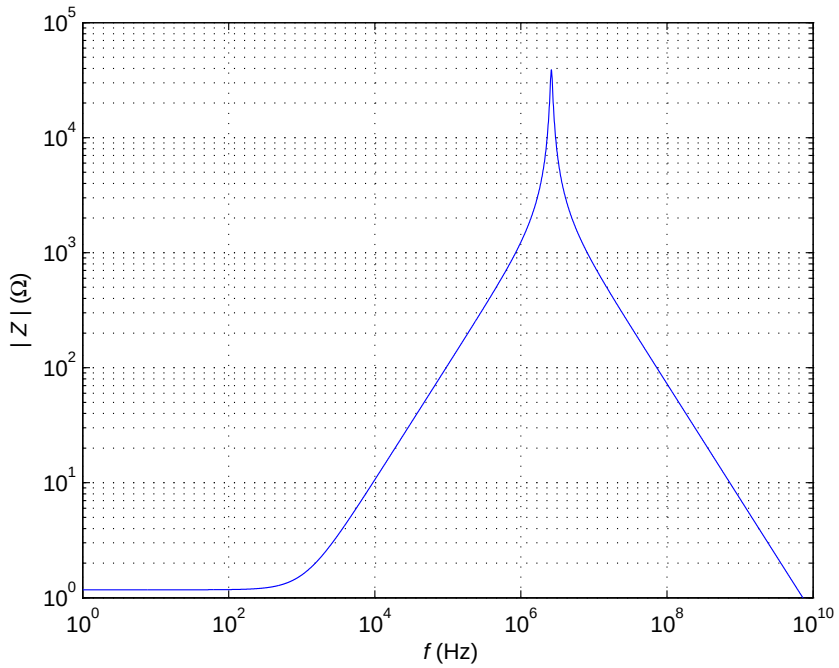

(a)

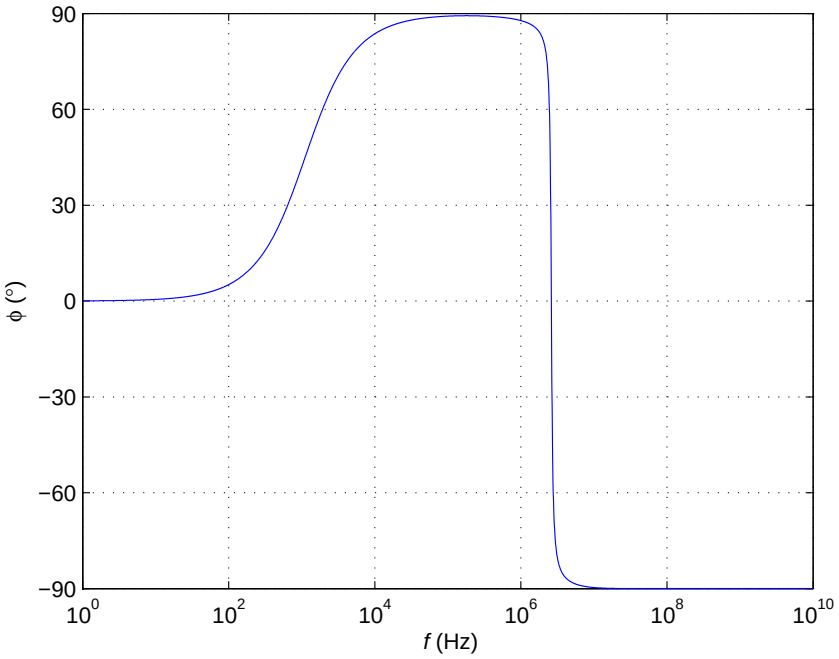

(b)

Figure 5.9: Magnitude and phase of inductor impedance Z as functions of frequency for $N_l = 4$, $N = 114$, $k = 20$, $d_{str} = 80$ μm, $L = 168$ μH, $l_T = 6$ cm, and $f_r = 2.62$ MHz. (a) Magnitude of inductor impedance $|Z|$. (b) Phase of inductor impedance ϕ.

The dc input power of the inverter is

$$P_I = \frac{P_O}{\eta_I} = \frac{38}{0.93} = 40.86 \text{ W}. \tag{5.43}$$

The overall resistance of the inverter can be calculated as

$$R = \frac{2V_I^2}{\pi^2 P_I} = \frac{2 \times 140^2}{\pi^2 \times 40.86} = 97.2 \ \Omega. \tag{5.44}$$

The load resistance of the inverter is

$$R_L = \eta_I R = 0.93 \times 97.2 = 90.396 \ \Omega. \tag{5.45}$$

The values of the reactive components of the resonant circuit are

$$L = \frac{Q_L R}{\omega} = \frac{7 \times 97.2}{2\pi \times 73 \times 10^3} = 1.48 \text{ mH} \tag{5.46}$$

and

$$C_s = \frac{1}{\omega Q_L R} = \frac{1}{2\pi \times 73 \times 10^3 \times 7 \times 97.2} = 3.2 \text{ nF}. \tag{5.47}$$

An inductor with inductance $L = 1.48$ mH wound with a copper litz wire was built and measured. The total number of turns in the inductor was $N = 24$ and the number of bundle layers was $N_l = 2$. The amplitude of the current density in the litz-wire bundle was $J_m = 1.156$ A/mm^2 and diameter of the solid-round wire using (5.28) was approximately $d \approx 1$ mm. Assuming initial porosity factor $\eta = 0.7$, from (5.27) the required number of strands is $k_1 = 30$. The litz-wire winding consisted of thirty strands ($k = 30$) made of AWG32 copper magnet wire, where the bare strand diameter was $d_{str} = 201.9$ μm and the insulated wire diameter was $d_o = 241$ μm. The optimum diameter of the bare strand computed from equation (13) given in [38] was $d_{str(opt)} = 191.259$ μm at $\eta = 1$. The optimum bare strand diameter computed from (5.24) was $d_{str(opt)} = 183.445$ μm at $\eta = 0.7$. The maximum value of porosity factor η occurs when the insulated strands are in intimate contact and it is expressed by

$$\eta_{max} = \left(\frac{d_{str}}{d_o}\right)^2 = \left(\frac{0.2019}{0.241}\right)^2 = 0.70184 \approx 0.702. \tag{5.48}$$

Hence, the maximum value of A_{str} for the litz-wire inductor due to intimate contact of the insulated strands is given by

$$A_{str(max)} = \left(\frac{\pi}{4}\right)^{\frac{3}{4}} \sqrt{\eta_{max}} \left(\frac{d_{str}}{\delta_w}\right) = 0.8343 \times \sqrt{0.70184} \times \left(\frac{d_{str}}{\delta_w}\right) = 0.6989 \left(\frac{d_{str}}{\delta_w}\right). \tag{5.49}$$

A Siemens Matsushita Components EC 41 B66339-G0000-X117 ungapped core was used with B66274 coil former (bobbin). The core material was MnZn ferrite N27 with relative permeability $\mu_r = 2000 \pm 20\%$. The cross-sectional area of the core was $A_c = 121$ mm^2. The breadth of the bobbin window was $b_b = 2.5$ cm, the breadth of the core window was $b_c = 2.7$ cm, and the mean turn length (MTL) was $l_T = 6.66$ cm.

The measurements were carried out using the HP4194A Impedance/Gain-Phase Analyzer equipped with the HP16047D test fixture. This meter measures the equivalent series resistance r and the equivalent series reactance x (both from 10 mΩ with a maximum resolution of 100 $\mu\Omega$) at a very low magnetic flux density B, resulting in negligible core losses. At high-frequencies f and high magnetic flux density B, the measurements of the winding resistance R_w of inductors with core is a challenging problem. This is because of the additional series core resistance R_c and parasitic self-capacitance C. The measured first self-resonant frequency of the inductor was f_r = 915 kHz.

Figure 5.10(a) shows the measured (circles) and computed (continuous line) equivalent series resistance r of the inductor as functions of frequency f. To compute the equivalent series resistance r given by (5.36), the winding ac resistance $R_{w(litz)}$, self-resonant frequency f_r, inductance as a function of frequency $L(f)$, inductance at resonant frequency L_{f_r}, and inductor stray-capacitance C has to be determined. The litz-wire winding resistance can be computed using (5.4). The first self-resonant frequency was measured at zero phase of the inductor impedance and it was $f_r = 915$ kHz. The inductance at the first self-resonant frequency was computed using the

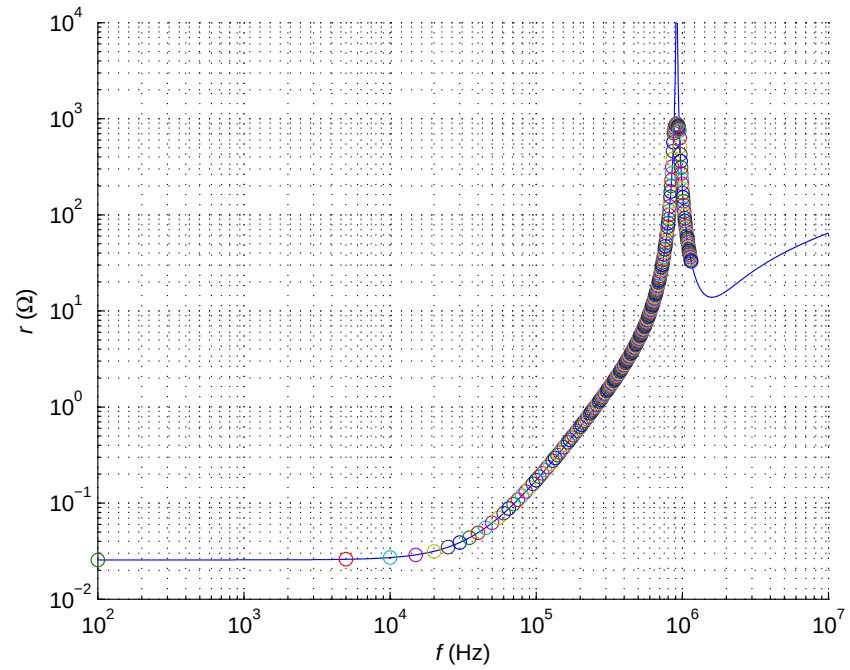

(a)

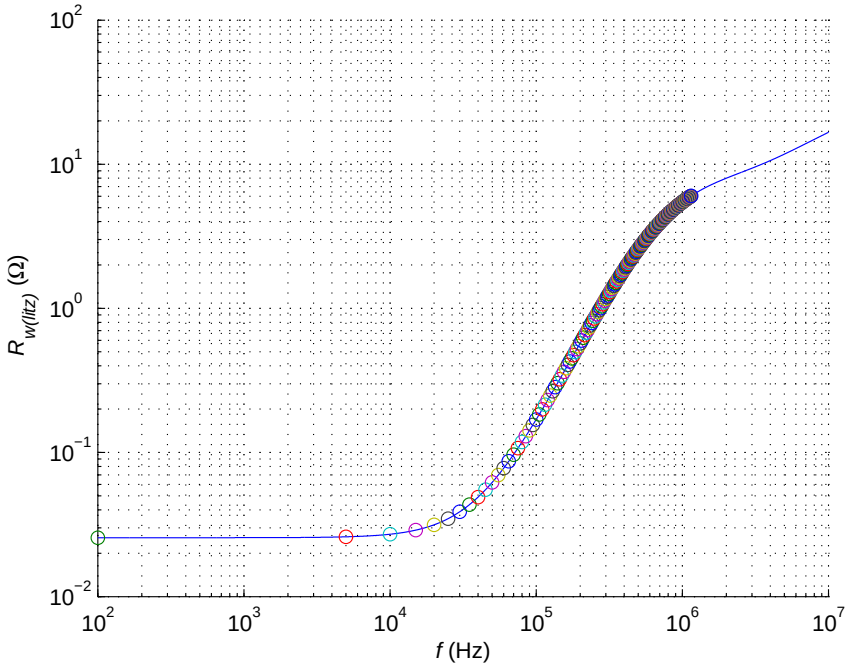

(b)

Figure 5.10: Measured (circles) and computed (continuous line) equivalent series resistance r and litz-wire winding ac resistance $R_{w(litz)}$ as functions of frequency f. (a) Equivalent series resistance r. (b) Litz-wire winding ac resistance $R_{w(litz)}$.

relationship

$$L_{f_r} = \frac{L}{\mu'_{rs(73\text{kHz})}} \mu'_{rs(915\text{kHz})}, \tag{5.50}$$

where $\mu'_{rs(73\text{kHz})} = 2000$ is the real part of series complex permeability of the core material N27 [86] at a frequency of 73 kHz and $\mu'_{rs(915\text{kHz})} = 2300$ is the real part of series complex permeability of the core material N27 at the self-resonant frequency $f_r = 915$ kHz. The inductance of the inductor at the self-resonant frequency f_r was $L_{f_r} = 1.702$ mH. Similarly, the inductance of the inductor as a function of frequency can be estimated as

$$L(f) = \frac{\mu'_{rs} L}{\mu'_{rs(73\text{kHz})}}, \tag{5.51}$$

where μ'_{rs} for the N27 material can be approximated by

$$\mu'_{rs} = \frac{2000}{\sqrt{\left[1 - \left(\frac{f}{12\times10^5}\right)^2\right]^2 + \left(\frac{f}{12\times10^5}\right)^2}} \quad \text{for} \quad f \leq 1.2 \text{ MHz}. \tag{5.52}$$

The stray-capacitance of the inductor is determined as

$$C = \frac{1}{\omega_r^2 L_{f_r}} = \frac{1}{(2 \times \pi \times 915 \times 10^3)^2 \times 1.702 \times 10^{-3}} = 17.776 \text{ pF}. \tag{5.53}$$

Computing the litz-wire winding ac resistance R_w from modified Dowell's equation (5.4) and using the component values calculated above, the equivalent series resistance r was calculated from the real part of equation (5.36). It can be seen from Fig. 5.10(a) that the theoretical equivalent series resistance r (ESR) calculated from (5.36) agrees with the measured equivalent series resistance r of the inductor wound with a litz wire.

Figure 5.10(b) shows the measured (circles) and computed (continuous line) litz-wire winding ac resistance $R_{w(litz)}$ as functions of frequency f. The measured winding ac resistance R_w was calculated using (5.37) from measured equivalent series resistance r. It can be seen that the theoretical winding ac resistance of the litz-wire winding $R_{w(litz)}$ given in (5.4) accurately tracks the measured winding ac resistance of the litz-wire winding R_w.

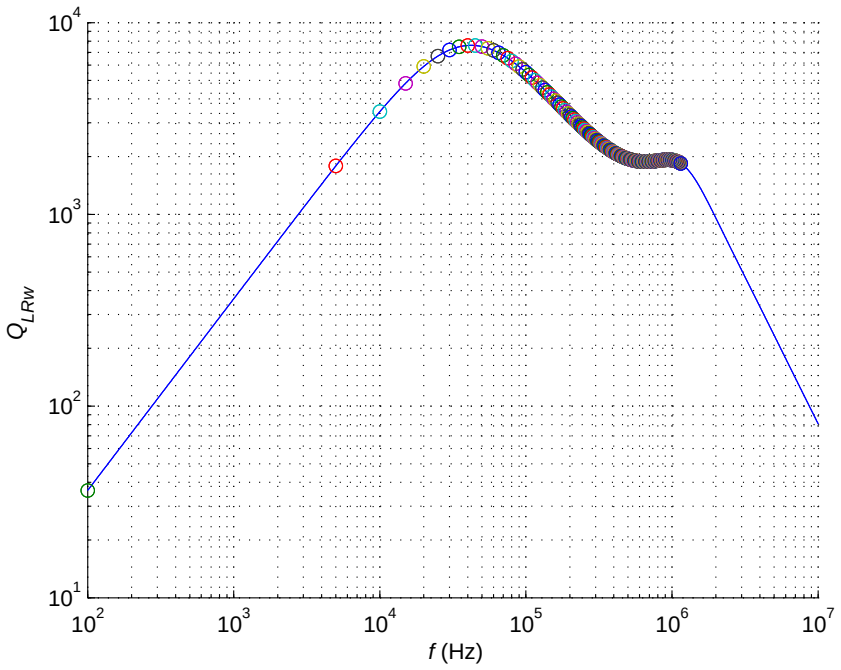

(a)

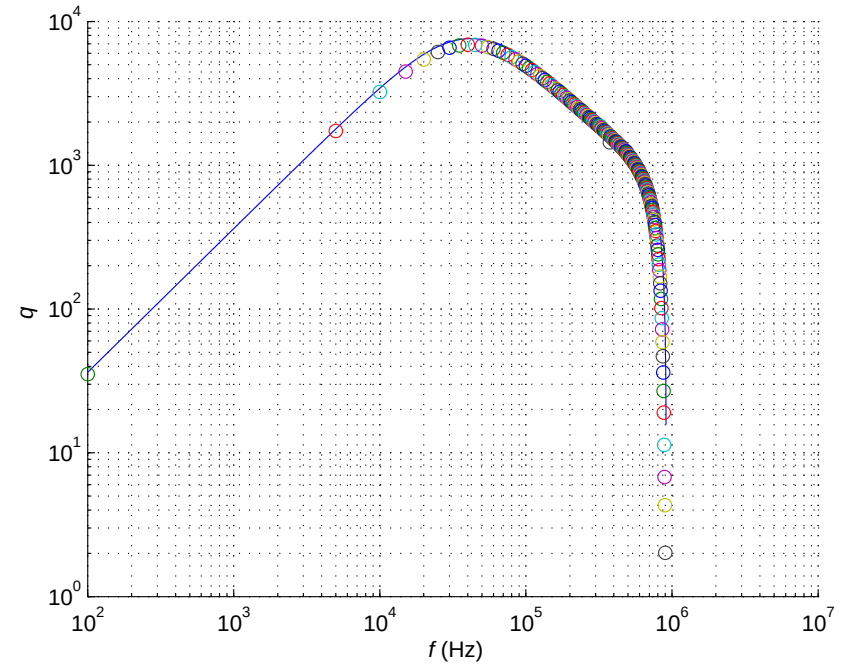

b)

Figure 5.11: Measured (circles) and computed (continuous line) quality factor and reactance factor of litz-wire inductor as functions of frequency f neglecting core losses. (a) Quality factor $Q_{LRw} = \omega L/R_{w(litz)}$. (b) Reactance factor $q = x/r$.

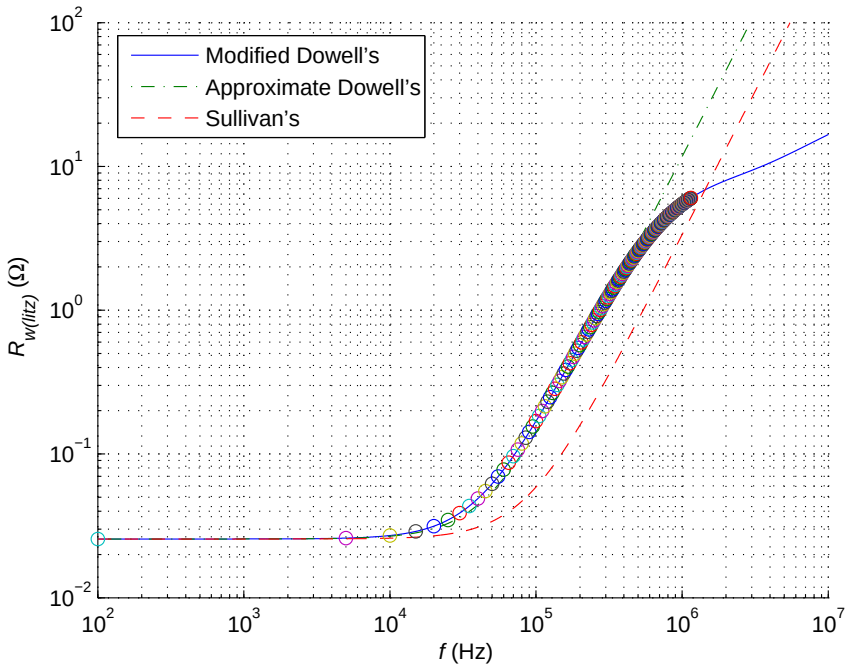

Figure 5.12: Plots of measured (circles) and computed litz-wire winding ac resistance $R_{w(litz)}$ as functions of frequency f described by modified Dowell's equation in (5.4), approximate Dowell's equation in (5.22), and Sullivan's equation in (5.54).

Figure 5.11 shows the measured (circles) and computed (continuous line) inductor quality factor due to winding ac resistance Q_{LRw} defined in (5.39) and the reactance factor q defined in (5.42) as functions of frequency f with subtracted core losses. The measured inductor quality factor due to the winding ac resistance Q_{LRw}, was calculated using (5.39) from the measured winding resistance R_w and the inductance L as a function of frequency given by (5.51). The measured inductor reactance factor was obtained by substitution of the measured equivalent series resistance r and measured equivalent series reactance x into (5.42).

Figure 5.12 compares the winding ac resistances of the litz-wire winding as a function of frequency for three different methods: modified Dowell's equation (5.4), approximate Dowell's equation (5.22), and Sullivan's equation [38], [39]. Additionally, the plot contains measured winding resistance (circles).

The Sullivan's equation for the litz-wire ac-to-dc winding resistance ratio is given

by [38], [39]

$$F_R = 1 + \frac{\pi^2 \omega^2 \mu_0^2 N^2 k^2 d_{str}^6}{768 \rho_w^2 b_c^2}. \tag{5.54}$$

It can be seen that the model and modified Dowell's equation in (5.4), proposed in this chapter, accurately track the actual measured data for the litz-wire winding ac resistance in a wide frequency range. The approximate Dowell's equation given in this chapter (5.22) for the winding ac resistance of the litz-wire winding also tracks the measured data very well at low and medium frequency ranges. However, for the high-frequency range, the approximation is not valid and the discrepancy between the computed and measured data is large. On the other hand, Sullivan's equation underestimates the litz-wire winding ac resistance introducing a 31% error at inductor operating frequency $f = 73$ kHz.

In this chapter, equation (5.54) is modified and expressed in terms of the effective number of layers N_{ll} and the porosity factor η

$$F_R = 1 + \frac{\pi^2 \mu_0^2 \omega^2 \eta^2 N_{ll}^2 d_{str}^4}{768 \rho_w^2} = 1 + \frac{\pi^2 \eta^2 N_{ll}^2}{192} \left(\frac{d_{str}}{\delta_w} \right)^4, \tag{5.55}$$

where the porosity factor of the litz-wire model shown in Fig. 5.1

$$\eta = \frac{d_{str}}{p} = \frac{d_{str}}{d_{str} + 2t}, \tag{5.56}$$

the number of strand turns per strand layer

$$N_{tl} = \frac{\eta b_c}{d_{str}}, \tag{5.57}$$

the number of strand layers is

$$N_{ll} = \frac{h_c}{d_{str} + 2t}, \tag{5.58}$$

$$Nk = N_{ll} N_{tl} = N_{ll} \frac{\eta b_c}{d_{str}}, \tag{5.59}$$

t is the insulation thickness, and h_c is the core winding window height. The litz-wire winding ac resistance calculated from equation (5.55) is identical as that calculated from approximate modified Dowell's equation (5.22) and shown in Fig. 5.12.

5.10 Conclusion

In this chapter, an approximate model and a modified Dowell's equation for litz-wire and multi-strand wire winding has been presented. The proposed model takes into account the proximity effect between strands within a litz-wire bundle as well as the proximity effect between the layers of the litz-wire bundles. The skin effect is also taken into account. For this model, Dowell's equation has been adapted, resulting in the analytical expressions for the ac-to-dc winding resistance ratio $F_{R(litz)}$ and winding ac resistance $R_{w(litz)}$ of litz-wire windings. Additionally, the low and medium frequency approximation of litz-wire ac-to-dc winding resistance ratio has been given, expression for the litz-wire optimum strand diameter, and equation for the number of strands in litz-wire bundle at which minimum winding resistance is achieved has been derived. An example of a design procedure of litz-wire winding inductor has been presented. The equation for the winding ac resistance $R_{w(litz)}$ of litz-wire winding has been experimentally verified. The predicted results were in good agreement with the measured ones.

It has been shown that as the diameter of the strand decreases, the low-frequency range increases, i.e., the range in which the winding ac resistance equals the winding dc resistance. Moreover, an increase in the number of strands k in a litz-wire bundle causes an increase of the frequency range where the ac resistance of litz-wire winding is lower than the ac resistance of solid-round wire winding with the same cross-sectional conductor area. Furthermore, it has been shown that for the litz-wire winding there is an optimum frequency at which litz-wire winding ac resistance has a minimum value. Additionally, for the very high-frequency operation, the litz-wire winding ac resistance is greater compared to the solid-round wire winding with the same cross-sectional conductor area.

In the chapter, the equations for the boundary frequency between low and medium-

frequency ranges for the litz-wire winding and the solid-round wire windings have been derived.

The following conclusions can be drawn from the analysis given in this chapter:

- The proposed approximate model and the modified Dowell's equation for litz-wire windings predicts the litz-wire winding resistance of the inductor.
- At the optimum strand diameter, the litz wire ac-to-dc winding resistance ratio is $F_{R(litz)} = F_{Rcr} = 2$.
- As the optimum strand diameter $d_{str(opt)}$ increases, the required number of strands in the bundle k_{cr} to achieve the minimum winding ac resistance decreases.
- As the number of bundle layers N_l increases, $d_{str(opt)}/\delta_w$ decreases.
- As the number of strands in the bundle k increases, $(d/\delta_w)_{opt}$ also increases.
- The minimum value of $\zeta = R_{w(litz)}/R_{w(solid)}$ decreases as the number of strands k increases.
- For a fixed conductor cross-sectional area of the litz-wire bundle, the boundary frequency between the low-frequency range and medium-frequency range increases as the number of strands in the litz-wire bundle k increases.
- The boundary frequency of the litz-wire winding $f_{B(litz)}$ is approximately $\sqrt{k}$ times higher than that of the solid-round wire winding with the same conductor cross-sectional area.
- As the number of layers N_l increases, $(d/\delta_w)_B$ and $(d_{str}/\delta_w)_B$ decrease.
- The ratio $(d_{str(opt)}/\delta_w)/(d_{str}/\delta_w)_B = \sqrt[4]{20} \approx 2.1147$.

- There is a frequency range, where the litz-wire and solid-round wire winding resistances with the same cross-sectional conductor area are the same. The maximum frequency of this range is nearly equal to the boundary frequency of the solid-round wire winding given by (5.15).

- There is a frequency range, where the litz-wire winding resistance is lower than the solid-round wire winding resistance.

- For a given litz-wire winding, there is a frequency at which it becomes worse than the solid-round wire winding with the same cross-sectional conductor area. This may increase winding losses at harmonics in inductors and transformers conducting currents with large harmonics, such as PWM converters, especially in discontinuous conduction mode (DCM) [15], [16].

6 Analytical Winding Foil Thickness Optimization of Inductors Conducting Harmonic Currents

6.1 Introduction

This paper presents analytical winding power loss minimization of foil inductors conducting ac harmonic currents with and without dc offset. The approximated equation for the ac winding power loss is derived and used to determine the optimum foil thickness of inductors operating with multi-harmonic ac currents. An approximated equation for the total winding power loss is also derived and used to determine the optimum foil thickness of inductors operating with multi-harmonic ac currents superimposed on the dc current. The design procedure for inductors with minimum total winding power loss is presented for a pulsewidth-modulated dc-dc boost converter operating in discontinuous conduction mode (DCM). The theoretical predictions have been verified by measurements of inductors with four different foil thicknesses.

Power loss in the winding of inductors play an important role in pulsewidth-modulated dc-dc power converters, especially for those operated in discontinuous conduction mode [2], [14], [15], [16], [18], [20], [21], [30], [71], and [76]. This is because the winding loss increases due to increased harmonic content in the inductor winding current. The ac power loss in the inductor winding is caused by two eddy-current effects: the skin effect and the proximity effect [1]-[51], [56]-[64], [65]-[71], [73]-[76], [78]-[84]. Both of these effects are frequency depended and their influence on the winding ac resistance and the ac winding power loss increases as the current frequency increases. Unfortunately, the content of harmonic currents in the inductor winding cannot be reduced and, therefore, one solution to reduce inductor winding power loss is to optimize the winding conductor size, taking into account inductor current harmonics.

The winding dc resistance depends on the width and the thickness of the foil

conductor. The larger are both dimensions the lower is the winding dc resistance. The skin and proximity effects in foil inductors depend on the foil thickness and are nearly independent of the foil width. Therefore, in the inductor design procedure, the foil width can be selected to maintain the dc current density below a certain value, typically, $J_{dc} \leq 5$ A/mm^2 [28], [14], and to fit the bobbin of the chosen core. The foil thickness can be optimized to minimize ac winding loss or total dc and ac winding losses.

The objectives of this paper are:

- to derive an expression for the optimum foil thickness in order to achieve the minimum ac winding power loss of a foil inductor conducting ac harmonic currents;
- to derive an expression for the optimum foil thickness in order to achieve the minimum total winding power loss of foil inductor conducting both dc and ac harmonic currents;
- to derive approximate expressions for the ac winding power loss of foil inductors;
- to derive approximate expressions for the total winding power loss of foil inductors;
- to present a design procedure for foil inductors with the optimum foil thickness for PWM dc-dc boost converter operating in DCM;
- to verify experimentally the theoretical results.

6.2 Dowell's Equation for Winding Resistance of Foil Inductors at n-th Harmonic

The dc and low-frequency winding resistance of a foil inductor is given by

$$R_{wdc} = \frac{\rho_w l_w}{A_w} = \frac{\rho_w l_w}{bh} = \frac{\rho_w l_w}{\delta_w b \left(\frac{h}{\delta_w}\right)} \tag{6.1}$$

where $\rho_w = 1/\sigma_w$ is the resistivity of the winding conductor, b is the foil width, h is the bare foil thickness, $A_w = bh$ is the cross-sectional area of the foil, $l_w = N_l l_T$ is the foil winding conductor length, N_l is the number of foil layers, l_T is the foil mean turn length (MTL), δ_w is the skin depth of the winding conductor, and h/δ_w is the normalized foil thickness. The skin depth of the winding conductor at the fundamental frequency of the inductor current is given by

$$\delta_w = \sqrt{\frac{2}{\omega\mu_0\sigma_w}} = \frac{1}{\sqrt{\pi\mu_0\sigma_w f}} = \sqrt{\frac{\rho_w}{\pi\mu_0 f}}. \tag{6.2}$$

From Dowell's equation, the exact ac-to-dc winding resistance ratio at the n-th harmonic (where $n = 1, 2, 3, ...$) is [14], [15], [30]

$$F_{Rn} = \frac{R_{wn}}{R_{wdc}} = \sqrt{n}\left(\frac{h}{\delta_w}\right)\left[\frac{\sinh\left(2\sqrt{n}\frac{h}{\delta_w}\right) + \sin\left(2\sqrt{n}\frac{h}{\delta_w}\right)}{\cosh\left(2\sqrt{n}\frac{h}{\delta_w}\right) - \cos\left(2\sqrt{n}\frac{h}{\delta_w}\right)}\right.$$

$$\left. + \frac{2(N_l^2 - 1)}{3}\frac{\sinh\left(\sqrt{n}\frac{h}{\delta_w}\right) - \sin\left(\sqrt{n}\frac{h}{\delta_w}\right)}{\cosh\left(\sqrt{n}\frac{h}{\delta_w}\right) + \cos\left(\sqrt{n}\frac{h}{\delta_w}\right)}\right] \quad \text{for } n = 1, 2, 3, ... \ . \tag{6.3}$$

The winding ac resistance of the inductor at n-th harmonic is

$$R_{wn} = R_{wdc}F_{Rn} = \frac{\rho_w l_w}{bh}F_{Rn}. \tag{6.4}$$

From Dowell's equation, the exact expression for the normalized winding ac resistance for the n-th harmonic at a fixed frequency of fundamental component, i.e., at fixed δ_w, is

$$F_{rn} = \frac{F_{Rn}}{\frac{h}{\delta_w}} = \frac{R_{wn}}{\left(\frac{\rho_w l_w}{b\delta_w}\right)} = \sqrt{n}\left[\frac{\sinh\left(2\sqrt{n}\frac{h}{\delta_w}\right) + \sin\left(2\sqrt{n}\frac{h}{\delta_w}\right)}{\cosh\left(2\sqrt{n}\frac{h}{\delta_w}\right) - \cos\left(2\sqrt{n}\frac{h}{\delta_w}\right)}\right.$$

$$\left. + \frac{2(N_l^2 - 1)}{3}\frac{\sinh\left(\sqrt{n}\frac{h}{\delta_w}\right) - \sin\left(\sqrt{n}\frac{h}{\delta_w}\right)}{\cosh\left(\sqrt{n}\frac{h}{\delta_w}\right) + \cos\left(\sqrt{n}\frac{h}{\delta_w}\right)}\right] \quad \text{for } n = 1, 2, 3, ... \ . \tag{6.5}$$

Fig. 6.1 shows a 3-D plot of the normalized winding ac resistance F_{rn} as a function of the normalized foil thickness h/δ_w and the order of harmonic n for the ten-layer foil copper inductor winding ($N_l = 10$) at a fixed frequency f. It can be seen that for

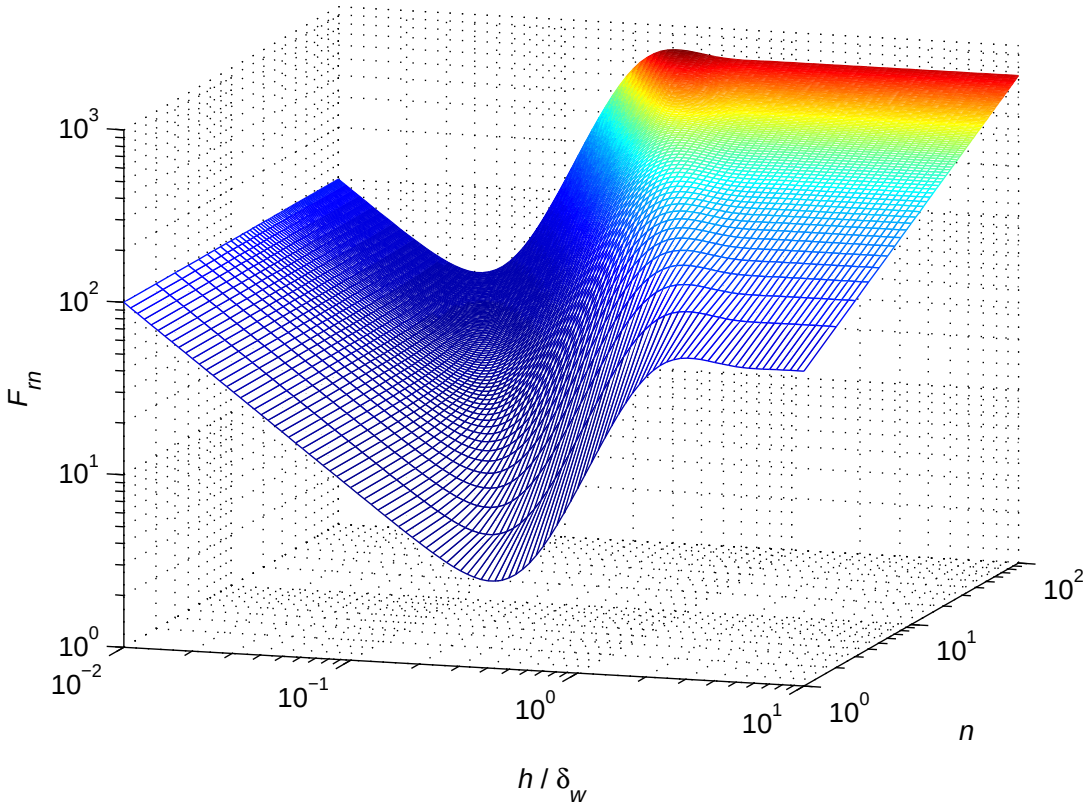

Figure 6.1: 3D plot of normalized winding ac resistance F_{rn} as a function of normalized foil thickness h/δ_w and order of harmonic n for the ten-layer foil winding inductor ($N_l = 10$) at a fixed frequency f.

each harmonic order n, the normalized winding ac resistance exhibit a minimum value (valley) located at the optimum normalized foil thickness. As the order of harmonic n increases, the optimum normalized foil thickness h/δ_w decreases, and the value of the minimum normalized winding ac resistance increases.

6.3 Ac Power Loss in Foil Inductors

Let us assume that the current flowing through the foil inductor winding is the ac current composed of many harmonics expressed by

$$i_l(t) = \sum_{n=1}^{\infty} I_{mn} \cos(n\omega t + \phi_n) = \sqrt{2} \sum_{n=1}^{\infty} I_n \cos(n\omega t + \phi_n) \tag{6.6}$$

where I_{mn} is the current amplitude of the n-th harmonic, $I_n = I_{mn}/\sqrt{2}$ is the RMS current of the n-th harmonic, $\omega = 2\pi f$ is the angular frequency, f is the frequency of the fundamental, and ϕ_n is the phase of the n-th harmonic.

The foil ac winding power loss at fundamental and harmonics is given by

$$P_{wac} = \sum_{n=1}^{\infty} R_{wn} I_n^2 = I_1^2 \sum_{n=1}^{\infty} \beta_n^2 R_{wn} \tag{6.7}$$

or in terms of the normalized winding ac resistance is

$$P_{wac} = \frac{\rho_w l_w I_1^2}{b\delta_w} \sum_{n=1}^{\infty} \beta_n^2 F_{rn} \tag{6.8}$$

where the RMS ac current at the n-th harmonic normalized with respect to the fundamental component is

$$\beta_n = \frac{I_n}{I_1} \quad \text{for } n = 1, 2, 3, \ldots . \tag{6.9}$$

6.4 Total Power Loss in Foil Inductors

The foil inductor current, which is composed of the ac current with many harmonics $i_l(t)$ superimposed on the dc component I_L is expressed by

$$i_L(t) = I_L + i_l(t) = I_L + \sum_{n=1}^{\infty} I_{mn} \cos(n\omega t + \phi_n) = I_L + \sqrt{2} \sum_{n=1}^{\infty} I_n \cos(n\omega t + \phi_n). \tag{6.10}$$

The dc winding power loss is given by

$$P_{wdc} = R_{wdc} I_L^2. \tag{6.11}$$

The total winding power loss due to the inductor current waveform $i_L(t)$ given in (6.10) is expressed by

$$P_w = P_{wdc} + P_{wac} = R_{wdc} I_L^2 + \sum_{n=1}^{\infty} R_{wn} I_n^2 = R_{wdc} I_L^2 + I_L^2 \sum_{n=1}^{\infty} \gamma_n^2 R_{wn}$$

$$= P_{wdc} + P_{wdc} \sum_{n=1}^{\infty} \gamma_n^2 \frac{R_{wn}}{R_{wdc}}$$

$$= P_{wdc}(1 + \sum_{n=1}^{\infty} \gamma_n^2 F_{Rn}) = P_{wdc} F_{Rh} \tag{6.12}$$

or in terms of the normalized winding ac resistance by

$$P_w = \frac{\rho_w l_w I_L^2}{b\delta_w} \left(\frac{1}{\frac{h}{\delta_w}} + \sum_{n=1}^{\infty} \gamma_n^2 F_{rn} \right) \tag{6.13}$$

where the RMS ac current at the n-th harmonic normalized with respect to the dc current is

$$\gamma_n = \frac{I_n}{I_L} \quad \text{for } n = 1, 2, 3, ... , \tag{6.14}$$

and the ac-to-dc winding resistance ratio at the fundamental frequency and at harmonic frequencies for a given amplitude spectrum of the inductor current waveform is

$$F_{Rh} = \frac{P_w}{P_{wdc}} = 1 + \sum_{n=1}^{\infty} \gamma_n^2 F_{Rn}. \tag{6.15}$$

Fig. 6.2 shows a typical winding loss for the 15-layer copper foil inductor operating in a pulsewidth-modulated dc-dc converter in discontinuous conduction mode at switching frequency $f_s = 50$ kHz with 100 significant harmonics, for $b = 10$ mm, $l_T = 5.3$ cm, the MOSFET on-duty cycle $D = 0.865$, the diode on-duty cycle $D_1 = 0.135$, the dc inductor current $I_L = 2.7435$ A, the maximum inductor current $\Delta i_L = 5.487$ A, and the current amplitudes for 100 harmonics computed using Fourier decomposition shown in Appendix 9.3 eq. (9.27) and in [15]. Note that the minimum ac winding loss occurs for the lower foil thickness than the minimum of the total winding loss. It can be shown that as the number of significant harmonics in the current increases, the minimum of ac winding loss and the minimum of total winding loss occur at the lower foil thicknesses. In this case, where the winding conducts 100 significant harmonics, the minimum of ac winding loss occurs at foil thickness approximately equal to $h_{opt(ac)} \approx 75$ μm and the minimum of total winding loss at thickness $h_{opt} \approx 103$ μm. However, for the same 15-layer foil winding inductor conducting the same dc current $I_L = 2.7435$ A and only fundamental component $I_{m1} = 1.9592$ A, the optimum foil

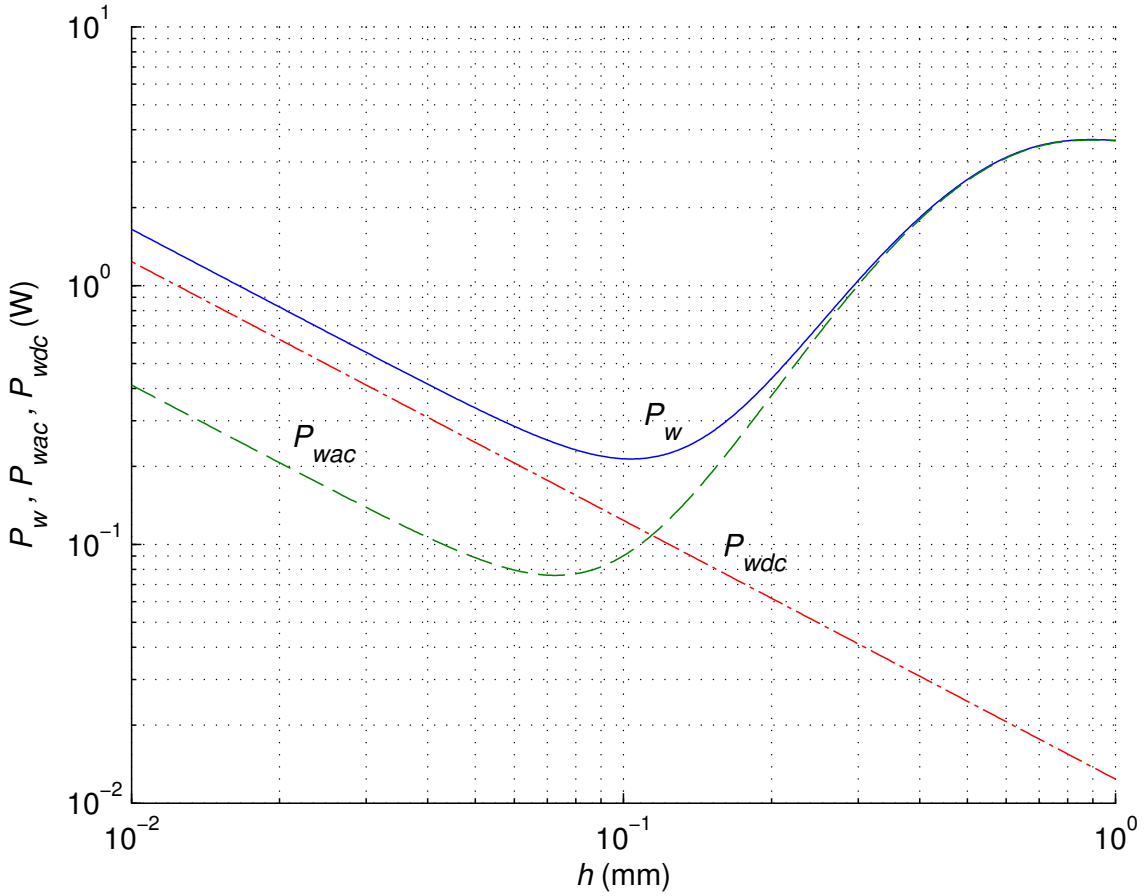

Figure 6.2: Plots of P_{wdc}, P_{wac}, and $P_w = P_{wdc} + P_{wac}$ as functions of foil thickness h for 15-layer foil winding inductor.

thickness for the ac winding loss is approximately $h_{opt(ac)} \approx 95$ μm and the optimum foil thickness for the total winding loss is $h_{opt} \approx 137$ μm. Therefore, optimization of the foil thickness for the foil inductors conducting harmonic currents is required.

6.5 Low- and Medium-Frequency Approximation of the Winding Ac Resistance For Foil Inductors

The analytical optimization of Dowell's equation (6.5) leads to the transcendental equation and, therefore, can only be solved numerically for $N_l \geq 2$. Hence, Dowell's approximate equation will be used in this section to determine analytically the optimum foil thickness for the windings conducting currents given in (6.6) and (6.10).

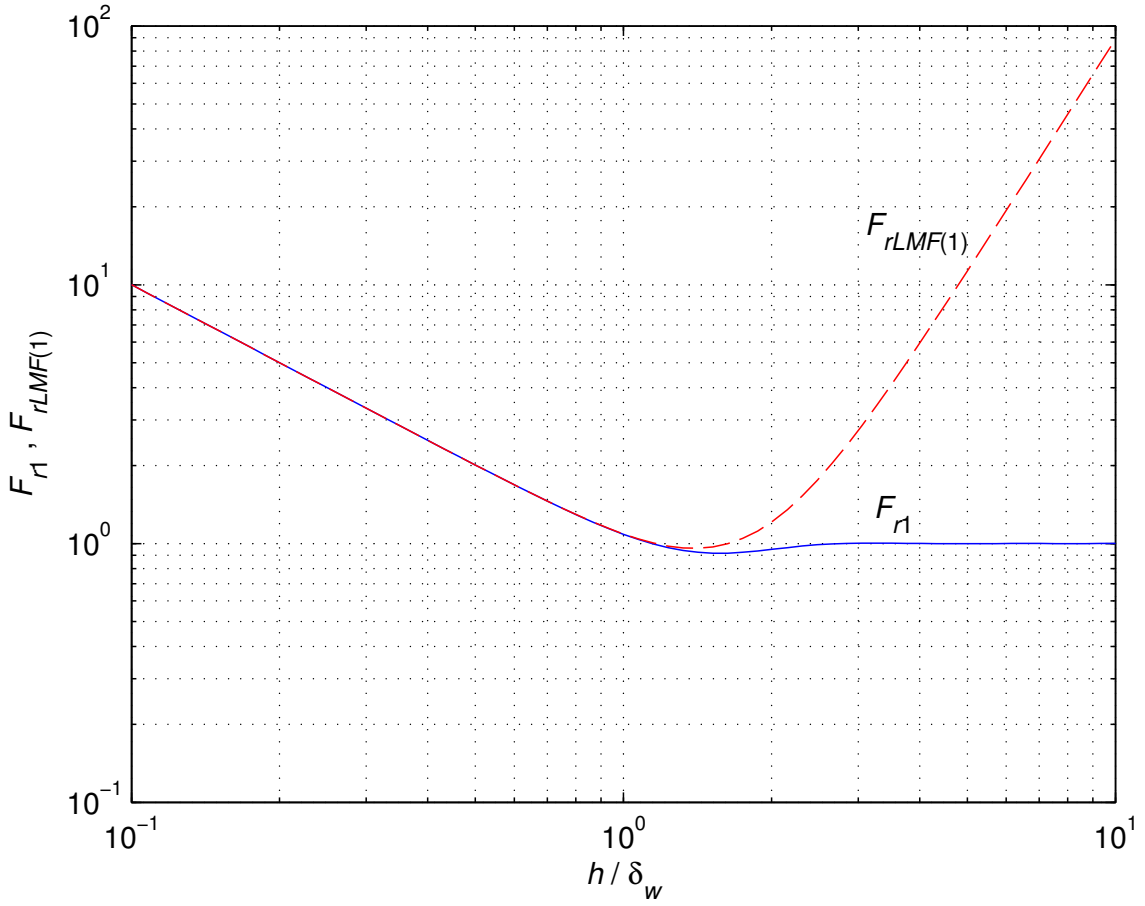

Figure 6.3: The exact (continuous line) and approximate (dashed line) plots of normalized winding ac resistance F_{r1} and $F_{rLMF(1)}$ as a function of h/δ_w for the single-layer inductor ($N_l = 1$).

For low and medium frequencies, the normalized winding ac resistance of the inductor with any number of layers N_l and at the n-th harmonic can be approximated by

$$F_{rLMF(n)} = \frac{R_{wLMF(n)}}{\left(\frac{\rho_w l_w}{b\delta_w}\right)} = \frac{F_{RLMF(n)}}{\frac{h}{\delta_w}} = \frac{1}{\frac{h}{\delta_w}} + \frac{n^2\left(5N_l^2 - 1\right)}{45}\left(\frac{h}{\delta_w}\right)^3 \tag{6.16}$$

where the detailed derivation is presented in the Appendix 9.2. Figs. 6.3, 6.4, 6.5, and 6.6 show the exact (continuous line) and approximate (dashed line) plots of normalized winding ac resistances F_{r1} and F_{r50} as functions of h/δ_w for the single-layer inductor ($N_l = 1$) and for the ten-layer inductor ($N_l = 10$), respectively. It can be seen that the approximation tracks the minimum of the exact normalized winding

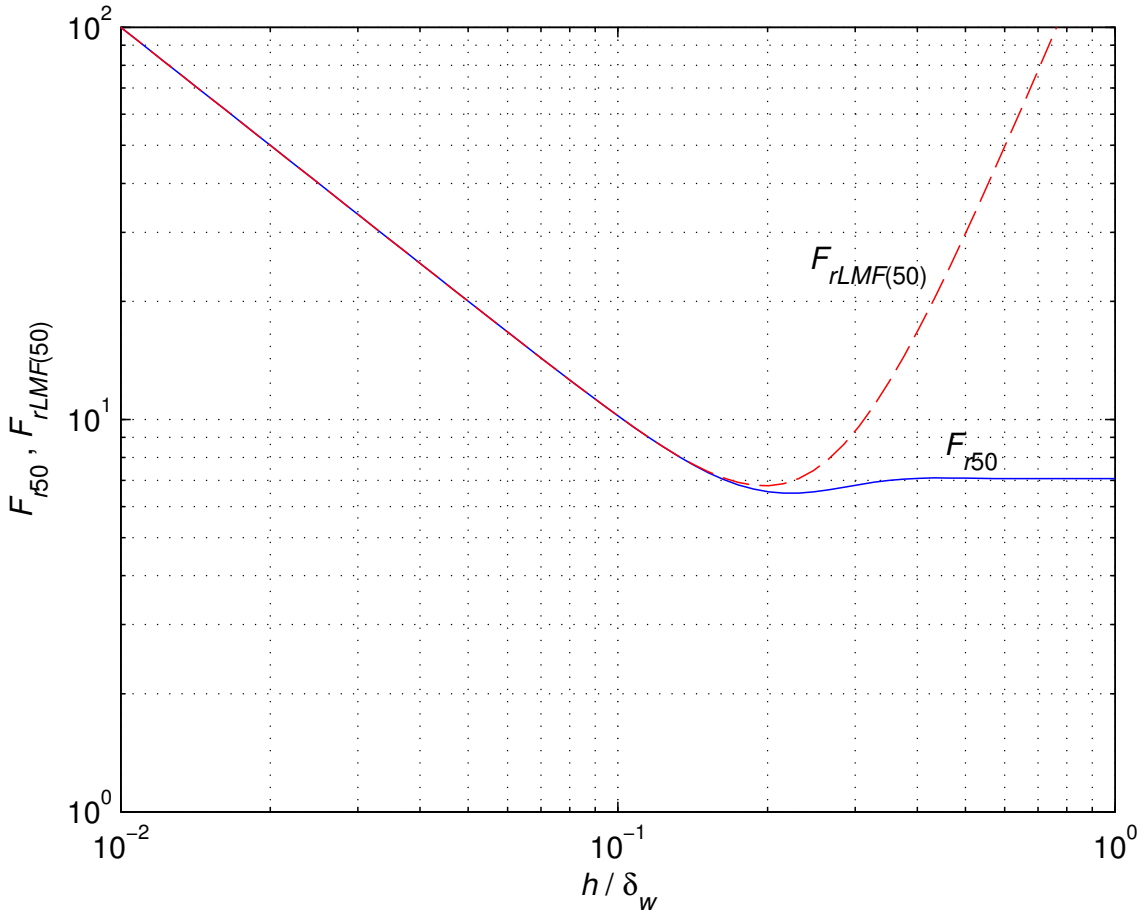

Figure 6.4: The exact (continuous line) and approximate (dashed line) plots of normalized winding ac resistance F_{r50} and $F_{rLMF(50)}$ as a function of h/δ_w for the single-layer inductor ($N_l = 1$).

ac resistance F_{rn} with high accuracy. Moreover, it can be seen that for the single-layer inductors the normalized winding ac resistance, due to the skin effect, increases as the order of harmonic for the inductor current increases. For the multi-layer inductors the normalized winding ac resistance, due to the skin and proximity effects, increases more rapid as the order of harmonic increases.

From (6.16), the approximate winding ac resistance at the n-th harmonic is

$$R_{wLMF(n)} = F_{RLMF(n)} R_{wdc} = \left(\frac{\rho_w l_w}{b\delta_w}\right)\left[\frac{1}{\frac{h}{\delta_w}} + \frac{n^2\left(5N_l^2 - 1\right)}{45}\left(\frac{h}{\delta_w}\right)^3\right]. \qquad (6.17)$$

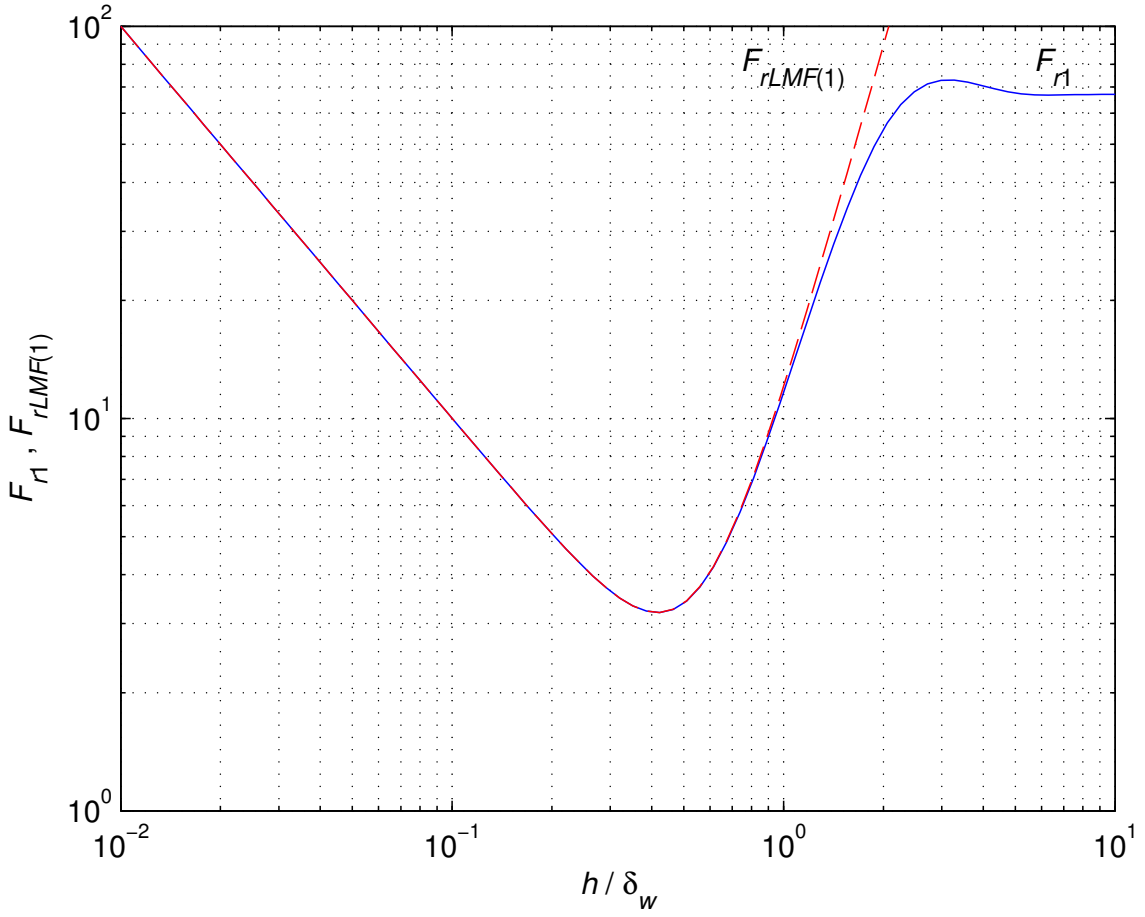

Figure 6.5: The exact (continuous line) and approximate (dashed line) plots of normalized winding ac resistance F_{r1} and $F_{rLMF(1)}$ as a function of h/δ_w for the ten-layer inductor ($N_l = 10$).

6.6 Optimum Foil Thickness for Inductors Conducting Ac Harmonic Currents

Substituting (6.16) into (6.8), the low- and medium-frequency approximate ac winding power loss that consists of ac harmonic winding power losses for an inductor conducting current $i_l(t)$ can be expressed as

$$P_{wac} \approx \frac{\rho_w l_w I_1^2}{b\delta_w} \sum_{n=1}^{\infty} \beta_n^2 F_{rLMF(n)} = \frac{\rho_w l_w I_1^2}{b\delta_w} \sum_{n=1}^{\infty} \beta_n^2 \left[\frac{1}{\frac{h}{\delta_w}} + \frac{n^2 \left(5N_l^2 - 1\right)}{45} \left(\frac{h}{\delta_w} \right)^3 \right]. \quad (6.18)$$

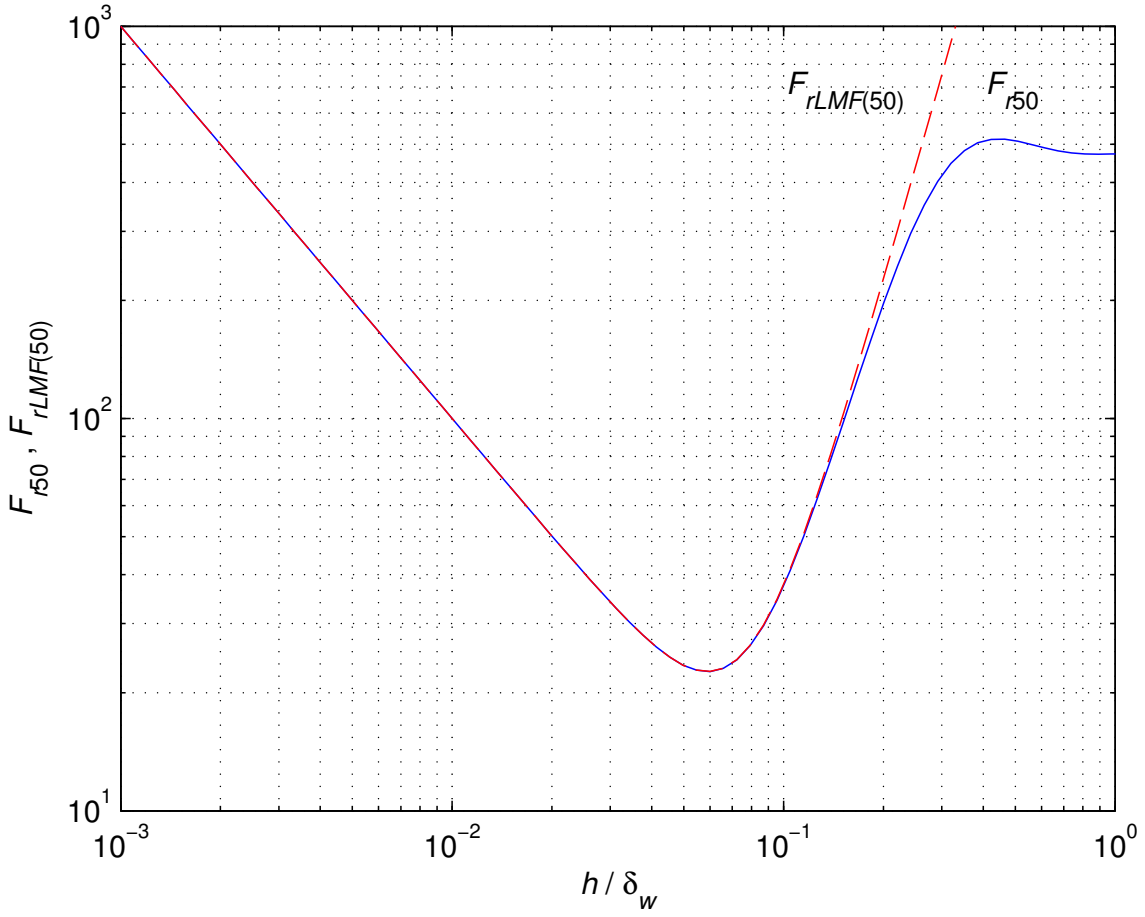

Figure 6.6: The exact (continuous line) and approximate (dashed line) plots of normalized winding ac resistance F_{r50} and $F_{rLMF(50)}$ as a function of h/δ_w for the ten-layer inductor ($N_l = 10$).

The minimum total winding power loss of an inductor may be found by taking the derivative of (6.18) with respect to h/δ_w and equating the result to zero

$$\frac{1}{\frac{\rho_w l_w I_1^2}{b\delta_w}} \frac{dP_{wac}}{d\left(\frac{h}{\delta_w}\right)} = -\frac{\sum_{n=1}^{\infty} \beta_n^2}{\left(\frac{h}{\delta_w}\right)^2} + \left(\frac{h}{\delta_w}\right)^2 \frac{(5N_l^2 - 1)}{15} \left(\sum_{n=1}^{\infty} \beta_n^2 n^2\right) = 0. \tag{6.19}$$

The solution of (6.19) produces the normalized optimum (valley) foil thickness of an inductor conducting ac harmonic currents

$$\frac{h_{opt(ac)}}{\delta_w} = \sqrt[4]{\frac{15}{(5N_l^2 - 1)\sum_{n=1}^{\infty} n^2}}. \tag{6.20}$$

Hence, using (6.2) and (6.20), the optimum (valley) foil thickness of an inductor conducting ac harmonic currents is expressed as

$$h_{opt(ac)} = \delta_w \sqrt[4]{\frac{15}{(5N_l^2-1)\sum_{n=1}^{\infty} n^2}} = \sqrt{\frac{\rho_w}{\pi\mu_0 f}} \sqrt[4]{\frac{15}{(5N_l^2-1)\sum_{n=1}^{\infty} n^2}}. \tag{6.21}$$

It can be seen that for the inductor conducting only ac harmonic currents the optimum foil thickness is inversely proportional to the square root of frequency $\propto 1/\sqrt{f}$, is inversely proportional to the square root of number of layers $\propto 1/\sqrt{N_l}$, and depends on number of harmonics n flowing through the winding.

6.7 Optimum Foil Thickness for Inductors With Dc and Ac Harmonic Currents

Substituting (6.16) into (6.13), the low- and medium-frequency approximate total winding power loss that consists of dc and ac harmonics winding power loss for an inductor conducting current $i_L(t)$ can be expressed as

$$P_w \approx \frac{\rho_w l_w I_L^2}{b\delta_w} \left(\frac{1}{\frac{h}{\delta_w}} + \sum_{n=1}^{\infty} \gamma_n^2 F_{rLMF(n)} \right) = \frac{\rho_w l_w I_L^2}{b\delta_w}$$

$$\left\{ \frac{1}{\frac{h}{\delta_w}} + \sum_{n=1}^{\infty} \gamma_n^2 \left[\frac{1}{\frac{h}{\delta_w}} + \frac{n^2\left(5N_l^2-1\right)}{45} \left(\frac{h}{\delta_w} \right)^3 \right] \right\}. \tag{6.22}$$

The minimum total winding power loss of an inductor may be found by taking the derivative of (6.22) with respect to h/δ_w and equating the result to zero

$$\frac{1}{\frac{\rho_w l_w I_L^2}{b\delta_w}} \frac{dP_w}{d\left(\frac{h}{\delta_w}\right)} = -\frac{1}{\left(\frac{h}{\delta_w}\right)^2} \left(1 + \sum_{n=1}^{\infty} \gamma_n^2 \right) + \left(\frac{h}{\delta_w} \right)^2 \frac{\left(5N_l^2-1\right)}{15} \left(\sum_{n=1}^{\infty} \gamma_n^2 n^2 \right) = 0. \tag{6.23}$$

The solution of (7.17) produces the normalized optimum (valley) foil thickness of an inductor conducting the dc current and ac harmonic currents

$$\frac{h_{opt}}{\delta_w} = \sqrt[4]{\frac{15(1+\sum_{n=1}^{\infty}\gamma_n^2)}{(5N_l^2-1)\sum_{n=1}^{\infty}\gamma_n^2 n^2}}. \tag{6.24}$$

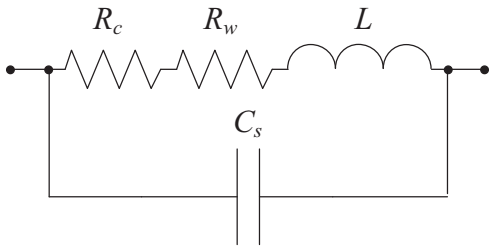

Figure 6.7: Lumped-parameter equivalent circuit of the foil inductor.

Hence, using (6.2) and (6.24), the optimum (valley) foil thickness of an inductor operating under dc and ac harmonic currents is expressed as

$$h_{opt} = \delta_w \sqrt[4]{\frac{15(1+\sum_{n=1}^{\infty}\gamma_n^2)}{(5N_l^2-1)\sum_{n=1}^{\infty}\gamma_n^2 n^2}} = \sqrt{\frac{\rho_w}{\pi\mu_0 f}} \sqrt[4]{\frac{15(1+\sum_{n=1}^{\infty}\gamma_n^2)}{(5N_l^2-1)\sum_{n=1}^{\infty}\gamma_n^2 n^2}}. \tag{6.25}$$

It can be seen that for the foil inductor conducting dc and ac harmonic currents, the optimum foil thickness is inversely proportional to the square root of frequency $\propto 1/\sqrt{f}$, is inversely proportional to the square root of the number of layers $\propto 1/\sqrt{N_l}$, depends on the number of harmonic currents, and depends on the RMS ac current of n-th harmonic normalized with respect to the dc current i.e, depends on γ_n.

6.8 Model of Foil Inductors

A lumped-parameter model of the foil inductor, valid for dc and ac currents, is depicted in Fig. 6.7. The model of the inductor consists of self-inductance L, winding ac resistance R_w, series core resistance R_c, and parasitic self-capacitance or a stray capacitance C_s. In reality L, R_w, and R_c are frequency dependent. However, in the subsequent analysis, the series core resistance is neglected ($R_c = 0$). This is because the core loss is very low at low values of magnetic flux density B, at which the inductor is measured. The impedance of the equivalent inductor circuit depicted in Fig. 6.7 is [4], [23], [22], [25], [14], [72]

$$Z = \frac{R_s + j\omega L\left[1-\omega^2 LC_s - (C_s R_s^2/L)\right]}{(1-\omega^2 LC_s)^2 + (\omega C_s R_s)^2} = r + jx \tag{6.26}$$

where $R_s = R_c + R_w$, r is the equivalent series resistance ESR, and x is the equivalent series reactance. Since $C_s R_s^2/L \ll 1$ [23], the first parallel self-resonant frequency of the inductor model occurs when the equivalent series reactance x is equal to zero and is given by

$$f_r = \frac{1}{2\pi\sqrt{LC_s}}. \tag{6.27}$$

For frequencies below the first self-resonant frequency, the impedance of the inductor is inductive. For frequencies above the first self-resonant frequency, the impedance of the inductor is capacitive and the currents are shorted out. Thus, the useful frequency range of inductors is from dc to $0.25 f_r \leq f_{max} \leq 0.45 f_r$.

Using (7.43), the ESR of inductor is

$$r = \frac{R_s}{(1-\omega^2 LC_s)^2 + (\omega C_s R_s)^2} \tag{6.28}$$

and the winding ac resistance neglecting core loss ($R_c = 0$) is

$$R_w = R_s\Big|_{R_c=0} = \frac{1-\sqrt{1-4\omega^2 r^2 C_s^2 (1-\omega^2 LC_s)^2}}{2r\omega^2 C_s^2}. \tag{6.29}$$

6.9 Design Example of Inductor with Optimum Foil Winding Thickness and Minimum Power Loss

In this section, a design procedure of an inductor with optimized foil thickness and minimum total winding power loss is given. The inductor operated in pulsewidth-modulated dc-dc boost converter in discontinuous conduction mode (DCM). The specifications of the converter were as follows: the converter input voltage $V_I = 10$ V, the converter output voltage $V_O = 70$ V, the converter switching frequency $f_s = 50$ kHz, the dwell-duty cycle $D_w = 0.05$. For these parameters, the converter output current, load resistance, dc voltage transfer function, and the dc inductor current are

$$I_O = \frac{P_O}{V_O} = \frac{30}{70} = 0.4286 \text{ A}, \tag{6.30}$$

$$R_L = \frac{V_O}{I_O} = \frac{70}{0.4286} = 163.33\ \Omega, \tag{6.31}$$

$$M_{VDC} = \frac{V_O}{V_I} = \frac{70}{10} = 10, \tag{6.32}$$

$$I_L = I_O M_{VDC} = 3 \text{ A}, \tag{6.33}$$

respectively. Assuming converter efficiency $\eta_c = 90\%$, the inductance of the converter, the MOSFET on-duty cycle, and the diode on-duty cycle are [14]

$$L = \frac{\eta_c R_L (M_{VDC} - 1)(1 - D_w)^2}{2 f_s M_{VDC}^3} = 23.21 \ \mu\text{H}, \tag{6.34}$$

$$D = \sqrt{\frac{2 f_s L M_{VDC}(M_{VDC-1})}{\eta_c R_L}} = 0.8143, \tag{6.35}$$

$$D_1 = \frac{D}{M_{VDC} - 1} = 0.1357, \tag{6.36}$$

respectively. The maximum inductor current is

$$\Delta i_L = \frac{D V_O}{f_s L M_{VDC}} = 7.02 \text{ A} \tag{6.37}$$

and the energy stored in the inductor magnetic field is

$$W_m = \frac{1}{2} \Delta i_L^2 L = 0.571 \text{ mJ}. \tag{6.38}$$

The core selection was based on the core area product method [28], [14]. Assuming the core window utilization factor $K_u = 0.4$, the maximum magnitude of the current density in the foil $J_{m(max)} = 5$ A/mm^2, and the peak value of the magnetic flux $B_{pk} = 0.2$ mT the minimum A_p product of the core is

$$A_p = \frac{2 W_m}{K_u J_m B_{pk}} = 0.286 \text{ cm}^4. \tag{6.39}$$

For the designed inductor, the Magnetics Inc. 0R42616 ferrite gapped pot core and the 00B261601 bobbin were selected. The core area product is $A_p = 0.39$ cm^4 and the gap length is $l_g = 800$ μm. The initial permeability of the core material is $\mu_r = 2300 \pm 25\%$, the mean turn length (MTL) is $l_T = 5.3$ cm, and the breadth of the bobbin is $b = 9.93$ mm. The required number of turns for the foil winding is

$$N = N_l = \sqrt{\frac{L\left(l_g + \frac{lc}{\mu_{rc}}\right)}{\mu_0 A_c}} = 12.76 \approx 13 \tag{6.40}$$

and the total length of the foil is $l_w = Nl_T = 0.689$ m.

Using (9.27), (9.25), (9.26), and (6.14) the RMS ac currents of the n-th harmonic normalized with respect to the dc current was computed for 100 harmonics ($n = 100$). Using (6.25), the optimum foil thickness at which the minimum of total winding power loss occurs is $h_{opt} \approx 120$ μm.

6.10 Experimental Results

To verify the total power loss and the optimum foil thickness, four inductors used in pulse-width modulated dc-dc boost converter with a different foil thicknesses were wind and measured. The measurements of the equivalent series resistance ESR r were performed for four thicknesses of the foil winding conductor $h_1 = 50$ μm, $h_2 = 100$ μm, $h_3 = 120$ μm, $h_4 = 220$ μm. The thickness of the foil insulation on each side of the foil sheet was $t = 25$ μm.

The inductors were measured using Hewlett Packard (HP) 4194A impedance/gain-phase analyzer with HP 16047D test fixture. The inductances of the four inductors were $L = 20$ μH, resonant frequencies were $f_r \approx 10.38$ MHz, the inductances at the resonant frequency $L_{fr} = 1.86$ μH, and self-capacitances were $C_s = 126$ pF.

Fig. 6.8 shows the actual and theoretical total power winding losses for the designed pulse-width modulated dc-dc boost converter taking into account the first 100 harmonic currents. It can be seen that the total winding loss for the foil thickness $h_3 = h_{opt} = 120$ μm was the lowest one.

6.11 Conclusion

In this paper, the minimization of the ac winding power loss and the total winding loss has been performed. Equations for optimum foil winding thickness conducting harmonic currents and optimum foil winding thickness conducting harmonic currents superimposed on the dc component have been derived. The low- and medium-frequency

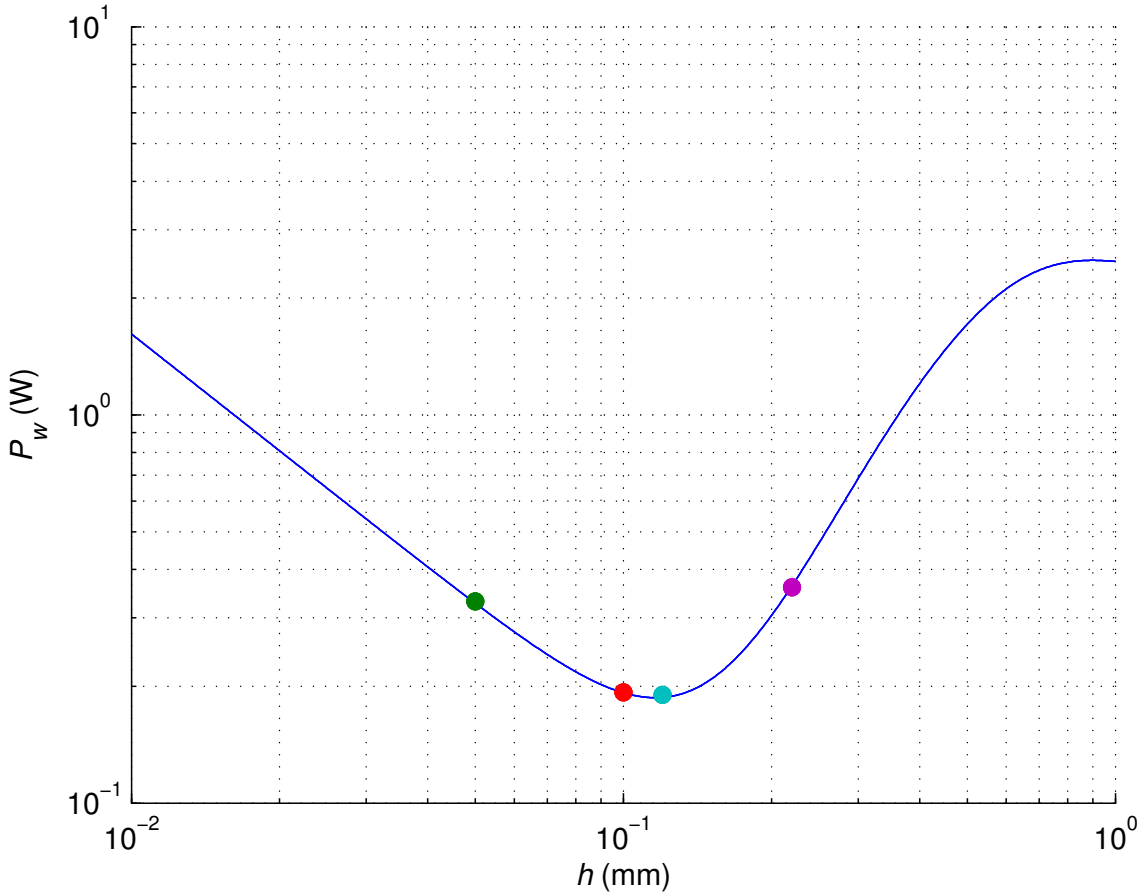

Figure 6.8: Plots of actual (circles) and exact (solid line) total winding power losses as functions of foil thickness h.

approximation of the normalized winding ac resistance has been used for ac winding power loss and total winding power loss optimizations. It has been shown that the optimum foil thickness for the foil inductor conducting only ac harmonic currents is lower than that conducting the same ac harmonic current superimposed on the dc component.

The design of the optimum foil thickness inductor winding has been shown for the pulse-width modulated dc-dc converter in the discontinuous conduction mode. The presented theory has been verified with measurements. The theoretical results were in agreement with the measurements.

The major conclusions drawn from the analysis performed in this paper are as

follows:

- The minimum of the ac winding loss of an inductor conducting only fundamental component occurs at a higher foil thickness than the minimum of the ac winding loss of inductor conducting multi-harmonic current;
- The minimum of the total winding loss of an inductor conducting only dc and fundamental components occurs at a higher foil thickness than the minimum of the total winding loss of inductor conducting dc and multi-harmonic currents;
- The minimum value of total dc and ac winding power losses occur at a larger foil thickness than the minimum of the winding ac power loss.
- The optimum foil thickness at which the minimum of the ac winding loss occurs depends on the number of inductor winding layers N_l and it decreases as the number of layers increases.
- The optimum foil thickness at which the minimum of the total winding loss occurs depends on the number of inductor winding layers N_l and it decreases as the number of layers increases.
- The optimum foil thicknesses at which the minimum of the ac winding loss occurs depends on the number of significant harmonic of the current $i_l(t)$ and it decreases as n increases.
- The optimum foil thicknesses at which the minimum of the total dc and ac harmonic winding losses occur depend on the number of significant harmonic of the current $i_L(t)$ and it decrease as n increases.
- As the RMS ac current of the n-th harmonic normalized with respect to the dc current γ_n decreases, the optimum foil thickness at which the minimum of the total winding loss occurs increases.

- As the number of significant harmonics n flowing through the winding increases, the winding ac power loss and the total winding loss increases.

7 Analytical Optimization of Solid-Round-Wire Windings Conducting Dc and Ac Non-Sinusoidal Periodic Currents

In the age of a constant improvement and development of new wide bandgap semiconductor devices such as silicon carbide (SiC) and gallium nitride (GaN), the problem of low efficiency at high frequencies of the switching-mode power converters due to the conduction and switching losses becomes less significant. This is mainly because these devices characterize with a low gate capacitance and low on-resistance, which permits much higher switching frequencies and much lower losses than those in competing silicon devices. However, improved performance of semiconductor devices eventually will not solve the problem of low efficiency in switching-mode power converters.

Accompanying losses in semiconductor devices for the switching-mode power converters are losses in magnetic devices [1]-[84]. Increased operating frequencies and high values of both the dc and ac non-sinusoidal periodic currents flowing through the inductor or transformer windings become a significant problem [14]-[30]. The results of these studies show that power losses in magnetic device windings may be similar or sometimes even greater, especially at high frequencies, than the losses in semiconductor devices.

The winding power losses of power inductors or power transformers operating in switching-mode dc-dc power converters are composed of the dc loss and the ac loss. The winding dc power loss is caused by the flow of the dc current through the winding. A reduction in the winding dc power loss can be achieved by increasing the cross-sectional area of the winding conductor. The ac winding power loss of power inductors or power transformers is a result of the superposition of two self-induced eddy-current density distributions. The self-induced distributions of eddy-current densities are caused by two orthogonal effects: the skin effect and the proximity

effect. The aforementioned effects are greatly dependent on the winding conductor size thickness or diameter. One method to diminish their influence on the winding resistance and the winding power loss as well as to increase efficiency of a magnetic component is to optimize the size of winding conductors. However, for the winding conducting dc and ac non-sinusoidal periodic currents, the optimum does not always exist. This is because at high values of the dc current the main winding power loss is often the winding dc power loss.

In general, inductor current waveforms are non-symmetrical, which means that the MOSFET on-duty cycle D is different than the diode on-duty cycle D_1, i.e., $D \neq D_1$. One of the contributions of this chapter is the minimization of total winding power loss for PWM dc-dc converters operated in discontinuous conduction mode where the inductor current waveform is non-symmetrical. This subject of practical importance has not been addressed yet in the literature.

Different kinds of winding conductors such as foil, strip (rectangular), square-wire, solid-round wire, and litz-wire are used in high-frequency magnetic devices. Their application depends on the electrical, mechanical, and thermal requirements of a designed magnetic component. The behavior of the winding resistance and the winding total power loss for the foil and strip wire windings, conducting sinusoidal or multi-harmonic currents with dc offset, is different than that of the square, solid-round, and litz-wire windings [14]. Solid-round-wire winding inductors are widely used in PWM dc-dc power converters, resonant power converters, resonant inverters, EMI filters, and magnetic sensors. The main advantage of solid-round-wire windings is low cost.

The purposes of this work are:

- to show the relationship among the fundamental current, the dc current, and the number of layers for which the local minimum of the total dc and ac solid-round-wire winding losses exists;

- to derive an expression for the normalized total-power-valley wire diameter of the solid-round-wire windings, where the local minimum of the winding dc and ac power losses (valley) occurs;
- to derive an expression for the normalized total-power-critical wire diameter of the solid-round-wire windings (greater than the normalized total-power-valley wire diameter), where the winding dc and ac power losses are equal to the winding dc and ac power losses at the local minimum (valley);
- to present the design procedure of the inductor optimized for the minimum of winding dc and ac power losses for the PWM dc-dc buck converter operating in discontinuous conduction mode (DCM);
- to verify the optimization by measurements.

The chapter is arranged in the following order. Section 7.1 derives equation for the winding power loss of the inductor conducting ac non-sinusoidal periodic current superimposed on the dc component. The behavior of the dc, ac, and total inductor winding losses in terms of the solid-round wire diameter for the PWM dc-dc buck converter in discontinuous conduction mode (DCM) is also presented. Section 7.2 gives Dowell's equation for the ac-to-dc winding resistance ratio at the n-th harmonic frequency for the solid-round-wire winding. Additionally, equation for the normalized ac resistance of the solid-round-wire winding at the n-th harmonic frequency is derived. In Section 7.3, the low- and medium-frequency approximations of Dowell's equation and normalized ac resistance at n-th harmonic frequency are given. The approximated equation for the normalized winding ac resistance of the solid-round-wire winding at the n-th harmonic frequency is used to derive an equation for the low- and medium-frequency total winding power losses for the winding conducting both the dc and ac non-sinusoidal periodic currents. Moreover, derivation of the normalized total-power-valley wire diameter and the local minimum (valley) of the total winding

power losses are shown. Section 7.4 concerns high-frequency approximations of Dowell's equation and normalized winding ac resistance at the n-th harmonic frequency. The approximate Dowell's equation is used to derive the approximate equation for the high-frequency total winding power loss of the winding conducting dc and ac non-sinusoidal periodic currents. The approximate equation for high-frequency total winding power loss along with the expression for the local minimum of total winding power loss are used to derive the normalized total-power-critical wire diameter. In Section 7.5, the procedure for the inductor design for the PWM dc-dc buck converter operating in DCM, with the local minimum of total winding power loss is presented. Core and winding selection steps are also shown. In Section 7.6, experimental verification of the presented theory and comparison of total winding loss of three inductors wind with different wire gauge are carried out. Ultimately, Section 7.7 draws conclusions.

7.1 Winding Power Loss in Solid-Round-Windings Due to Dc and Ac Harmonic Currents

The time-varying inductor current consisting of an ac non-sinusoidal periodic current $i_l(t)$ superimposed on the dc component I_{DC} is given by

$$i_L(t) = I_{DC} + i_l(t) = I_{DC} + \sum_{n=0}^{\infty} I_{Lmn} \sin(n\omega t + \phi_n)$$

$$= I_{DC} + \sqrt{2} \sum_{n=0}^{\infty} I_n \sin(n\omega t + \phi_n) \quad \text{for } n = 1, 2, 3, ..., \tag{7.1}$$

where I_{Lmn} is the amplitude of the n-th harmonic current, $I_n = I_{Lmn}/\sqrt{2}$ is the RMS value of the n-th harmonic current, $\omega = 2\pi f$ is the angular frequency of the inductor current, f is the frequency of the ac current fundamental component, and ϕ_n is the phase shift of the n-th harmonic current.

The solid-round-wire winding dc resistance is given by

$$R_{wdc} = \frac{4\rho_w l_w}{\pi d^2} = \frac{4\rho_w l_w}{\pi \delta_w^2 \left(\frac{d}{\delta_w}\right)^2}, \tag{7.2}$$

where d is the diameter of the bare round wire, $l_w = Nl_T$ is the total conductor length, $N = N_l N_{lt}$ is the number of turns, N_l is the number of layers, N_{lt} is the number of turns per layer, l_T is the mean turn length (MTL), $\rho_w = 1/\sigma_w$ is the conductor resistivity, δ_w is the conductor skin depth expressed as

$$\delta_w = \sqrt{\frac{2}{\mu_0 \sigma_w \omega}} = \frac{1}{\sqrt{\pi \mu_0 \sigma_w f}} = \sqrt{\frac{\rho_w}{\pi \mu_0 f}}, \tag{7.3}$$

and μ_0 is the free-space permeability.

The total winding power loss due to the current $i_L(t)$ flow is

$$P_w = P_{wdc} + P_{wac} = R_{wdc} I_{DC}^2 + \sum_{n=1}^{\infty} R_{wn} I_n^2 = R_{wdc} I_{DC}^2 + \sum_{n=1}^{\infty} R_{wn} \gamma_n^2 I_{DC}^2$$

$$= P_{wdc} + \sum_{n=1}^{\infty} \gamma_n^2 F_{Rn} P_{wdc} = P_{wdc} \left(1 + \sum_{n=1}^{\infty} F_{Rn} \gamma_n^2\right) = \frac{4 \rho_w l_w I_{DC}^2}{\pi \delta_w^2} \left[\frac{1}{\left(\frac{d}{\delta_w}\right)^2} + \sum_{n=1}^{\infty} \gamma_n^2 F_{rn}\right], \tag{7.4}$$

where the winding dc power loss is

$$P_{wdc} = R_{wdc} I_{DC}^2 = \frac{4 \rho_w l_w}{\pi d^2} I_{DC}^2, \tag{7.5}$$

R_{wn} is the winding ac resistance at n-th harmonic frequency

$$R_{wn} = \frac{4 \rho_w l_w}{\pi d^2} F_{Rn} = R_{wdc} F_{Rn}, \tag{7.6}$$

the winding ac power loss is given by

$$P_{wac} = \sum_{n=1}^{\infty} R_{wn} I_n^2, \tag{7.7}$$

$F_{Rn} = R_{wn}/R_{wdc}$ is the ac-to-dc winding resistance ratio at the fundamental ($n = 1$) and at the n-th harmonic frequency (where $n = 2,\ 3,\ 4, ...$) [14], the RMS ac current at the n-th harmonic frequency normalized with respect to the dc current is

$$\gamma_n = \frac{I_n}{I_{DC}} = \frac{I_{Lmn}}{\sqrt{2} I_{DC}} \quad \text{for } n = 1, 2, 3, ..., \tag{7.8}$$

and $F_{rn} = F_{Rn}/(d/\delta_w)^2$ is the normalized winding ac resistance at the fundamental ($n = 1$) and at the n-th harmonic frequency (where $n = 2,\ 3,\ 4, ...$). Fig. 7.1 shows the

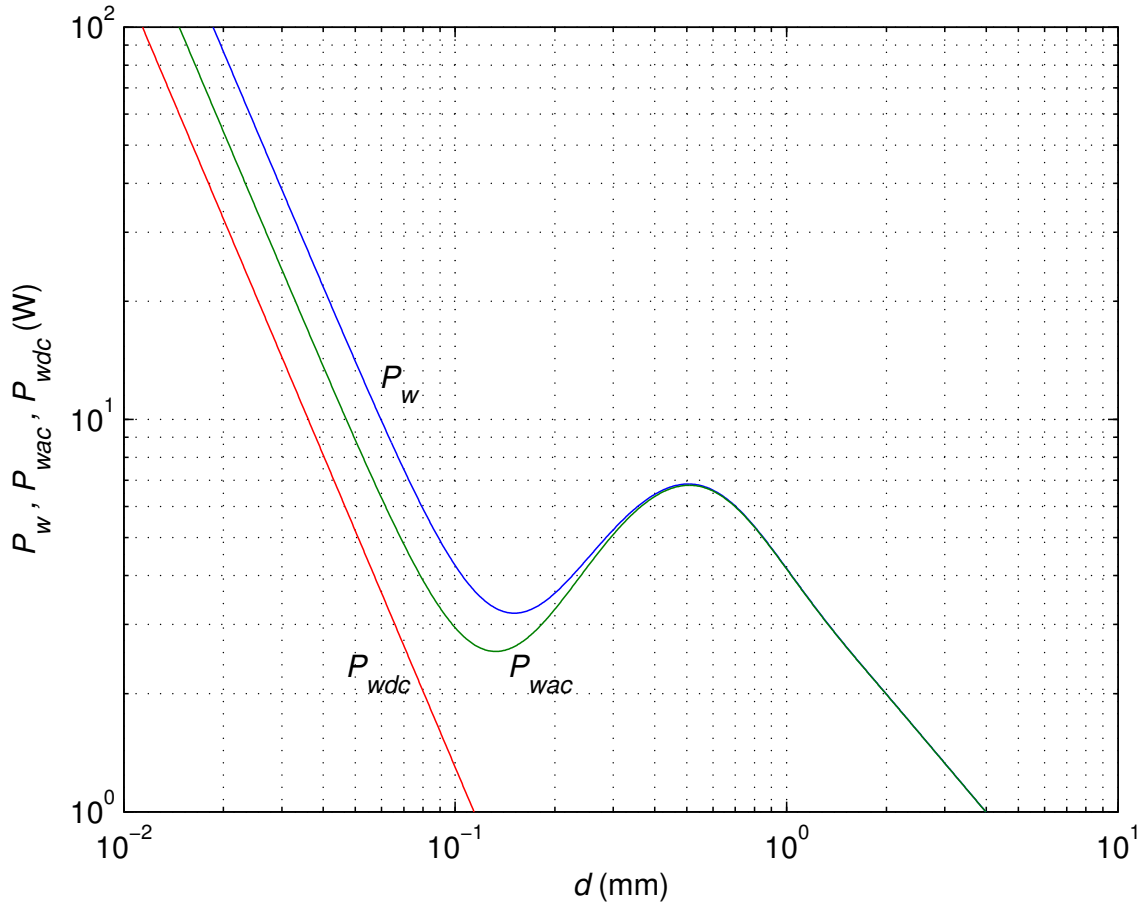

Figure 7.1: Plots of P_w, P_{wac}, and P_{wdc} as functions of the solid-round wire diameter d for the eight-layer inductor ($N_l = 8$) of the PWM dc-dc buck converter in discontinuous conduction mode at switching frequency $f_s = 100$ kHz and with 100 harmonics.

total winding power loss P_w, winding ac power loss P_{wac}, and winding dc power loss P_{wdc} as functions of the bare solid-round wire diameter d for the inductor operating in PWM dc-dc buck converter in discontinuous conduction mode (DCM). The inductor parameters were: the MTL $l_T = 5.3$ cm, the number of turns $N = 47$, the number of layers $N_l = 8$, and the porosity factor $\eta = d/p = 0.9$, where p is the distance between the centres of the adjacent conductors in a layer . Dowell's equation [2], [15] was used to compute the ac-to-dc winding resistance ratio for 100 harmonics. The PWM dc-dc buck converter parameters were: the switching frequency $f_s = 100$ kHz, the maximum inductor current $I_{Lmax} = \Delta i_{Lmax} = 1.3785$ A, the MOSFET

on-duty cycle $D = 0.1265$, and the diode on-duty cycle $D_1 = 0.3735$. Eq. (21) given in [15] was used to compute the amplitudes of the fundamental component and 100 harmonics of inductor current waveform and eq. (7.8) to compute the RMS ac currents at the n-th harmonic frequency normalized with respect to the dc current for 100 harmonics. It can be seen that the winding dc power loss decreases as the wire diameter increases. This is because, according to (7.5), the winding dc loss is inversely proportional to d^2. As the wire diameter increases, the winding ac power loss P_{wac} first decreases, reaches a local minimum, then increases, reaches a local maximum, and finally decreases. As the wire diameter increases, the total winding power loss P_w, which is the sum of winding dc and ac power losses, first decreases, reaches a local minimum, then increases, reaches a local maximum, and finally decreases. The diameter of the wire at which the local minimum of the total winding loss P_w occurs is called the total-power-valley diameter d_{vt}. Observe that the local minimum of the total winding power loss occurs for the larger wire diameter than the local minimum of the winding ac power loss. However, the local minimum of the total winding power loss does not always exists.

7.2 Dowell's Equation of Solid-Round-Wire Windings For Harmonics

One-dimensional model of the inductor and transformer windings was used by Dowell [2] to derive an equation for the winding resistance of the high-frequency magnetic components utilizing Maxwell's equations. The main assumption in his derivation is that the winding consists of straight parallel foil conductors. As a result, the magnetic field is everywhere parallel to the conducting layers. The curvature, edge, and end effects are neglected. This equation takes into account both the skin and proximity effects. Dowell's equation derived for foil conductor was adapted to other shapes of winding conductors, such as rectangular, square, and round conductors. In

reality, the magnetic field exhibits also perpendicular or circumferential component in addition to the parallel component, whose distribution requires a 2-D analysis. The magnitude of the perpendicular component depends on many factors such as the distance between the turns, the actual geometry of the winding, the distance between the layers, and the number of layers and turns.

From Dowell's equation, the ac-to-dc winding resistance ratio for the solid-round-wire winding at the n-th harmonic frequency is [14], [15], [16], [30]

$$F_{Rn} = \frac{R_{wn}}{R_{wdc}} = \sqrt{n}A\left[\frac{\sinh\left(2\sqrt{n}A\right) + \sin\left(2\sqrt{n}A\right)}{\cosh\left(2\sqrt{n}A\right) - \cos\left(2\sqrt{n}A\right)} + \frac{2(N_l^2 - 1)}{3}\frac{\sinh\left(\sqrt{n}A\right) - \sin\left(\sqrt{n}A\right)}{\cosh\left(\sqrt{n}A\right) + \cos\left(\sqrt{n}A\right)}\right] \tag{7.9}$$

where the variable A (which is the effective diameter of the solid-round-wire winding) is given by [14]

$$A = \left(\frac{\pi}{4}\right)^{0.75}\frac{d}{\delta_w}\sqrt{\eta}. \tag{7.10}$$

Fig. 7.2 shows F_{R5}, R_{w5}, and R_{wdc} of the solid-round-wire winding at 5-th harmonic frequency as functions of d for the eight-layer inductor ($N_l = 8$), the fundamental frequency $f = 100$ kHz, the length of the round wire $l_w = 8$ m, and the porosity factor $\eta = d/p = 0.9$. Observe that the winding ac resistance at the 5-th harmonic frequency $R_{w5} = F_{R5}R_{wdc}$ has a local minimum. It can be shown that as the number of harmonic n increases, the local minimum of the winding ac resistance occurs at lower solid-round wire diameter d. Note that the winding ac resistance always exhibit a local minimum.

The expression for the normalized winding ac resistance at the n-th harmonic frequency determined from Dowell's equation (at a fixed frequency of fundamental component, i.e., at a fixed δ_w) is

$$F_{rn} = \frac{F_{Rn}}{\left(\frac{d}{\delta_w}\right)^2} = \frac{R_{wn}}{\frac{4\rho_w l_w}{\pi\delta_w^2}}$$

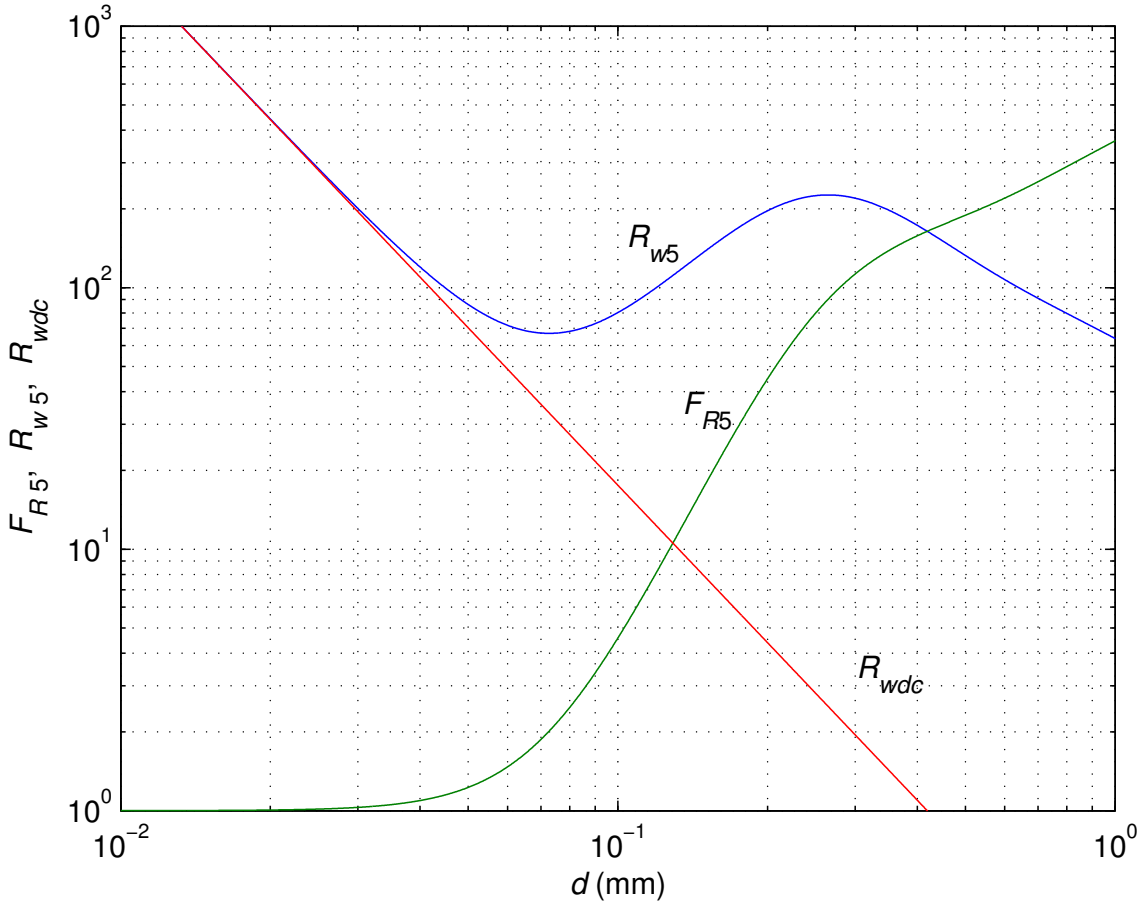

Figure 7.2: Plots of F_{R5}, R_{w5}, and R_{wdc} of the solid-round-wire winding at 5-th harmonic frequency as functions of solid-round wire diameter d for the eight-layer inductor ($N_l = 8$), the fundamental frequency $f = 100$ kHz, the length of the round wire $l_w = 8$ m, and the porosity factor $\eta = d/p = 0.9$.

$$= \frac{\left(\frac{\pi}{4}\right)^{0.75}\sqrt{n\eta}}{\frac{d}{\delta_w}}\left[\frac{\sinh\left(2\sqrt{n}A\right)+\sin\left(2\sqrt{n}A\right)}{\cosh\left(2\sqrt{n}A\right)-\cos\left(2\sqrt{n}A\right)}+\frac{2(N_l^2-1)}{3}\frac{\sinh\left(\sqrt{n}A\right)-\sin\left(\sqrt{n}A\right)}{\cosh\left(\sqrt{n}A\right)+\cos\left(\sqrt{n}A\right)}\right]. \tag{7.11}$$

Fig. 7.3 shows the normalized ac resistance at the n-th harmonic frequency F_{rn} of the solid-round-wire winding as a function of d for the eight-layer inductor ($N_l = 8$) at the fundamental frequency $f = 100$ kHz ($n = 1$), the higher harmonic order $n = 5,\ 20,\ 50,\ 100$, and the porosity factor $\eta = d/p = 0.9$. Observe that as the wire diameter of the inductor increases, the normalized winding ac resistance F_{rn} first decreases, reaches a local minimum, then increases, reaches a local maximum,

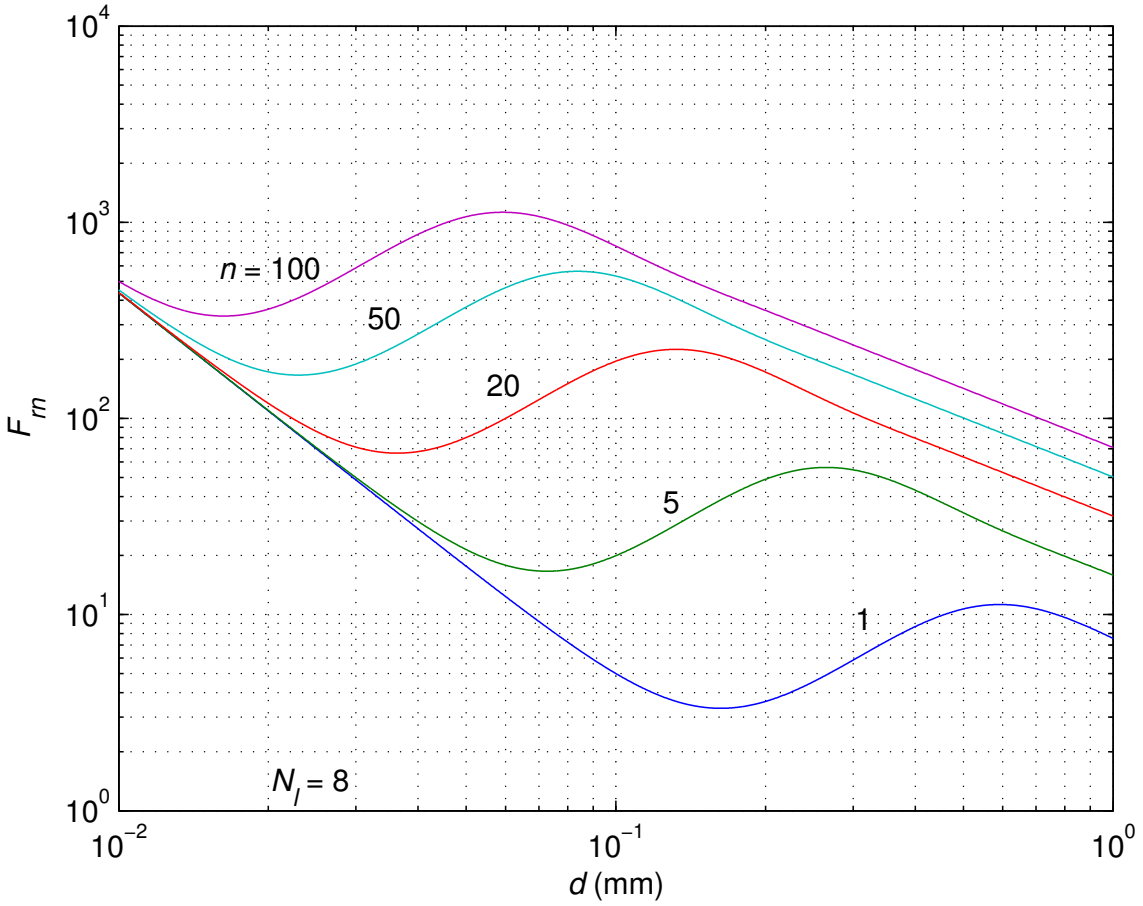

Figure 7.3: Normalized winding ac resistance at the n-th harmonic frequency F_{rn} of the solid-round-wire winding as a function of d for the eight-layer inductor ($N_l = 8$) at fundamental frequency $f = 100$ kHz ($n = 1$), the higher harmonic order $n = 5,\ 20,\ 50,\ 100$, and the porosity factor $\eta = d/p = 0.9$.

and finally decreases. It can be seen that the normalized winding ac resistance at the n-th harmonic frequency increases as the order of the harmonic current increases. Note also that for different harmonic orders, the normalized winding ac resistance of the multi-layer inductor exhibits a local minimum at different wire diameters.

Even though Dowell's equation describes the winding resistance for the n-th harmonic in a wide frequency range taking into account skin and proximity effects, it is impossible to use it in analytical optimization of total winding power loss. This is because Dowell's equation contains trigonometric and hyperbolic functions. Therefore, to perform analytical optimization, the approximations of (7.11) are used in the

subsequent sections.

7.3 Low- and Medium-Frequency Approximation of Dowell's Equation for Harmonics

For low and medium frequencies, the ac-to-dc winding resistance ratio of the solid-round wire inductor winding at the n-th harmonic frequency can be approximated by (Appendix 9.4)

$$F_{RLMFn} = \frac{R_{wn}}{R_{wdc}} = 1 + \frac{n^2(5N_l^2 - 1)}{45} A^4 = 1 + \frac{\left(\frac{\pi}{4}\right)^3 \eta^2 n^2 (5N_l^2 - 1)}{45} \left(\frac{d}{\delta_w}\right)^4. \quad (7.12)$$

Fig. 7.4 shows plots of a Dowell's ac-to-dc winding resistance ratio F_{R5} and low- and medium-frequency approximation F_{RLMF5} at 5-th harmonic frequency as functions of effective solid-round wire diameter A for the eight-layer inductor ($N_l = 8$) at the porosity factor $\eta = 0.9$. It can be seen that the approximation of the Dowell's ac-to-dc winding resistance ratio for the eight-layer inductor ($N_l = 8$) is valid at low- and medium-frequency range.

The approximate normalized winding ac resistance of the solid-round wire inductor winding with any number of layers N_l and for the n-th harmonic is given by

$$F_{rLMFn} = \frac{F_{RLMFn}}{\left(\frac{d}{\delta_w}\right)^2} = \frac{1}{\left(\frac{d}{\delta_w}\right)^2} + \frac{\left(\frac{\pi}{4}\right)^3 \eta^2 n^2 (5N_l^2 - 1)}{45} \left(\frac{d}{\delta_w}\right)^2. \quad (7.13)$$

Fig. 7.5 shows plots of Dowell's normalized winding ac resistance F_{r5} in (7.11) and low- and medium-frequency approximation F_{rLMF5} in (7.13) at 5-th harmonic frequency as functions of effective solid-round wire diameter A for the eight-layer inductor ($N_l = 8$) at the porosity factor $\eta = 0.9$. Assuming a constant skin depth δ_w, i.e., a constant frequency, the approximate normalized solid-round-wire winding ac resistance F_{rLMF5} at the n-th harmonic frequency ($n = 5$) decreases with increasing wire diameter, reaches a local minimum value, and then increases. Observe that the approximation captures the minimum of Dowell's normalized winding ac resistance

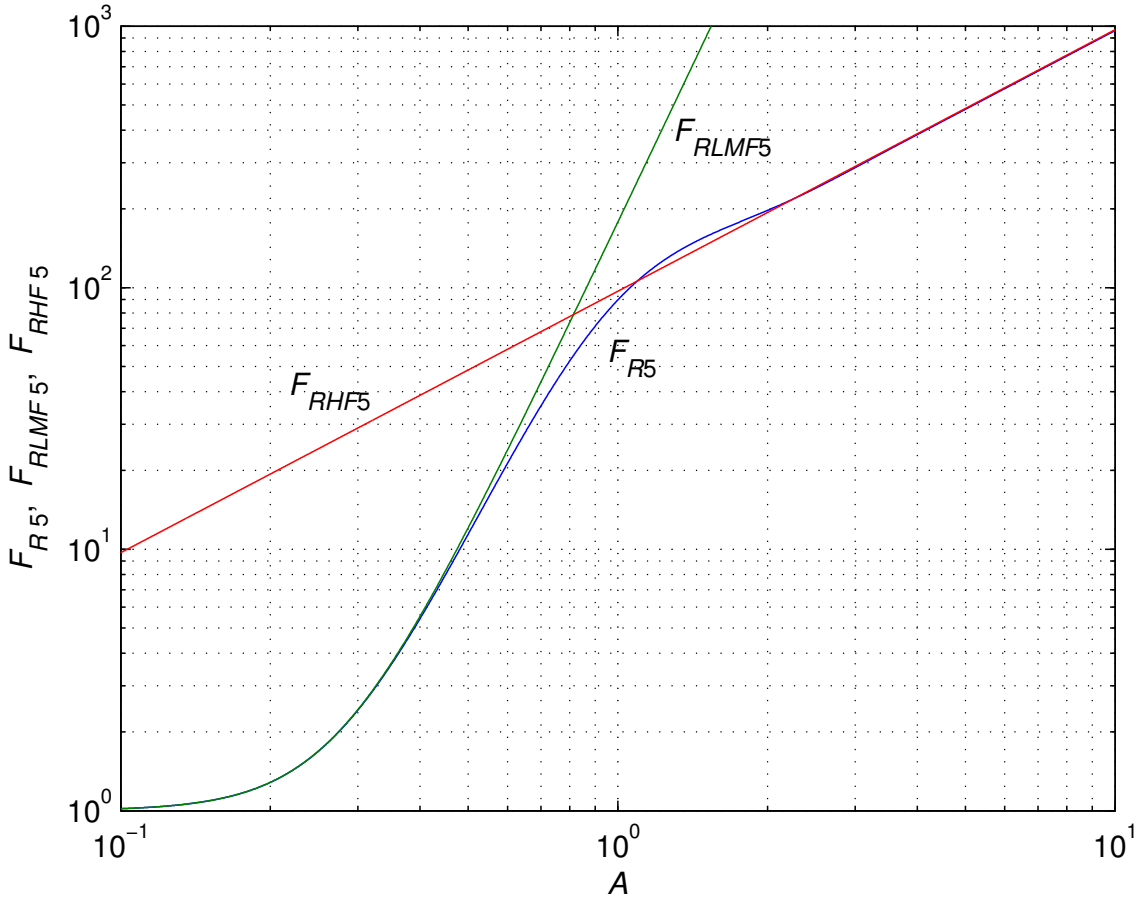

Figure 7.4: Plots of F_{R5}, F_{RLMF5}, and F_{RHF5} as functions of A for the eight-layer inductor ($N_l = 8$) and the porosity factor $\eta = d/p = 0.9$.

with very high accuracy. The derived eq. (7.13) is used in total winding power loss minimization.

Substituting (7.13) into (7.4), one obtains the approximate total winding power loss for the multi-layer solid-round-wire winding inductors conducting both the dc and ac non-sinusoidal periodic currents

$$P_w = \frac{4\rho_w l_w I_{DC}^2}{\pi\delta_w^2}\left[\frac{1}{\left(\frac{d}{\delta_w}\right)^2} + \sum_{n=1}^{\infty}\gamma_n^2 F_{rn}\right]$$

$$\approx \frac{4\rho_w l_w I_{DC}^2}{\pi\delta_w^2}\left\{\frac{1}{\left(\frac{d}{\delta_w}\right)^2} + \sum_{n=1}^{\infty}\gamma_n^2\left[\frac{1}{\left(\frac{d}{\delta_w}\right)^2} + \frac{\left(\frac{\pi}{4}\right)^3 n^2\eta^2(5N_l^2-1)d^2}{45\delta_w^2}\right]\right\}. \qquad (7.14)$$

Hence, the normalized total winding power loss of the multi-layer solid-round-wire

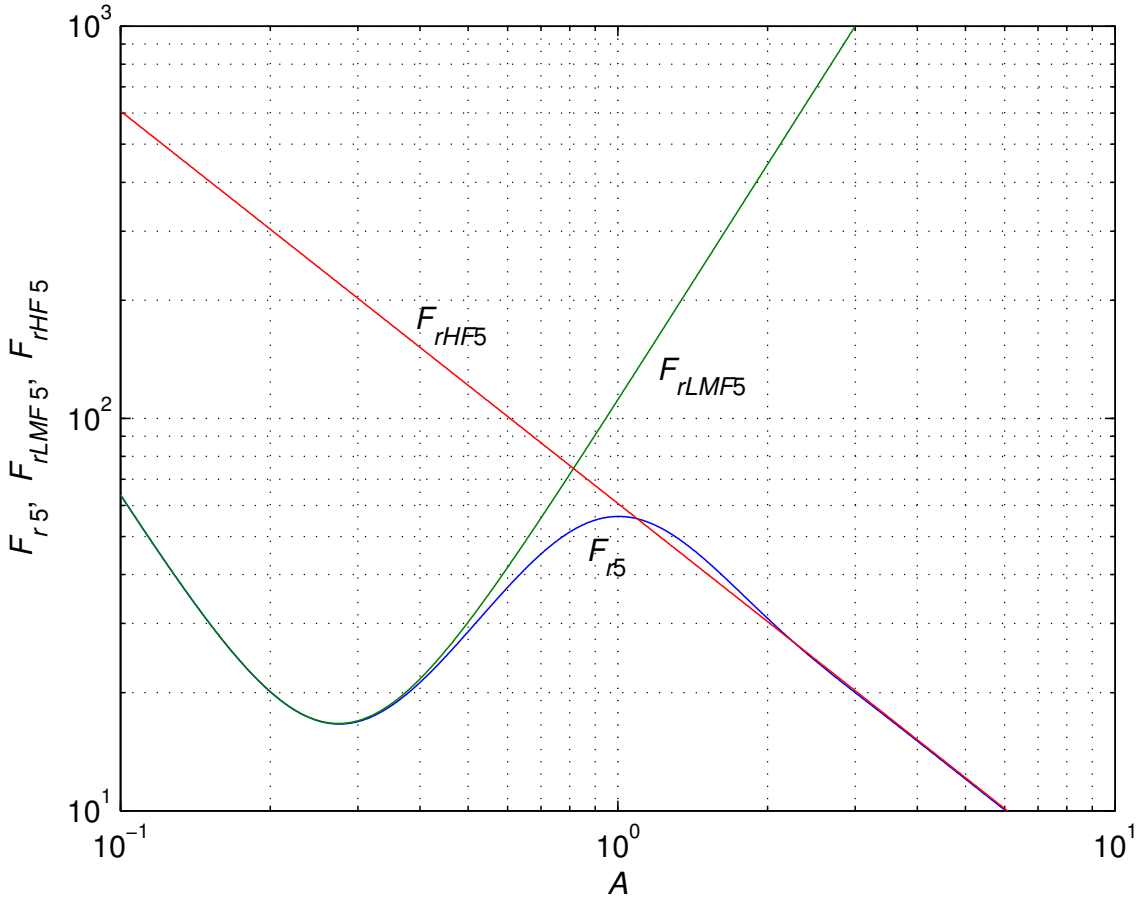

Figure 7.5: Plots of F_{r5}, F_{rLMF5}, and F_{rHF5} as functions of A for the eight-layer inductor ($N_l = 8$) and the porosity factor $\eta = d/p = 0.9$.

windings at a fixed frequency (i.e., a fixed δ_w) can be written as

$$P_{wnor} = \frac{P_w}{\frac{4\rho_w l_w I_{DC}^2}{\pi\delta_w^2}} = \frac{P_w}{P_\delta} = \frac{1}{\left(\frac{d}{\delta_w}\right)^2} + \sum_{n=1}^{\infty} \gamma_n^2 F_{rn}$$

$$\approx \frac{1}{\left(\frac{d}{\delta_w}\right)^2} + \sum_{n=1}^{\infty} \gamma_n^2 \left[\frac{1}{\left(\frac{d}{\delta_w}\right)^2} + \frac{\left(\frac{\pi}{4}\right)^3 n^2\eta^2(5N_l^2 - 1)}{45} \left(\frac{d}{\delta_w}\right)^2 \right] \tag{7.15}$$

where the dc power loss of the solid-round wire winding of the conductor diameter δ_w is

$$P_\delta = \frac{4\rho_w l_w I_{DC}^2}{\pi\delta_w^2}. \tag{7.16}$$

The optimization of the multi-layer solid-round-wire windings at a fixed frequency (i.e., a fixed δ_w) can be achieved by taking the derivative of (7.15) with respect to

d/δ_w and equating the result to zero

$$\frac{dP_{wnor}}{d\left(\frac{d}{\delta_w}\right)} = -\frac{1}{\left(\frac{d}{\delta_w}\right)^3}\left(1+\sum_{n=1}^{\infty}\gamma_n^2\right) + \frac{\left(\frac{\pi}{4}\right)^3\eta^2(5N_l^2-1)}{45}\left(\frac{d}{\delta_w}\right)\sum_{n=1}^{\infty}n^2\gamma_n^2 = 0. \quad (7.17)$$

Solution of this equation produces the normalized total-power-valley diameter of a solid-round-wire winding at which the local minimum of total winding power loss for the multi-layer inductor operating under dc and ac non-sinusoidal periodic currents occurs

$$\frac{d_{vt}}{\delta_w} = \frac{1}{\left(\frac{\pi}{4}\right)^{0.75}\sqrt{\eta}}\sqrt[4]{\frac{45(1+\sum_{n=1}^{\infty}\gamma_n^2)}{(5N_l^2-1)\sum_{n=1}^{\infty}n^2\gamma_n^2}} = k_o k_w \quad (7.18)$$

where the normalized solid-round wire valley diameter of the winding conducting only the fundamental component of the inductor current is [84]

$$k_o = \frac{d_v}{\delta_w} = \frac{1}{\left(\frac{\pi}{4}\right)^{0.75}\sqrt{\eta}}\sqrt[4]{\frac{45}{(5N_l^2-1)}} \quad (7.19)$$

d_v is the valley diameter of the solid-round-wire winding [84], and the inductor current waveform factor is

$$k_w = \sqrt[4]{\frac{1+\sum_{n=1}^{\infty}\gamma_n^2}{\sum_{n=1}^{\infty}n^2\gamma_n^2}}. \quad (7.20)$$

As the number of layers N_l increases, the normalized total-power-valley wire diameter decreases. Moreover, the normalized total-power-valley wire diameter increases as the RMS ac current at the n-th harmonic frequency normalized with respect to the dc current γ_n decreases. It can be shown that the normalized total-power-valley wire diameter decreases as the number of significant harmonic currents increases.

Substituting (7.18) into (7.12), and the obtained result into (7.4), one obtains the total winding power loss at the local minimum (valley) for the solid-round-wire windings

$$P_{wvt} = P_{wdc}\left(1+\sum_{n=1}^{\infty}F_{Rn}\gamma_n^2\right)$$

$$= P_{wdc}\left[1+\sum_{n=1}^{\infty}\gamma_n^2\left(1+\frac{\left(\frac{\pi}{4}\right)^3\eta^2n^2(5N_l^2-1)}{45}\frac{45(1+\sum_{n=1}^{\infty}\gamma_n^2)}{\left(\frac{\pi}{4}\right)^3\eta^2(5N_l^2-1)\sum_{n=1}^{\infty}n^2\gamma_n^2}\right)\right]$$

$$= 2P_{wdc}\left(1+\sum_{n=1}^{\infty}\gamma_n^2\right) = \frac{\eta\rho_w l_w I_{DC}^2}{\delta_w^2}\sqrt{\frac{(5N_l^2-1)\sum_{n=1}^{\infty}n^2\gamma_n^2(1+\sum_{n=1}^{\infty}\gamma_n^2)}{45\pi}}. \quad (7.21)$$

In general, the local minimum of the total winding power loss P_{wvt} depends on the dc current and the RMS ac current at the n-th harmonic frequency normalized with respect to the dc current $\gamma_n^2 = (I_n/I_{DC})^2$. In particular, the local minimum of the total power loss P_{wvt} is proportional to the square of the dc current I_{DC}^2, the number of layers N_l, the length of the winding conductor l_w, and the skin depth of the winding conductor.

When the dc current is much grater than the RMS of the fundamental, the local minimum (valley) of the total winding power loss does not exists and the total winding power loss is approximately equal to the winding dc power loss. This situation is typical for PWM dc-dc converters operating in continuous conduction mode CCM. When the dc current is approximately equal or smaller than the fundamental the local minimum (valley) exists and it depends on the number of layers N_l. This situation is typical for PWM dc-dc converters operating in discontinuous conduction mode DCM.

Using the least square mean method [85], the minimum value of the fundamental RMS ac current normalized with respect to the dc current above which the local optimum of the total winding power loss exists is given by

$$\gamma_{1(min)} = \frac{I_1}{I_{DC}} = \frac{4.9782}{N_l^4} + 0.0233. \quad (7.22)$$

7.4 High-Frequency Approximation of Dowell's Equation for Harmonics

The approximate Dowell's equation for the solid-round-wire windings for the n-th harmonic at high frequencies is given by (Appendix 9.5)

$$F_{RHFn} = \frac{R_{wn}}{R_{wdc}} = \sqrt{n}A\frac{(2N_l^2+1)}{3} = \left(\frac{\pi}{4}\right)^{0.75}\frac{\sqrt{\eta n}(2N_l^2+1)}{3}\frac{d}{\delta_w}. \quad (7.23)$$

The high-frequency normalized winding ac resistance of the solid-round-wire winding at n-th harmonic frequency is

$$F_{rHFn} = \frac{F_{rHFn}}{\left(\frac{d}{\delta_w}\right)^2} = \left(\frac{\pi}{4}\right)^{0.75} \frac{\sqrt{\eta n}(2N_l^2+1)}{3} \left(\frac{\delta_w}{d}\right). \tag{7.24}$$

Fig. 7.4 shows plots of Dowell's ac-to-dc winding resistance ratio F_{R5} and high-frequency approximation F_{RHF5} at 5-th harmonic frequency as functions of effective solid-round wire diameter A for the eight-layer inductor ($N_l = 8$) at the porosity factor $\eta = d/p = 0.9$. It can be seen that approximation of the Dowell's ac-to-dc resistance ratio for the eight-layer inductor ($N_l = 8$) is valid at high-frequency range, where the Dowell's ac-to-dc winding resistance ratio is proportional to d.

Fig. 7.5 shows plots of Dowell's normalized winding ac resistance F_{r5} in (7.11) and high-frequency normalized winding ac resistance at 5-th harmonic frequency F_{rHF5} as functions of effective solid-round wire diameter A for the eight-layer inductor ($N_l = 8$) at the porosity factor $\eta = 0.9$. It can be seen that the high-frequency normalized winding ac resistance at 5-th harmonic frequency is valid in the range, where the normalized winding ac resistance in (7.11) decreases, below the local minimum of normalized winding ac resistance.

The approximate high-frequency total winding power loss is

$$P_{wHF} \approx P_{wdc}\left(1+\sum_{n=1}^{\infty}\gamma_n^2 F_{RHFn}\right) \approx P_{wdc}\left[1+\left(\frac{\pi}{4}\right)^{0.75}\sqrt{\eta}\frac{2N_l^2+1}{3}\left(\frac{d}{\delta_w}\right)\sum_{n=1}^{\infty}\sqrt{n}\gamma_n^2\right]$$

$$\approx \frac{4\rho_w l_w I_{DC}^2}{\pi\delta_w^2}\left[\frac{1}{\left(\frac{d}{\delta_w}\right)^2}+\frac{\left(\frac{\pi}{4}\right)^{0.75}\sqrt{\eta}(2N_l^2+1)\delta_w}{3d}\sum_{n=1}^{\infty}\sqrt{n}\gamma_n^2\right]. \tag{7.25}$$

Referring to Fig. 7.1, it can be seen that there is the solid-round wire diameter range, for $d \gg d_{vt}$, where the total winding power loss is equal or lower than the total winding power loss at the local minimum. The diameter of the solid-round wire at which the total winding power loss is equal to the total winding power loss at the local minimum is called the total-power-critical diameter d_{crt}, where $d_{crt} \gg d_{vt}$.

Equating the total winding loss at the local minimum given in (7.21) with the approximate high-frequency total winding power loss given in (7.25) and solving for d, one obtains the normalized total-power-critical wire diameter for solid-round-wire windings given by

$$\frac{d_{crt}}{\delta_w} = \frac{\sqrt{2.5}(2N_l^2+1)\sum_{n=1}^{\infty}\sqrt{n}\gamma_n^2}{\pi^{\frac{3}{4}}\sqrt{\eta(5N_l^2-1)\sum_{n=1}^{\infty}n^2\gamma_n^2(1+\sum_{n=1}^{\infty}\gamma_n^2)}}$$
$$+\frac{\sqrt{45\left(2N_l^2+1\right)^2\left(\sum_{n=1}^{\infty}\sqrt{n}\gamma_n^2\right)^2+72\sqrt{45(5N_l^2-1)\sum_{n=1}^{\infty}n^2\gamma_n^2(1+\sum_{n=1}^{\infty}\gamma_n^2)}}}{12\sqrt{\left(\frac{\pi}{4}\right)^{\frac{3}{2}}\eta(5N_l^2-1)\sum_{n=1}^{\infty}n^2\gamma_n^2(1+\sum_{n=1}^{\infty}\gamma_n^2)}}. \tag{7.26}$$

It can be shown that the normalized total-power-critical wire diameter increases as the number of layers in the winding increases. Moreover, the total-power-critical wire diameter increases as the number of significant harmonics increase and as the RMS ac current at the n-th harmonic frequency normalized with respect to the dc current γ_n increase.

7.5 Inductor Design

In this section, the inductor with a local minimum of total winding power losses P_{wvt} was designed. The inductor was used in the PWM dc-dc buck converter, operating in the discontinuous conduction mode (DCM). The buck converter specifications were as follows: input voltage $V_I = 373$ V, output voltage $V_O = 85$ V, output current $I_O = 0.3$ A, and switching frequency $f_s = 40$ kHz. In the design, the efficiency of the buck converter was assumed to be $\eta_{conv} = 0.97$ and the dwell-duty cycle was assumed to be $D_w = 0.4$.

For these parameters, the output power is

$$P_O = V_O I_O = 25.5 \text{ W}. \tag{7.27}$$

The load resistance is

$$R_L = \frac{V_O}{I_O} = \frac{85}{0.3} = 283.3\ \Omega. \tag{7.28}$$

The dc voltage transfer function is

$$M_{VDC} = \frac{V_O}{V_I} = \frac{85}{120} = 0.2277. \tag{7.29}$$

The inductance of the designed buck converter operating in DCM with the required dwell-duty cycle is [14], [54]

$$L = \frac{\eta_{conv} R_L (1 - M_{VDC})(1 - D_w)^2}{2 f_s} = \frac{0.97 \times 283.3 \times (1 - 0.253) \times (1 - 0.25)^2}{2 \times 40 \times 10^3}$$

$$= 955.18 \ \mu\text{H}. \tag{7.30}$$

Selecting the inductance $L = 952$ μH, the MOSFET on-duty cycle is [54]

$$D = \sqrt{\frac{2 f_s L M_{VDC}^2}{\eta_{conv} R_L (1 - M_{VDC})}} = \sqrt{\frac{2 \times 40 \times 10^3 \times 952 \times 10^{-6} \times 0.253^2}{0.97 \times 283.3 \times (1 - 0.253)}} = 0.1364. \tag{7.31}$$

and the diode on-duty cycle is [54]

$$D_1 = D \left(\frac{1}{M_{VDC}} - 1 \right) = 0.1364 \times \left(\frac{1}{0.2277} - 1 \right) = 0.4626 \tag{7.32}$$

The maximum inductor current is

$$I_{Lmax} = \Delta i_{Lmax} = \frac{D(V_I - V_O)}{f_s L} = \frac{0.1364 \times (373 - 85)}{40 \times 10^3 \times 952 \times 10^{-6}} = 1.0326 \text{ A}. \tag{7.33}$$

The maximum energy that can be stored in the magnetic field of the inductor is

$$W_m = \frac{1}{2} L I_{Lmax}^2 = \frac{1}{2} \times 952.47 \times 10^{-6} \times 1.0326^2 = 0.508 \text{ mJ}. \tag{7.34}$$

Assuming the core window utilization factor $K_u = 0.4$ [14], the peak of magnetic flux density $B_{pk} = 0.2$, and the maximum magnitude value of the current density $J_{m(max)} = 5$ A/mm^2, the core area product is

$$A_p = \frac{2 W_m}{K_u J_{m(max)} B_{pk}} = \frac{2 \times 0.508 \times 10^{-3}}{0.4 \times 5 \times 10^6 \times 0.2} = 0.2538 \text{ cm}^4. \tag{7.35}$$

The Magnetics 0R42616 ferrite gapped pot core with the gap length $l_g = 1$ mm and with the 00B261601 bobbin was chosen. According to the Magnetics pot core

catalogue [88], this core satisfies the minimum area product value with an $A_p = 0.39$ cm^4. The initial permeability of the core R material was $\mu_r = 2300 \pm 25\%$.

The parameters of the 0R42616 pot core and the bobbin were: the core cross-section area $A_c = 0.939$ cm^2, the length of the core $l_c = 3.76$ cm, the volume of the core $V_c = 3.53$ cm^3, the height of the bobbin window $E_b = 0.993$ cm, and the MTL $l_T = 5.3$ cm.

For the chosen core, the required number of winding turns is

$$N = \sqrt{\frac{(l_g + l_c/\mu_{rc})\, L}{\mu_0 A_c}} = \sqrt{\frac{(10^{-3} + 3.76 \times 10^{-2}/2300) \times 952 \times 10^{-6}}{4 \times \pi \times 10^{-7} \times 0.939 \times 10^{-4}}} \approx 90. \quad (7.36)$$

The cross-sectional area of the winding conductor is given by [14]

$$A_w = \frac{\pi d^2}{4} = \frac{I_m}{J_m}, \quad (7.37)$$

where $I_m = I_{Lm1}$ is the amplitude of the fundamental component of the inductor current and J_m is the magnitude value of the current density. Typical magnitudes of current density range from 1 to 5 A/mm^2 [14]. Using [15, eq. (21)], the amplitude of the fundamental component of the inductor current is $I_m = 0.4426$ A. Therefore, rearranging (7.37) for the maximum magnitude value of the current density $J_{m(max)} = 5$ A/mm^2, the minimum diameter of the winding conductor is

$$d_{min} = \sqrt{\frac{4I_m}{\pi J_{m(max)}}} = \sqrt{\frac{4 \times 0.4426}{\pi \times 5 \times 10^6}} \approx 0.336 \text{ mm}. \quad (7.38)$$

The nearest diameter to the calculated d_{min} is for AWG27 with the bare wire diameter $d = 0.36$ mm and the insulated wire diameter is $d_o = 0.409$ mm. The maximum number of turns in the inductor layer is

$$N_{tl} = \frac{E_b}{d_o} = \frac{9.93 \times 10^{-3}}{0.409 \times 10^{-3}} = 24.27 \approx 24. \quad (7.39)$$

Hence, the minimum number of inductor layers is

$$N_l = \frac{N}{N_{tl}} = \frac{90}{27} = 3.75 \approx 4. \quad (7.40)$$

Using (7.18), for the four-layer inductor ($N_l = 4$) at the porosity factor $\eta = d/p = 0.9$, the total-power-valley diameter of the inductor winding at which the local minimum of the winding power losses occur is $d_{vt} = 0.399$ mm. The closest gauge to the total-power-valley diameter is for AWG26 with $d = 0.405$ mm and $d_o = 0.452$ mm.

For the minimum magnitude value of the current density $J_{m(min)} = 1$ A/mm^2 [14], the maximum diameter of the winding conductor is

$$d_{max} = \sqrt{\frac{4I_m}{\pi J_{m(min)}}} = \sqrt{\frac{4 \times 0.4426}{\pi \times 10^6}} \approx 0.751 \text{ mm}. \tag{7.41}$$

The nearest diameter to the calculated d_{max} is for AWG21 with the bare wire diameter $d = 0.7229$ mm and the insulated wire diameter $d_o = 0.785$ mm.

The value of the fundamental RMS ac current normalized with respect to the dc current for the designed inductor is

$$\gamma_1 = \frac{I_1}{I_{DC}} = \frac{0.3129}{0.3093} = 1.0118. \tag{7.42}$$

Therefore, for the four-layer inductor, $\gamma_1 > \gamma_{1(min)} = 0.0427$ and the local optimum exists. Using (7.26), for the four-layer inductor ($N_l = 4$) conducting 100 harmonics at $\eta = d/p = 0.9$, the total-power-critical diameter of the inductor winding at which the total winding power loss is the same as this at the local minimum is $d_{crt} = 1.2$ mm. The closest gauge to the total-power-critical wire diameter is AWG16 with $d = 1.29$ mm and $d_o = 1.37$ mm. However, for the chosen core, it is impossible to wind the four-layer inductor with the total-power-critical solid-round wire diameter due to low available space in the winding window of the core bobbin.

Fig. 7.6 shows the total winding power loss P_w as a function of the converter output power P_O for three different dc input voltages $V_I = 353,\ 373$, and 393 V. It can be seen that the maximum winding power loss P_w occurs at the maximum output power $P_{Omax} = 25.5$ W and the input voltage $V_I = 393$ V. Fig. 7.7 shows the total

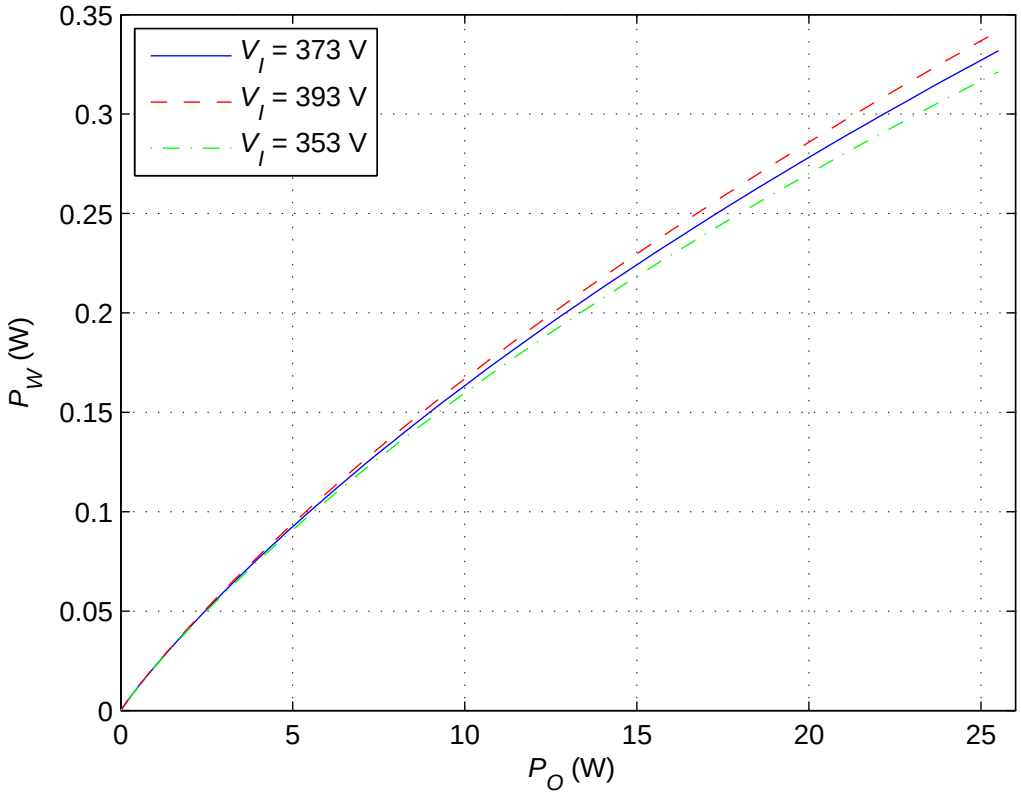

Figure 7.6: Plots total winding power losses P_w as a function of converter output power P_O of the designed inductor for the PWM dc-dc converter at three different input voltages $V_I = 353,\ 373$, and 393 V.

winding power loss P_w as a function of the converter dc input voltage V_I for three different converter output powers $P_O = 25.5,\ 10$, and 5 W. It can be seen that the total winding power loss P_w increases as the input dc voltage increases and that the total winding power loss is the highest for the maximum output power $P_o = 25.5$ W.

Fig. 7.8 shows the inductor current waveform factor k_w as a function of the output power P_O for the designed PWM dc-dc buck converter at $V_I = 373$ V. It can be seen that as the converter output power P_O increases, the inductor current waveform factor k_w also increases. Therefore, when the output power increases, the normalized total-power-valley diameter d_{vt}/δ_w increases. Observe that for the converter output power $P_O \approx 2.87$ W, the inductor current waveform factor is $k_w = 1$. According to (7.18),

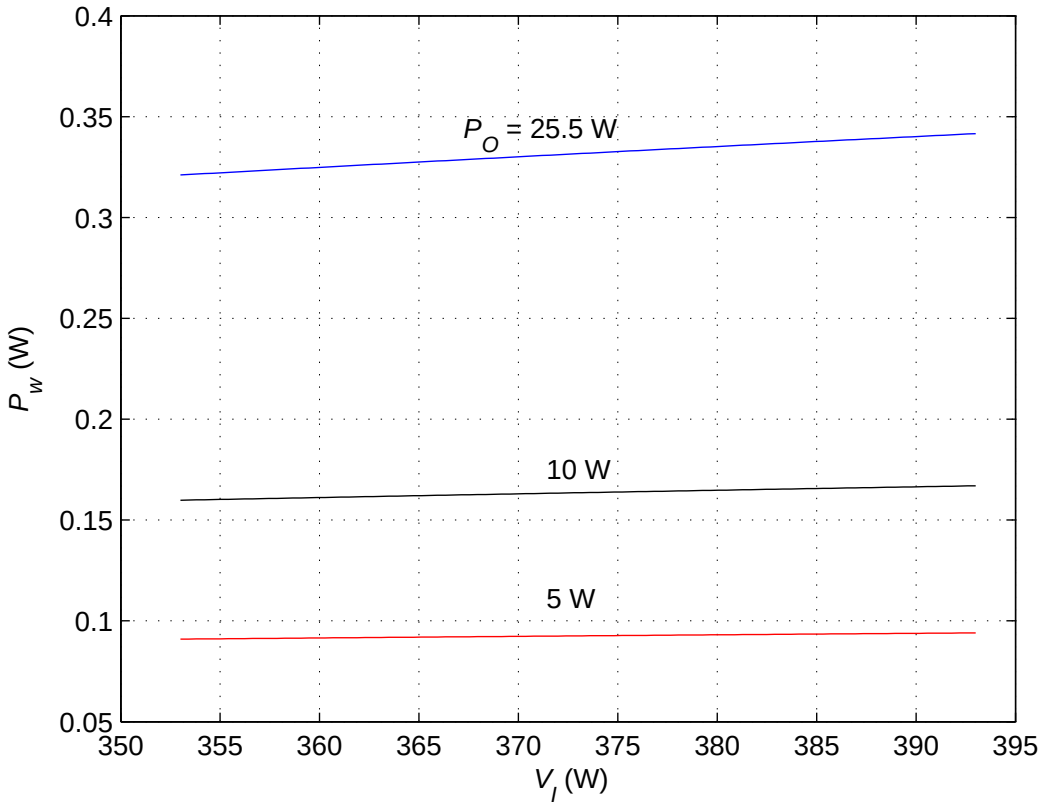

Figure 7.7: Plots total winding power lossesP_w as a function of converter input voltage V_I of the designed inductor for the PWM dc-dc converter at three different converter output powers $P_O = 25.5,\ 10$, and 5 W.

when the inductor current waveform factor k_w is equal to unity, the normalized total-power-valley diameter d_{vt}/δ_w is equal to the normalized valley diameter d_v of the solid-round-wire winding conducting only sinusoidal current [84]. Note that when the inductor current waveform factor k_w is less than unity ($k_w < 1$), the normalized total-power-valley diameter is lower than the normalized valley diameter d_v of the solid-round-wire winding conducting only sinusoidal current [84]. Fig. 7.9 shows the inductor current waveform factor k_w for the designed PWM dc-dc buck converter as a function of the dc input voltage V_I. It can be seen that as the input voltage increases the current waveform factor decreases and, therefore, the normalized total-power-valley diameter d_{vt}/δ_w decreases.

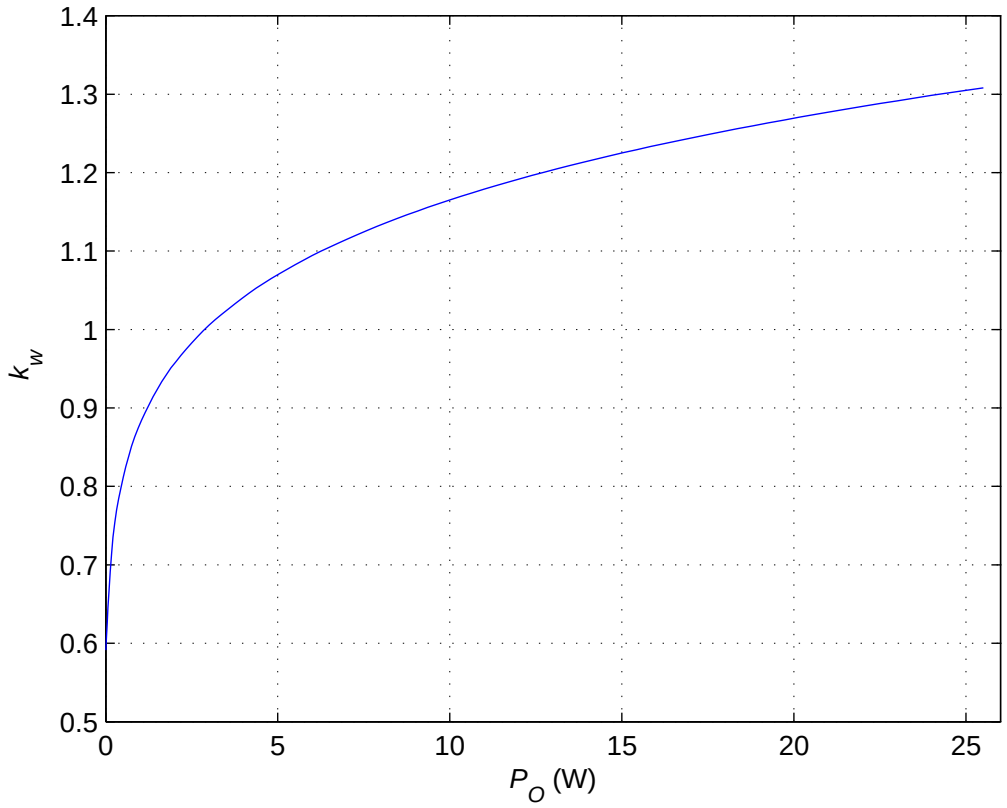

Figure 7.8: Inductor current waveform factor k_w as a function of the output power P_O for the designed PWM dc-dc buck converter at $V_I = 373$ V.

7.6 Experimental Verification

In this section, experimental verification of equations (7.4) and (7.18) is performed. For this purpose, 3 four-layer inductors ($N_l = 4$), wound with AWG26, AWG24, and AWG20 magnet wire have been build and measured. To achieve the required inductance $L \approx 952$ μH of the four-layer inductors wound with AWG24 and AWG20 at switching frequency $f_s = 40$ kHz, the gap length was varied. The inductor equivalent series resistance r (ESR) [4], [14], the self-inductance L, and first self-resonant frequency f_r were measured using the HP 4194A impedance/gain-phase analyzer with 16047D test fixture. Table 7.1 gives parameters of measured inductors.

Referring to the lumped parameter inductor model in [14, Fig. 9.2(b)], and ne-

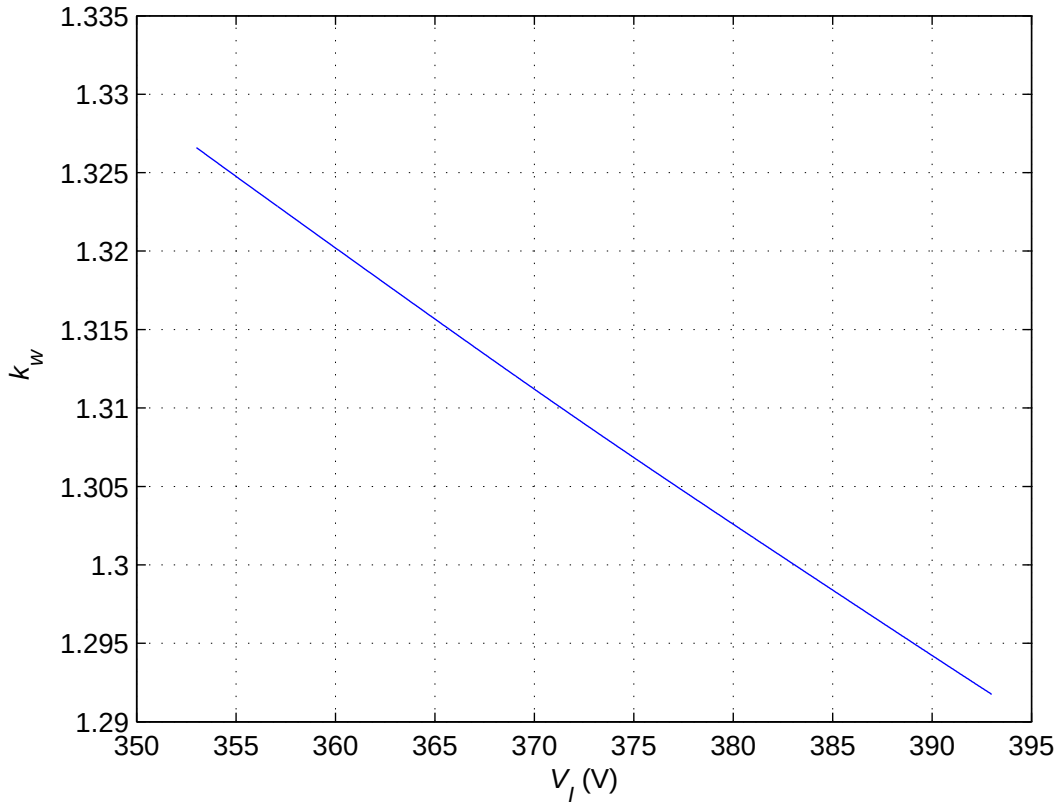

Figure 7.9: Inductor current waveform factor k_w as a function of the dc input voltage V_I for the designed PWM dc-dc buck converter at $P_O = 25.5$ W.

glecting the core resistance R_{cs}, the impedance of the inductor model is

$$Z = \frac{R_s}{(1-\omega^2 LC)^2 + (\omega C R_s)^2} + j\omega L \frac{1 - \omega^2 LC - \frac{CR_s^2}{L}}{(1-\omega^2 LC)^2 + (\omega C R_s)^2} = r + jx, \qquad (7.43)$$

Inductor Number #	American Wire Gauge	Number of Turns N	Capacitance C (pF)	Res. Freq. f_r (MHz)
1	26	88	13.13	1.425
2	24	70	13.75	1.392
3	20	44	25.41	1.087

Table 7.1: Parameters of designed and measured inductors.

where x is the equivalent series reactance, C is the parasitic self-capacitance of the inductor, and R_s is the total ac inductor series resistance. Neglecting the core losses, $R_s = R_w$.

To transform the measured equivalent series resistance r into the actual winding ac resistance, the following expression is used [4], [22]

$$R_s = R_{wn} = \frac{1 - \sqrt{1 - 4\omega^2 r^2 C^2 (1 - \omega^2 LC)^2}}{2r\omega^2 C^2}. \tag{7.44}$$

The first self-resonant frequency of the inductor is

$$f_r = \frac{\omega_r}{2\pi} = \frac{1}{2\pi\sqrt{LC}}. \tag{7.45}$$

For $f << f_r = 1/(2\pi\sqrt{LC})$ and $f << 1/(2\pi C R_s)$, $r \approx R_s$. Typically, for the frequencies from $0.4f_r$ to $2f_r$, $r > R_s$. For $f > 2f_r$, $r < R_s$.

Fig. 7.10 shows Dowell's and actual winding ac resistances for the four-layer inductor ($N_l = 4$) wound with the AWG26 solid-round wire. It can be seen that winding ac resistance given by Dowell's equation tracks actual inductor winding resistance with high accuracy.

The actual total winding power loss was obtained from measured winding dc and ac resistances. Fig. 7.11 shows the theoretical and actual total winding power loss of the designed inductor wound with an AWG26 round wire. It can be seen that the predicted minimum power winding losses exactly occurred for the AWG26 solid-round-wire winding.

From (7.4), the winding power loss per unit length due to the current in (7.1) is given by

$$P_{lw} = \frac{P_w}{l_w} = \frac{4\rho_w I_{DC}^2}{\pi d^2}\left(1 + \sum_{n=1}^{\infty} F_{Rn}\gamma_n^2\right) = \frac{4\rho_w I_{DC}^2}{\pi \delta_w^2}\left[\frac{1}{\left(\frac{d}{\delta_w}\right)^2} + \sum_{n=1}^{\infty}\gamma_n^2 F_{rn}\right]. \tag{7.46}$$

This equation is used to compare the winding power losses of the inductors with the same number of layers but wound with different wire gauge and, therefore, different

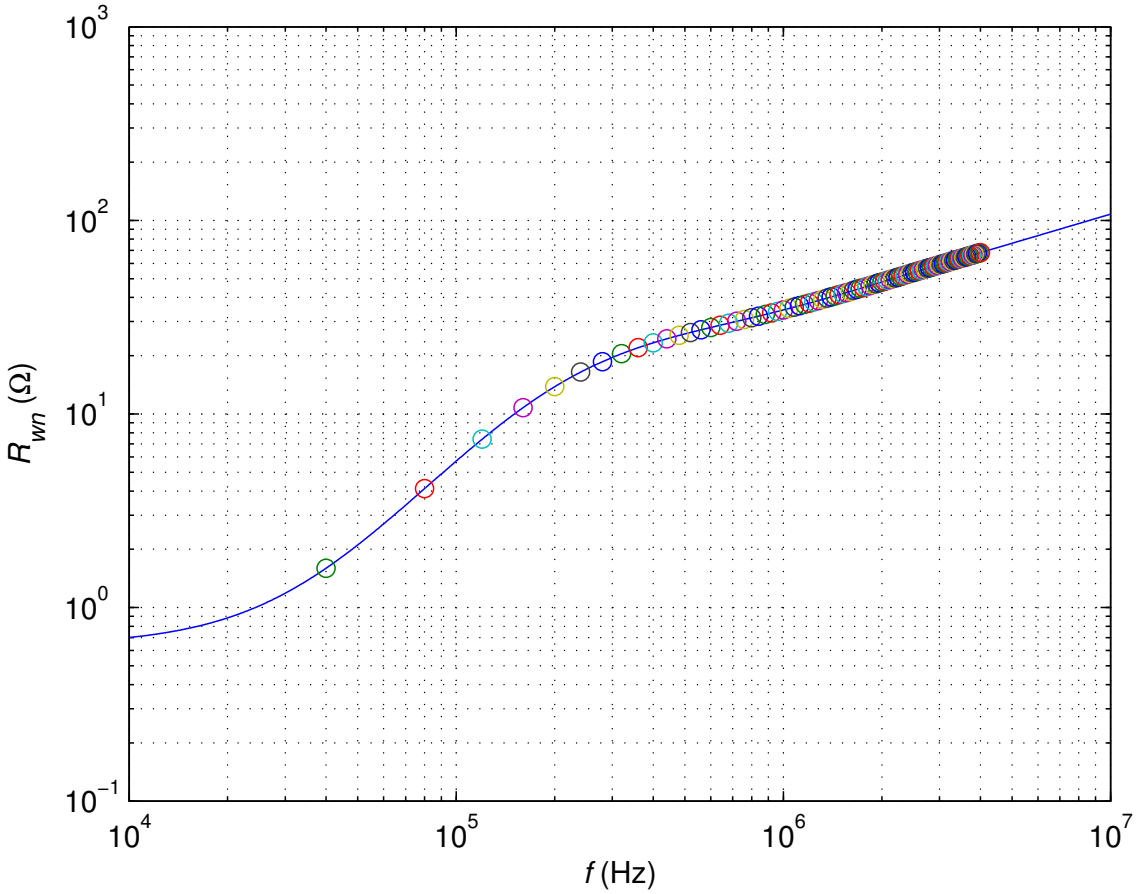

Figure 7.10: Plots of Dowell's winding ac resistance (solid line) and actual ac resistance (circles) as functions of frequency for the four-layer inductor ($N_l = 4$) wound with AWG26 operating in PWM dc-dc buck converter in DCM.

solid-round wire length l_w. Fig. 7.12 compares actual total winding power loss per unit length for inductors wound with AWG26, AWG24, and AWG20 round wire windings. Observe that the actual total winding power loss per unit length is the lowest for the inductor wound with AWG26 solid-round wire. It can be seen that the predicted total winding power loss per unit length accurately track the actual total winding power loss per unit length of inductors #1, #2, and #3.

7.7 Conclusion

In this chapter, analytical optimization of the solid-round-wire windings conducting both the dc and ac non-sinusoidal periodic currents has been performed. The normal-

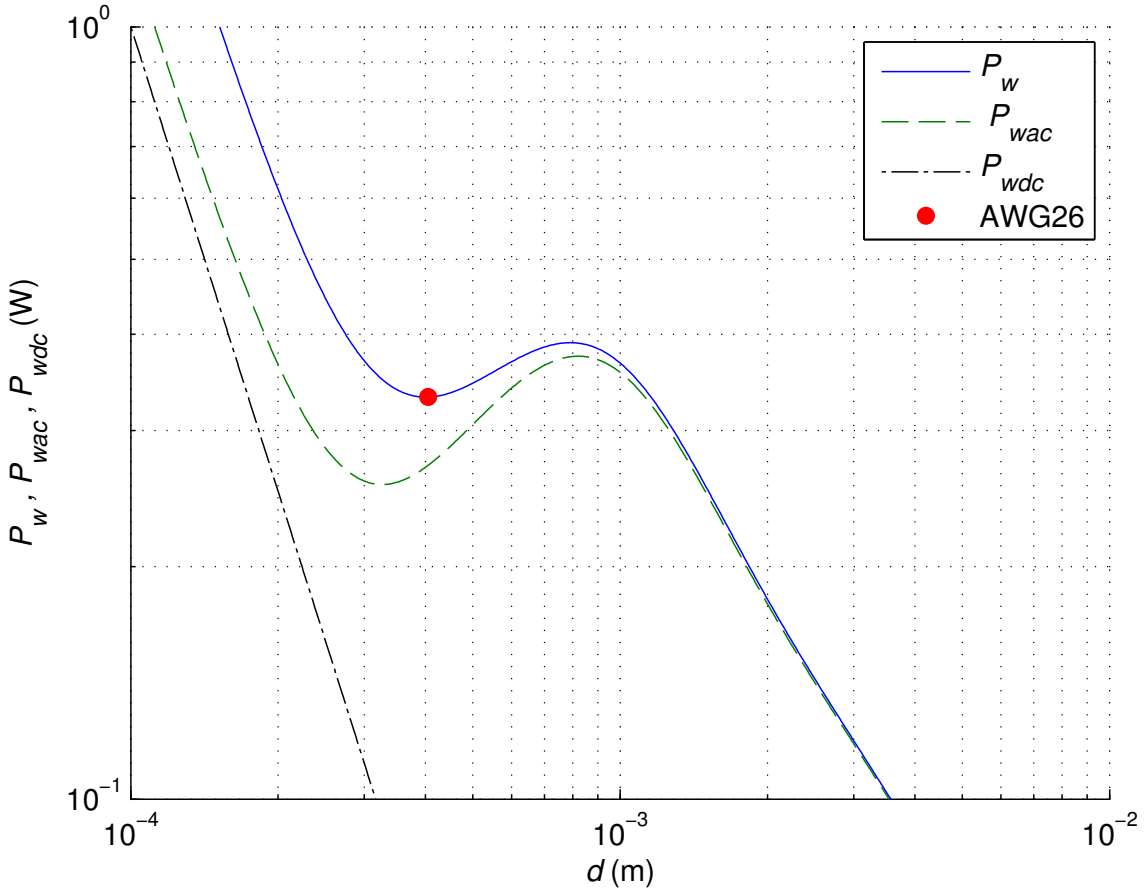

Figure 7.11: Plots of winding dc power loss P_{wdc}, winding ac power loss P_{wac} total power loss P_w, and actual total winding power loss for inductor wound with AWG26 round wire as function of diameter d for four-layer inductor ($N_l = 4$) of a winding conductor length $l_w = 4.664$ m operating in PWM dc-dc buck converter in DCM at full power.

ized total-power-valley wire diameter of the solid-round-wire windings at which the local minimum of the total winding power loss (dc and ac) occurs has been derived. The expression for the local minimum of the total winding power loss has been given. One of the contributions of this chapter is the minimization of winding power loss for PWM dc-dc converters operated in discontinuous conduction mode. Another contribution of this chapter to the discussion on the winding power loss minimization is that it shows that the local minimum of the total winding power loss does not always exist. This subjects have not been addressed yet in the literature.

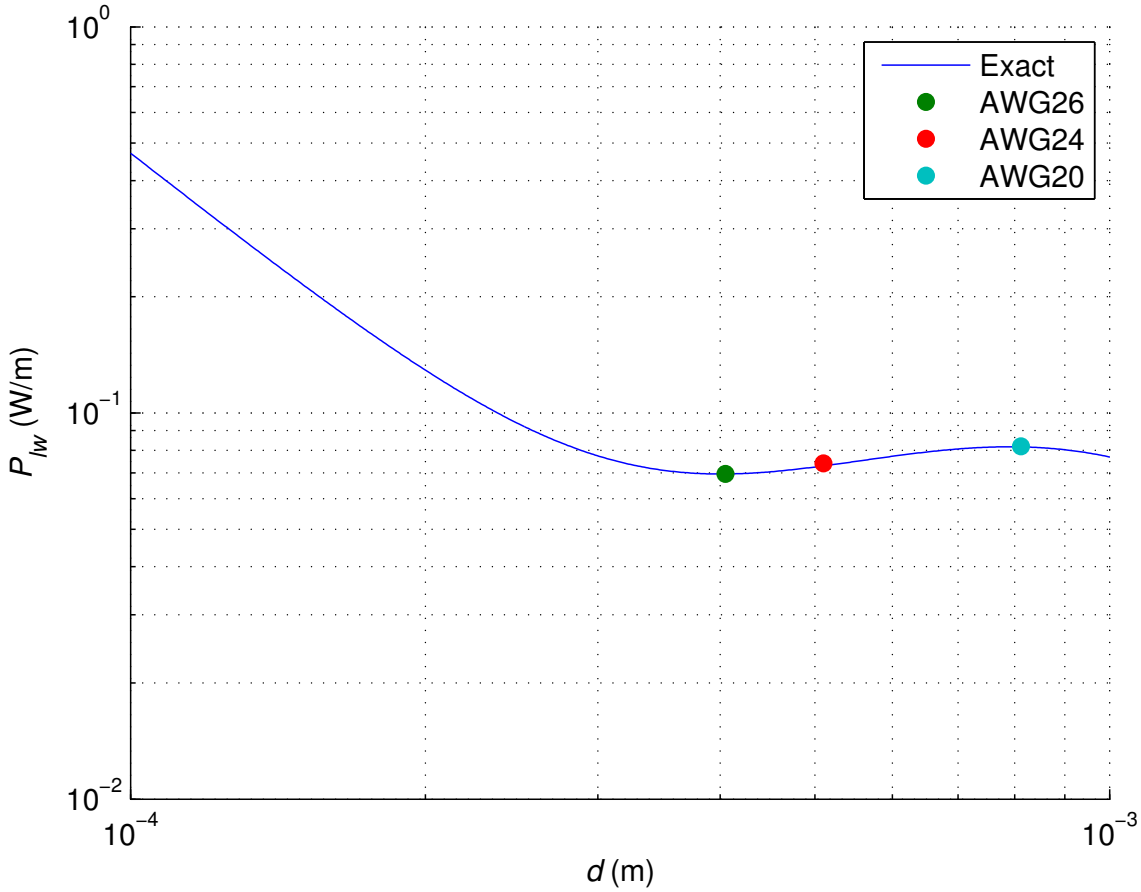

Figure 7.12: Plots of winding power loss per unit length (solid line) P_{lw}, and actual winding power loss per unit length (circles) as function of diameter d for inductors wound with AWG26, AWG24, and AWG20 round wire for four-layer inductor ($N_l = 4$) operating in PWM dc-dc buck converter in DCM at full power.

A low- and medium-frequency approximation of Dowell's equation for the ac-to-dc resistance ratio at the n-th harmonic frequency has been derived. The expressions for the normalized total-power-valley diameter and the local minimum of total winding power loss have been obtained using low- and medium-frequency approximation of the total winding power losses (dc and ac). It has been shown that the normalized total-power-valley diameter depends on the number of layers N_l and the fundamental frequency f of the current. As both the fundamental frequency and the number of winding layers increase, the normalized total-power-valley diameter decreases. This results in a lower cross-sectional area of the conductor and the higher magnitude of

the current density J_m.

The high-frequency approximation of Dowell's equation for the ac-to-dc winding resistance ratio at the n-th harmonic frequency has been derived. Based on the high-frequency ac-to-dc winding resistance ratio, the approximate high-frequency total winding power loss have been derived for windings conducting dc and ac non-sinusoidal periodic currents. Additionally, the normalized total-power-critical wire diameter of the solid-round-wire windings, at which total winding loss is equal to the total winding loss at the local minimum, has been given.

From the analysis performed in this chapter, the following main conclusions can be drawn:

- For the solid-round-wire winding conducting both the dc and ac non-sinusoidal periodic currents, the local minimum value of total winding power losses occurs at a larger solid-round wire diameter than that for the solid-round-wire winding conducting only ac non-sinusoidal periodic currents.

- As the number of significant harmonic currents flowing through the winding increases, the winding ac power loss and total winding power loss increase.

- The total-power-valley wire diameter at which the local minimum of the total winding losses (both dc and ac) occurs depends on the number of inductor winding layers N_l and it decreases as the number of layers increases.

- The total-power-valley wire diameter depends on the number of significant harmonic currents and it decreases as the number of significant harmonics n increases.

- The total-power-valley diameter increases the RMS ac current at the n-th harmonic frequency normalized with respect to the dc current γ_n decreases.

- The total-power-critical wire diameter increases as the number of layers in the inductor winding N_l increase.

- The total-power-critical wire diameter increases as the number of significant harmonics n flowing through the inductor winding increases.

- When the dc current is much grater than the RMS value of the fundamental, i.e., $\gamma_1 < \gamma_{1(min)}$ the local minimum of the total winding power loss does not exists and the total winding power loss is approximately equal to the winding dc power loss.

8 Conclusions

8.1 Summary

The winding resistance and the winding power loss of high-frequency power inductors has been addressed in this research. Using approximate equation for the ac-to-dc winding resistance ratio of the individual layer of the foil inductor the optimum foil thickness of each layer has been derived. Low- and medium-frequency approximation of Dowell's equation has been derived and used for optimization of foil thickness in the multi-layer foil windings conducting sinusoidal currents. The normalized valley foil thickness h_v/δ_w at which the global minimum of winding ac resistance occurs has been derived. The normalized hill foil thickness h_h/δ_w at which the local maximum of the winding ac resistance occurs has been given. It has been shown that for the windings made of the foil thickness larger than the hill thickness h_h the winding resistance remains constant. The low- and medium-frequency approximation of Dowell's equation for the foil winding has been adapted for the solid-round-wire winding conducting sinusoidal currents. It has been shown that the behavior of the winding ac resistance of the foil winding is different than the solid-round wire winding. Using low- and medium-frequency approximation of Dowell's equation analytical optimization of solid-round-wire winding has been performed. The equation for the normalized valley diameter d_v/δ_w, at which the local minimum of the winding ac resistance occurs, has been derived. The equation for the winding ac resistance at the valley R_{wv} (local minimum) has been also derived. Using least-square fitting method the normalized hill diameter d_h/δ_w of the solid-round-wire windings at which the local maximum of winding ac resistance occurs has been given. For the solid-round-wire winding, using high-frequency approximation of Dowell's equation along with the equation for the winding ac resistance at the valley R_{wv} (local minimum) the normalized critical wire diameter has been derived d_{cr}/δ_w. The winding ac resistance of the winding made

of gauge grater than the critical diameter, i.e., $d > d_{cr}$, is lower than that for the winding made of valley diameter d_v.

An approximate model and a modified Dowell's equation for litz-wire and multi-strand wire winding has been presented. The proposed model takes into account the proximity effect between strands within a litz-wire bundle as well as the proximity effect between the layers of the litz-wire bundles. For this model, Dowell's equation has been adapted, resulting in the analytical expressions for the ac-to-dc winding resistance ratio $F_{R(litz)}$ and winding ac resistance $R_{w(litz)}$ of litz-wire windings. The low- and medium-frequency approximation of litz-wire ac-to-dc winding resistance ratio has been given, expression for the litz-wire optimum strand diameter, and equation for the number of strands in litz-wire bundle at which minimum winding resistance is achieved has been derived. An example of a design procedure of litz-wire winding inductor has been presented. The equation for the winding ac resistance $R_{w(litz)}$ of litz-wire winding has been experimentally verified. The predicted results were in good agreement with the measured ones.

The minimization of the ac winding power loss and the total winding loss has been performed. Equations for the optimum foil winding thickness conducting harmonic currents and the optimum foil winding thickness conducting harmonic currents superimposed on the dc component have been derived. The low- and medium-frequency approximation of the normalized winding ac resistance has been used for ac winding power loss and total winding power loss optimizations. It has been shown that the optimum foil thickness for the foil inductor conducting only ac harmonic currents is lower than that conducting the same ac harmonic current superimposed on the dc component. The design of the optimum foil thickness inductor winding has been shown for the pulse-width modulated dc-dc converter in the discontinuous conduction mode. The presented theory has been verified with measurements. The theoretical results were in agreement with the measurements.

Analytical optimization of the solid-round-wire windings conducting both the dc and ac non-sinusoidal periodic currents has been performed. The normalized total-power-valley wire diameter of the solid-round-wire windings at which the local minimum of the total winding power loss (dc and ac) occurs has been derived. The expression for the local minimum of the total winding power loss has been given. One of the contributions of this research is the minimization of winding power loss for PWM dc-dc converters operated in discontinuous conduction mode. Another contribution of this research to the discussion on the winding power loss minimization is that it shows that the local minimum of the total winding power loss does not always exist. This subjects have not been addressed yet in the literature.

8.2 Contributions

The contributions of this dissertation are:

- Approximation of Dowell's equation has been derived.
- For the foil windings conducting sinusoidal currents:
  - Expression for the normalized valley thickness of the foil at which the global minimum of the winding ac resistance occurs has been derived.
  - Expression for the winding ac resistance at the valley (global minimum) has been derived.
- For the solid-round-wire windings conducting sinusoidal currents:
  - Expression for the normalized valley diameter d_v/δ_w at which the local minimum of winding ac resistance occurs has been derived.
  - Expression for the normalized hill diameter d_h/δ_w at which the local maximum of winding ac resistance occurs has been given.

  - Expression for the normalized critical diameter d_{cr}/δ_w, where $d_{cr} \gg d_v$, at which the winding ac resistance is the same as at the local minimum has been derived.

- For the litz-wire and multi-strand wire windings conducting sinusoidal currents:
  - The proposed approximate model and the modified Dowell's equation for litz-wire windings predicts the litz-wire winding resistance of the inductor.
  - A relatively simple equation for the winding resistance of litz-wire and multi-strand wire winding has been developed.
  - Expression for the optimum strand diameter has been derived.
  - Expression for the number of strands in the litz-wire bundle at which the minimum winding ac resistance is obtained has been derived.
  - A design of the inductor with optimized litz-wire winding has been shown.

- For the foil windings conducting non-sinusoidal periodic currents with and without dc offset:
  - Expression for the optimum foil thickness in order to achieve the minimum ac winding power loss of a foil inductor conducting ac harmonic currents has been derived.
  - Expression for the optimum foil thickness in order to achieve the minimum total winding power loss of foil inductor conducting both dc and ac harmonic currents has been derived.
  - Approximate expressions for the ac winding power loss of foil inductors at low and medium frequencies has been derived.
  - Approximate expressions for the total winding power loss of foil inductors at low- and medium-frequencies has been derived.

  - Design procedure for foil inductors with the optimum foil thickness for PWM dc-dc boost converter operating in DCM has been shown.

- For the solid-round-wire windings conducting non-sinusoidal periodic currents with dc offset:

  - Relationship among the fundamental current, the dc current, and the number of layers for which the local minimum of the total dc and ac solid-round-wire winding losses exists has been given.

  - Expression for the normalized total-power-valley wire diameter of the solid-round-wire windings, where the local minimum of the winding dc and ac power losses (valley) occurs has been derived.

  - Expression for the normalized total-power-critical wire diameter of the solid-round-wire windings (greater than the normalized total-power-valley wire diameter), where the winding dc and ac power losses are equal to the winding dc and ac power losses at the local minimum (valley) has been derived.

  - Design procedure of the solid-round wire inductor optimized for the minimum of winding dc and ac power losses for the PWM dc-dc buck converter operating in discontinuous conduction mode (DCM) has been given.

9 Appendices

9.1 Approximation of Dowell's Equation using Maclaurin's Serieses

Assuming function $f(x)$ that has derivatives of all orders at the point $x = a$ Taylor's series about the point $x = a$ is defined as

$$f(x) = \sum_{n=0}^{\infty} \frac{f^{(n)}(a)}{n!}(x-a)^n = f(a) + f'(a)(x-a) + \frac{f''(a)}{2!}(x-a)^2 + \frac{f'''(a)}{3!}(x-a)^3 + ... + \frac{f^{(n)}(a)}{n!}(x-a)^n. \tag{9.1}$$

Maclaurin's series for $f(x)$ is the Taylor's series for $f(x)$ about the point $x = 0$

$$f(x) = \sum_{n=0}^{\infty} \frac{f^{(n)}(0)}{n!}(x)^n = f(0) + f'(0)(x) + \frac{f''(0)}{2!}(x)^2 + \frac{f'''(0)}{3!}(x)^3 + ... + \frac{f^{(n)}(0)}{n!}(x)^n. \tag{9.2}$$

Below are given Maclaurin's series of the hyperbolic and trigonometric functions used in Dowell's equation

$$\sinh ax = \sum_{n=0}^{\infty} \frac{1}{(2n+1)!}(ax)^{2n+1} = ax + \frac{(ax)^3}{3!} + \frac{(ax)^5}{5!} + \frac{(ax)^7}{7!} + ... + \frac{1}{(2n+1)!}(ax)^{2n+1} \tag{9.3}$$

$$\sin ax = \sum_{n=0}^{\infty} \frac{(-1)^n}{(2n+1)!}(ax)^{2n+1} = ax - \frac{(ax)^3}{3!} + \frac{(ax)^5}{5!} - \frac{(ax)^7}{7!} + ... + \frac{(-1)^n}{(2n+1)!}(ax)^{2n+1} \tag{9.4}$$

$$\cosh(ax) = \sum_{n=0}^{\infty} \frac{1}{(2n)!}((ax))^{2n} = 1 + \frac{(ax)^2}{2!} + \frac{(ax)^4}{4!} + \frac{(ax)^6}{6!} + ... + \frac{1}{(2n)!}(ax)^{2n} \tag{9.5}$$

$$\cos(ax) = \sum_{n=0}^{\infty} \frac{(-1)^n}{(2n)!}((ax))^{2n} = 1 - \frac{(ax)^2}{2!} + \frac{(ax)^4}{4!} - \frac{(ax)^6}{6!} + ... + \frac{(-1)^n}{(2n)!}(ax)^{2n} \tag{9.6}$$

Taking into account only first three components of (9.3), (9.4), (9.5), (9.6) the skin-effect factor can be approximated by

$$F_S = \frac{\sinh(2x) + \sin(2x)}{\cosh(2x) - \cos(2x)} = \frac{2x + \frac{8x^3}{3!} + \frac{32x^5}{5!} + 2x - \frac{8x^3}{3!} + \frac{32x^5}{5!}}{1 + \frac{4x^2}{2!} + \frac{16x^4}{4!} - 1 + \frac{4x^2}{2!} - \frac{16x^4}{4!}}$$

$$= \frac{4x\left(1+\frac{16}{120}x^4\right)}{4x^2} = \frac{1}{x} + \frac{4}{30}x^3. \tag{9.7}$$

Taking into account only first two components of (9.3), (9.4), (9.5), (9.6) the proximity-effect factor can be approximated by

$$F_P = \frac{\sinh(x)-\sin(x)}{\cosh(x)+\cos(x)} = \frac{x+\frac{x^3}{3!}-x+\frac{x^3}{3!}}{1+\frac{x^2}{2!}+1-\frac{x^2}{2!}} = \frac{1}{6}x^3. \tag{9.8}$$

Therefore, substituting A instead of x in (9.7) and (9.8), Dowell's equation can be approximated by

$$F_R = A\left[\frac{\sinh(2A)+\sin(2A)}{\cosh(2A)+\cos(2A)} + \frac{2(N_l^2-1)}{3}\frac{\sinh(A)-\sin(A)}{\cosh(A)+\cos(A)}\right]$$

$$\approx A\left[\frac{1}{A} + \frac{4A^3}{30} + \frac{2(N_l^2-1)}{3}\frac{A^3}{6}\right] \approx 1 + \frac{10N_l^2+2}{90}A^4 \approx 1 + \frac{5N_l^2+1}{45}A^4. \tag{9.9}$$

However, in the research modified approximation of Dowell's equation [45] will be used, since it describes the winding resistance is wider frequency range. The modified equations is given by

$$F_{RLMF} = 1 + \frac{5N_l^2-1}{45}A^4. \tag{9.10}$$

9.2 Derivation of Low- and Medium-Frequency Approximation of Dowell's Equation for Foil Windings at Harmonic Frequency

The approximate equations for the ac-to-dc winding resistance ratio F_{RLMF} of the inductor conducting sinusoidal current is given by [45], [14], [69]

$$F_{RLMF} = \frac{R_{wLMF}}{R_{wdc}} \approx 1 + \frac{5N_l^2-1}{45}\left(\frac{h}{\delta_w}\right)^4. \tag{9.11}$$

Hence, the low- and medium-frequency winding ac resistance for the inductor conducting sinusoidal current is given by

$$R_{wLMF} = F_{RLMF}R_{wdc}$$

$$= \frac{\rho_w l_w}{b\delta_w\left(\frac{h}{\delta_w}\right)}\left[1+\frac{5N_l^2-1}{45}\left(\frac{h}{\delta_w}\right)^4\right] = \frac{\rho_w l_w}{b\delta_w}\left[\frac{1}{\left(\frac{h}{\delta_w}\right)} + \frac{5N_l^2-1}{45}\left(\frac{h}{\delta_w}\right)^3\right]. \tag{9.12}$$

The normalized winding ac resistance for the inductor conducting sinusoidal current is given by [14]

$$F_{rLMF} = \frac{F_{RLMF}}{\left(\frac{h}{\delta_w}\right)} \approx \frac{1}{\frac{h}{\delta_w}} + \frac{5N_l^2 - 1}{45}\left(\frac{h}{\delta_w}\right)^3. \tag{9.13}$$

The skin depth of the winding conductor at the n-th harmonic of the inductor current is given by [14]

$$\delta_{wn} = \sqrt{\frac{2}{\omega_n \mu_0 \sigma_w}} = \frac{1}{\sqrt{\pi \mu_0 \sigma_w n f}} = \sqrt{\frac{\rho_w}{\pi \mu_0 n f}} = \frac{\delta_w}{\sqrt{n}} \quad \text{for } n = 1, 2, 3, ... \tag{9.14}$$

Substituting the skin depth at n-th harmonic in (9.14) into (9.11), we obtain the ac-to-dc winding resistance ratio at the n-th harmonic for low- and medium-frequencies

$$F_{RLMF(n)} = \frac{R_{wLMF(n)}}{R_{wdc}} \approx 1 + \frac{n^2(5N_l^2 - 1)}{45}\left(\frac{h}{\delta_w}\right)^4. \tag{9.15}$$

Therefore, the winding ac resistance ratio at the n-th harmonic for low- and medium-frequencies is expressed as

$$R_{wLMF(n)} = F_{RLMF(n)} R_{wdc}$$

$$= \frac{\rho_w l_w}{b\delta_w\left(\frac{h}{\delta_w}\right)}\left[1 + \frac{n^2(5N_l^2 - 1)}{45}\left(\frac{h}{\delta_w}\right)^4\right] = \frac{\rho_w l_w}{b\delta_w}\left[\frac{1}{\left(\frac{h}{\delta_w}\right)} + \frac{n^2(5N_l^2 - 1)}{45}\left(\frac{h}{\delta_w}\right)^3\right]. \tag{9.16}$$

Hence, the normalized winding ac resistance for the n-th harmonic is

$$F_{rLMF(n)} = \frac{F_{RLMF(n)}}{\left(\frac{h}{\delta_w}\right)} = \frac{R_{wLMF(n)}}{\frac{\rho_w l_w}{b\delta_w}} \approx \frac{1}{\frac{h}{\delta_w}} + \frac{n^2(5N_l^2 - 1)}{45}\left(\frac{h}{\delta_w}\right)^3. \tag{9.17}$$

9.3 Fourier Series of The Inductor Current for the Pulsewidth-Modualted Dc-Dc Converters in DCM

From Fig. 9.1, the inductor current waveform for the pulsewidth-modulated dc-dc converter in DCM is

$$i_L = \begin{cases} \frac{\Delta i_L}{DT} t, & \text{for } 0 < t \le DT \\ \frac{-\Delta i_L}{D_1 T}(t - DT) + \Delta i_L, & \text{for } DT < t \le (D + D_1)T \\ 0, & \text{for } D_w T < t \le T \end{cases} \tag{9.18}$$

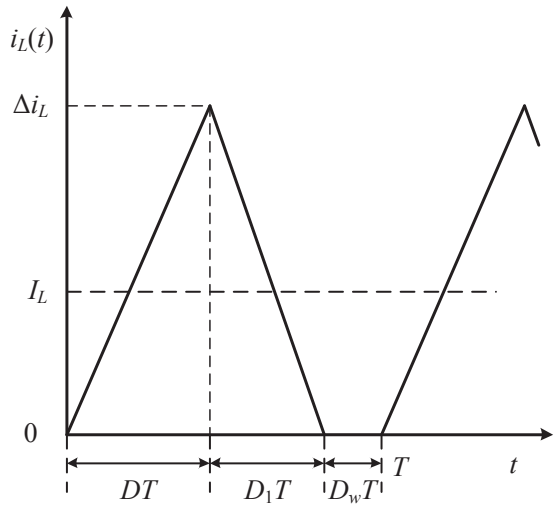

Figure 9.1: Inductor current waveform $i_L(t)$ for the PWM dc-dc power converters operating in DCM.

The Fourier series of the inductor current in (9.18) is given by

$$\begin{aligned} i_L(t) &= I_L + \sum_{n=1}^{\infty}(a_n \cos\ n\omega t + b_n \sin\ n\omega t) \\ &= I_L + \sum_{n=1}^{\infty} I_{mn} \cos(n\omega t + \phi_n) \end{aligned} \tag{9.19}$$

where the amplitude of each harmonic is

$$I_{mn} = \sqrt{a_n^2 + b_n^2} \tag{9.20}$$

and the phase shift is

$$\phi_n = -\arctan\left(\frac{b_n}{a_n}\right). \tag{9.21}$$

The dc component of the inductor current is

$$I_L = \frac{1}{T}\int_0^{(D+D_1)T} i_L(t)dt = \frac{\Delta i_L(D+D1)}{2}. \tag{9.22}$$

The Fourier series coefficients are

$$a_n = \frac{2}{T}\int_0^{(D+D_1)T} i_L(t)\cos(n\omega t)dt = \frac{\Delta i_L}{2\pi^2 n^2 D D_1}X_n = \frac{I_L}{\pi^2 n^2 D D_1(D+D_1)}X_n \tag{9.23}$$

and

$$b_n = \frac{2}{T}\int_0^{(D+D_1)T} i_L(t)\sin(n\omega t)dt = \frac{\Delta i_L}{2\pi^2 n^2 D D_1}Y_n = \frac{I_L}{\pi^2 n^2 D D_1(D+D_1)}Y_n \tag{9.24}$$

where

$$X_n = D_1[\cos(2\pi nD) - 1] - D\{\cos[2\pi n(D + D_1)] - \cos(2\pi nD)\} \tag{9.25}$$

and

$$Y_n = D_1 \sin(2\pi nD) - D\{\sin[2\pi n(D + D_1)] - \sin(2\pi nD)\}. \tag{9.26}$$

Substituting (9.23), (9.24), (9.25), and (9.26) into (9.20), one obtains amplitudes of the fundamental component and the harmonics of the inductor current of the PWM dc-dc converters operating in DCM

$$I_{mn} = \sqrt{a_n^2 + b_n^2} = \frac{\Delta i_L}{2\pi^2 n^2 D D_1}\sqrt{X_n^2 + Y_n^2} = \frac{I_L}{\pi^2 n^2 D D_1 (D + D_1)}\sqrt{X_n^2 + Y_n^2}. \tag{9.27}$$

9.4 Derivation of Low- and Medium-Frequency Approximation of Dowell's Equation for Solid-Round-Wire Windings at Harmonic Frequency

The low and medium frequency approximation of the ac-to-dc winding resistance ratio for the winding conducting sinusoidal current $i_l(t) = I_{Lm} \sin \omega t$ is expressed as [45]

$$F_{RLMF} \approx 1 + \frac{5N_l^2 - 1}{45} A^4 = 1 + \frac{5N_l^2 - 1}{45} \left(\frac{\pi}{4}\right)^3 \eta^2 \left(\frac{d}{\delta_w}\right)^4. \tag{9.28}$$

The skin depth of the winding conductor at the n-th harmonic of the inductor current is given by [14]

$$\delta_{wn} = \sqrt{\frac{2}{\mu_0 \sigma_w n \omega}} = \frac{1}{\sqrt{\pi \mu_0 \sigma_w n f}} = \sqrt{\frac{\rho_w}{\pi \mu_0 n f}} = \frac{\delta_w}{\sqrt{n}}. \tag{9.29}$$

Substituting the right side of (9.29) in place of δ_w in (9.28), one obtains the low and medium frequency approximation of the ac-to-dc winding resistance ratio of the inductor winding at the n-th harmonic in terms of δ_w, i.e., fundamental frequency, as

$$F_{RLMFn} = 1 + \frac{\left(\frac{\pi}{4}\right)^3 \eta^2 (5N_l^2 - 1)}{45} \left(\frac{d\sqrt{n}}{\delta_w}\right)^4 = 1 + \frac{n^2(5N_l^2 - 1)}{45} A^4. \tag{9.30}$$

9.5 Derivation of High-Frequency Approximation of Dowell's Equation for Harmonics

The high-frequency approximation of the ac-to-dc winding resistance ratio for the winding conducting sinusoidal current $i_l(t) = I_{Lm} \sin \omega t$ is expressed as [14]

$$F_{RLMF} = \frac{2N_l^2 + 1}{3} A = \frac{2N_l^2 + 1}{3} \left(\frac{\pi}{4}\right)^{0.75} \sqrt{\eta} \frac{d}{\delta_w}. \tag{9.31}$$

Substituting the right side of (9.29) in place of δ_w in (9.31), one obtains the high-frequency approximation of the ac-to-dc winding resistance ratio of the inductor winding at the n-th harmonic in terms of δ_w at the fundamental frequency, as

$$F_{RLMFn} = \frac{2N_l^2 + 1}{3} \left(\frac{\pi}{4}\right)^{0.75} \sqrt{\eta n} \frac{d}{\delta_w} = \frac{\sqrt{n}(2N_l^2 + 1)}{3} A. \tag{9.32}$$

Publications

Journal Papers

1. R. P. Wojda and M. K. Kazimierczuk, "Analytical optimization of solid-round-wire windings," *IEEE Transactions on Industrial Electronics*, Digital Object Identifier : 10.1109/TIE.2012.2189543, Feb. 2012, accepted and in print.
2. R. P. Wojda and M. K. Kazimierczuk, "Winding resistance of litz-wire and multi-strand inductors," *IET Proceedings on Power Electronics*, vol. 5, no. 2, pp. 254-268, Feb. 2012.
3. R. P. Wojda and M. K. Kazimierczuk, "Optimum foil thickness of inductors conducting dc and non-sinusoidal periodic currents," *IET Proceedings on Power Electronics*, accepted and in print.
4. R. P. Wojda and M. K. Kazimierczuk, "Proximity effect winding loss in different conductors using magnetic field averaging," *COMPEL: International Journal for Computation and Mathematics in Electrical and Electronic Engineering*, vol. 31, no. 6, Nov. 2012, accepted and in print.
5. M. K. Kazimierczuk and R. P. Wojda, "Foil winding resistance and power loss in individual layers of inductors," *JET International Journal of Electronics and Telecommunications*, vol. 56, no. 3, pp. 237-246, Sept. 2010.

Conference Papers

6. R. P. Wojda and M. K. Kazimierczuk, "Analytical optimization of foil windings of inductors conducting non- sinusoidal periodic currents," in *Proceedings of Electrical Manufacturing and Coil Winding Conference*, Milwaukee, WI, May 8-10, 2012.
7. R. P. Wojda and M. K. Kazimierczuk, "Analytical optimization of solid-round-wire windings of inductors conducting non-sinusoidal periodic currents," in *Proceedings of Electrical Manufacturing and Coil Winding Conference*, Milwaukee, WI, May 8-10, 2012.
8. M. K. Kazimierczuk and R. P. Wojda, "Maximum drain efficiency class F3 RF power amplifier," in *Proceedings of IEEE International Symposium on Circuits and Systems*, Rio de Janeiro, Brazil, May 15-18, 2011, pp. 2785-2788.
9. R. P. Wojda and M. K. Kazimierczuk, "Proximity-effect winding loss in rectangular conductors," in *Proceedings of Electrical Manufacturing and Coil Winding Conference*, Nashville, TN, Sept. 19-21, 2011.
10. R. P. Wojda and M. K. Kazimierczuk, "Comparison of winding resistance with litz-wire and solid-round wire," in *Proceedings of Electrical Manufacturing and Coil Winding Conference*, Dallas, TX, Oct. 18-20, 2011.

References

[1] E. Bennett and S. C. Larson, "Effective resistance to alternating currents of multilayer windings," *Trans. Amer. Inst. Elect. Eng.*, vol. 59, pp. 1010–1017, Dec. 1940.

[2] P. J. Dowell, "Effects of eddy currents in transformer windings," *Proc. IEE*, vol. 113, no. 8, pp. 1387–1394, Aug. 1966.

[3] M. P. Perry, "Multiple layer series connected winding design for minimum losses," *IEEE Trans. Power App. Syst.*, vol. PAS-98, no. 1, pp. 116–123, Jan./Feb. 1979.

[4] M. Bartoli, N. Noferi, A. Reatti, and M. K. Kazimierczuk, "Modeling winding losses in high-frequency power inductors," *J. Circuits, Syst. Comput.*, vol. 5, no. 4, pp. 607–626, Dec. 1995.

[5] N. H. Kutkut and D. M. Divan, "Optimal air-gap design in high-frequency foil windings," *IEEE Trans. Power Electron.*, vol. 13, no. 5, pp. 942–949, Sept. 1998.

[6] N. H. Kutkut, "A simple technique to evaluate winding losses including two-dimensional edge effect," *IEEE Trans. Power Electron.*, vol. 13, no. 5, pp. 950–958, Sept. 1998.

[7] A. Reatti and M. K. Kazimierczuk, "Comparison of various methods for calculating the ac resistance of inductors," *IEEE Trans. Magn.*, vol. 37, no. 3, pp. 1512–1518, May 2002.

[8] N. Das and M. K. Kazimierczuk, "An overview of technical challenges in the design of current transformers," in *Proc. of the Electrical Manufacturing and Coil Winding Conference*, Indianapolis, IN, USA, Oct. 24-26, 2005.

[9] M. J. Hole and L. C. Appel, "Stray capacitance of a two-layer air-cored inductor," *IEE. Proc., Part G, Circuits, Devices and Systems*, vol. 152, no. 6, pp. 565–572, Dec. 2005.

[10] P. Scoggins, "A guide to design copper-foil inductors," *Power Electronics Technology*, pp. 30–34, July 2007.

[11] D. C. Pentz and I. W. Hofsajer, "Improved AC-resistance of multiple foil winding by varying of thickness of successive layers," *COMPEL, Int. J. Computat. Math. Elect. Electron. Eng.*, vol. 27, no. 1, pp. 181–195, Jan. 2008.

[12] M. K. Kazimierczuk and H. Sekiya, "Design of ac resonant inductors using area product method," in *IEEE Energy Conversion Conference and Exhibition*, San Jose, CA, USA, Sept. 20-24, 2009, pp. 994–1001.

[13] H. Sekiya and M. K. Kazimierczuk, "Design of RF-choke inductors using core geometry coefficient," in *Proc. Electrical Manufacturing and Coil Winding Conference*, Nashville, TN, USA, Sept./Oct. 29-1, 2009.

[14] M. K. Kazimierczuk, *High-Frequency Magnetic Components*. Chichester, UK: John Wiley & Sons, Nov. 2009.

[15] D. Murthy-Bellur and M. K. Kazimierczuk, "Harmonic winding loss in buck dc-dc converter for discontinuous conduction mode," *IET Power Electron.*, vol. 3, no. 5, pp. 740–754, Sept. 2010.

[16] ——, "Winding losses caused by harmonics in high-frequency flyback transformers for pulse-width modulated dc-dc converters in discontinuous conduction mode," *IET Power Electron.*, vol. 3, no. 5, pp. 804–817, Sept. 2010.

[17] J. Lameraner and M. Stafl, *Eddy Currents*. Illife Books, 1966.

[18] P. S. Venkatraman, "Winding eddy current losses in switch mode power transformers due to rectangular wave currents," in *Proc. Powercon 11*, 1984, pp. 1–11.

[19] A. W. Lotfi, P. M. Gradzki, and F. C. Lee, "Proximity effects in coils for high frequency power applications," *IEEE Trans. Magn.*, vol. 28, no. 5, pp. 2169–2171, Sept. 1992.

[20] J. Vandalec and P. D. Ziogas, "A novel approach for minimizing high-frequency transformer copper loss," *IEEE Trans. Power Electron.*, vol. 3, no. 3, pp. 166–176, July 1988.

[21] A. M. Urling, V. A. Niemela, G. R. Skutt, and T. G. Wilson, "Characterizing high-frequency effects in transformer windings-a guide to several significant articles," in *IEEE APEC*, Baltimore, MD, USA, Mar. 11-17, 1989, pp. 373–385.

[22] M. Bartoli, A. Reatti, and M. K. Kazimierczuk, "High-frequency models of ferrite core inductors," in *Proc. IEEE Int. Conf. Ind. Electron., Cont., Instrumentat., (IECON94)*, Bologna, Italy, Sept. 5-9, 1994, pp. 170–175.

[23] ——, "Predicting the high-frequency ferrite-core inductor performance," in *Proc. Conf. on Electrical Manufacturing and Coil Winding*, Chicago, IL, USA, 1994, pp. 409–413.

[24] ——, "Modeling iron-powder inductors at high frequencies," in *Proc. IEEE Industry Applications Society Annual Meeting*, vol. 2, Denver, CO, USA, Oct. 2-6, 1994, pp. 1225–1232.

[25] M. Bartoli, N. Noferi, A. Reatti, and M. K. Kazimierczuk, "Modeling litz-wire winding losses in high-frequency power inductors," in *Proceedings of the IEEE Power Electronics Specialists Conference*, Baveno, Italy, June 23-27, 1996, pp. 1960–1696.

[26] M. Bartoli, A. Reatti, and M. K. Kazimierczuk, "Minimum copper and core losses power inductors design," in *Proceedings of the 1996 Thirty-First IEEE Industry Applications Society IAS Annual Meeting*, vol. 3, San Diego, CA, USA, Oct. 6-10, 1996, pp. 1369–1376.

[27] R. Petkov, "Optimum design of a high-power, high-frequency transformer," *IEEE Trans. Power Electron.*, vol. 11, no. 1, pp. 33–42, Jan. 1996.

[28] W. T. Mclyman, *Transformer and Inductor Design Handbook*, 3rd ed. Marcel Dekker, 2004.

[29] D. C. Hanselman and W. H. Peake, "Eddy-current effects in slot-bound conductors," *Proc. Inst. Elect. Eng. B Electr*, vol. 142, no. 2, pp. 131–136, Mar. 1995.

[30] N. Kondrath and M. K. Kazimierczuk, "Inductor winding loss owing to skin and proximity effects including harmonics in non-isolated pulse-width modulated dc-dc converters operating in continuous conduction mode," *IET, Power Electron.*, vol. 3, no. 6, pp. 989–1000, Nov. 2010.

[31] P. N. Murgatroyd, "Calculation of proximity losses in multistranded conductor branches," *IEE Proceedings, Part A, Physical Science, Measurements and Instrumentation, Management and Education*, vol. 136, no. 3, pp. 115–120, May 1989.

[32] J. A. Ferreira, "Analytical computation of ac resistance of round and rectangular litz wire windings," *IEE Proceedings, Part B, Electric Power Applications*, vol. 139, no. 1, pp. 21–25, Jan. 1992.

[33] ——, "Improved analytical modeling of conductive losses in magnetic components," *IEEE Trans. Power Electronics*, vol. 9, no. 1, pp. 127–131, Jan. 1994.

[34] A. W. Lotfi and F. C. Lee, "A high frequency model for litz wire for switch-mode magnetics," in *Proc. of the 1993 IEEE Industry Applications Society Annual Meeting*, vol. 2, Toronto, Ont., Canada, Oct. 2-8, 1993, pp. 1169–1175.

[35] F. Robert, P. Mathys, and J.-P. Schauwers, "Ohmic losses calculation in SMPS transformers: numerical study of Dowell's approach accuracy," *IEEE Trans. Magn.*, vol. 34, no. 4, pp. 1255–1257, July 1998.

[36] W. G. Hurley, W. H. Wolfe, and J. G. Breslin, "Optimized transformer design: Inclusive of high-frequency effects," *IEEE Trans. Power Electron.*, vol. 13, no. 4, pp. 651–659, July 1998.

[37] W. G. Hurley, E. Gath, and J. G. Breslin, "Optimizing the ac resistance of multilayer transformer windings with arbitrary current waveforms," *IEEE Trans. Power Electron.*, vol. 15, no. 2, pp. 369–376, Mar. 2000.

[38] C. R. Sullivan, "Optimal choice for number of strands in a litz-wire transformer winding," *IEEE Trans. Power Electron.*, vol. 14, no. 2, pp. 283–291, Mar. 1996.

[39] ——, "Cost-constrained selection of strand diameter and number in a litz-wire transformer winding," *IEEE Trans. Power Electron.*, vol. 16, no. 2, pp. 281–288, Mar. 2001.

[40] A. V. den Bossche and V. C. Valchev, *Inductors and Transformers for Power Electronics*. Boca Ranton, FL, USA: Taylor & Francis, 2005.

[41] M. Albach, "Two-dimensional calculation of winding losses in transformers," in *Proceedings of the IEEE 31st Annual Power Electronics Specialists Conference PESC00*, Galway, Ireland, June 18-23, 2000, pp. 1639–1644.

[42] J. Schutz, J. Roudet, and A. Schellmanns, "Modeling litz-wire windings," in *Proc. IEEE Industry Appl. Soc. Annual Meeting (IAS)*, vol. 2, New Orleans, LA, USA, Oct. 5-9, 1997, pp. 1190–1195.

[43] G. W. O. Howe, "The high-frequency resistance of multiply-stranded insulated wire," *Proc. Royal Soc. Lon.*, vol. 93, pp. 468–492, 1917.

[44] F. Tourkhani and P. Viarouge, "Accurate analytical model of winding losses in round litz wire winding," *IEEE Transactions on Magnetics*, vol. 37, no. 1, pp. 538–443, Jan. 2001.

[45] E. C. Snelling, *Soft Ferrites, Properties and Applications*, 2nd ed. London, U.K.: Butterworth, 1988.

[46] F. Robert, P. Mathys, and J.-P. Schauwers, "A closed-form formula for 2-d ohmic losses calculation in SMPS transformer foil," *IEEE Transactions on Power Electronics*, vol. 16, no. 3, pp. 437–444, May 2001.

[47] X. Nan and C. R. Sullivan, "Simplified high-accuracy calculation of eddy-current losses in round-wire windings," in *35th Annual IEEE Power Electronics Specialist Conference*, Aachen, Germany, June 20-25, 2004, pp. 873–879.

[48] ——, "An improved calculation of proximity-effect loss in high-frequency windings of round conductors," in *IEEE Power Electronics Specialist Conference*, June 20-25, 2003, pp. 853–860.

[49] J. Acero, P. Hernandez, J. M. Burdio, R. Alonso, and L. A. Barragan, "Simple resistance calculation in litz-wire planar windings for induction cooking appliances," *IEEE Transactions on Magnetics*, vol. 41, no. 4, pp. 1280–1288, April 2005.

[50] J. Acero, J. M. Burdio, R. Alonso, L. A. Barragan, , and D. Puyal, "Frequency-dependent resistance in litz-wire planar windings for domestic induction heating appliances," *IEEE Transactions on Power Electronics*, vol. 21, no. 4, pp. 856–866, July 2006.

[51] X. Nan and C. R. Sullivan, "An equivalent complex permeability model for litz-wire windings," *IEEE Transactions on Industry Applications*, vol. 45, no. 2, pp. 854–860, Mar./Apr. 2009.

[52] M. K. Kazimierczuk and D. Czarkowski, *Resonant Power Converters*. New York, NY, USA: IEEE Press/John Wiley & Sons, 2011.

[53] A. Aminian and M. Kazimierczuk, *Electronic Devices. A Design Approach*. Upper Saddle, NJ: Prentice Hall, 2004.

[54] M. K. Kazimierczuk, *Pulse-Width Modulated DC-DC Power Converters*. Chichester, UK: John Wiley & Sons, 2008.

[55] ——, *RF Power Amplifiers*. Chichester, UK: John Wiley & Sons, 2008.

[56] K. W. E. Cheng and P. D. Evans, "Calculation of winding losses in high frequency toroidal inductors using single strand conductors," *IEE, Electric Power Applications*, vol. 141, no. 2, pp. 56–62, Mar. 1994.

[57] ——, "Calculation of winding losses in high frequency toroidal inductors using multistrand conductors," *IEE, Electric Power Applications*, vol. 142, no. 5, pp. 313–322, Sept. 1995.

[58] D. C. Hamill, "An efficient active ripple filter for use in dc-dc conversion," *IEEE Trans. Aerosp. Electron. Syst.*, vol. 32, no. 3, pp. 1077–1084, July 1996.

[59] M. Veerachary, T. Senjyu, and K. Uezato, "Voltage-based maximum power point tracking control of pv system," *IEEE Trans. Aerosp. Electron. Syst.*, vol. 38, no. 1, pp. 262–270, Jan. 2000.

[60] M. Veerachary, "Fourth-order buck converter for maximum power point tracking applications," *IEEE Trans. Aerosp. Electron. Syst.*, vol. 47, no. 2, pp. 896–911, Apr. 2011.

[61] M. K. Kazimierczuk, G. Sanciento, U. Reggiani, and A. Massarini, "High-frequency small-signal model of ferrite core inductors," *IEEE Trans. Magn.*, vol. 35, no. 5, pp. 4185–4191, Sept. 1999.

[62] G. Grandi, M. K. Kazimierczuk, A. Massarini, U. Reggiani, and G. Sanciento, "Model of laminated iron-core inductors for high-frequencies," *IEEE Trans. Magn.*, vol. 40, no. 4, pp. 1839–1845, July 2004.

[63] P. M. Gradzki, M. M. Jovanovic, and F. C. Lee, "Computer-aided design for high-frequency power transformer," in *in Proc. 5th Annu. Appl. Power Electron. Conf. Expo.*, Los Angeles, CA, USA,, Mar. 11-16, 1990, pp. 336–343.

[64] U. Kirchenberger, M. Marx, and D. Schroder, "A contribution to the design optimization of resonant inductors for high power resonant dc-dc converters," in *in Proc. IEEE IAS Annu. Meet.*, Huston, TX, USA, Oct. 4-9, 1992, pp. 994–1001.

[65] A. M. Pernia, F. Nuno, and J. M. Lopera, "1D/2D transformer electric model for simulation in power converters," in *in Proc. 26th Annu. IEEE Power Electron. Spec. Conf.*, Atlanta, GA, USA, June 18-22, 1995, pp. 1043–1049.

[66] A. Massarini and M. K. Kazimierczuk, "Self-capacitance of inductors," *IEEE Trans. Power Electron.*, vol. 12, no. 4, pp. 671–676, July 1997.

[67] G. Grandi, M. K. Kazimierczuk, A. Massarini, and U. Reggiani, "Stray capacitance of single layer solenoid air-core inductors," *IEEE Trans. Ind. Appl.*, vol. 35, no. 5, pp. 1162–1168, Sept./Oct. 1999.

[68] R. Wrobel, N. McNeill, and P. H. Mellor, "Performance analysis and thermal modeling of a high-energy-density prebiased inductor," *IEEE Trans. Ind. Electron.*, vol. 57, no. 1, pp. 201–208, Jan. 2010.

[69] M. K. Kazimierczuk and R. P. Wojda, "Foil winding resistance and power loss in individual layers of inductors," *Int. J. Electron. Telecommun.*, vol. 56, no. 3, pp. 237–246, Sept. 2010.

[70] M. L. Heldwein, H. Ertl, J. Biela, and J. W. Kolar, "Implementation of a transformer-less common mode active filter for off-line converter systems," *IEEE Trans. Ind. Electron.*, vol. 57, no. 5, pp. 1772–1786, May 2010.

[71] D. Murthy-Bellur, N. Kondrath, and M. K. Kazimierczuk, "Transformer winding loss caused by skin and proximity effects including harmonics in pwm dc-dc flyback converter for continuous conduction mode," *IET Power Electron.*, vol. 4, no. 4, pp. 363–373, Apr. 2011.

[72] M. K. Kazimierczuk and R. P. Wojda, "Maximum drain efficiency class f3 rf power amplifier," in *IEEE International Symposium on Circuits and Systems (ISCAS)*, Rio de Janeiro, Brasil, May 15-18, 2011, pp. 2785–2788.

[73] R. Wrobel and P. H. Mellor, "Thermal design of high-energy-density wound components," *IEEE Trans. Ind. Electron.*, vol. 58, no. 9, pp. 4096–4104, Sept. 2011.

[74] R. Wrobel, A. Mlot, and P. H. Mellor, "Contribution of end-winding proximity losses to temperature variation in electromagnetic devices," *IEEE Trans. Ind. Electron.*, vol. 59, no. 2, pp. 848–857, Feb. 2012.

[75] R. P. Wojda and M. K. Kazimierczuk, "Winding resistance of litz-wire and multi-strand inductors," *IET Power Electron.*, vol. 5, no. 2, pp. 257–268, Feb. 2012.

[76] D. A. Nagarajan, D. Murth-Bellur, and M. K. Kazimierczuk, "Harmonic winding losses in the transformer of a forward pulse width modulated dc-dc converter for continuous conduction mode," *IET Power Electron.*, vol. 5, no. 2, pp. 221–236, Feb. 2012.

[77] Y. Hinago and H. Koizumi, "A switched-capacitor inverter using series/parallel conversion with inductive load," *IEEE Trans. Ind. Electron.*, vol. 59, no. 2, pp. 878–887, Feb. 2012.

[78] R. P. Wojda and M. K. Kazimierczuk, "Proximity-effect winding loss in different conductors using magnetic field averaging," *COMPEL, Int. J. Computat. Math. Elect. Electron. Eng.*, vol. 31, no. 6, Nov. 2012.

[79] R. J. Kemp, P. N. Murgatroyd, and N. J. Walker, "Self resonance in foil inductors," *Electron. Lett.*, vol. 11, no. 15, pp. 337–338, July 1975.

[80] R. Reeves, "Air-cored foil-wound inductors," *Proc. Inst. Elect. Eng.*, vol. 125, no. 5, pp. 460–464, Jan. 1978.

[81] N. H. Kutkut, D. W. Novotny, D. M. Divan, and E. Yeow, "Analysis of winding losses in high frequency foil wound inductors," in *in Proc. 30th. IEEE IAS Annu. Meet.*, Orlando, FL, USA,, Oct. 8-12, 1995, pp. 859–867.

[82] M. Yamaguchi, K. Yamada, and K. H. Kim, "Slit design consideration on the ferromagnetic RF integrated inductor," *IEEE Tran. Magn.*, vol. 42, no. 10, pp. 3341–3343, Oct. 2006.

[83] S. Muroga, Y. Endo, Y. Sasaki, M. Nagata, and M. Yamaguchi, "Evaluation of thin film noise suppressor applied to noise emulator chip implemented in 65 nm CMOS technology," *IEEE Tran. Magn.*, vol. 47, no. 10, pp. 4485–4488, Oct. 2011.

[84] R. P. Wojda and M. K. Kazimierczuk, "Analytical optimization of solid-round-wire windings," *IEEE Trans. Ind. Electron.*, vol. DOI: 10.1109/TIE.2012.2189543, in print.

[85] B. N. Datta, *Numerical Linear Algebra and Applications*, 2nd ed. SIAM, 2010.

[86] www.siemens.de/.

[87] www.pack feindraehte.de/.

[88] www.mag inc.com/.